Crystallisation of glycine and dipicolinic acid (DPA) from microemulsions

CHEN, CEN

Crystallisation of glycine and dipicolinic acid (DPA) from microemulsions

Cen Chen

A thesis submitted for the degree of Doctor of Philosophy at the University of Durham

Department of Chemistry

December 2012

Acknowledgements

Eventually, upon submitting my thesis, there are so many people that I need to say ‘thank you’ to; without them, I could never have progressed this far:

To work colleagues:

- My supervisor, Dr. Sharon Cooper, for her support, guidance, and patience over the past 3 years and 3 months. She herself is a lovely and intelligent lady, who is like a fountain of knowledge for me. Many of our discussions have certainly inspired and encouraged me to continue working on this project.
- GlaxoSmithKline (GSK) for funding
- Dr. Catherine Nicholson (Kate) and Natasha Loines (soon to be Hargreaves), thanks to their great amount of enthusiasm and patience when correcting and proof-reading this thesis. I know both of you had (or probably are still having) a really tough time. I hope tea and chocolate can make it a little better.
- Emma Talbot and Alex Hargreaves for very useful discussions, in addition to company at tea break.
- All my lab colleagues, past and present, for collaborative work, idea discussion, general lab work support and keeping me company.

To technical support:

- Dr. Budhika Mendis (Department of Physics) for training and helping me run analysis samples on the TEM.
- Dr. Dima Yufit (Durham Crystallography service) for running my single crystal samples and solving them.
- Mr. William Douglas Carswell (Department of Chemistry) for analysing my samples on the DSC and TGA.
- Ms. Judith Magee for running elemental and ion analysis on my samples.
- Ms. Helen Riggs for running and training me on both the SAXS and ESEM.

To family and friends

- My dear parents, for their trust, support and encouragement. In particular, thanks to their wise decision for 'posting' me to this country when I was 16. Otherwise I would never become who I am now and would never know these lovely people.

  （中文翻译:亲爱的父母，非常感谢你们长期以来对我的支持和鼓励。尤其是在我 16 岁时就把我送到英国的明智决定，以及给予我最大程度的信任，鼓励以及自由的成长空间。否则，我无法成为现在的这个我，也没有机会认识这些可爱又可敬的人们。）

- Natasha and Kate, for being both my excellent work colleagues and best friends, who have introduced me a large number of British cultural traditions.

Statement of Copyright

Publication List

The following publications have arisen from work presented in this thesis:

1. 'Leapfrogging Ostwald's rule of stages: Crystallization of stable γ-glycine directly from microemulsions' Methodology' C. Chen, O. Cook, C. E. Nicholson, S. J. Cooper *Cryst. Growth Des.* **2011**, *11*, 2228-2237.

2. 'Stable Polymorphs Crystallized Directly under Thermodynamic Control in Three-Dimensional Nanoconfinement: A Generic Methodology' C. E. Nicholson, C. Chen, B. Mendis, S. J. Cooper *Cryst. Growth Des.* **2011**, *11*, 363-366.

Abstract

Crystallisation under confinement conditions can produce nanocrystals with high surface-to-volume ratio, altered intrinsic properties (e.g. melting point depression), preferred orientation, selective polymorphic form and well-controlled morphology. The confinement conditions are normally achieved by nanopores prepared from polymers, which provide physical constraints on the size of the crystal. In this thesis, microemulsions, which have been extensively used for nanoparticle synthesis, are employed to achieve the 3D-nanoconfinement, owing to their spherical morphology to provide volume control and excellent droplet size control (< 50 nm) via the addition of dispersed phase.

Thermodynamic control has been achieved during the crystallisation of glycine under the 3D-nanoconfinement generated by microemulsions. These microemulsions were prepared from heptane, Span 80/Brij 30, glycine solution, and methanol antisolvent. Polymorph selection has been obtained by varying the microemulsion compositions. A majority of γ-glycine was observed when the microemulsion droplet size was in the range of 3.3–4.2 nm. This is when the microemulsions just had sufficient glycine for crystallization. Below this, no crystallization was observed. The microemulsions comprised of 0.25 g 4% glycine solution and 0.8–1.5 g methanol per sample, with crystallisation yielding visible crystals in 2–3 weeks. Higher concentration of glycine solution (> 4.5%) yielded mostly the α form and excess amount of methanol (> 1.5 g) produced the β form, due to the loss of confinement within the microemulsion and the participation of solvent templating effects introduced by methanol. The polymorph outcome was not affected by the surfactant-continuous phase ratio.

.

Following on from the success of glycine and other organic/pharmaceutical compounds studied within the research group, dipicolinic acid (DPA) was chosen to study the thermodynamic control of hydrates within 3D-nanoconfinement. The hydration or solvation control was demonstrated in the microemulsions. In particular, hydration was only observed when the droplet sizes were greater than 4.3 nm with 15 mg/ml of DPA solution in the AOT system. However unexpected

formation of metal salts occurred, i.e. Na^+ and K^+ ions from impurities participated in the crystal structures, regardless of the surfactants or solvents employed. Upon treatment with 2M HCl solution, metal salt participation in DPA crystallisation could be prevented. From the acidified microemulsions employing Trion X-100/1-hexanol as surfactants, no macroscopic sized crystals were seen. Instead, square plate-shaped nanoaggregates (30–100 nm in dimension) of 2–10 nm nanoparticles were obtained for samples with a droplet size of 4.01 nm, prepared from 18 mg/ml DPA in 2M HCl solution. Despite the strong electron density contrast across the nanocrystal surface, single crystal-like diffraction pattern (DP) was seen from these crystals, which was considered to be consistent with these nanocrystals being iso-oriented crystals/mesocrystals. The size and morphology of these nanoparticles can be controlled by varying the microemulsion composition. Lower DPA concentrations of 10–12 mg/ml and smaller droplet sizes of 2.40–3.15 nm produced much less organised nanoaggregates, with ‘arcing’ and ‘rings’ appearing in the DP, indicating the polycrystalline nature, whereas the highest DPA concentration of 18 mg/ml and the largest droplet of 4.01 nm could produce organized nanoaggregates that were barely distinguishable from single crystal structure.

Thesis Outline

This thesis contains six chapters and seven appendices, which are structured as follows.

Chapter 1 states the aim of this project and provides the background information for this thesis. The topics covered in this chapter include polymorphism, surfactant and colloidal systems, phase diagrams, crystallisation (nucleation and crystal growth), and kinetic and thermodynamic control of crystallisation. Further, a brief summary of the literature regarding previous studies on microemulsion synthesis and crystallisation is presented.

Chapter 2 covers the experimental techniques, both microemulsion preparation methods and various detection techniques, used to identity and analysis the liquid and solid components.

Chapter 3 details the crystallisation work of glycine from the microemulsion. This chapter begins with an introduction and a literature study, followed by the experimental detail. The results are discussed with respect to the literature and the conditions required to achieve thermodynamic control of this small organic molecule within the microemulsion are assessed.

Chapter 4 moves on to the crystallisation of dipicolinic acid, a molecule that may exist as two hydrate forms. The experimental details and results are discussed with respect to the control of the hydration level achieved. However the effect of impurities, in particular, the participation of metal ions, is highlighted.

Chapter 5 develops the study of dipicolinic acid (DPA) crystallisation, with the modification of microemulsion components and compositions, in an attempt to prevent the metal ion incorporation. The crystallisation products are examined and the microenvironment inside the microemulsions is studied to provide a rationale for the observations in both Chapter 4 and 5.

Chapter 6 briefly concludes the work presented in this thesis and suggests further work to provide further insight into the microemulsion crystallisation.

Appendix 1 lists the surfactants used, in addition to their structures and properties. Appendix 2 and 3 detail the derivation of the Gibbs free energy of homogeneous and heterogeneous nucleation, respectively. Appendix 4 uses the optimum formulation in Chapter 3 as an example to illustrate the calculation of the geometric droplet size. Appendix 5 details the estimation of free water region in a w/o microemulsion, providing the GIFT radius is known. Appendices 6 and 7 contain the crystal structural information of the potassium salt trihydrate and the sodium salt methanol solvate of DPA, respectively.

List of abbreviations

15-Crown-5	1,4,7,10,13-Pentaoxacyclopentadecane
AOT	Dioctyl sulfosuccinate sodium salt
ATR-FTIR	Attenuated Total Reflectance Fourier Transform Infrared Spectroscopy
BCF	Burton, Cabrera and Frank
Brij® 30	Polyethylene Glycol Dodecyl Ether
CH_2/CH_3	Methylene/methyl group
CHN	Carbon Hydrogen Nitrogen
CMC	Critical Micelle Concentration
CN	Coordination Number
CNT	Classical Nucleation Theory
CPG	Controlled Pore Glass
CSD	Cambridge Structural Database
D_2O	Deuterated water
DLS	Dynamic Light Scattering
DP	Diffraction Pattern
DPA	Dipicolinic Acid
DSC	Differential Scanning Calorimetry
EDX	Energy-Dispersive X-Ray Spectroscopy
FFT	Fast Fourier Transform
GIFT	Generalised Indirect Fourier Transform
GSK	GlaxoSmithKline
H_2O	Water
HCl	Hydrochloric Acid
HLB	Hydrophile-Lipophile Balance
HREM	High Resolution Electron Microscopy
KOH	Potassium Hydroxide
MeOH	Methanol
MF	Metastable Polymorphic Form
NA	nanoaggregate
NaCl	Sodium Chloride

NaDPA/ Na_2DPA	Dipicolinic Acid Sodium Salt
NaOH	Sodium Hydroxide
NH_2/NH_3	Amine group
NMR	Nuclear Magnetic Resonance
o/w	Oil in Water
OH	Alcohol Group
PIT	Phase Inversion Temperature
p-PCHE	Poly(cyclohexalethylene)
ppm	Parts Per Million
PS-PMMA	Polystyrene-Polydimethylacrylamide
PXRD	Powder X-Ray Diffraction
RH	Relative Humidity
ROY	5-methyl-2[(2-nitrophenyl)-amino]-3-thio-phenecarbonitrile
S.D.	Standard Deviation
S.E.	Standard Error
SANS	Small Angle Neutron Scattering
SAXS	Small Angle X-Ray Scattering
SF	Stable Polymorphic Form
SO_3^-	Sulfur Trioxide Anion
Span® 80	Sorbitan Monooleate
SXRD	Single X-Ray Diffraction
TEM	Transmission Electron Microscopy
TGA	Thermogravimetric Analysis
Triton X-100	4-(1,1,3,3-Tetramethylbutyl)phenyl-polyethylene glycol
Triton X-114	(1,1,3,3-Tetramethylbutyl)phenyl-polyethylene glycol
UHP	Ultra High Purity
UV-Vis	Ultra-Violet Visible
VDWs	Van der Waals Interactions
w/o	Water in Oil
w/w	Weight/Weight
WAXS	Wide Angle X-Ray Scattering

List of symbols

Δ	Change in a given quantity
$\sum$	Interfacial area per unit volume
A	Surface area of a cluster
c	Number of components within a system
C_s	Spherical aberration coefficient
d	Crystal interplanar spacing
D	Encounter rate factor
ds_1	Diffraction limited spot size
f	Degrees of freedom
F	Helmholtz free energy
G	Gibbs free energy
h	Planck's constant
i	Number of monomers in a cluster
$I(q)$	Scattering function
J	Rate of nucleation
k_B	Boltzmann constant
k_D	Collision frequency
k_{en}	Encounter rate
k_{ex}	Material exchange rate
l	Depth of the disc shaped nuclei
m_e	Mass of electron
M_r	Molecular weight
n	Concentration of crystallising species
N	Population of nuclei in a given state
$n(i^*)$	Equilibrium concentration of critical nuclei
N_A	Avogadro's constant
Ne^-	Number of electrons in a molecule
p	Number of phases
P	Pressure
$p(r)$	Pair distribution function
q	Length of the scattering vector

r	Radial distance
R	Rate of crystal growth
S	Solute supersaturation ratio
S	Entropy
T	Temperature
U	Internal energy
v	Velocity
V	Volume
v_l	Molecular volume of a liquid
W^*	Impingement rate of a solute onto a nuclei
α, β, γ	Alpha, Beta and gamma polymorphs of glycine
δ	Net resolution
$\Delta\mu$	Supersaturation, the difference in chemical potentials between 2 phases
δ_1	Diffraction limit
δ_2	Spherical aberration
ε	Refractive index
η	Viscosity
θ	Angle
κ	Rate constant
λ	Wavelength
ρ	Density
ρ_e	Electron density
σ	Surface energy
τ_{en}	Collision time
φ	Semi-convergence angle
Ω	Pre-exponential factor
Φ	Volume fraction
ξ	Kinetic coefficient

Contents

Chapter 1 Introduction

1.1 Aim of this project

Polymorphism is vitally important in the pharmaceutical industries, due to intrinsic crystal properties affecting the stability, bioavailability, and toxicity[1]. As a consequence, various screening techniques, e.g. thermal cycling and high through-put screening, have been extensively utilised. Most of these techniques rely on either Ostwald's rule of stages[2] (i.e. kinetic control) or solvent effects (i.e. templating effects) to induce the formation of a specific polymorph, usually the most thermodynamically stable form. However, for the former (Ostwald's rule), the duration of transformation from the metastable to stable form is highly variable, whereas solvates are often produced from the latter case (solvent effect). For this reason, thermodynamic control of the polymorphic outcome is investigated, employing microemulsions as the vehicle to achieve 3D-nanoconfinement.

Inspired by Allen and Garti's work[3, 4] on emulsion/microemulsion crystallisation on glycine polymorphs, glycine was chosen as the model compound, owing to the high difficulty in obtaining the thermodynamically most stable γ form from pH neutral solutions. This study can thus test the sensitivity of the thermodynamic control in microemulsions. Furthermore, surfactants that can promote metastable forms were used to illustrate any competing effect (i.e. heterogeneous nucleation) due to the presence of surfactant templates.

Upon the success of glycine and other organic/pharmaceutical compounds studied by my colleagues, our research interests have extended to the area of hydrates, solvates and salts, which are also common forms of marketed drugs. Thus, dipicolinic acid (DPA), a key fragment of a GlaxoSmithKline (GSK) compound has attracted our attention, due to its one anhydrous and two hydrate forms. DPA was therefore studied to investigate and rationalise any possible hydrate formation in microemulsions.

1.2 Polymorphism

Polymorphism is defined as the ability of a crystalline solid to adopt more than one lattice structure in the solid state whilst retaining the same molecular composition[5-8]. The term crystalline implies the regular and indefinite three dimensional repetitions of structural units, termed unit cells. This structural difference may result from different molecular arrangements, conformations, or hydrogen bonding schemes, or any combination of the above, causing significantly different chemical and (or) physical properties. Crystal morphology, compressibility, density, viscosity, surface energy, mechanical and optical properties are all dependent on the crystal structures. Polymorphs are often distinguishable based on their thermal properties such as melting or sublimation properties, latent heat of fusion, heat of solution and enthalpy.

In the pharmaceutical industry, active pharmaceutical ingredients (APIs) are frequently produced in the solid state, typically exhibiting a variety of solid forms, including polymorphs, solvates and hydrates. Solvates and hydrates, also referred to as pseudo polymorphs, contain solvent and water respectively. Each polymorph of the drug candidate may display unique properties, including solubility, bioavailability, purity and stability. Therefore, it is important to confirm the identity of the polymorph in question.

The thermodynamically most stable polymorph (least soluble form) is generally the most desirable drug candidate, as the metastable systems are likely to fall to a lower energy state (a more thermodynamically stable form) upon slight perturbation of conditions in the system; such as temperature, pressure and humidity.[9-11]. In addition, certain pharmaceutical processes such as grinding, drying, milling and compaction are reported to accelerate the phase transition in pharmaceutical solids. Essentially, identifying the stable polymorph in the early stage of the drug development is crucial and failing to do so might lead to devastating consequences, such as an incorrect dosage, form re-working and delay in marketing the product[12-14].

The infamous case of Ritonavir[13, 14] has illustrated the importance of polymorph identification. Ritonavir is a marketed anti-HIV drug product, where a new polymorph with much lower solubility was discovered after the initial launch. As a result, this drug product had to be withdrawn from the market and redeveloped. It has been postulated that the solubility difference is a result of the difference in the hydrogen bonding networks[14] between the two forms (as shown in Figure1.1). All of the good hydrogen bond donors and acceptors are fully utilised in form II but the OH group in form I is vacant.

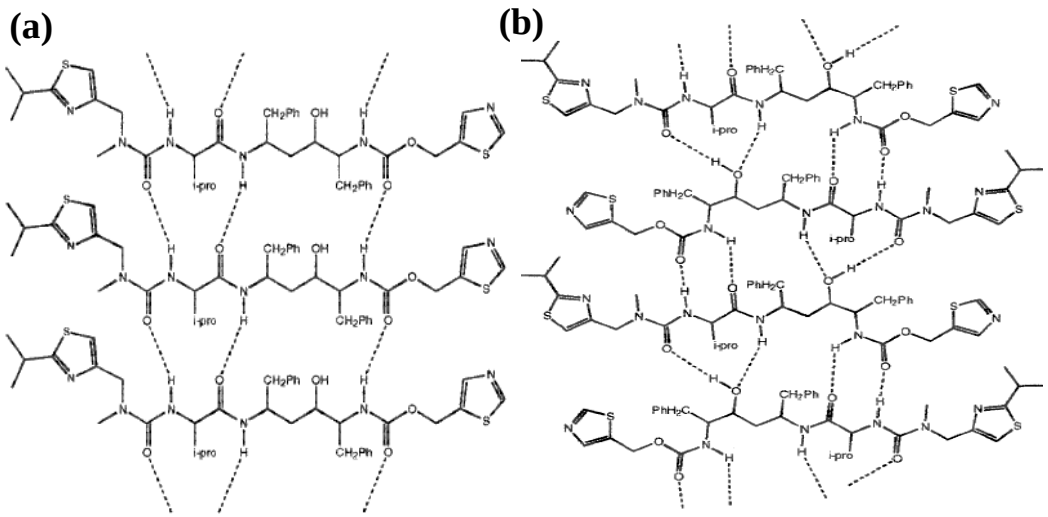

Figure 1.1[14] Hydrogen bonding networks for Ritonavir: (a) form I-beta like stacks; (b) form II. (Redrawn with permission from ref. 14, Copyright © 2001 Springer Science and Business Media)

In the polymorph screen prior to launch, form II was not found due to the energetically unfavoured cis conformation requiring higher input energy to crystallise. Upon surmounting the energy barrier, the strong hydrogen bonding compensates for the energy cost and thus form II is more stable. Thus to avoid future 'Ritonavir'-like cases, a generic approach of obtaining the thermodynamically most stable form is desired.

1.3 Surfactants

Surfactants, also known as surface active agents, are amphiphilic molecules containing both a hydrophilic head group and a hydrophobic chain. They are characterised by their ability to reside at an interface and thus lowering the free energy of that phase boundary; also known as the interfacial tension[15].

Based on the properties of the different head groups, surfactants can be classified into two major types: ionic surfactants and non-ionic surfactants. Non-ionic surfactants are those with charge neutral head groups, whereas ionic surfactants have charged head groups. Ionic surfactants can be further divided into three further subclasses: anionic, cationic, and zwitterionic/amphoteric surfactants. Examples of non-ionic surfactants include Span® 80 (Sorbitan monooleate), Brij® 30 (Polyethylene glycol dodecyl ether), and Triton X-100. AOT (Dioctyl sulfosuccinate sodium salt) is an example of ionic (anionic) surfactant (Figure 1.2). Appendix 1 lists the surfactants that are commonly used to prepare microemulsions.

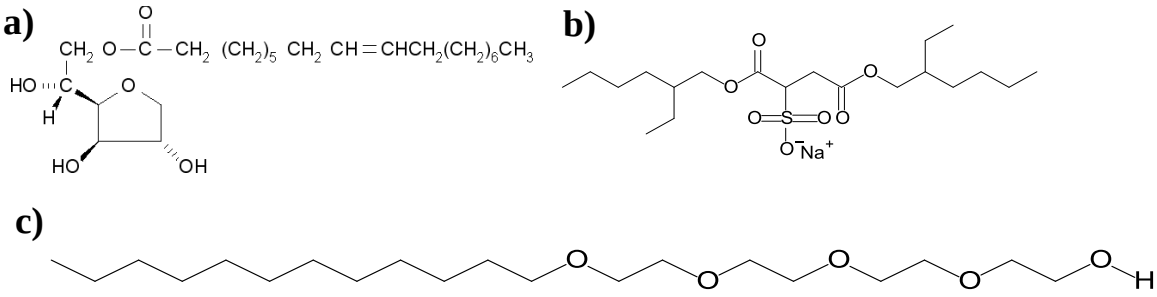

Figure 1.2 Examples of surfactants: (a) Non-ionic surfactant Span 80; (b) Ionic surfactant AOT; (c) Non-ionic surfactant Brij 30.

Surfactants can form a wide range of both homogeneous and heterogeneous structures. Homogeneous structures can be further divided into solid crystals having both long and short range of order, liquid crystals that only have short range order, or isotropic liquids that are completely random. Since micelles and microemulsions belong to the catalogue of isotropic liquids, only the homogeneous systems will be discussed in detail. Examples for heterogeneous systems are emulsions, foams and gels that consist of two or more phases.

1.3.1 Critical micelle concentration (CMC)

The critical micelle concentration (CMC) is the concentration at which the surfactant monomers start to agglomerate into micelles. At the CMC, many physical properties of the solution abruptly change, including surface tension, osmotic pressure, turbidity, solubilisation, and conductivity[15, 16], as illustrated in Figure 1.3.

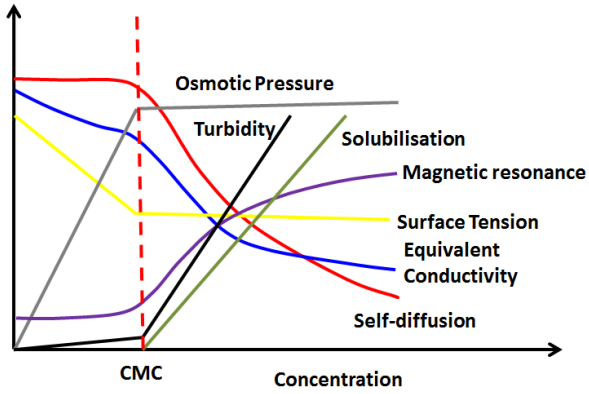

Figure 1.3[15-17] Changes in physical properties of an ionic surfactant against surfactant concentration (Redrawn with permission from ref. 15, Copyright © 2002, John Wiley and Sons)

The CMC in aqueous solution is dependent on many factors, foremost of which, the chemical structure of the surfactant. Surfactants with long alkyl chains have significantly lower CMCs than shorter ones. For instance triethylene glycol monohexyl ether (C_6E_3) has a CMC value of 10^5 μM whilst for hexaethylene glycol monododecyl ether ($C_{12}E_6$) the CMC is 68 μM[15]. Generally, the CMCs of non-ionic surfactants are at least two orders of magnitude lower than the ionic equivalents. Furthermore, the hydrophilic head group contributes to the CMC. Additionally, for surfactants containing non-ionic ethoxylate, increasing the number of ethylene oxide units would give a higher CMC. Other structural variations such as branching, conjugation and comprising aromatic structures to an alkyl chain will tend to decrease the CMC.

Temperature is another factor that influences the CMC. The CMCs of ionic surfactants such as sodium dodecylsulfate (SDS) are highly temperature sensitive[18]. Up to 25℃, the CMC decreases slightly with temperature (~0.5 mM) but increases rapidly once above 25℃. Non-ionic surfactants such as

penta(ethylene glycol)monodecyl ether ($C_{10}E_5$) only show a small reduction in CMC with a temperature increase (~0.5 mM) [16, 19]. In contrast pressure has a much smaller effect on the CMCs of surfactants[20-22]. The CMC of Triton X-100 only varies by *approx.* 0.05 mM, even with pressure increased up to 300 MPa, at 295 K[21].

Further to the two factors above, the addition of cosolutes, particularly electrolytes, to ionic surfactants can dramatically alter the CMC. For instance, addition of salt (NaCl)[23] decreases the CMC of ionic surfactants greatly, but this effect is largely related to the valency of the ions or counterions. For example, Muller *et. al* reported that the CMC values of $CH_3(CH_2)_8COONa$ and $CF_3(CH_2)_{10}COONa$ surfactants were different in NaOH and NaCl solutions[24]. Overall this reduction is more pronounced for longer chain surfactants than shorter ones. In contrast, salt addition only slightly affects the CMC of non-ionic surfactants. Other co-solutes may perturb the CMCs by varying degrees, depending on factors such as their polarity, water solubility, and possibly amphiphilic character among others. The best example to demonstrate this would be the addition of alcohols that preferentially partition into the oil/water interface due to their lower polarity (compared to water), lowering the CMCs by acting like non-ionic surfactants. Thus, alcohols are often used as a co-surfactant to further stabilise the micelles/microemulsions.

1.3.2 Krafft temperature

The Krafft temperature[16] is defined as the temperature where the ionic surfactant solubility is equal to the CMC. At this temperature, an abrupt increase in solubility occurs, potentially by orders of magnitude. As the Krafft temperature is closely related to the CMC, factors influencing the CMC value would also affect the Krafft temperature. Molecules with a polar head group or long alkyl chains generally have high Krafft temperatures, with the addition of salts typically increasing the Krafft temperature. The Krafft temperature is also defined as the triple point, because solid hydrated surfactants, micelles and the un-dissolved monomers co-exist and reach an equilibrium state (as Figure 1.4 shown). Below the Krafft temperature, the ionic surfactant tends to form a gel phase.

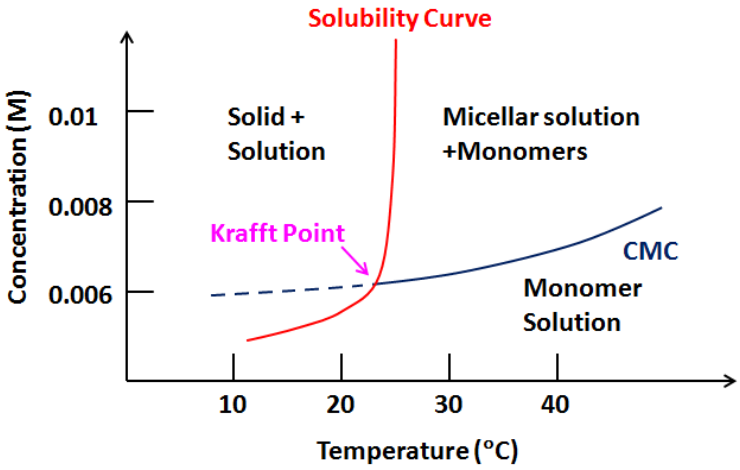

Figure 1.4[15, 16, 25] An example of the binary phase diagram with surfactant concentration plotted as a function of temperature. (Redrawn with permission from ref. 15, Copyright © 2002, John Wiley and Sons)

A low Krafft temperature is a desirable property for a surfactant; hence many approaches have been carried out to achieve this, including introduction of a methyl group, branching, or a double bond in the alkyl chain, insertion of polar groups between the alkyl chain and the ionic group, among others.

1.3.3 Cosurfactant

There are several factors determining the amount of surfactants required to reduce the interfacial tension to a certain level, including the efficiency of the surfactants at the interface, the partitioning between bulk and interface, and how good the surfactants can form micelles. Thus the efficiency and effectiveness of surfactants are commonly employed to describe these behaviours[26]. The efficiency of a surfactant is defined as the negative logarithm of the surfactant concentration in bulk needed to reduce the interfacial tension by a given amount, which also reflects the interfacial densities required to achieve this interfacial behaviour[27]. Surfactant effectiveness is defined as the maximum reduction of the interfacial tension a surfactant can produce, regardless of amount used.

When the surfactant alone cannot achieve the desirable interfacial behaviour, a cosurfactant, which is a weak amphiphilic molecule (typically an alcohol), is usually used to assist the micellar formation by further lowering the interfacial tension[28-30]. The efficiency of such a cosurfactant often depends on its

hydrocarbon chain length[31]. Medium linear chain alcohols comprising of ~3–8 carbon atoms are generally the most efficient co-surfactants, with short chain alcohols such as methanol having a reduced effect.

Sawada *et. al.*[32] studied the effect of the alcohol solubilising ability of water in a solution consisting of pentaethylene glycol n-octyl ether in supercritical carbon dioxide. Optimal performance was observed with n-pentanol (5 carbon atoms).

1.3.4 HLB concept

The hydrophile-lipophile balance (HLB) was defined by Griffin in 1949[33] to verify the hydrophilicity of a non-ionic surfactant[34] and its functionality in solution. Before the concept of HLB was introduced, Bancroft's rule[35], which states that '*the phase in which an emulsifier is more soluble constitutes the continuous phase*', was the widely adopted rule in the emulsion industry. However, it does not provide a quantitative analysis of the surfactant behaviour. For Griffin's method, HLB values can be estimated from the following relationships:

1) For alcohol ethoxylates and alkylphenol ethoxylates:

$$\text{HLB} = \frac{\text{Weight \% ethylene oxide}}{5} \tag{1.1}$$

2) For polyol ethoxylates:

$$\text{HLB} = \frac{\text{Weight \% ethylene oxide + weight \% polyol}}{5} \tag{1.2}$$

3) For fatty acid ester of polyols:

$$\text{HLB} = 20 \times \left(1 - \frac{\text{saponification number*}}{\text{acid number*}}\right) \tag{1.3}$$

*Where Saponification number is defined as the mass (typically in mg) of potassium hydroxide (KOH) required to saponify 1 g of fatty acid under specified conditions and it is thus a measure of the average molecular weight (or chain length) of the fatty acids. Acid number is the mass (in mg) of KOH required to neutralise 1 g of fatty acid and thus is used to estimate the number of carboxylic groups in the fatty acids.

Overall, the HLB scale extends from 0 to 20, where the higher HLB values indicate the surfactant is more water-soluble. Consequently, surfactants with diverse HLB values can have distinctively different applications and appearances

in aqueous solutions (Table 1.1). Generally, for HLB values between 3 and 8, surfactants are predominantly hydrophobic and hence w/o (water-in-oil) systems are favoured. However for HLB values > 8, the surfactants are hydrophilic and o/w (oil-in-water) systems are favoured.

Table 1.1[16] HLB scale and the applications

HLB	Appearance of its aqueous solution	Application	
1-4	No dispersibility	N/A	w/o systems
3-6	Poor dispersibility	w/o emulsifier	
7-9	Milky dispersion after mixing	Wetting agent	
8-10	Stable dispersion	N/A	o/w systems
10-13	From translucent to clear	N/A	
13-15	Clear Solution	Detergent	
15-18		Solubiliser	

Davies further developed the HLB determination procedure by introducing a HLB group value to each chemical component of a surfactant. Typical values for common chemical groups are listed in Table 1.2, and Davies' formula[36] for calculating the HLB is

$$HLB = 7 + \sum (\text{hydrophilic group numbers}) + \sum (\text{lipophilic group numbers}) \quad (1.4)$$

Table 1.2[36] Davies' HLB group numbers

Classification	Chemical component	HLB group number
Hydrophilic groups	$-SO_4Na$	35.7
	$-CO_2K$	21.1
	$-CO_2Na$	19.1
	-N(tertiary amine)	9.4
	Ester (sorbitan ring)	6.3
	Ester (free)	2.4
	$-CO_2H$	2.1
	-OH (free)	1.9
	-O-	1.3
	-OH (sorbitan ring)	0.5
Lipophilic groups	$-CF_3$	-0.870
	$-CF_2-$	-0.870
	$-CH_3$	-0.475
	$-CH_2-$	-0.475
	-CH	-0.475

The advantage of Davies' method is that the effects of either particularly strong or weak hydrophilic groups are taken into account during the calculation. Despite this exception, both Griffin's and Davies' methods can generate reliable predictions for emulsion selection.

1.3.4 Phase inversion temperature (PIT)

Non-ionic surfactants can be very sensitive to temperatures. For instance, above the cloud point, phase separation would take place. Another example that affects the surfactant stability would be the phase inversion temperature (PIT). As a consequence, it is very important to understand the temperature range within which each surfactant works to fulfil these conditions.

Certain non-ionic surfactants can form water-continuous systems at low temperatures but prefer oil-continuous systems at high temperatures. Consequently, to quantitatively describe this property, the concept of PIT was introduced by Shinoda *et. al.*[37] and defined as; the temperature at which an o/w system (usually an emulsion) would convert to a w/o system. Whilst the HLB concerns the surfactant properties regardless of the surrounding environment, the PIT is a property of the entire system. However, there are also correlations between the HLB and the PIT[31]. For instance, increasing the length of the polyoxylene chain of the surfactant increases the HLB value and thus leads to a higher PIT. Other factors may further contribute to the PIT, including polarity of the oil phase, additives, and the relative proportions of oil/water. Usually, the more polar the oil phase the lower the PIT. Therefore, the addition of salts or any compound that increases the polarity of the oil phase will reduce the PIT, while increasing the oil-water ratio would increase the PIT. Figure 1.5 illustrates the change in interfacial curvature during the conversion from an o/w system to a w/o system. The PIT can normally be detected by an abrupt drop in the conductivity with increased temperature.

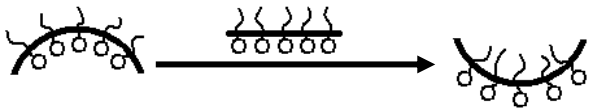

Figure 1.5 Interfacial curvature change from an o/w system to a w/o system.

1.3.4 Microemulsions

Above the CMC, surfactants start to agglomerate into micelles. Upon the addition of dispersed phase, the micelles start to swell. Normal micelles (o/w) have an internal oil dispersed phase and an aqueous continuous phase, as shown in Figure 1.6a. Reversed micelles (or w/o) will form from the dispersion of an aqueous

phase in an oil continuous phase (Figure 1.6c). Addition of further dispersed phase causes a micelle to swell to a microemulsion (sometimes termed as swollen micelles)[38], a nanoemulsion and an emulsion, with larger proportions of inner phases respectively .

Microemulsions are transparent, thermodynamically stable o/w, w/o or bicontinuous colloidal systems where the two phases are separated by a layer or film of amphiphilic molecules. With respect to emulsions (macroemulsions), microemulsions consist of much smaller aggregates with an average size ~10 nm, which are highly dynamic and can undergo rapid droplet collisions. For a microemulsion system in a low viscosity solvent with an dispersed volume fraction of 0.1 and an average droplet size of 10 nm, the encounter rate constant is 10^6 s^{-1} and the average time between collisions is therefore 1 μs[39].

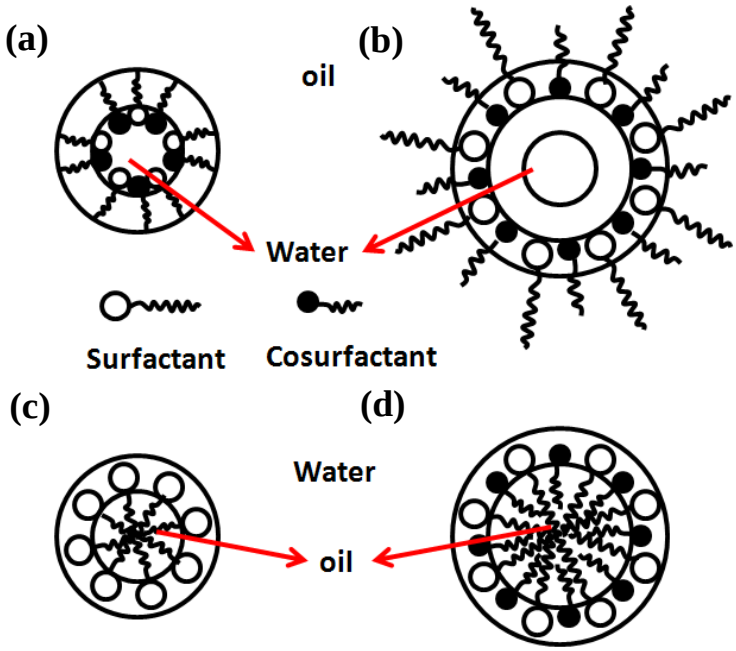

Figure 1.6[40] Colloidal structures of: (a) w/o micelles (reversed), (b) w/o microemulsion (reversed), (c) o/w micelles (normal), and (d) o/w microemulsion (reversed). (Redrawn with permission from ref.43, Copyright © 1998, Elsevier)

To form a microemulsion a high proportion of surfactant is required to achieve the ultralow interfacial tension (typically[41, 42] in the range of 10^{-4}–10^{-5} Nm^{-1}). This is because the surfactants are packed in a monolayer at the interface[43] and are thus required to form a highly curved interfacial film layer. Emulsions are

thermodynamically unstable systems with droplets in the range of 1–10 μm which will eventually undergo coalescence. Nanoemulsions[44] are thermodynamically unstable colloidal systems with droplet radii less than 100 nm and thus can be alternatively be described as an emulsion with very small particles[45].

Microemulsions are structurally very similar to the simple micellar systems; however the internal structure differs slightly. The internal phase of a w/o microemulsion can be comprised of two regions: a rigidly held shell of water molecules at the surfactant(s) polar head groups and a 'free water pool' in the centre (Figure 1.6b). The area of immobilised water is dependent on the water binding ability of the surfactant polar head groups. For example, AOT can strongly bond to six water molecules per SO_3^- group[40] and may structurally perturb 10–15 water molecules. A normal micelle (Figure 1.6c) can be swollen to become an oil-in-water microemulsion (Figure 1.6d). Equivalently, an o/w microemulsion can have a central 'free oil pool' and a tightly bound oil region, depending on the properties of the surfactant hydrocarbon tail.

Due to their unique physicochemical properties[46], in recent years microemulsions have been well studied, developed and applied in many fields, such as drug delivery[47], separation method enhancement[48], oil recovery[49], nanoparticle synthesis[50], biomolecule extraction[51], fuel replacement[52], industrial coating and textile finishing[46].

1.3.4a Winsor Classification

Microemulsions can achieve equilibrated systems even with the addition of an excess amount of water or oil. Winsor[53], independently of Griffin discovered the existence of microemulsions and classified the different equilibrium phases of microemulsions into four types (Figure 1.7). Type I: o/w microemulsion with an excess amount of oil phase. Type II: w/o microemulsion with an excess amount of aqueous phase. Hence both Types I and II are two phase systems. Type III: a triple layer system with an excess oil phase and an excess water phase, where the microemulsions are in equilibrium state. This microemulsion (Type III) is also called a middle phase microemulsion because the o/w and w/o microemulsions mutually exist. Type IV: an isotropic microemulsion system that comprises only

the homogeneous single phase microemulsion, without any excess water or oil; this may be o/w, bicontinuous or w/o in structure. Type IV microemulsions are to be utilised for this project.

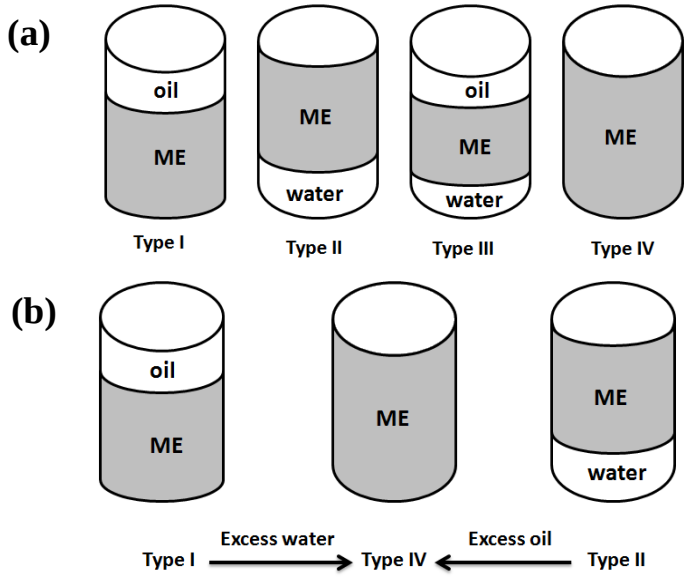

Figure 1.7[53, 54] Winsor forms of microemulsions (labelled as ME) with excess water or oil (a) and the inter-conversion between the forms (b).

Winsor microemulsions can interconvert between each other. For instance, with additional surfactant or removal of excess oil (water), Type I(II) may become Type IV. Type III can be thought of as the 'extended' version of Type IV but with an excess amount of both oil and water phase.

1.3.4b Microemulsion exchange

Microemulsions have been chosen as the vehicle to study the effect of 3D-nanoconfinement, due to their stability and appropriate droplet sizes. Within such microemulsions, the nano-sized droplets, driven by Brownian motion, are able to move and collide. The most energetic collisions can lead to the formation of a short-lived transient dimer (also regarded as the 'fusion-mass transfer-fission' process[31, 40]) where material exchange can occur through the channel in the dimer as shown in Figure 1.8. Despite microemulsion droplets being relatively monodisperse with respect to emulsion and nanoemulsion droplets, there can still be a degree of polydispersity, depending on the bending elasticity of the surfactant film[43, 55, 56]. These larger droplets have more material available for nucleation. If such a (near) stable nucleus exists in one of the dimer droplets, the local

concentration of material around the nucleus would be lower than in the other droplet. This concentration gradient causes solute to flow from the higher concentrated droplet to the nucleus, allowing coalescence-growth to proceed (Figure 1.8a). Once the crystal size exceeds the size of the droplet, it will break out of the confinement of the microemulsion into the continuum. If a stable nucleus exists in each of the dimer droplets, the concentration gradient would be much smaller between the droplets and hence material exchange would be a time-consuming process. If material transfer takes longer than the duration for which the transient dimer can exist, the droplets split apart to their original states (Figure 1.8b). If the nuclei in both droplets are much smaller than both the droplet diameter and the passage created by the elastic film between the droplets, there is a potential that the nuclei may merge together to form a larger crystal; this process is called coagulation-growth.

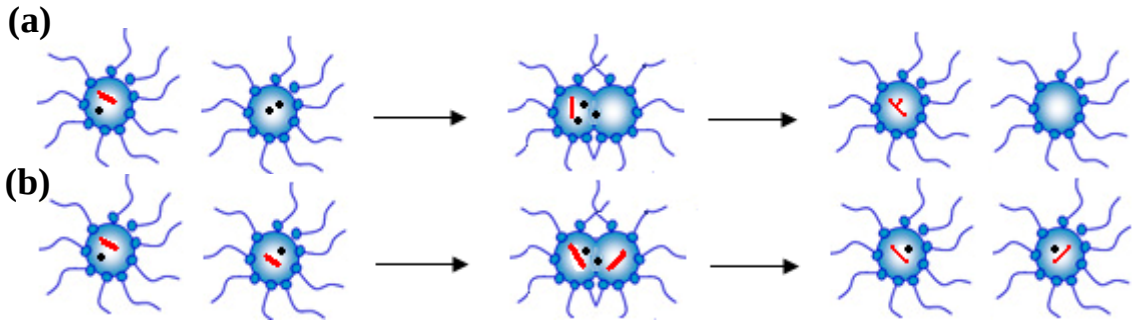

Figure 1.8 Transient dimmer formation and material exchange for two collided microemulsion droplets: (a) only one nucleus in one of the droplet; (b) both droplets contain one nucleus.

1.3.5 Emulsions

Emulsions[57] are thermodynamically unstable systems with a positive free energy of formation (ΔG), which means they have a tendency to degrade due to the interfacial tension being of the order of 1 – 10 mN m^{-1} and a large interfacial area with respect to the relatively small entropy term. Despite emulsions being thermodynamically unstable, they are kinetically stable since the amphiphiles present at the interface can act as an effective barrier between the continuous and dispersed phase. Therefore, droplets are less likely to directly contact each other and subsequently it is less probable for them to coalesce. In contrast, microemulsions have ultralow interfacial tension, which is in the order of 10^{-4}-10^{-5} N m^{-1}, and a much higher entropy contribution resulting from the small nano-

sized radius and thus higher population. Consequently, microemulsions are thermodynamically stable owing to the negative free energy of formation. Emulsions can break down via several routes detailed in Figure 1.9.

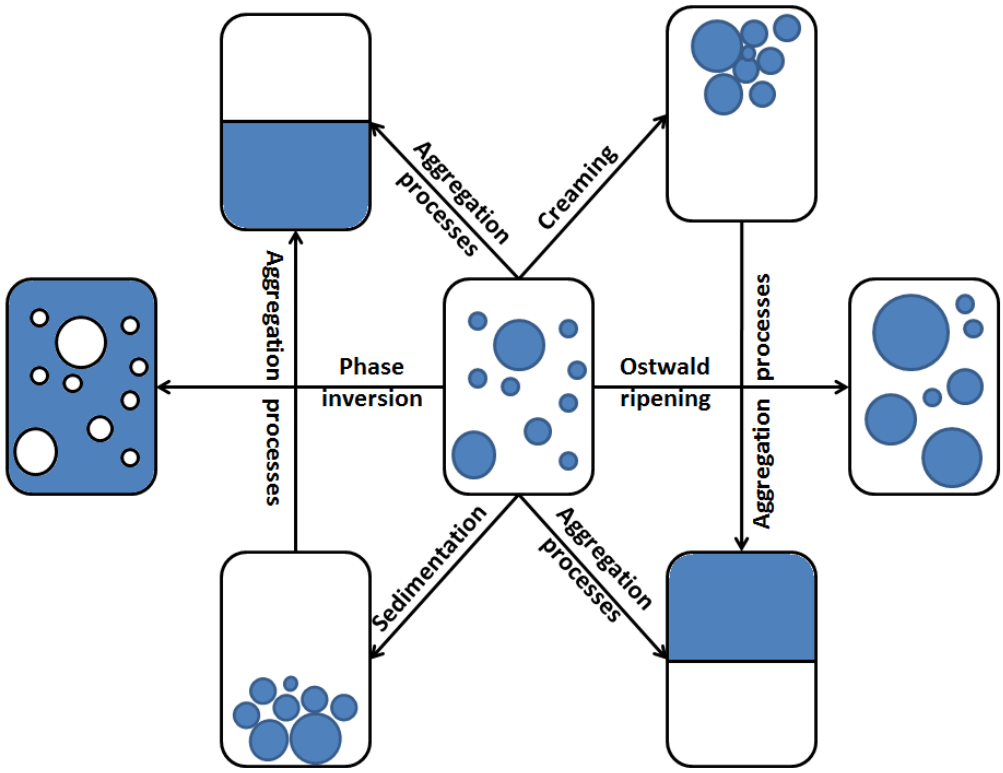

Figure 1.9 Emulsion destabilising processes

There are four major processes through which an emulsion can break:

- Phase separation type: i.e. creaming and sedimentation
- Ostwald ripening
- Aggregation processes: i.e. flocculation, coalescence, and coagulation
- Phase inversion

The detail for each process is described in the following, except phase inversion, which is covered in Section 1.3.4.

1.3.5.1 Creaming and Sedimentation[58-60]

Creaming is the formation of a more concentrated layer on the top of an oil/water emulsion, with a constant droplet size distribution under gravity or via centrifuging. The creaming process can be described by Stoke's law:

$$v_{stoke} = \frac{2r^2(\rho_1 - \rho_2)}{9\eta} \quad (1.5)$$

Where v_{stoke} is the velocity of creaming, r is the emulsion droplet radius, ρ_1 is the density of the continuous phase, ρ_2 is the density of the dispersed phase, and η is the shear viscosity of the continuous phase.

Similar to creaming, the origin of sedimentation is also a density difference between the phases. If the dispersed phase is lighter, then creaming occurs; whereas sedimentation is observed if the dispersed phase is heavier.

1.3.5.2 Flocculation and Coalescence[58-60]

Flocculation is a process of droplets agglomeration and the formation of loosely bound clusters that have an open structure, providing the total surface area remains constant. This often results from unbalanced attractive and repulsive forces within the droplets. Generally, flocculation can be divided into two further types (depletion and bridging flocculation) depending on the interface-droplet interaction. Depletion flocculation is often caused by the addition of non-adsorbing polymers while bridging flocculation occurs when a high molecular weight but less concentrated polymer adsorbs to the emulsion droplets and forms bridges[58, 59]. After flocculation, the droplets in close proximity are only separated by a thin layer of film. Various forces acting on the film can cause it to rupture and result in coalescence. De-flocculation is the opposite process that involves the breakdown of agglomerates into their individual units.

Unlike the above reversible processes, coalescence is irreversible, since the increase in droplet size can lead to gradual separation of the oil and the aqueous phase. This process requires the thinning of the film at the oil-water interface to a critical thickness followed by rupturing of the film.

1.3.5.3 Ostwald ripening

Ostwald ripening is another process by which emulsions can destabilise. It can be described as the growth of a large emulsion droplet at the expense of a smaller one due to their chemical potential (or solubility) difference, resulting in the lowering of free energy due to a reduction in the interfacial area. Thus it is energetically favourable for the more soluble smaller droplet to dissolve back into the bulk phase, before diffusing and re-depositing on to the larger one.

1.4 Phase diagrams[61]

The concept of a phase, which has uniform environmental and molar properties at equilibrium, was first introduced by Gibbs to define regions of matter enclosed by interface. A simple example of a multi-phase equilibrium is an ice and water mixture in that it contains both solid and liquid phases. Consequently, a phase diagram can be employed to interpret the regions of stability for a solid, liquid, and gas under various conditions, such as temperature and pressure. Since the state of the surfactant systems to be discussed will vary dramatically with diverse conditions (e.g. temperature, pressure and composition), a phase diagram is essential to distinguish the existence of different phases of the surfactant systems and their equilibrium state.

1.4.1 Phase rule

1.4.1.1 Single component system

For a single component system, the number of degrees of freedom, *f*, available to *p* phases is expressed by the following equation (simplified Gibbs phase rule)

$$f = 3 - p \tag{1.6}$$

where p is the number of phases in equilibrium. Figure1.10 shows the phase diagram for a single component system, e.g. pure water. In practice, at a specific pressure *a*, with increasing temperature a solid can melt into a liquid before becoming a vapour. Therefore there is only one degree of freedom for a single component two-phase system. However, there is an exception at the triple point (labelled as *T*) where solid, liquid and vapour phases coexist, and subsequently there are no degrees of freedom. Thus the triple point only occurs at a fixed temperature and pressure.

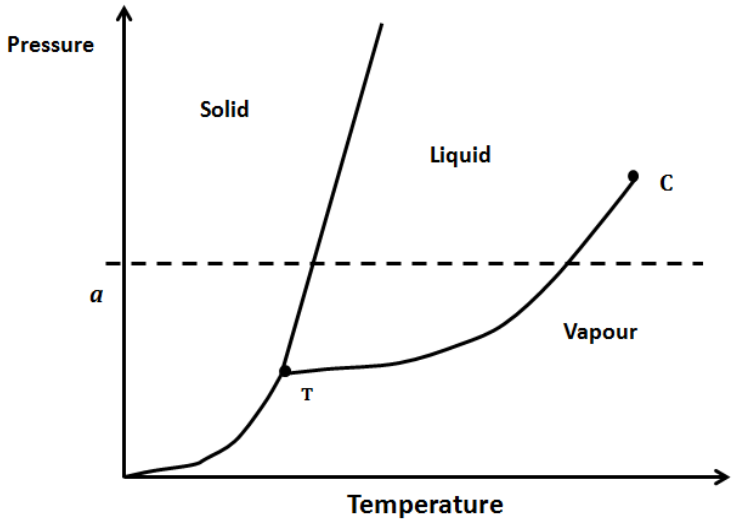

Figure 1.10 An example of a single component phase diagram

This is due to restrictions imposed by the second law of thermodynamics. For a single component system with p phases in equilibrium with 2 degrees of freedom (i.e. temperature and pressure), there would be p-1 restrictions. It is given that a decrease in entropy/energy is favourable for a closed system, where the Gibbs free energy in this case consists of both temperature and pressure. In such cases, the Gibbs free energy of all phases in equilibrium must be equal, which gives rise to p -1 restrictions. Overall the number of degrees of freedom f available to p phases is

$$f = 2 - (p - 1) = 3 - p \qquad (1.7)$$

Hence for a two-phase system $p = 2, f = 1$; and at the triple point, $p = 3, f = 0$.

Additionally, at high temperature on the liquid/vapour line the critical point is found. The critical temperature is roughly 1.5 times the normal boiling point, i.e. $T_c \approx 1.5 T_b$. The critical pressure for a system that is liquid at room temperature is usually above 100 atm.

1.4.1.2 Multi-component systems

For a multi-component system, the total number of degrees of freedom for a system with c components and p phases is expressed as (Gibbs phase rule)

$$f = 2 + c - p \qquad (1.8)$$

Firstly, the number of components is defined as the minimum number of independent chemical substances that can be mixed and reach equilibrium. Secondly, in addition to the 2 degrees of freedom (temperature and pressure), the

composition of the phases should be considered. Hence there would be $p(c - 1)$ mole fractions for p phases, since for each phase the composition is described by $c - 1$. However, as mentioned for a single component system, the Gibbs free energy of all phases in equilibrium must be equal. Thus there are $c(p - 1)$ restrictions for c components. Finally, the total number of degrees of freedom is

$$f = 2 + p(c - 1) - c(p - 1) = 2 + c - p \quad (1.9)$$

The most common phase diagram encountered in this study is the 3-component system and thus the Gibbs phase rule would indicate $f = 5 - p$. However, for such a complex system, it can be assumed that the liquids at constant temperature and pressure are in equilibrium, leading to the loss of two degrees of freedom, with $3 - p$ degrees of freedom overall. A 3-component system can be represented by a triangular coordinate diagram, as per the example shown in Figure 1.11. The total vertical distance (a, b, and c) from any point in the triangle to the three sides always equal to the height of the triangle, and the sum contribution of each component at any point on the diagram equals 1.

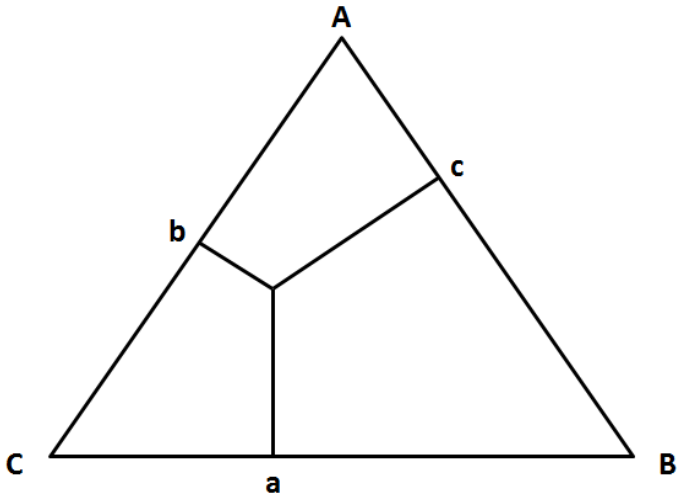

Figure 1.11 Triangular coordinate diagram

1.4.2 Ternary phase diagrams

Taking temperature into account adds a fourth component, which creates an elongated prism-shaped phase diagram. Since investigating a phase prism is time-consuming, it more efficient to study only certain phase-cuts by keeping some components constant or combining two or more components. The careful choice of constant components allows the reduction to a ternary or binary phase diagram. Ternary phase diagrams are typically done at constant temperature (i.e. the three

variables being water, oil and surfactants). The co-surfactant may be listed as an individual component for a fixed water-to-oil ratio. Binary phase diagrams are then the product of maintaining the oil-to-water ratio constant (or constant surfactant concentration) whilst investigating the effect of temperature.

Ternary phase diagrams of microemulsions constructed from water, oil and surfactant can further be divided into either 2 or 4 regions depending on the Winsor type. As Figure 1.12 illustrated[62], the region above the solid line represents a single phase (1ϕ) of microemulsion, whilst below the solid line it is the two or three phase region. The tie-lines in the two phase region indicate the compositions of the equilibrium phases. For different types of surfactants, the Winsor I→III→II phase transition can be achieved under different conditions. For non-ionic surfactants the transition can be induced by a temperature increase, whilst for ionic surfactants, a salinity increase can have a similar effect. The example shown in Figure 1.12a is a Winsor type I, with a non-ionic surfactant with hydrophilic nature, i.e. favouring w/o microemulsion systems, at low temperatures. For this Winsor type I, only a minute amount of oil is soluble in the equilibrated o/w microemulsion, with the vast majority of the oil phase. Upon an increase in temperature, an increasing amount of oil can be solubilised in the o/w microemulsion as the surfactant nature becomes more hydrophobic. The microemulsion apex also starts to shift from left to right (i.e. from low water fraction to high). The special case is when the apex is in the middle of the phase diagram, indicating that equal amounts of oil and water are contained within the microemulsion. Such a system is referred to as balanced. In a balanced system, a three-phase region (Winsor III) will also exist, adjacent to both the Winsor I and Winsor II regions. This completes the Winsor I→III transition. The height of the microemulsion apex can be used to define the efficiency of the surfactant, i.e. surfactants with lower apex heights are typically more efficient. Continuing the temperature increase, the Winsor III type will shift to Winsor II, which is the mirroring process of the Winsor I→III transition.

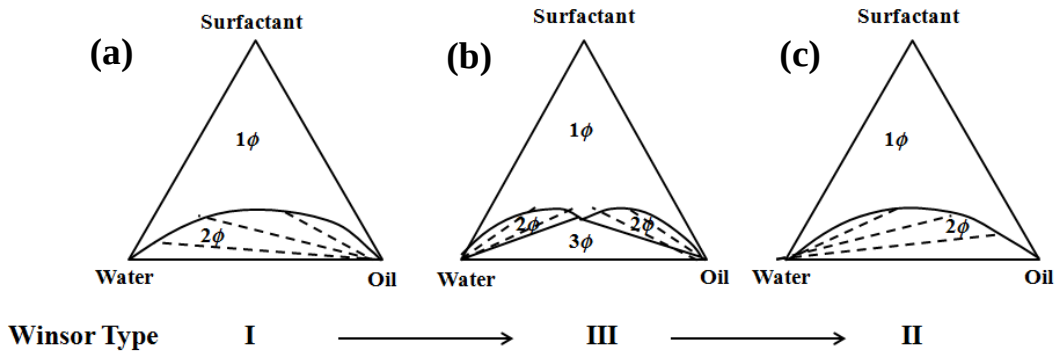

Figure 1.12[62] Ternary phase diagrams of Winsor microemulsion types which consist of surfactant, water and oil systems: (a) Winsor I; (b) Winsor III; (c) Winsor II. (Reproduced with permission from ref.60, Copyright © 2005 Bristol Colloid Centre and John Wiley and Sons)

1.4.3 Binary Phase diagram

When maintaining the water-to-oil ratio at 1:1 but varying both the temperature and surfactant concentration, a binary phase diagram is obtained as shown in Figure 1.13[62, 63], also known as a 'fish diagram'. The three phase region (Winsor III) only exists between temperatures *T1* and *T2*. This temperature range is determined by the nature of the surfactant. At temperatures above *T1*, the system is a Winsor II type, comprising an equilibrated microemulsion and an excess water phase. Below *T2*, the system behaves like a Winsor I type. Between *T1* and *T2*, there is an equilibrium/balanced temperature, *T**, where the three phase region (Winsor III) can intersect the single phase microemulsion region. This occurs at a critical surfactant concentration, known as *C**, which refers to the microemulsion apex on the ternary phase diagram. As surfactant concentration increases further, lamellar phases start to appear.

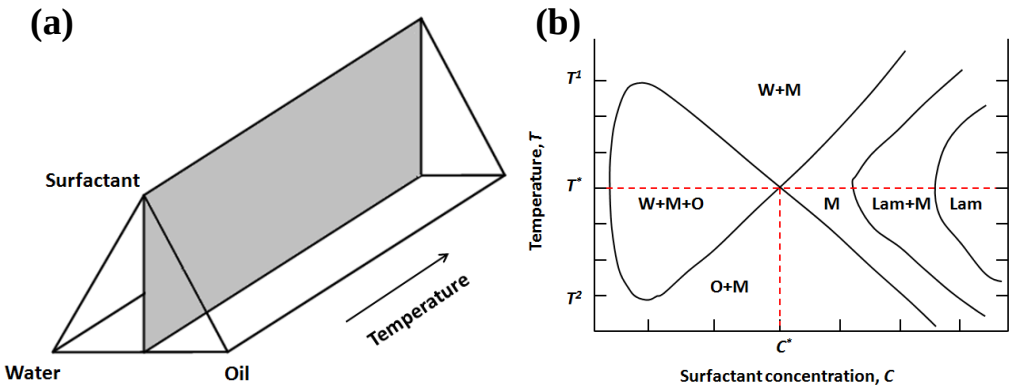

Figure 1.13[62, 63] 'Fish diagram' of temperature, *T* against surfactant concentration, *C*: (a) Phase-cut in a phase prism; (b) Binary 'fish diagram'. (Reproduced with permission from ref. 61, Copyright © 1994, Elsevier)

If the restricted component is surfactant concentration with two variables of the water-to-oil ratio and temperature, a slightly different binary phase diagram can be obtained, as presented in Figure 1.14[62, 63]. The water-to-oil ratio is expressed as the weight fraction of oil. There is a narrow channel of a microemulsion region running from the low oil fraction at low temperatures to higher oil fractions at high temperatures. The reasoning for such an observation is due to the hydrophilic nature of the surfactant at low temperature, thus it is more soluble in aqueous systems. Any addition of an oil phase would therefore lead to phase separation and a Winsor I type. At high temperatures the surfactant becomes increasingly hydrophobic and thus is more soluble in the oil phase. Addition of aqueous solution would encourage phase separation into a Winsor II type. At intermediate temperatures, lamella regions exist at both low and high oil fractions.

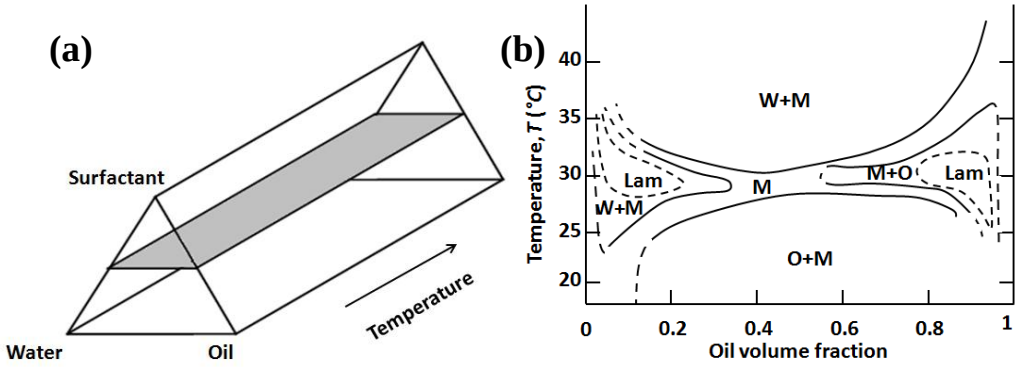

Figure 1.14[62, 63] Phase-cut of ternary phase diagram when the surfactant concentration is constant: a) Phase-cut of the phase prism; b) Binary phase diagram of temperature against oil volume fraction. (Reproduced with permission from ref. 61 Copyright © 1994, Elsevier)

1.5 Crystallisation[64-66]

Crystallisation is a process to form solid state crystals. It consists of two major steps: nucleation and crystal growth. Nucleation was first described by Gibbs[65] as the formation of small clusters of building units in the supersaturated/metastable regions and its appearance is a prerequisite for crystallisation. Once stable nuclei exist, crystal growth can proceed. If no distortions are evident within the crystal structure or no change in orientation, it can be deemed to be a single crystal[64]. Polycrystalline aggregates are solids containing many single crystals with different orientations.

1.5.1 Supersaturation

The driving force behind crystallisation is the degree of supersaturation, i.e. the extent of the deviation from the equilibrium concentration curve. This curve is defined as the point where no material/energy exchange between the solute and crystals, and neither dissolution nor crystallisation can occur. Therefore, to achieve crystallisation, either a supercooled system (via lowering the temperature) or an increased supersaturation (via concentrating the solutes by evaporation) is required. However, both can be expressed in terms of a chemical potential difference[64] that represents for the deviation from the solubility curve between two phases:

$$\Delta\mu = k_B T_B \ln(S) \tag{1.10}$$

where k_B is the Boltzman constant, T_B is the absolute temperature, and S is the solute supersaturation ratio.

For the purpose of illustration, a supersaturated[65] solution is used as the example here. This can be defined as a saturated solution containing more dissolved solid than at equilibrium at a specified temperature. It may also be depicted by a hypothetical solubility curve as shown in Figure 1.15.

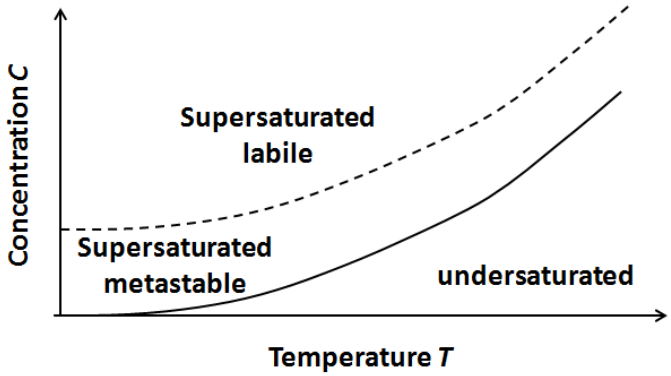

Figure 1.15 Hypothetical solubility curve

Solutions with concentration values lower than the equilibrium solubility curve at a defined temperature are referred to as under-saturated. Existing crystals in such solutions will dissolve. The effect of supersaturation has been described previously by Ostwald's rule of stages[67], which states that upon crystallisation occurring from a solution, a thermodynamically unstable phase will appear prior to the recrystallization of the thermodynamically stable phase (detailed in Section

1.6). Both nucleation and crystal growth are highly affected by the degree of supersaturation.

A supersaturation ratio is often used to quantify the degree of supersaturation, and it is equal to the concentration of solute dissolved in the system divided by the concentration of solute in the saturated solution.

1.5.2 Classical nucleation theory (CNT)

Nucleation involves the formation of a nucleus from which crystals may grow via a molecular aggregation process. The number of molecules required to form a nucleus is referred to as the critical number, and the molecular arrangement is regarded as a critical cluster/nucleus (Figure 1.16).

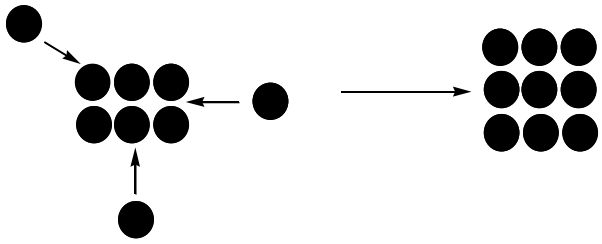

Figure 1.16 Formation of the critical cluster.

For CNT, to enable further growth of the crystalline phase, the critical nuclei needs to reach a certain equilibrium concentration, *n(i*)*, with the rate of nucleation, *J*, depending on both *n(i*)*, and the impingement rate of the solute onto the nuclei, *W**.

Therefore

$$J = W^* n(i^*) \tag{1.11}$$

However, *n(i*)* is determined by the Gibbs free energy of formation of the critical nucleus, ΔG^*, from the following equation:

$$n(i^*) = n \exp\left(\frac{-\Delta G^*}{k_B T}\right) \tag{1.12}$$

where n is the concentration of crystallising species, k_B is Boltzmann constant and T is the absolute temperature.

There are two classifications of nucleation, homogeneous and heterogeneous. The former spontaneously occurs in the interior of the sample but not on the surface,

whilst heterogeneous nucleation is induced by the presence of foreign particles or surfaces. ΔG^* is different for the two scenarios, thus they will be discussed individually.

1.5.2.1 Homogeneous nucleation

The change in Gibbs free energy of nucleation, ΔG, is known to depend on the size of the cluster, r_c, as shown in Figure.1.17[64]. An increase in nucleation energy is observed with increasing nucleus radius, r_c, until the critical nuclear radius, r^*, (corresponding to ΔG^*) is reached. Beyond r^* the free energy decreases. The overall nucleation energy is a competition between the volume free energy, ΔG_v, the energy released from the formation of the critical cluster and the surface free energy, ΔG_s, the energy spent on the creation of a surface. At small r_c, ΔG_s, proportional to r_c^2 dominates, whilst for larger r_c, ΔG_v, proportional to r_c^3 dominates.

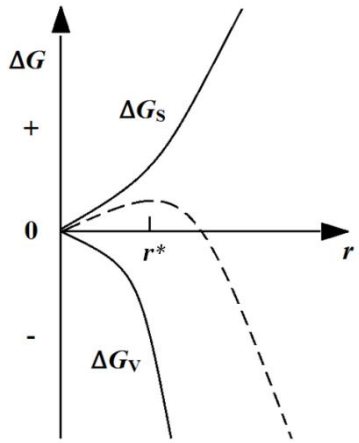

Figure 1.17[64, 66] Change in nucleation energy as a function of nuclear radius.

Thus for homogeneous nucleation[65], the change in nucleation free energy, ΔG_{Homo}, is given by

$$\Delta G_{\text{Homo}} = \Delta G_v + \Delta G_s = -i(\Delta\mu) + \sum_n \sigma_n A_n$$

$$= -\frac{4}{3}\frac{\pi r^3}{v_l}\Delta\mu + 4\pi r^2\sigma \quad \text{for a spherical cluster.} \qquad (1.13)$$

where i is the number of monomers in the cluster, A is the surface area, v_l is the molecular volume of the liquid, $\Delta\mu=\mu_v - \mu_l$ is the supersaturation, and σ is the surface energy for a flat surface. This equation is derived mathematically in Appendix 2.

As shown in Figure 1.18, when the liquid phase is stable ($\Delta\mu = \mu_v - \mu_l > 0$), the maximum free energy ΔG^*_{Homo} can be obtained by differentiating Equation 1.1 giving the critical nucleus size, r^*,

$$r^* = \frac{2\sigma v_l}{\Delta\mu} \tag{1.14}$$

Equation 1.14 is the Gibbs-Thomson equation. By substituting (1.14) into (1.13), the Gibbs free energy of formation of the critical nucleus can be expressed as:

$$\Delta G^*_{Homo} = \frac{16\pi\sigma^3 v_l^2}{3\Delta\mu^2} \tag{1.15}$$

When the vapour phase is stable ($\Delta\mu = \mu_v - \mu_l < 0$), the Gibbs free energy will grow infinitely with nucleus size, hence further growth is prohibited.

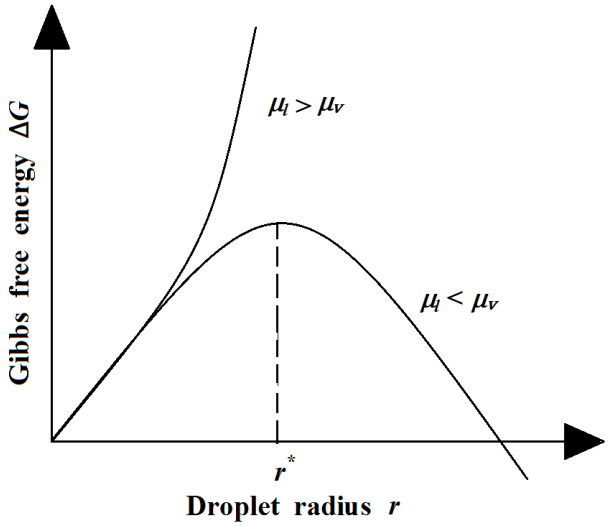

Figure 1.18[65] Gibbs free energy curve as a function of nucleus size for homogeneous nucleation

From ΔG^*_{Homo}, the homogeneous nucleation rate, J_{Homo}, can be determined:

$$J_{Homo} = W^* n \exp\left[\frac{-\Delta G^*_{Homo}}{k_B T}\right] \tag{1.16}$$

where W^*n is a pre-exponential factor, termed as Ω, with a typical value of ~10^{25}–10^{35} cm^{-3} s^{-1}. J is usually negligible below the Ostwald metastable limit, i.e. where the supersaturation reaches a critical level, it then starts to increase dramatically. Overall CNT (homogeneous) is generally suitable to describe systems with low to moderate supersaturations under the following assumptions: 1) the system is in equilibrium and 2) the critical nucleus is expected to have comparable properties to the bulk, e.g. the surface energy.

Several modifications to CNT (homogeneous) have been suggested over the years to improve the applicability of the theory. For instance, the Zeldovich factor[68], Z, has been adopted to account for deviation of the system from the equilibrium state, since the tendency of a subcritical nucleus to shrink/dissolve back into solution is a thermally activated process. As a consequence, the steady-state concentration is utilised rather than the equilibrium concentration of the critical nuclei, $n(i^*)$. Moreover, as aggregation of molecules can also occur in the vapour phase, the replacement term, taking into account the statistical contributions from the translational and rotational motions of the gaseous molecules, has been embraced. Furthermore, the applicability of bulk properties (e.g. surface tension, temperature and vapour pressure) has also been closely examined. This is due to the surface tension of spherical particles tending to decrease with size whilst temperature and vapour pressure rise due to liberated latent heat, which is termed thermal non-accommodation.

1.5.2.2 Heterogeneous nucleation

As heterogeneous nucleation relies on the presence of a foreign substrate or surface, it is expected to occur at a greater rate than homogenous nucleation. Thus, the equation is similar to the homogeneous case except for an extra wetting factor, $\sigma_d(\theta_w)$, as wetting (contact angle $\theta_w < 0$) encourages nucleation upon a surface.

The free energy change for heterogeneous nucleation, ΔG_{Hete}, is given by

$$\Delta G_{Hete} = \Delta G_v + \Delta G_s$$

$$= -\frac{V_l}{v_l}\Delta\mu + \sigma_d$$

$$= -\frac{4}{3}\pi r^3 \frac{(1-\cos\theta_w)^2(2+\cos\theta_w)}{4}\frac{\Delta\mu}{v_l} + 2\pi r^2\sigma_i(1-\cos\theta_w) - \pi r^2\sigma\sin^2\theta_w\cos\theta_w \quad (1.17)$$

where V_l is the volume of the sphere cap in Figure 1.19a, v_l is the molecular volume of the liquid, θ_w is the wetting angle between the vapour phase and the tangent of the droplet surface, $\Delta\mu$ is the supersaturation, σ_d is the surface energy of the liquid droplet and σ_i is the surface energy of the interface between the liquid phase and the solid substrate. The full derivation is provided in Appendix 3.

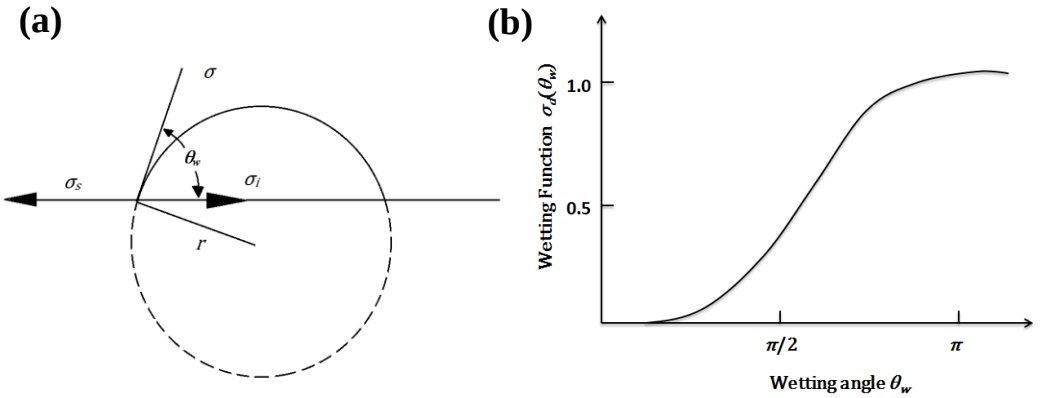

Figure 1.19[65, 66] Heterogeneous nucleation of a droplet on substrate surface (a) where σ_s, σ, and σ_i are the surface energy of free surfaces of substrate, droplet and the interface between the substrate surface and the liquid droplet, respectively; Wetting function as a function of wetting angle (b).

The Gibbs free energy curve reaches the maximum at a critical nucleus size of

$$r^* = \frac{2\sigma_i v_l}{\Delta\mu} \qquad \text{if } \Delta\mu > 0. \qquad \text{(recall 1.14)}$$

In this case, the Gibbs-Thomson equation is obtained for the Gibbs free energy of formation of the critical nucleus:

$$\Delta G^*_{Hete} = \frac{16\pi\sigma_i{}^3 v_l^2}{3\Delta\mu^2}\frac{(1-\cos\theta)^2(2+\cos\theta_w)}{4} = \frac{16\pi\sigma_i{}^3 v_l^2}{3\Delta\mu^2}\sigma_d(\theta_w) = \Delta G^*_{Homo} \times \sigma_d(\theta_w) \quad (1.18)$$

due to Equation 1.15 for ΔG^*_{Homo} and the additional $\sigma_d(\theta_w)$ wetting function, shown in Figure1.19b:

$$\sigma_d(\theta_w) = \frac{1}{2} + \frac{3}{4}\cos(\theta_w) - \frac{1}{4}\cos^3(\theta_w) \qquad (1.19)$$

In extreme conditions (the plateau region of the wetting function):

θ_w =180 °, the nucleation is independent of the surface and thus the scenario is simplified to the homogeneous case.

θ_w = 0 °, complete wetting is achieved and thus no nucleation barrier exists; however, the critical nuclei form a strongly adsorbed monolayer on the surface, thus Equation (1.19) is no longer applicable.

The nucleation rate for CNT(heterogeneous), J_{Hete}, is therefore:

$$J_{Hete} = W^* n_s \exp\left(\frac{-\Delta G^*_{Hete}}{k_B T}\right) \qquad (1.20)$$

Where n_s is the density of adsorption site, $W^* n_s$ is again known as Ω, the pre-exponential factor, that typically has a value between ~10^{17}-10^{22} cm^{-3} s^{-1}.

Improvements, such as the Zeldovich factor[68] and thermal non-accommodation, have also been performed with the heterogeneous case.

1.5.3 Non-classical crystallisation: Orientated attachment[69-71]

The concept of non-classical crystallisation was described by Cölfen and Antonietti[69] as '*the processes involving parallel, multiple nucleation events to form nanoparticles, which then form a superstructure (in stark contrast to a single nucleation event to form a single crystal*.' They involve the orientated attachment of nanoparticle building units onto a highly organised structure, which then transforms into a single crystalline structure. These organised structures, termed 'mesocrystals' (i.e. mesoscopically structured crystals), are usually transient (e.g. intermediates) and kinetically metastable, thus they can undergo mesoscopic transformations.

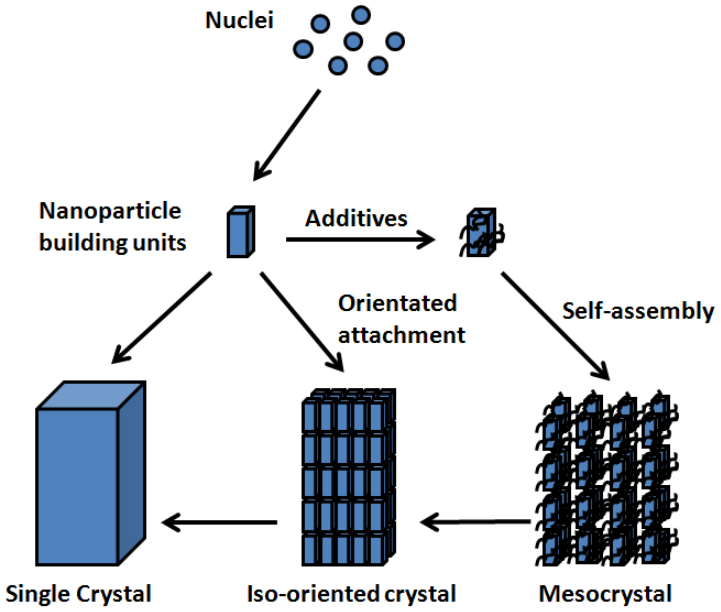

Figure 1.20[71, 72] Non-classical crystallisation mechanism (Reproduced with permission from ref.70, Copyright © 2003 WILEY-VCH Verlag GmbH & Co. KGaA, Weinheim)

Mesocrystal formation starts from the growth of nuclei clusters into the nanoparticle building units, which are then covered by certain additives (e.g. polymers and surfactants), promoting their self-assembly to form mesocrystals. Further, the nanoparticle building units can form single crystals or undergo oriented attachment to iso-oriented crystals, as illustrated in Figure 1.20. Since

mesocrystals are a transient state, they can transform to either of the other two types of crystals upon systematic perturbation, e.g. drying and heating.

Mesocrystal formation has been reported for a wide range of materials, including biominerals (e.g. $CaCO_3$[70, 73], sea urchins[74] and Hydroxyapatite[75, 76]), metal complexes (e.g. CuO[77], V_2O_5[78], and CeO_2[79]), and a few organic compounds (e.g. $_{DL}$-Alanine[80]). One of the predominant features of mesocrystals is their single-crystal like properties, and thus many diffraction and spectroscopy techniques have been used to identify the formation of such. The size of a mescocrystal can vary from the nanometre scale to a few hundred micrometres and therefore different techniques are employed accordingly. For example, TEM (Transmission electron microscope) is suitable for samples in the order of ~nm with the advantage of EDX (Energy-dispersive X-ray spectroscopy) providing elemental details in local regions of a mesocrystal. SANS (Small angle neutron scattering) and SAXS (Small angle X-ray scattering) are also appropriate for the study of particle shape and size distribution in this size range. Once the particles exceed ~50 nm, DLS (dynamic light scattering) can be used to monitor the early particle formation. SEM (scanning electron microscopy) can be used to observe the morphology of the mesocrystals as well as to provide element mapping of the sample. WAXS technique can also be utilised for solid crystalline samples of mesocrystals.

1.5.4 Crystal growth

After achieving the critical nucleus size, the building units (atoms/molecules) in the solution can become part of the crystal when their chemical potential equals the chemical potential of the crystal. This process is termed crystal growth. It usually requires a much lower expense of energy than that necessary for nucleation.

1.5.4.1 Crystal faces

The mechanism of crystal growth can be unambiguously determined from the structure of the crystal face. The crystal morphology is thus bounded by the slowest crystal face, i.e. that with the lowest surface energy and often the most close-packed. Such faces are typically atomically flat and have low Miller indices.

Therefore adjacent faces at a small angle to the low energy face will not be atomically flat and consist of terraces and steps.

Overall three types of faces exist in a Kossel crystal as indicated in Figure 1.21:

1) F faces: are flat and parallel to at least two dense atomic rows, described as 'complete planes' by Kossel[81].
2) S faces: consist of steps and are parallel to one dense atomic row.
3) K faces: contain kinks, but are not parallel to any dense atomic rows, which are also known as 'incomplete planes'.

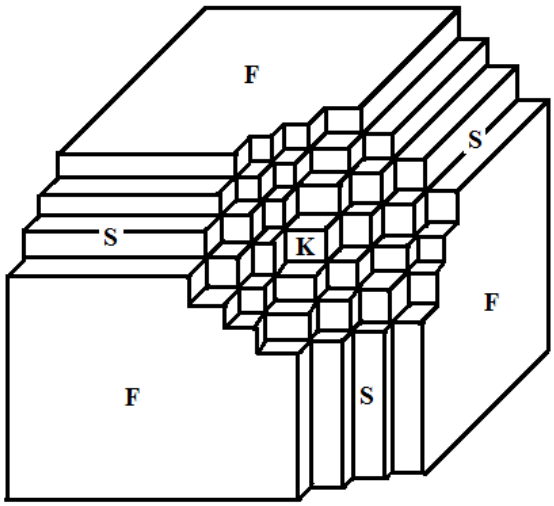

Figure 1.21 Kossel crystal[81] illustrating the F, S, and K faces

1.5.4.2 Crystal surface sites

Different types of crystal surface sites have different attachment/detachment energy in a Kossel crystal. As shown in Figure 1.22, each of the cubes represents a type of crystal surface site. The number of faces connected to the crystal decreases with the position (Table 1.3), revealing a reduction in energy of attachment for the crystal growth building block to become incorporated into the crystal. Positions 1, 2, and 3 are termed a smooth (terrace) face, a step, and a kink, respectively. Position 3 has 3 saturated bonds (connecting to the neighbouring crystal) and 3 unsaturated bonds. The attachment energy of a kink site is equal to one-half of the bonding energy between the adjacent units, hence it is also called a half-crystal site. Consequently, detaching any atoms from the kink sites will not affect the surface energy of the crystal.

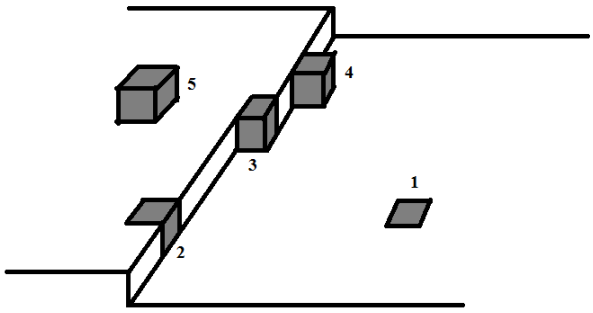

Figure 1.22 Crystal surface sites

Table 1.3 Surface site position and the number of bonds connected to the crystal

Position	Description	No. of faces connected to the crystal
1	Within Face	5
2	Within Step	4
3	Within Kink	3
4	Upon Step	2
5	Upon Face	1

Overall, unique properties of kink sites include:

1) their desorption energy is equal to the crystal enthalpy of evaporation;
2) these sites determined the equilibrium of an infinitely large crystal within the ambient phase;
3) their chemical potential is equal to the chemical potential of the crystal;
4) an ad-atom would be favourable to attach at the kink site of the crystal and thus the crystal growth is via an adhesive-type mechanism.

1.5.5 Growth mechanisms

The growth mechanisms for atomically flat surfaces and rough surfaces are very different. Flat surfaces are formed via layer growth, but rough surfaces expand via continual growth. F faces are normally atomically flat, however, they can undergo surface roughening at a critical temperature (the roughening temperature, T_r) where continual growth overtakes.

1.5.5.1 Continual growth of rough faces

As stated previously, rough surfaces (i.e. steps, kinks and flat faces above T_r) expand via a continuous growth mechanism. The growth rate, R, is related to the

flux of atoms arriving at the crystal surface from the parent phase and is therefore linearly proportional to the driving force (i.e. supersaturation):

$$R = \xi \Delta\mu \tag{1.21}$$

where ξ is the kinetic coefficient proportional to the surface roughness and also related to the activation energy, ΔE. $\Delta\mu$ is proportional to the logarithm of the supersaturation ratio (i.e. the concentration of the solute in a particular this system over the concentration of the solute in the saturated system).

Crystals grown via this mechanism tend to have rounded morphologies since all crystal faces are likely to grow at the same rate.

1.5.5.2 Layered growth of flat faces

For a perfectly flat face, a single ad-atom is bound much more weakly than a cluster of ad-atoms. However, an energy barrier is required to be overcome in order to form such a cluster. This is the 2D analogy of homogeneous nucleation and therefore the growth rate is determined by the rate of critical nuclei formation.

1.5.5.3 2D nucleation growth

The growth of a smooth crystal surface is a periodic process, comprising the formation of a 2D nucleus and the growth of this nucleus to cover the crystal surface. The 2D nucleus formation is the rate determining step, similar to the 3D nucleation case. The rate of formation of this nucleus is determined by:

$$R_{2D} = \Omega_{2D} \exp\left(-\frac{\Delta G_{2D}{}^{*}}{k_B T}\right) \tag{1.22}$$

Where Ω_{2D} is the pre-exponential factor for 2D nucleation and $\Delta G_{2D}{}^{*}$ is the Gibbs free energy for the formation of the 2D critical nucleus.

$\Delta G_{2D}{}^{*}$ for monolayer disc shaped nuclei, with depth l, can be rewritten as

$$\Delta G_{2D}{}^{*} = \pi r^{*} l \sigma = \frac{\pi l v_c \sigma^2}{\Delta\mu} \tag{1.23}$$

Thus R can be re-determined as

$$R_{2D} = \Omega_{2D} \exp\left(-\frac{\pi l v_c \sigma^2}{\Delta\mu k_B T}\right) \tag{1.24}$$

From Equation 1.22 the nucleation rate, R_{2D}, is affected by the supersaturation $\Delta\mu$ exponentially. At high supersaturation, the multilayer growth mechanism can take place, leading to the change of exponent into $(-\Delta G_{2D}^{*}/3k_BT)$.

With increasing supersaturation, the size of a 2D critical nucleus decreases by only a few atoms. The density of a 2D critical nucleus can increase to a larger level that the atoms arriving at the nucleus can incorporate into any site. Then the surface becomes atomically rough and the growth becomes continuous. This type of crystal face roughening occurs at very high supersaturations below the thermodynamic roughening transition temperature and is known as kinetic roughening.

1.5.5.4 Spiral (Screw dislocation) growth

2D nucleation growth will only occur if the solution has a relatively high supersaturation to overcome the energy barrier for nucleation. This is because the layer by layer growth model, proposed by Kossel[81] and Stranski[82] is based on the assumption that the crystals are perfect. However real crystals are not and they often have impurities and dislocations. The appearance of a screw dislocation (i.e. a type of line defect in the crystal) can thus act as a lasting source of steps, which allows the crystal to grow without the need to form 2-D nuclei. Thus crystal growth is possible for solutions below the critical supersaturation required for 2D nucleation growth. Burton, Cabrera and Frank (BCF)[83] developed a theory to describe this screw dislocation/spiral growth. The rate of growth is defined as

$$R = \kappa \left(\frac{S^2}{S_c}\right) \tan\left(\frac{S^c}{S}\right) \tag{1.25}$$

Where S is the supersaturation parameter $\Delta\mu/k_BT$, S_c is the characteristic supersaturation of the system and κ is the rate constant. According to the supersaturation of the solution, 2 scenarios can be observed:

a) at low $\Delta\mu$, $S_c >> S$, so $\tan\left(\frac{S^c}{S}\right)$ is ~1, then Equation 1.25 becomes BCF parabolic law:

$$R = \kappa \left(\frac{S^2}{S_c}\right) \tag{1.26}$$

Bennema and Gilmer[84] further simplified Equation 1.26 by combining κ and S_c into another constant, κ', into the second parabolic law:

$$R = \kappa' S^2 = \kappa' (\frac{\Delta\mu}{k_B T})^2 \quad (1.27)$$

b) When $\Delta\mu$ is sufficiently higher than S_c, $\tan\left(\frac{S^c}{S}\right) \approx \frac{S^c}{S}$, then the BCF linear growth rate is obtained:

$$R = \kappa S = \kappa (\frac{\Delta\mu}{k_B T}) \quad (1.28)$$

Thus the growth rate-supersaturation profile can be plotted, as shown in Figure 1.23[64]. If the solution concentration is lower than the characteristic supersaturation, S_c, the parabolic law is used to describe the growth rate, R. Above S_c, R slowly changes into a linear relationship. With the increase in supersaturation, the density of kinks on the surface also increases. Eventually the crystal face becomes rough, leading to a continuous growth mechanism.

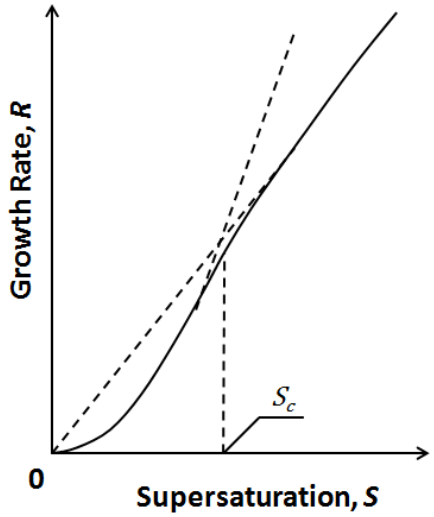

Figure 1.23[64, 66] Growth rate-supersaturation profile

1.5.5.5 Conclusions

Since S and K faces are rough, they always follow the continuous growth mechanism, so their growth rate is proportional to the supersaturation. For F faces, they will be able to grow continuously only if they become rough. There are two roughing processes, known as thermodynamic roughing if the roughing temperature, T_r, is reached, and kinetic roughing if the supersaturation is very high. Otherwise, F face can only grow by either 2D nucleation growth or spiral growth,

where the former is required to overcome the nucleation energy barrier and the latter needs screw dislocation to occur. Figure 1.24 has illustrated the transition from smooth to rough surface and the growth rate for each type of surface.

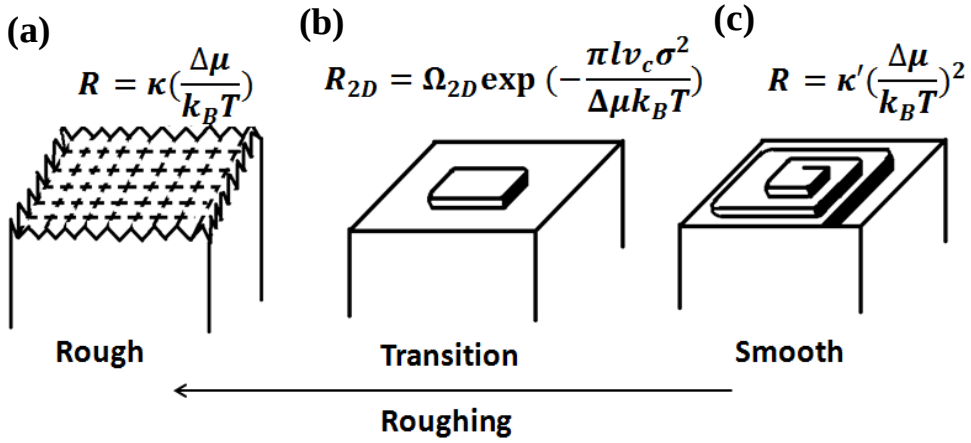

Figure 1.24[64] Transition from smooth to rough surface via 2D-nucleation and their growth rate: (a) Rough surface-Continuous growth; (b) Transition stage - 2D-nucleation growth; (c) Smooth surface-Spiral growth

1.6 Ostwald's Rule of Stages[2] (Kinetic control)

Ostwald's rule of stages[2] describes the trend of polymorph crystallisation as: '*an unstable system does not necessarily transform directly into the most stable state, but into one which most closely resembles its own, i.e. into another transient state whose formation from the original is accompanied by the smallest loss of free energy*.' However, this rule was only an observation and did not have any general proof. Thus several studies have been performed in order to provide experimental support as well as theoretical rationale. The most likely and well accepted explanation is the kinetics of polymorph transformation, depending on the relative rate of crystal nucleation and growth of the polymorph, in combination with the relative thermodynamic stability of the polymorphs. The polymorph crystallised out first is the most soluble but thermodynamically least stable one with the smallest activation energy barrier to overcome. Thus this form is the kinetically most stable form but will then transform into the next kinetically stable forms over time. Therefore, the immediate product described by Ostwald's rule is the kinetically stable (i.e. fastest nucleation and growth rate) one rather than the thermodynamically most stable one. For this reason, Ostwald's rule is classified as kinetic control.

1.7 Thermodynamic control in microemulsions (confined volumes)

To understand the thermodynamics behind the outcome of crystallisation of the polymorph materials, we need to look at their energy profiles first. Figure 1.25[85] shows the Helmholtz free energy of nucleation for the meta-stable form, *MF*, and a more thermodynamically stable form, *SF*, from melt state (i.e. the solid and liquid phase have the same composition).

Helmholtz free energy, *F*, was employed rather than Gibbs free energy, since nucleation/crystallisation was performed under constant volume, *V*, and temperature, *T*, and thus *F* does not have the extra '*PV*' term.

$$F = U - TS \tag{1.29}$$

$$G = U - TS + PV \tag{1.30}$$

where *P* is pressure, *U* is the internal energy and *S* is the entropy.

ΔF^* represents the maximum free energy change and crystallisation will only occur when this energy barrier can be surmounted. The critical nuclear radius, *r**, is the radius when the Helmholtz free energy equals ΔF^*. It is the minimum size that a (near) stable nucleus needs to be, before it can become viable. The radius, r_0, is the radius when $\Delta F = 0$. This is when there is just enough material to form a stable nucleus. The meta-stable form, *MF*, has a lower energy barrier and typically larger critical nuclear size, r^*_{MF}, in comparison to the critical nuclear size, r^*_{SF} , of the thermodynamically stable form, *SF*. As a result, the meta-stable form, *M*, will generally crystallise out first from an unconfined system. However, if crystallisation can be controlled to the region where r lies between r_0^{SF} and r_0^{MF}, there will be only enough material for the most thermodynamically stable form, *S*, to nucleate and grow ($\Delta F_{MF} \geq 0$ but $\Delta F_{SF} \leq 0$). Consequently, any existing metastable nuclei will re-dissolve. This is how thermodynamic control of the polymorphic system via confined volumes ($r_0^{SF} < r < r_0^{MF}$) under melt conditions is achieved.

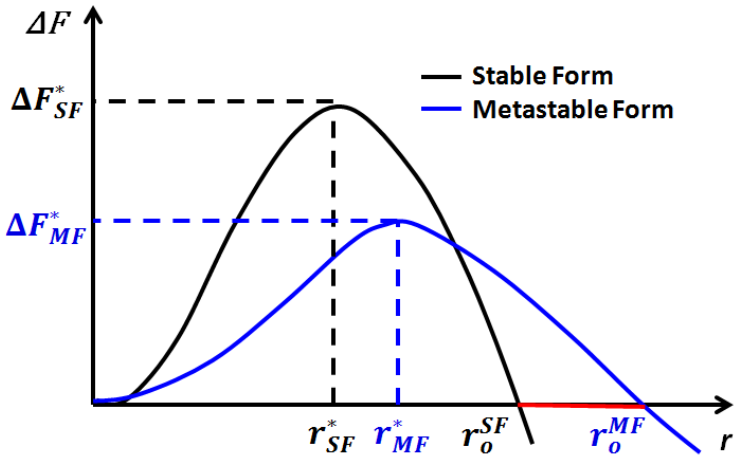

Figure 1.25[85]: The Helmholtz free energy curve, for the crystallisation from a melt as a function of nuclear radius for the metastable(ΔF_{MF},r_{MF}) and the most stable form(ΔF_{SF}, r_{SF}).

In the supersaturated solution state (i.e. liquid state is diluted compared to the solid or melt phase) the theory applied to the melt state is adopted except for the energy minimum has increased as a result of the decreased solute concentration (with respect to the melt state). The supersaturated state in this system is often achieved by anti-solvent addition. If the energy minima of both forms are above k_BT, i.e. from Maxwell-Boltzmann distribution, $\frac{N_i}{N_j} = A\exp(-\frac{\Delta E}{k_BT})$, as shown in Figure 1.26a[86], no crystallisation would occur. By carefully controlling the anti-solvent quantity, thermodynamic control can be reached so that the Helmholtz free energy for the stable form ΔF_{SF} will only be below k_BT (the red region in Figure 1.26b[86]). As a result, only the stable nuclei can form and have a sizeable population whereas any metastable nuclei tend to dissolve back into the solution. If too much anti-solvent is added, the Helmholtz free energy for both the stable form and meta-stable form will have the $\Delta F<k_BT$ region (Figure 1.26b). Thus kinetic control will dominate and the metastable form will nucleate and grow, due to the lower energy barrier to overcome.

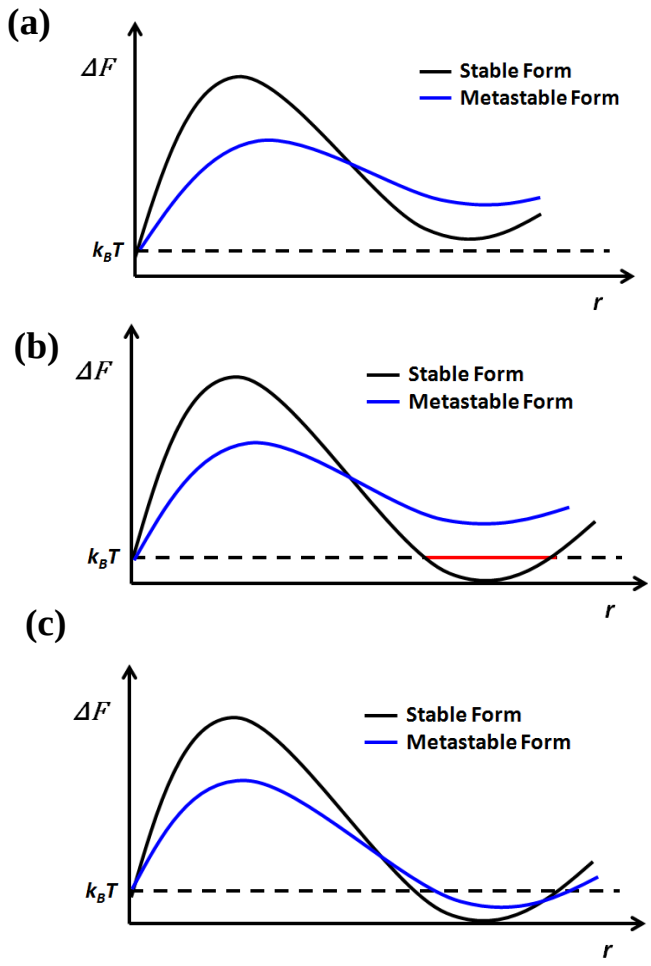

Figure 1.26[86] Free energy change during crystallisation from solution as a function of nuclear radius for metastable (in blue) and the most stable form (in black): (a) ΔF for both forms above k_BT, no crystallisation will occur; (b) only the energy minimum of ΔF for the most stable form below k_BT, thermodynamic control is achieved; (c) the energy minimum for both forms below k_BT, kinetic control/(i.e. Ostwald's rule of stages) will dominate. (Reproduced with permission from ref 84, Copyright © 2011, American Chemical Society)

1.8 Literature review of synthesis/crystallisation within microemulsions

As previously described in section 1.3.4, beneficial from the ultra low interfacial tension and 3D-nanoconfinement, the microenvironment inside a microemulsion (particularly w/o) can have distinct properties[87], such as low micropolarity[88], altered nucleophilicity[89] and viscosity[90], compared to the bulk solutions. These qualities provide a unique environment for reactions to take place that would otherwise not occur in the bulk conditions. Thus make microemulsions ideal nanoreactors for a wide range of reactions including electron/proton transfer,

catalytic reactions, and polymerisation, among others. Nanoparticle synthesis from microemulsions has attracted significant interest since the groundbreaking work of Boutonnet *et. al.*[91] (1982) describing the preparation of Pd, Rd, Ir and Pt metal nanoparticle from CTAB w/o microemulsions. Further successful attempts include; metallic nanoparticles (Au[92], Ag[93-95]), metal oxides (Fe_2O_3[96], ZnO[97], TiO_2[98-100], $CaCO_3$[101], SiO_2), metal sulfides (ZnS[102]). The majority of these studies focused on either the kinetic aspects[39] (i.e. reaction rate, droplet collision rate, and material exchange rate), or particle morphology and size control[98]; by varying the microemulsion components to alter the properties (e.g. fluidity and rigidity) of the interfacial film or by the addition of additives to induce heterogeneous nucleation. However, the thermodynamic control aspect of microemulsion was barely explored; even when investigating the crystallisation of polymorphic systems, the outcome was attributed to effects, such as surfactant templating[3], stirring[98-100], and pH levels[100]. For example, the formation of anatase and rutile of TiO_2 and aragonite and calcite of $CaCO_3$ were postulated to be a result of variation in the pH[103] or counterions[100, 101, 103]. Further, the polymorph outcome of other materials such as glycine[3], obtained from AOT microemulsions, were related to the surfactant induced crystallisation (templating effect) and relative supersaturations within the microemulsion. Thus the ability to exhibit thermodynamic control over crystallisation from the microemulsion remained unrecognised[86].

1.9 Previous crystallisation work performed under confinement conditions

Crystallisation under confinement conditions has attracted much research interest in recent years since these conditions have been reported to alter the intrinsic properties of the crystals (i.e. melting point depression), regulate certain polymorphs, induce preferred orientation of certain crystal faces and control the morphology of crystals.

Crystallisation within nanopores can introduce physical constrains on the size of materials, and increasing the surface-to-volume ratios can result in dramatic differences in physical properties compared to its bulk material. For example, melting point depression, arising from the balance between an unfavourable

surface energy and stabilizing volume energy from the classical nucleation theory point of view, is often observed[104]. Christenson[105] and Alcoutlabi *et. al.*[106] studied previous works where the relationship between the confinement size and the glass transition temperature/melting points were investigated. A linear correlation was often found due to the reduction of energy of fusion. This reduction was possibly due to the disordered liquid-like layer surrounding the small nuclei, generating a significant surface-to-volume ratio and causing the melting point depression.

Polymorphic control is very important to the pharmaceutical industry for reasons stated in Chapter 1.2. Ha *et. al.*[107] demonstrated the polymorphic control of anthranilic acid and ROY (5-methyl-2[(2-nitrophenyl)-amino]-3-thio-phenecarbonitrile) within nanopores of controlled pore glass (CPG). This work revealed a size dependent polymorph stability. Similarly Beiner[108], Rengarajan[109, 110] and co-workers[111] studied the polymorphs of acetaminophen with respect to the pore size and observed melting point depression. An amorphous phase was obtained for the smallest pores with 4.6 nm in diameter, possibly due to this form having a smaller critical nucleus size or the kinetic stabilisation of the amorphous phase due possibly to a suppression of a solvent-mediated transformation to a more stable form. With an increase in pore size, a transition from the metastable form III to the most stable form II occurred, also supporting the hypotheses that either the solvent-mediated transformation to more stable forms was restricted when crystallising from small solvent volume, and/or that the smaller critical nucleus size of less stable forms favoured their formation in the small pores[108].

Ha *et. al.*[112] also reported the discovery of new polymorphs of pimelic acid, glutaric acid, suberic acid and coumarin in nanopores of CPG and poly(cyclohexalethylene) (p-PCHE) monoliths. Further, under nanoconfinement, the enantiotropic relationships between the bulk polymorphs of glutaric acid and suberic acid have been altered into monotropic relationships, presumably because of a size dependency on the relative stability of the polymorphs.

In addition, Jackson and McKenna[113] have reported the stabilisation of amorphous phase and suppression of crystallisation of *o*-terphenyl and benzyl alcohol within CPG powders when the nanopores having diameters both less than and greater

than twice the critical nucleus size. This implies both the kinetic stabilisation of the amorphous phase in pores large enough to accommodate the postcritical nuclei and thermodynamic stabilization of the amorphous phase in pores too small to support stable crystals.

Nanopores can also act as a template to induce preferred orientation of the nanocrystals. For instance, Hamilton *et. al.* observed the growth of β-glycine nanocrystals in the pores of polystyrene-polydimethylacrylamide (PS-PDMA), oriented with the bulk fast-growing [010] axis parallel to the pore direction[114]. In addition ROY nanocrystals were aligned with the preferred (111) face parallel to the pore direction of the p-PCHE monoliths[115].

Further, Meldrum *et. al*. and co-workers has comprehensively demonstrated the morphological control of biominerals[116] under confinement conditions. In particular, many of their works focus on $CaCO_3$ crystals. It was reported that[117, 118] by employing sponge-like polymer membranes with sea urchin networks as crystallisation templates, single crystals of $CaCO_3$, $SrSO_4$, $CuSO_4 \cdot 5H_2O$ and many others, packed in a similar manner to the polymer mould, can be yielded. Such a templating effect has also been observed in systems crystallising from close-packed monolayer surfaces, e.g. polystyrene or silica spheres[119] and polymer thin films[120], e.g. polystyrene, poly(methyl methacrylate) and the blend of two. In addition, when using a block-copolymer scaffold to template the crystal structure and to control the pore size, gyroid networks (i.e. triple periodic minimal surface structures) of calcite single crystals can also be obtained[121]. Further, the group successfully engineered calcite single crystals that mimic the direct opal and inverse opal structures, via ion-by-ion precipitation methods, when applying polystyrene reverse opals and colloidal systems as templates, respectively[122].

Overall, the above work has demonstrated the wide range of potential applications that confinement conditions can be utilised for. Thus it would be very intriguing to investigate the crystallisation outcome under volume confinement conditions generated by microemulsion environments.

1.10 References

1. L. K. McCluggage, S. A. Voils and M. R. Bullock, *Neurocrit Care*, 2009, **10**, 222-224.
2. W. Ostwald, *Z. Phys. Chem.*, 1897, **22**, 289-330.
3. K. Allen, R. J. Davey, E. Ferrari, C. Towler, G. J. Tiddy, M. O. Jones and R. G. Pritchard, *Cryst Growth Des*, 2002, **2**, 523-527.
4. J. Yano, H. Füredi-Milhofer, E. Wachtel and N. Garti, *Langmuir*, 2000, **16**, 10005-10014.
5. R. Hilfiker, F. Blatter and M. v. Raumer, in *Polymorphism in Pharmaceutical Industry*, ed. R. Hilfiker, WILEY-VCH Verlag CmbH & Co. KGaA, Weinheim, 2006.
6. T. Gelbrich, D. S. Hughes, M. B. Hursthouse and T. L. Threlfall, *CrystEngComm*, 2008, **10**, 1328-1334.
7. J. M. Kelleher, S. E. Lawrence and H. A. Moynihan, *CrystEngComm*, 2006, **8**, 327-332.
8. G. J. Kruger and G. Gafner, *Acta Cryst. B*, 1972, **28**, 272-283.
9. P. T. A. Galek, L. Fábián, W. D. S. Motherwell, F. Allen and N. Feeder, *Acta Cryst. B*, 2007, **63**, 768–782.
10. P. A. Wood, E. Pidcock and F.H. Allen, *Acta Cryst. B*, 2008, **64**, 491-496.
11. T. Threlfall, *Org. Process Res. Dev.*, 2003, **7**, 1017-1027.
12. L. F. Huang, and W.Q. Tong, *Adv. Drug Deliv. Rev.*, 2004, **56**, 321.
13. J. M. Miller, B. M. Collman, L. R. Greene, D. J. W. Grant and A. C. Blackburn *Pharmaceut Dev Tech*, 2005, **10**, 291-297.
14. J. Bauer, S. Spanton, R. Henry, J. Quick, W. Dziki, W. Porter and J. Morris., *Pharm. Res.* , 2001, **18**, 859-866.
15. K. Holmberg, B. Jönsson, B. Kronberg and B. Lindman, *Surfactants and Polymers in Aqueous Solution*, Wiley, 2002.
16. T. F. Tadros, *Applied Surfactants Principles and Applications*, WILEY-VCH Verlag GmbH & Co. KGaA, Weinheim, 2005.
17. B. Lindman and H. Wennerström, in *Micelles*, Springer Berlin Heidelberg, 1980, vol. 87, pp. 1-83.
18. S. Paula, W. Sues, J. Tuchtenhagen and A. Blume, *J. Phys. Chem.*, 1995, **99**, 11742-11751.
19. P. H. Elworthy, A. T. Florence and C. B. Macfarlane, *Solubilization by surface-active agents and its applications in chemistry and the biological sciences*, Chapman & Hall, 1968.
20. S. D. Hamann, *Rev. Phys. Chem. Jpn*, 1978, **48**, 60-62.
21. K. Hara, H. Kuwabara, O. Kajimoto and K. Bhattacharyya, *J. Photochem. Photobiol., A* 1999, **124**, 159-162.
22. K. Hara, H. Suzuki and N. Takisawa, *J. Phys. Chem.*, 1989, **93**, 3710-3713.
23. N. J. Turro and A. Yekta, *J. Am. Chem. Soc.*, 1978, **100**, 5951-5952.
24. N. Muller and R. H. Birkhahn, *J. Phys. Chem.*, 1968, **72**, 583-588.
25. K. Shinoda, T. Nakagawa, B. Tamamushi and T. lsemura, *Colloidal surfactants: some physicochemical properties*, Academic Press, London, 1963.
26. M. J. Rosen, *Surfactants and interfacial phenomena*, 2nd edn., Wiley, New York, 1989.
27. L. Rekvig, M. Kranenburg, J. Vreede, B. Hafskjold and B. Smit, *Langmuir*, 2003, **19**, 8195-8205.
28. J. D. York and A. Firoozabadi, *J. Phys. Chem. B*, 2008, **112**, 10455-10465.
29. J. S. Zhou and M. Dupeyrat, *J. Colloid Interface Sci.* , 1990, **134**, 320.
30. G. Palazzo, F. Lopez, M. Guistini, G. Colafemmina, and A. Ceglie, *J. Phys. Chem. B*, 2003, **107**, 1924-1931.

31. M. Fanun, *Microemulsions: properties and applications*, 1st edn., CRC Press, Taylor & Francis Group, Boca Raton, 2008.
32. H. B. N. Chennamsetty, L. F. Scanu, F. R. Siperstein and K. E. Gubbins, *J. Chem. Phys.*, 2005, **122**, 094710.
33. W. C. Griffin, *J. Soc. Cosmet. Chem.*, 1949, **1**, 311-326.
34. W. C. Griffin, *J. Soc. Cosmet. Chem.*, 1954, **5**, 249.
35. W. D. Bancroft, *J. Phys. Chem.*, 1912, **17**, 501-519.
36. J. T. Davies, *Proc. Int. Cong. Surf. Activity*, 1957, 426-438.
37. K. Shinoda and H. Kuineda, *J. Colloid Interface Sci.* , 1973, **42**, 381-387.
38. J. H. Schulman, W. Stoeckenius and L. M. Prince, *J. Phys. Chem.*, 1959, **63**, 1677-1680.
39. M. A. López-Quintela, C. Tojo, M. C. Blanco, L. García Rio and J. R. Leis, *Curr. Opin. Colloid Interface Sci.*, 2004, **9**, 264-278.
40. S. P. Moulik and B. K. Paul, *Adv. Colloid Interface Sci.*, 1998, **78**, 99-195.
41. S. A. Safran, D. Roux, M. E. Cates and D. Andelman, *Phys. Rev. Lett.*, 1986, **57**, 491-494.
42. M. Schick and W.-H. Shih, *Phys. Rev. Lett.*, 1987, **59**, 1205-1208.
43. B. P. Binks, J. Meunier and D. Langevin, *Prog Coll Pol Sci S*, 1989, **79**, 208-213.
44. T. Tadros, R. Izquierdo, J. Esquena and C. Solans, *Adv. Colloid Interface Sci.*, 2004, **108-109**, 303-318.
45. D. J. McClements, *Soft Matter*, 2012, **8**, 1719-1729.
46. S. P. Moulik and A. K. Rakshit, *J. Surface. Sci. Technol.*, 2006, **22**, 159-186.
47. M. J. Ansari, K. Kohli and N. Dixit, *PDA J. Pharm. Sci. Tech.*, 2008, **62**, 66-79.
48. H. Watarai, *J. Chromatogr. A*, 1997, **780**, 93-102.
49. T. Kumar, A. Bera and A. Mandal, *WASET*, 2012, **64**, 1114-1119.
50. J. Eastoe, M. J. Hollamby and L. Hudson, *Adv. Colloid Interface Sci.*, 2006, **128–130**, 5-15.
51. S. H. Mohd-Setapar, S. N. Mohamad-Aziz, N. H. Harun and C. Y. Mohd-Azizi, *APCBEE Procedia*, 2012, **3**, 78-83.
52. A. C. Hansen, Q. Zhang and P. W. L. Lyne, *Bioresour. Technol.* , 2005, **96**, 277-285.
53. P. A. Winsor, *Trans. Faraday Soc.*, 1948, **44**, 376-398.
54. P. A. Winsor, *Chem. Rev.*, 1968, **68**, 1-40.
55. L. T. Lee, D. Langevin, J. Meunier, K. Wong and B. Cabane, *Prog. Colloid Polym. Sci.*, 1990, **81**, 209-214.
56. F. Sicoli, D. Langevin, L. T. Lee and M. Monkenbusch, *Prog. Colloid Polym. Sci.*, 1993, **93**, 105-107.
57. P. Taylor, *Adv. Colloid Interface Sci.*, 1998, **75**, 107-163.
58. P. Ghosh, *Colloid and Interface Science*, PHI Learning Private Limited, New Delhi, 2009.
59. A. Thompson, M. Boland, and L. Singh, *Milk Proteins: From Expression to Food*, Academic Press, Elsevier Inc., Amsterdam, Boston, Heidlberg, New York, Oxford, Paris, San Diego, San Francisco, Singapore, Sydney, Tokyo, 2009.
60. L. L. Schramm, *Emulsions, Foams, and Suspensions: Fundamentals and Applications*, WILEY-VCH Werlag GmbH & Co. KGaA, 2005.
61. J. N. Murrell and A. D. Jenkins, *Properties of liquids and solutions*, 2nd edn., Wiley & Sons, Chester, 1994.
62. J. Eastoe, in *Colloid Science*, Blackwell Publishing Ltd., 2009, pp. 77-97.
63. U. Olsson and H. Wennerström, *Adv. Colloid Interface Sci.*, 1994, **49**, 113-146.
64. I. Sunagawa, *Crystals Growth, Morphology, and Perfection*, 1 edn., Cambridge University Press, New York, 2005.
65. I. V. Markov, *Crystal growth for beginners : fundamentals of nucleation, crystal growth, and epitaxy*, 2 edn., World Scientific Publishing Co.Pte.Ltd., MA, USA, 2003.
66. J. W. Mullin, *Crystallization*, 4th edn., Butterworth-Heinemann, Oxford, 2001.

67. T. Threlfall, *Org. Process Res. Dev.*, 2003, **7**, 1017-1027.
68. Y. B. Zeldovich, *Acta Physicochim. USSR*, 1943, **18**, 1.
69. H. Cölfen and M. Antonietti, *Mesocrystals and nonclassical crystallization*, John Wiley & Sons Ltd, Chichester, 2008.
70. T. Wang, H. Cölfen and M. Antonietti, *J. Am. Chem. Soc.*, 2005, **127**, 3246-3247.
71. S. Wohlrab, N. Pinna, M. Antonietti and H. Cölfen, *Chem. Eur. J.*, 2005, **11**, 2903-2913.
72. H. Cölfen and S. Mann, *Angew. Chem. Int. Ed.*, 2003, **42**, 2350-2365.
73. M. G. Page and H. Cölfen, *Cryst Growth Des*, 2006, **6**, 1915-1920.
74. J. Seto, Y. Ma, S. A. Davis, F. Meldrum, A. Gourrier, Y.-Y. Kim, U. Schilde, M. Sztucki, M. Burghammer, S. Maltsev, C. Jäger and H. Cölfen, *P. Natl. Acad. Sci. USA*, 2012.
75. Y. Cai and R. Tang, *J. Mater. Chem.*, 2008, **18**, 3775-3787.
76. J. Tao, H. Pan, Y. Zeng, X. Xu and R. Tang, *J. Phys. Chem. B*, 2007, **111**, 13410-13418.
77. S. Sun, X. Zhang, J. Zhang, L. Wang, X. Song and Z. Yang, *CrystEngComm*, 2012.
78. C. Lausser, H. Cölfen and M. Antonietti, *ACS Nano*, 2011, **5**, 107-114.
79. E. Matijević and P. Scheiner, *Colloid Interface Sci.*, 1978, **63**, 509-524.
80. D. Schwahn, Y. Ma and H. Cölfen, *J. Phys. Chem. C.*, 2007, **111**, 3224-3227.
81. W. Kossel, *Nachur. Ges. Gottingen.*, 1927, **2**, 135-145.
82. I. N. Stranski, *Z. Phys. Chem.*, 1928, **136**, 259-278.
83. W. K. Burton, N. Cabrera and F. C. Frank, *Philos. T. R. Soc. Lond.*, 1951, **243**, 299-358.
84. P. Bennema and G. Gilmer, *J. Cryst. Growth*, North Holland co., 1973.
85. S. J. Cooper, C. E. Nicholson and J. Liu, *J. Chem. Phys.*, 2008, **129**, 124715.
86. C. E. Nicholson, C. Chen, B. Mendis and S. J. Cooper, *Cryst Growth Des*, 2011, **11**, 363-366.
87. L. Qi and J. Ma, *J. Colloid Interface Sci.* , 1998, **197**, 36-42.
88. N. M. Correa, M. A. Biasutti and J. J. Silber, *J. Colloid Interface Sci.*, 1995, **172**, 71-76.
89. E. Fernández, L. García-Río, M. Parajó and P. Rodriguez-Dafonte, *J. Phys. Chem. B*, 2007, **111**, 5193-5203.
90. M. Hasegawa, T. Sugimura, Y. Suzaki, Y. Shindo and A. Kitahara, *J. Phys. Chem.*, 1994, **98**, 2120-2124.
91. M. Boutonnet, J. Kizling and P. Stenius, *Colloids Surf.*, 1982, **5**, 209-225.
92. M. G. Spirin, S. B. Brichkin and V. F. Razumov, *Colloid J*, 2005, **67**, 485-490.
93. C. Petit, P. Lixon and M. P. Pileni, *J. Phys. Chem.*, 1993, **97**, 12974-12983.
94. Y. Xie, R. Ye and H. Liu, *Colloids Surf., A*, 2006, **279**, 175-178.
95. W. Zhang, X. Qiao and J. Chen, *Chem. Phys.*, 2006, **330**, 495-500.
96. K. Wongwailikhit and S. Horwongsakul, *Mater. Lett.*, 2011, **65**, 2820-2822.
97. D. Sarkar, S. Tikku, V. Thapar, R. S. Srinivasa and K. C. Khilar, *Colloids Surf., A*, 2011, **381**, 123-129.
98. M. Fernández-García, X. Wang, C. Belver, J. C. Hanson and J. A. Rodriguez, *J. Phys. Chem. C*, 2006, **111**, 674-682.
99. M. Wu, J. Long, A. Huang, Y. Luo, S. Feng and R. Xu, *Langmuir*, 1999, **15**, 8822-8825.
100. M. Andersson, L. Österlund, S. Ljungström and A. Palmqvist, *J. Phys. Chem. B* 2002, **106**, 10674-10679.
101. C. Y. Tai and C.-K. Chen, *Chem. Eng. Sci.*, 2008, **63**, 3632-3642.
102. C. Tawatchai, C. Amornsak, D. Joydeep, R. Uracha and T. Wiwut, *Sci. Technol. Adv. Mat.*, 2005, **6**, 266.
103. X. Shen, J. Zhang and B. Tian, *J. Hazard. Mater.*, 2011, **192**, 651-657.
104. B. D. Hamilton, J.-M. Ha, M. A. Hillmyer and M. D. Ward, *Acc. Chem. Res.*, 2012, **45**, 414-423.

105. K. C. Hugo, *J. Phys.: Condens. Matter.*, 2001, **13**, R95-R133.
106. A. Mataz and B. M. Gregory, *J. Phys.: Condens. Matter.*, 2005, **17**, R461-R524.
107. J.-M. Ha, J. H. Wolf, M. A. Hillmyer and M. D. Ward, *J. Am. Chem. Soc.*, 2004, **126**, 3382-3383.
108. M. Beiner, *J. Polym. Sci. Part B: Polym. Phys.*, 2008, **46**, 1556-1561.
109. G. T. Rengarajan, D. Enke, M. Steinhart and M. Beiner, *J. Mater. Chem.*, 2008, **18**, 2537-2539.
110. G. T. Rengarajan, D. Enke and M. Beiner, *Open Phys. Chem. J*, 2007, **1**, 18-24.
111. M. Beiner, Rengarajan, S. Pankaj, D. Enke and M. Steinhart, *Nano Lett.*, 2007, **7**, 1381-1385.
112. J.-M. Ha, B. D. Hamilton, M. A. Hillmyer and M. D. Ward, *Cryst Growth Des*, 2009, **9**, 4766-4777.
113. C. L. Jackson and G. B. McKenna, *Chem. Mater.*, 1996, **8**, 2128-2137.
114. B. D. Hamilton, I. Weissbuch, M. Lahav, M. A. Hillmyer and M. D. Ward, *J. Am. Chem. Soc.*, 2008, **131**, 2588-2596.
115. J. M. Ha, *Crystallization and Thermotropic Properties of Organic Solids in Nanoscopic Reactors*, University of Minnesota, 2006.
116. F. C. Meldrum and S. Ludwigs, *Macromol. Biosci.*, 2007, **7**, 152-162.
117. R. J. Park and F. C. Meldrum, *Adv. Mater.*, 2002, **14**.
118. R. J. Park and F. C. Meldrum, *J. Mater. Chem.*, 2004, **14**, 2291.
119. N. J. B. Hetherington, A. N. Kulak, K. Sheard and F. C. Meldrum, *Langmuir*, 2006, **22**, 1955.
120. S. Lugwigs, U. Steiner, A. N. Kulak, R. Lam and F. C. Meldrum, *Adv. Mater.*, 2006, **18**, 2270.
121. A. S. Finnemore, M. R. J. Scherer, R. Langford, S. Mahajan, S. Ludwigs, F. C. Meldrum and U. Steiner, *Adv. Mater.*, 2009, **21**, 3928-3932.
122. N. B. J. Hetherington, A. N. Kulak, Y.-Y. Kim, E. H. Noel, D. Snoswell, M. Butler and F. C. Meldrum, *Adv. Funct. Mater.*, 2011, **21**, 948-954.

Chapter 2 Experimental Techniques

2.1 Introduction of Methods

2.1.1 Microemulsion preparation

To prepare a microemulsion, the first step is to dissolve the surfactant(s) in the continuous phase. The solution used as the dispersed phase is then added to the above mixture, followed by vigorous shaking, vortexing, or ultrasound sonication, to achieve a clear and single homogenous phase. This general procedure is illustrated in Figure 2.1, and applied throughout this thesis unless stated otherwise. The detailed composition of the microemulsions used for each compound is stated in each chapter.

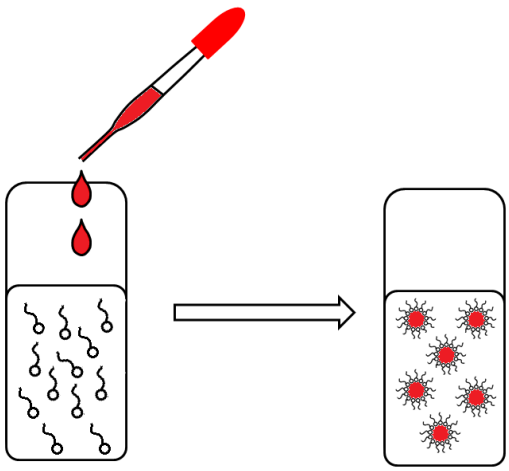

Figure 2.1 Microemulsion formation

2.1.2 Antisolvent addition

When the supersaturation of the crystallisable material contained in the microemulsion is too low, an antisolvent, a solvent which the target compound has very low or no solubility in, was used to increase the supersaturation and thus promote crystallisation in the microemulsion. There are three methods used to add an antisolvent: a) Direct addition; b) Vapour diffusion; c) Microemulsion mixing.

The standard procedure for each of the above methods is detailed below:

a) For the direct addition method (Figure 2.2a), antisolvent is pipetted into the pre-prepared compound containing microemulsion.

b) For the vapour diffusion method (Figure 2.2b), the compound containing microemulsion is left in a small open-topped vial, placed within a large sealed vial. The antisolvent is enclosed in the outer large vial, allowing diffusion into the microemulsion to elevate the supersaturation.

c) For the mixed microemulsion method, the antisolvent is encapsulated in a microemulsion (Figure 2.2c) before being added to the compound containing microemulsion to achieve a single mixed microemulsion phase.

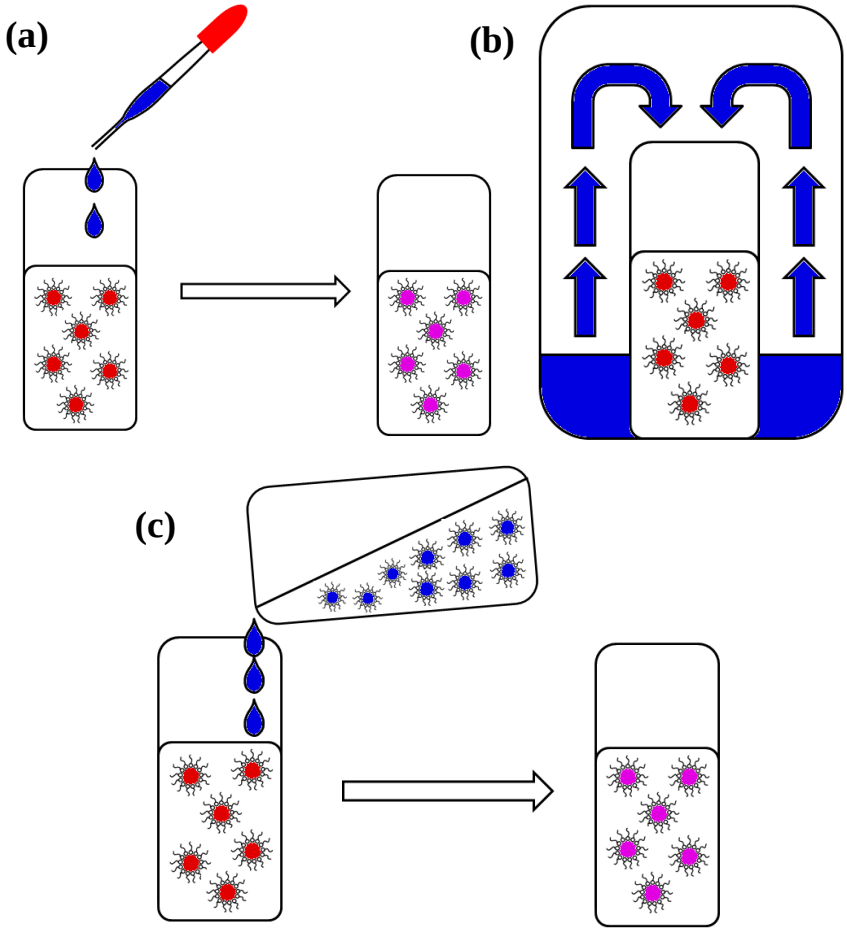

Figure 2.2 Three antisolvent addition methods to the microemulsion: (a) direct addition; (b) vapour diffusion; (c) mixed microemulsion.

The pros and cons for each method will be discussed in Chapter 3 and demonstrated by the example of glycine microemulsion crystallisation.

2.2 Experimental Techniques

Extracted macroscopic crystals were analysed by the following techniques; optical microscope, FTIR, Diffraction techniques (PXRD and SXRD), thermal analysis (DSC/TGA), and Ion/elemental analysis. Nanocrystalline materials, too small for the above techniques, were analysed by TEM.

2.2.1 Attenuated Total Reflectance-Fourier transform infrared spectroscopy (ATR-FTIR)

Infrared (IR) spectroscopic technique detects the vibrational and rotational frequencies of the atoms and functional groups in a molecule. Since different functional groups can have different symmetry, atomic masses and electronic structures, their absorption patterns for a particular group would be unique, allowing fast analysis and identification of the compound.

ATR-FTIR spectra were obtained using a single-bounce Thunderdome (Spectra-Tech) ATR accessory in the sample chamber of a Nicolet Nexus spectrometer, equipped with a liquid nitrogen cooled HgCdTe detector. Either a Thunderdome ATR accessory incorporating a germanium internal reflection element or a Golden-gate diamond internal reflection accessory with a fixed incident angle of 45° and ≈1 mm (*S2*) contact area was used. Typically, samples are clamped to the ATR element using a fixed torque clamp. 128 scans at 4 cm^{-1} spectral resolution were acquired for each spectrum between 4000 and 650 cm^{-1}. The spectra were ratioed against the appropriate background spectrum, taken prior to the sample data collection.

Figure 2.3 Nicolet Nexus spectrometer

2.2.2 X-ray diffraction techniques

X-ray diffraction techniques are used to detect the structures of materials and for diffraction to be observed, Bragg condition must be satisfied, which stated that the particle size, d, is inversely related to the scattering angle, θ_s:

$$m\lambda = 2dsin(\theta_s) \tag{2.1}$$

where

- m is an integer
- λ is the wavelength of X-rays
- d is the spacing between the planes in the atomic lattice
- θ_s is the angle between the incident ray and the scattering planes

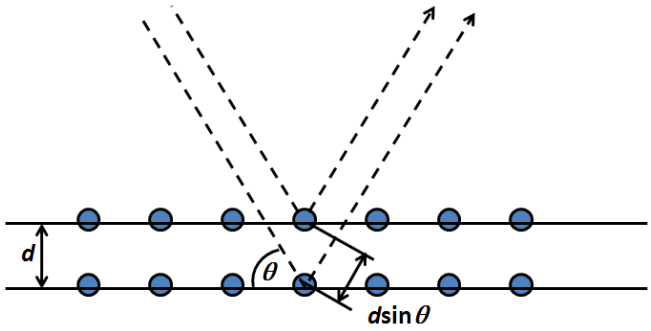

Figure 2.4 Bragg's Law

Two diffraction techniques, i.e. wide angle X-ray scattering (WAXS) and small angle X-ray scattering (SAXS), are employed in this study. The major difference between the two techniques is their scattering angles. WAXS focuses on samples

with 2θ greater than 5 ° whilst SAXS focuses on samples with much lower 2θ (0.1–10 °). WAXS can further divide into powder X-ray diffraction (PXRD), allowing fast identification and crystallinity check of powder crystalline samples, and single crystal X-ray diffraction (SXRD), providing structural determination (e.g. d-spacing, packing, bond length and angle) for the single crystal samples.

2.2.2.1 Wide angle X-ray scattering (WAXS)

WAXS provides structural information (crystallinity and d-spacings) of solid crystalline samples with scattering angles, 2θ, greater than 5 °.

The requirement for the size and shape of the crystalline samples to be analysed in PXRD is much lower than those for SXRD, thus allowing fast identification of the solids. PXRD measurements were acquired on a Bruker D8 diffractometer, equipped with a Cu Kα X-ray source of wavelength 1.54Å and a Hi-star 2D detector. The images captured by the WAXS camera were processed using GADDS software, giving 2θ, *d*-spacings, and peak intensities of a given compound. The samples were ground to a fine powder before being placed on a silica wafer (100 face) to minimise background scattering. 2θ values within the range of 12 °–50 ° are covered in the detection range of WAXS.

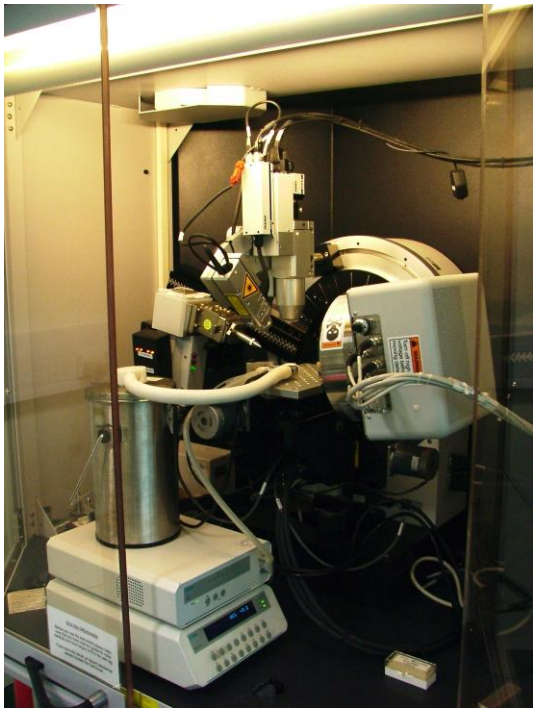

Figure 2.5[1] Bruker D8 diffractometer, fitted with Linkam temperature control unit (Reproduced with permission from ref.1)

X-ray crystallography or Single crystal X-ray diffraction (SXRD) is a technique used to determine the structural information in a crystal, e.g. molecular arrangements and bonding motifs, which provide a more detailed study compared to PXRD. However, the sample required for this technique must be a single crystal with a minimum size of ~100 μm.

Any crystal of SXRD standard was submitted to Durham University Chemistry department crystallography service for structural determination. The crystal was analysed on a Bruker Smart machine equipped with a Mo X-ray source and a State-of-the-art CCD detector at 120 K.

2.2.2.2 Small angle X-ray scattering (SAXS)

Small angle X-ray scattering (SAXS) operates at a low 2θ angle (typically 0.1–10˚) enabling the structural features of ~nanometer particulates to be studied. Such systems include colloids, proteins, and polymers amongst other macromolecules. SAXS relies on a contrast of electron density between the different regions in the particle, providing details on both the shape and structure of the particles.

SAXS measurements were performed on a Bruker Nanostar SAXS instrument, with cross coupled Gδbel mirrors and pin-hole collimation for point focus geometry. The X-ray source is kept inside a sealed tube operated at 40 kV and 35 mA to produce Cu Kα radiation of wavelength 1.54 Å. The SAXS camera is fitted with a Hi-star 2D detector with an effective pixel size of 100 μm. Samples are contained in 2 mm glass capillaries. The optics and sample chamber are under vacuum to minimise air scatter.

Figure 2.6 The Bruker Nanostar SAXS instrument (Reproduced with permission from ref.1)

The scattering data collected was analysed using GADDS software. The background scattering from the solvent is subtracted and the scattering pattern of the sample can be integrated to give the one-dimensional scattering function $I(q)$. q is the length of the scattering vector, defined by $q = (4\pi/\lambda)\sin\theta/2$, with λ being the wavelength and θ the scattering angle. The sample to detector distance was chosen to be 1090 mm or 650 mm, providing a q range of 0.2 to 2.0 nm^{-1}, or 0.2 to 3.2 nm^{-1}, respectively. The collection time was either 2 or 8 hours depending on the electron density contrast between the different components in the sample.

2.3 Generalised Indirect Fourier Transformation (GIFT) analysis

GIFT analysis was used to obtain the pair distance distribution function $p(r)$ and a mean droplet size, r of the microemulsions. A Porod extrapolation was first undertaken on the SAXS data, with this residual background then subtracted from the scattering function $I(q)$. The subtraction of the residual background ensures the $p(r)$ function has a value ≈0, at r = 0 but has little effect on the distribution at larger distances, and the determined droplet sizes. The $p(r)$ function;

$$p(r) = (\frac{\pi^2}{2}) \int I(q)qrsin(qr)dq \qquad (2.2)$$

gives the frequency of occurrence of vectors of length *r*, weighted by the electron density at either end of the vector. It contains essential information about the size and shape of the scattering particles, without any additional hypothesis. The $p(r)$ function was obtained, by employing a structure factor to remove any interparticle interactions. The droplet concentrations were sufficiently low that interparticle interactions were negligible. Droplet radii obtained from the GIFT analysis were compared to the geometric radii calculated from the simple relationship, $r_{Core} = \frac{3\phi}{\Sigma}$, where ϕ is the volume fraction of the confined phase comprising the dispersed phase plus the surfactant hydrophilic or hydrophobic portion in contact with this dispersed phase, and Σ is the interfacial area per unit volume of the microemulsion. Σ is the product of the surfactant area per molecule and the number of surfactant molecules per unit volume. This equation is based on the assumptions that droplets are spherical and the number of surfactant molecules at the droplet interface is negligible.

2.4 Optical Microscopy

Polarised microscopy utilises cross polarisers (a polariser and an analyser) to improve the image contrast of birefringent materials when compared to other contrasting methods, such as bright field imaging generated by light absorption, and dark field illumination produced by light scattering, where their phase contrasts are created by the interference of light with different path lengths.

Crossed polarizer works in the following manner; when a polarised light source (before the specimen) interacts with birefringent materials, their inherent character (i.e. non-uniform spatial distribution of properties and different refractive index at different planes), causes two individual wave components known as ordinary and extraordinary rays to be produced. These two rays are polarised to planes that are perpendicular to each other. These two rays travel at different velocities along the direction of propagation through the specimen. Upon exited the specimen, they become out of phase, and are recombined with constructive and destructive interference after passing through the analyser.

This technique is widely used in many fields, including mathematical sciences, geology, chemistry, biology, and medicine, to distinguish anisotropic and isotropic materials. Isotropic materials, such as gas, liquid, glass and cubic crystals, have only 1 refractive index and thus have no restriction on the vibration direction of the light passing through them (i.e. they are optically identical in all directions). Consequently, they remain permanently extinct under cross polarised light.

This technique is thus employed in this study to distinguish the birefringent materials, particularly the crystals obtained from microemulsions. In addition, crystal habit or morphology can easily be identified using this procedure. Considering the typical compounds used in this study are either polymorphic or pseudo-polymorphic, it is important to understand that variations in size, shape or colour between two samples of a given compound do not definitively classify them as distinct polymorphs. Clarity may be obtained by combining a polarising

microscope with a temperature controlled stage, enabling phase transitions to be observed, similar to a DSC.

Sample measurements were performed using an Olympus optical microscope, fitted with an Olympus MPlan 10x/0.25 ∞/- (10x lens) or LMPlanFI 50x/0.50 objective lens ∞/0 (50x lens) of either. The microscope is equipped with a Linkam F600 heated stage and TMS93 Temperature Controller Module, enabling the operation temperature in the range of -50°C→300℃. Images were captured using an Olympus Camedia 2.1 megapixel digital camera (Pixelink A602 2.0 megapixel camera) and processed by Linkam Linksys software.

Figure 2.7 Olympus optical microscope (Reproduced with permission from ref.1)

2.5 Transmission Electron Microscopy (TEM)

The transmission electron microscope[2] is a further microscopy technique providing higher resolution images of the microstructure of a material compared to a light microscope. The electron beam is transmitted to the specimen and forms images that will be magnified, focused and finally detected by a sensor such as a

CCD camera. The high resolution comes from the small de Broglie wavelength of the electrons in Equation (2.3), enabling fine details of the materials, such as the shape, size or structure of the nanocrystals, to be examined.

$$\lambda = \frac{h}{m_e v} \tag{2.3}$$

where

- λ is the wavelength;
- h is Plank's constant and equals to 6.63×10^{-34} J s;
- m_e is the mass, for an electron, m is 9.11×10^{-31} kg;
- v is the velocity of the beam, which is a significant fraction (50–70% at 80–200 kV) of the speed of light (3.00×10^8 m/s).

For TEM, the electron wavelength is typically ~0.02 Å (in contrast to a ~few Å for X-rays). The net resolution (δ) is affected by the diffraction limit (δ_1) and the spherical aberration (δ_2). The (theoretical) resolution limit, δ_1 is ~0.1–0.2 Å when calculated from Equation (2.3). Assuming the wavelength is ~0.02 Å and the semi-convergence angle is ~0.1 radians (5˚), the (theoretical) resolution limit δ_1 is found by:

$$\delta_1 = \frac{d_{S1}}{2} = \frac{0.61\lambda}{\varepsilon \sin \varphi} \tag{2.4}$$

where

- d_{S1} is diffraction limited spot size
- ε is the refractive index of the medium between the object and the objective lens
- φ is the semi-convergence angle
- $\varepsilon = 1$ for air and at small angles $\sin \varphi = \tan \varphi = \varphi$

However, this theoretical value is not achievable due to lens aberrations. Although chromatic aberrations can be eliminated by refining electrons within a very narrow range of wavelength, the (monochromatic) spherical aberrations, causing rays being at much larger angles, tend to bring a problematic premature focus. To minimise this effect, a small aperture is often employed to ensure the electrons

can only pass through the centre of the lens. However this process is at the expense of the resolution degradation, as illustrated in Equation (2.5). The degradation of spherical aberration resolution, δ_2, can be found as:

$$\delta_2 = C_s\varphi^3 \tag{2.5}$$

Where C_s is the aberration coefficient. The JEOL 2100F FEG TEM used for this work has a high resolution pole piece with 1.0 mm C_s, giving 2.3 Å point resolution and 1.0 Å information limit. This instrument belongs to the GJ Russell Microscopy Facility in the Physics department, Durham University, as shown in Figure 2.8.

Figure 2.8 The JEOL 2100F FEG TEM

To prepare the TEM sample, the material was first deposited onto a holey carbon grid and examined in a JEOL 2100F Schottky field emission gun TEM (FEG TEM) operating at 200 kV. Phase contrast, high resolution electron microscopy (HREM) and diffraction patterns (DP) were imaged by a Gatan Orius Camera and enabling imaging of nanometre size crystals. The structure of an individual nanocrystal was determined by indexing the fast Fourier transform (FFT), extracted from the appropriate region of the image. A qualitative determination of the chemical composition of the sample was performed using an Oxford INCAx-Sight Si(Li) detector for Energy-dispersive X-ray spectroscopy (EDX). Digital Micrograph® platform software was used to capture the images and to perform further analysis, including generating Fast-Fourier Transform (FFT) images of a selected area and plotting thickness profiles of the nanoparticles.

2.6 Thermogravimetric analysis (TGA)

Thermogravimetric analysis (TGA) is a type of thermal analysis used to measure the amount and rate (velocity) of change in the mass of a sample as a function of temperature and/or time in a controlled atmosphere. Consequently it has been used in this study to determine the weight loss of solvates and salts of DPA upon heating.

Samples for TGA were cleaned and dried before being submitted to the thermal analysis service in the Chemistry department, Durham University. The samples were weighed to 0.01 mg and sealed in an aluminium pan. The measurements were run in a Perkin Elmer Pyris 1 TGA instrument from room temperature to 400 ℃ at 10 ℃ /min, which was equipped with a fine balance and a mass spectrometer to monitor the weight loss.

Figure 2.9 Perkin Elmer Pyris 1 TGA instrument

2.7 Viscosity measurement

Viscosity is the principal parameter to be considered when measuring the flow of any fluid. For Newtonian fluids, viscosity is constant over a wide range of shear rates; for non-Newtonian fluids, viscosity varies with shear rates. The vast majority of microemulsions are Newtonian, with their viscosity directly linked to the kinetics of the system, e.g. droplet collision rate.

The viscosity of the microemulsions was measured using a Brookfield DV-II+ PRO Digital Viscometer (Figure 2.9), equipped with a LV-1 spindle and controlled by Rheocalc® software. The shear velocity was varied between 0–200 RPM, with the measurements being undertaken under ambient conditions.

Figure 2.10 Brookfield DV-II+ PRO Digital Viscometer

2.8 pH meter

pH measures the activity of the solvated hydrogen ions and mathematically can be expressed as $-\log [H^+]$ or $-\log [OH^-]$ for strong acids or bases. A pH meter is an electronic device used to measure the pH of a liquid. The probe is made of a doped glass membrane that is sensitive to H^+ ions and measures the pH, based on the activity of H^+ surrounding the probe. Despite pH typically being a measure of aqueous solutions, it can also be employed to detect the H^+ concentration in non-aqueous solvents. pH values for these systems are usually defined by a different scale to the aqueous pH values, due to the different standard states used. From this aspect, reversed microemulsions are classified as non-aqueous or half-aqueous systems and one should not compare the pH values to the aqueous phase. However, literature studies regarding microemulsions have revealed the possibility of using water/aqueous solutions as standards[3].

Figure 2.11 A Hanna HI 221 pH/mV/℃ bench meter.

A Hanna HI 221 pH meter, equipped with HI 1131P glass body in a single junction refillable cell and a HI 7669/2W stainless steel probe was used for measurements in the pH and temperature range of -2 to 16 and -20 to 120 ℃, respectively, with an accuracy of 0.01 and 0.01 ℃, respectively. Prior to any measurement, a pH meter was calibrated with reference solutions of pH 4 and 10.

2.9 References

1. C. E. Nicholson, *Crystallisation in emulsion and microemulsion systems*, Durham University, Ph.D thesis, 2006.
2. P. J. Goodhew, J. Humphreys and R. Beanland, *Electron Microscopy and Analysis*, 3rd edn., Taylor & Francis, London and New York, 2001.
3. F. M. Menger and K. Yamada, *J. Am. Chem. Soc.*, 1979, **101**, 6731-6734.

Chapter 3 Glycine

3.1 Introduction

Glycine (Figure 3.1) (aminoacetic acid) is the simplest of the 20 amino acids commonly found in proteins. It exists in the form of a zwitterion in the solution state and acts as an inhibitory neurotransmitter that acts in the central nervous system[1] such as the spinal cord, brainstem and retina. It is a polymorphic compound that has been employed in a number of emulsions and/or microemulsion studies[2-5] owing to its well-known properties and the difficulty in obtaining the most stable form. For this reason, it is an ideal compound for this study to illustrate the thermodynamic 3D-nanoconfinement effect.

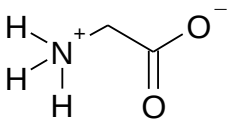

Figure 3.1 Structure of Glycine

3.2 Background of Glycine

Glycine is reported to have five non-solvated polymorphs[6] (the α, β, γ, δ, and ε forms) to date, where the α, β, and γ forms can be obtained under ambient conditions whist the δ and ε cases are high pressure forms obtained at 0.8 GPa and 1.9 GPa, respectively. Herein, only α, β, and γ forms are discussed. The monoclinic α form is centrosymmetric bipyramidal shaped with a space group $P2_1/n$. The monoclinic β form has an acicular morphology with a $P2_1$ space group, and the trigonal γ form is prismatic shaped and noncentric with a $P3_1$ space group (some also refer to the γ form as being in the polar space group $P3_2$[7, 8]). Under ambient conditions, the most stable form is the γ form, then the α form, with the β form being the least stable[9, 10].

In all three forms, there is only one molecule within the asymmetric unit but each has a different number of molecules within the unit cell (Figure 3.2). For the α form, there are four glycine molecules forming two cyclic dimers via $NH_{gly}\cdots O{=}C$ hydrogen bond (Figure 3.2a). However, hydrogen bonding only exists across the layers of dimers but not between the layers (Figure 3.3a). The

unit cell of the β form contains two molecules (Figure 3.2b), which are also hydrogen bonded via N-H_{gly}…O=C in addition to molecules in different layers being connected to each other by hydrogen bonding (Figure 3.3b). The γ form has three glycine molecules that form a trimer structure (Figure 3.2c) with the hydrogen bonds linking different trimer layers (Figure 3.3).

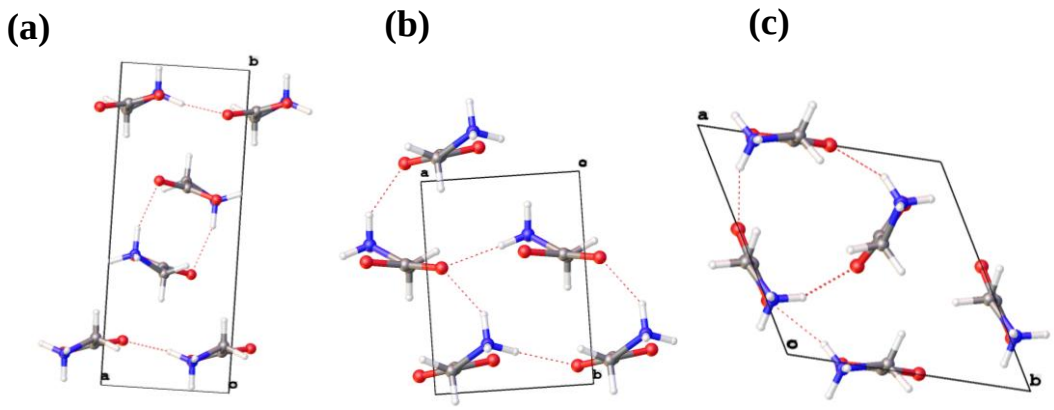

Figure 3.2 Unit cell in α, β, and γ forms of glycine prepared from Olex-2[11] (cif files obtained from Mercury[12]): (a) α form (refcode: GLYCIN 29); (b) β form(refcode: GLYCIN 31); (c) γ form (refcode: GLYCIN 33); It is reported all three forms were measured under ambient temperature and pressure.

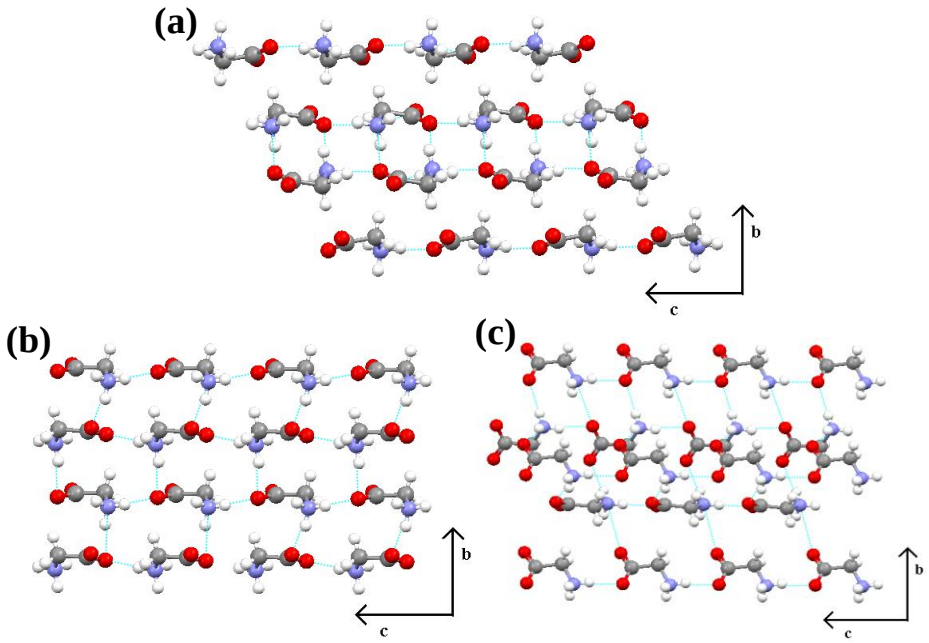

Figure 3.3 Hydrogen bonding schemes for α, β, and γ forms from *Mercury*[12]: (a) α form (refcode: GLYCIN 29); (b) β form (refcode: GLYCIN 31); (c) γ form (refcode: GLYCIN 33).

Of these three polymorphs, the α and γ forms are very close in lattice energy (~0.2 kJ mol^{-1} at ambient temperatures)[13] but the α form grows ~500 times faster than the γ form in an aqueous solution with a supersaturation ratio of ~1.1[14], which was attributed to the solvent effect that assisting the dimer formation in α form. It has been reported that the α form can be obtained from the aqueous saturated glycine solution at ambient conditions, whilst the γ form was reported to form under extreme conditions such as: employing acidic/basic solutions to poison the fast growing α-form, using heavy water as a solvent (D_2O)[15], via γ-form seeding of aqueous solutions, addition of α-form inhibiting additives[16], applying electromagnetic fields[17] or by induction with a nonphotochemical laser[18]. The β form is known to rapidly form in the presence of alcohols (e.g. methanol and ethanol),[19] but it is highly unstable and readily transforms to the α or γ form on exposure to moisture[2, 20]. The rate of phase transition depends on many factors such as the temperature and solution concentrations. Typically, due to the very small thermodynamic driving force, a high temperature and/or a high humidity level is required to enhance the transition from β to α[21]. In terms of the solubility in water at ambient conditions, the γ form (0.228 g per gram of solution[20]) is slightly less soluble than the α form (0.234 g per gram of solution[20]). These factors led to the difficulty in growing γ crystals from pH neutral aqueous supersaturated solutions. Very few studies performed under these conditions were able to obtain γ form crystals, with the exception of He *et. al*[7] who reported the growth of γ form single crystals from supersaturated solution on silanized glass slides by a slow-evaporation method.

Due to the very small thermodynamic driving force, the α form very rarely[13] undergoes polymorph transformation into the γ form at room temperature except at high temperature and humidity conditions[8]. The γ form will only transform to the α form upon heating to ~160–177 ℃[22], which was attributed to their hydrogen bonding networks[23].

Although the α, β and γ forms are thermodynamically close in energy, they have distinct peaks in the FT-IR spectrum.[24] The α form has a peak at ~911 cm^{-1}, the β form at ~915 cm^{-1}, and the γ form has a peak at ~928 cm^{-1}, as shown in Figure 3.4.

These peaks represent a combination of CH_2 rocking[25] and the CH_2 vibrational frequency that is strongly coupled with the adjacent NH_2 or NH_3[26].

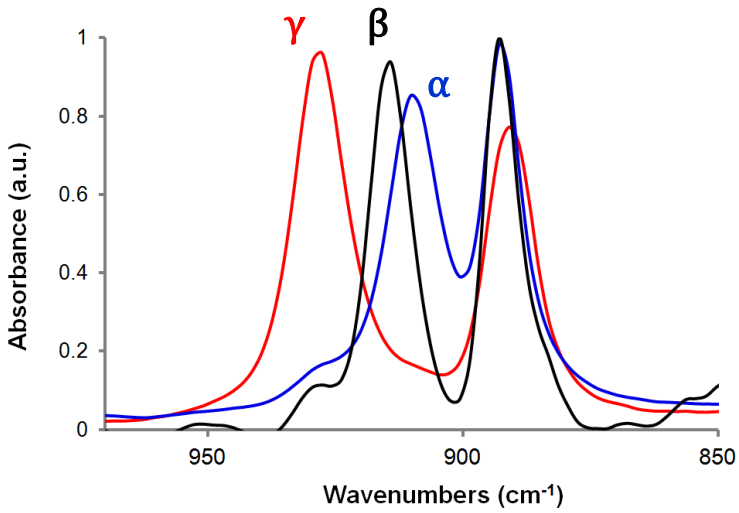

Figure 3.4 FTIR of the α, β, and γ forms of glycine

3.3 Phase Diagrams

A phase diagram is a prerequisite for any emulsion/microemulsion related work. It is used to investigate the boundaries of different phases in a surfactant containing system so that regions of interest can be quickly identified.

In this glycine chapter, two types of surfactants had been tested: 1) an anionic surfactant, AOT, which has been previously used in the emulsion crystallisation work of Garti *et. al.*[5] and Davey *et. al.*[2]; and 2) a new combined non-ionic surfactants systems Span 80 and Brij 30.

1) The salt-free H_2O/AOT/heptane phase diagram at 25 ℃ has previously been reported in the literature[27] as shown in Figure 3.5. Herein regions I, II, III, and IV represent stable w/o microemulsions, liquid crystals, bicontinuous phases and o/w microemulsions, respectively. This is compared with the phase diagram obtained in our study to test the robustness of our method. As illustrated in Figure 3.5, the (single phase) microemulsion regions are in agreement with each other, although small discrepancies were observed.

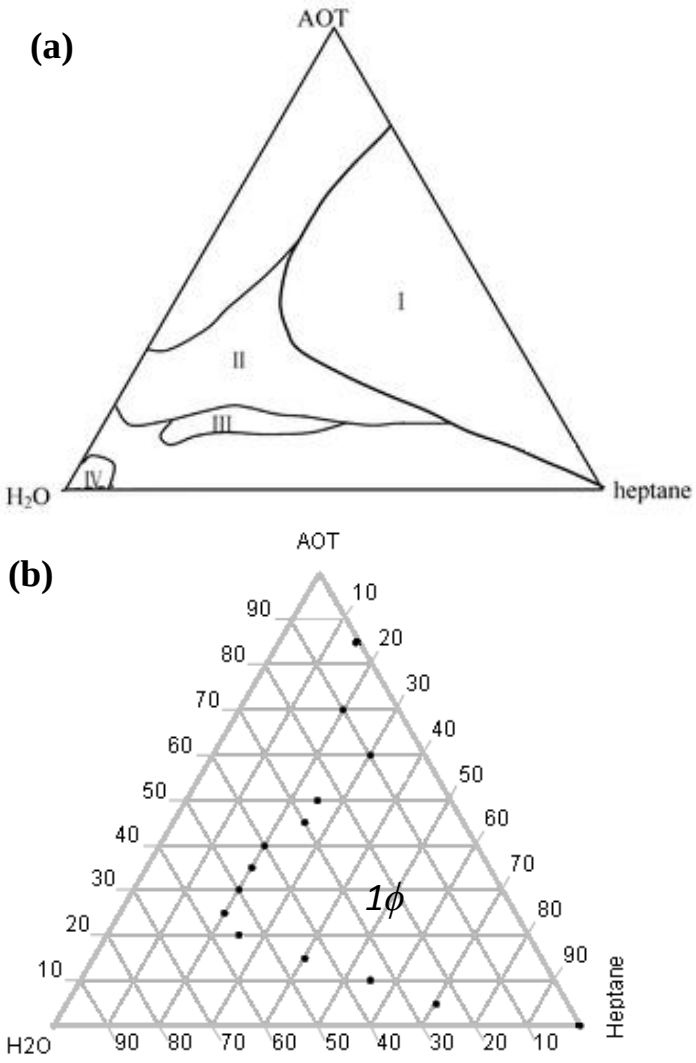

Figure 3.5 Ternary phase diagrams of water/AOT/heptane systems: (a) from literature[27] where regions I, II, III, and IV represent stable w/o microemulsions, liquid crystals, bicontinuous phases and o/w microemulsions, respectively (reproduced with permission, Copyright © 2003, Springer-Verlag); (b) in our quick phase diagram determination with 1ϕ standing for a single phase microemulsion region.

2) H_2O/Span 80 + Brij 30 (1:1 w/w)/heptane is a new system, hence the phase diagram was partially investigated to determine the w/o microemulsion region, which is shown in Figure 3.6. Upon the addition of methanol into the dispersed phase, the w/o microemulsion region was enlarged, thus the results for 1:1 and 2:1 MeOH: H_2O by weight were also included. This is expected since methanol can behave partially like a cosurfactant, lowering the interfacial tension and stabilising the microemulsion.

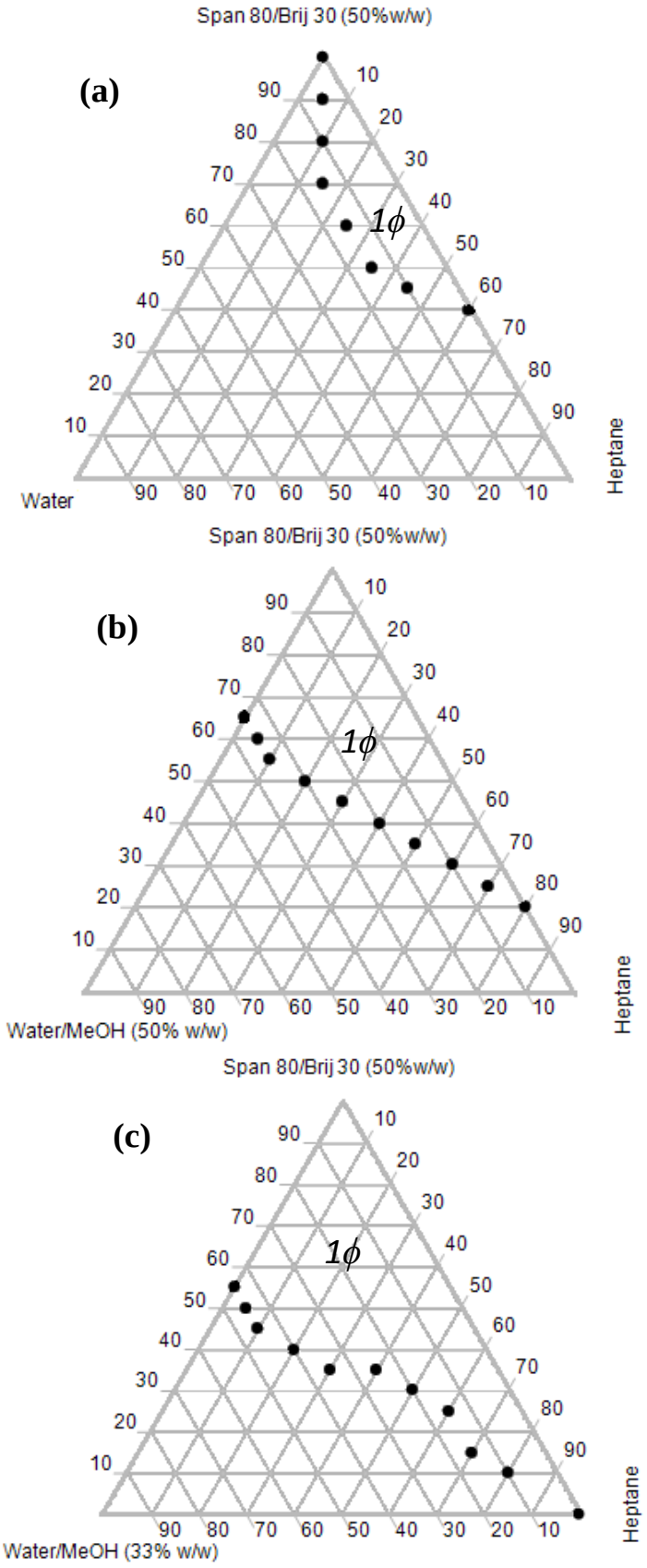

Figure 3.6 Ternary phase diagrams for water-MeOH mixture/Span 80+Brij 30 (50%:50% w/w)/ heptane systems with various water-MeOH compositions: (a) pure aqueous phase; (b) water-MeOH at 50%: 50% w/w; (c) water-MeOH at 33%: 67% w/w.

3.4 Methods of microemulsion preparation

All materials were purchased from Sigma-Aldrich and used without further purification. Ultra high purity (UHP) water with a resistance 18 $M\Omega^{-1}$ was obtained from a UHP water filtration unit.

Microemulsions were prepared as stated in Chapter 2.1.1–2.1.2. The glycine microemulsions were prepared from heptane (continuous phase), surfactant(s) (e.g. AOT or Span 80/Brij 30 at 1:1 w/w) and glycine solution (dispersed phase). The surfactant(s): heptane ratios are kept at 1:3 w/w for AOT and 2:3 w/w for Span 80/Brij 30. To per gram of the surfactant(s) in heptane continuous phase, the volume of glycine solution added varied between 25–45 µl.

Then methanol was added via direct addition, vapour diffusion or microemulsion encapsulation to the glycine microemulsion as an antisolvent to achieve supersaturation and thus to induce crystallisation.

3.5 Control experiments

Control experiments were performed to determine the solubility of glycine in the microemulsions, to investigate glycine crystallisation form bulk solutions and emulsions allowing the comparison of results with glycine crystallisation in microemulsions.

3.5.1 Solubility tests

The solubility of glycine within the microemulsion was determined to allow the calculation of supersaturation ratio. The mixed microemulsions were prepared as per the procedure described in section 3.4, except in this case the dispersed phase was pure water. Further, various amounts of finely ground glycine solid (3–6 mg glycine per gram surfactant solution) was added to the bottom of a range of vials, before the addition of the mixed microemulsion. The mixtures were left to equilibrate at 25 ℃ for ~5–6 weeks allowing the glycine to slowly diffuse through the heptane continuous phase into the aqueous droplets until saturation is achieved.

3.5.2 Bulk solution experiments

For the bulk solution experiments, comparable compositions to the inner phase of the optimised microemulsion formulations were adopted. 0.25 g of the 3%–18% w/w glycine aqueous solutions were mixed with 1.25 g 80% w/w methanol-water solution, inducing rapid crystallisation and hence allowing the investigation of the polymorphic outcome under unconfined conditions.

3.5.3 Emulsion preparation

Glycine emulsions were prepared prior to the addition of methanol antisolvent. The glycine emulsion were prepared from 1.17 g of 2%–6% w/w glycine solutions, 4.2 g of heptane, and 2.8 g of Span 80/Brij 30 (50%/50% w/w). The methanol microemulsion contained 2.33 g of methanol, 1.8 g of heptane, and 1.2 g of Span 80/Brij 30 (50%:50% w/w). The methanol microemulsion was poured into the glycine emulsion followed by immediate vigorous shaking to obtain an overall emulsion. However, emulsions of Span 80/Brij 30 were not long-lived and thus slowly phase separated overnight.

3.6 Results and Discussion

3.6.1 AOT system

AOT, an anionic surfactant, is capable of forming stable microemulsion without the assistant of a cosurfactant. Glycine microemulsions prepared using AOT produced mostly the γ form after 2–5 weeks, regardless of the preparation method or the microemulsion composition (i.e. varying the concentration and quantity of glycine and methanol). Albeit, at 18% (w/w) glycine solution where a high supersaturation is induced, the immediate crystallisation of the metastable α form was observed. The γ-form crystals retrieved here were about ~10–100 μm in size and an example of which is shown in Figure 3.7.

Owing to the trimer polar structure of the γ-form, charged/polar materials such as KCl[28] and NaCl[16] were reported to assist the formation of the polar chains and thus promote both the nucleation and growth of the γ-form. Being an anionic surfactant, AOT can provide this charged surface, enhancing γ formation. Indeed,

previous studies by Allen *et. al.*[2] had demonstrated this templating effect, thus the formation of the γ form could not be solely attributed to the thermodynamic control afforded by the 3D-nanoconfinement in the microemulsion droplets.[2].

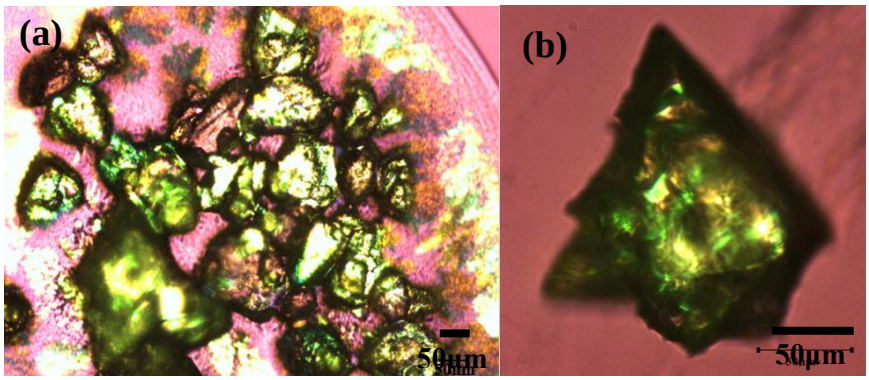

Figure 3.7 The γ crystals obtained from AOT microemulsions: (a) Crystal aggregated under magnification x10; (b) Single crystal under magnification x50

As a consequence, non-ionic surfactants were employed for further studies in order to assess the sole effect of thermodynamic 3D nano-confinement in microemulsions. A combination of the non-ionic surfactants, Span 80 and Brij 30, were chosen as they had previously been found to help induce α-glycine crystallisation[29].

3.6.2 Span 80/Brij 30 system

The use of the non-ionic Span 80/Brij 30 system rigorously tests the robustness of our methodology – to achieve thermodynamic control of crystallisation via 3D-nanoconfinement. It is a great challenge to obtain the γ form from this system due to the following factors:

- Span 80/Brij 30 is known to favour the formation of metastable forms; this suggests γ-glycine nucleation is hindered within their micelles despite confinement. This is further explored in the bulk crystallisation experiments in section 3.6.2.7.
- There is only a very small lattice energy preference for the γ form over the α form of ~0.2 kJ/mol[13]

- The slow growth rate of the γ form in aqueous solution (~500 times slower than the α form[30]) indicates that there is a huge kinetic preference (~15 kJ mol^{-1} in activation energy[13]) for the nucleation of α form over the γ form.

Upon variation of the microemulsion compositions, all three glycine polymorphs can be obtained. The results of variations in the crystallisation method, glycine concentration, methanol concentration, surfactant concentration, and crystallisation time are discussed in detail below. Figure 3.8 shows the microscope images of the three forms, where the α form has a bipyramidal shape, the β form is thin needle/plate-like and the γ form is pyramidal.

The emergence of the γ form illustrates the importance of crystallisation within 3D nano-confinement. It can be inferred that preferentially, homogeneous nucleation occurs within the water pool of the micelles. Thus, it is expected, due to the close proximity of the amphiphiles to the site of nucleation, if surfactant templating was to play a role, the metastable form would dominate. Hence, surfactant templating can be ruled out or be overcome to allow the preferred crystallisation of the stable γ form.

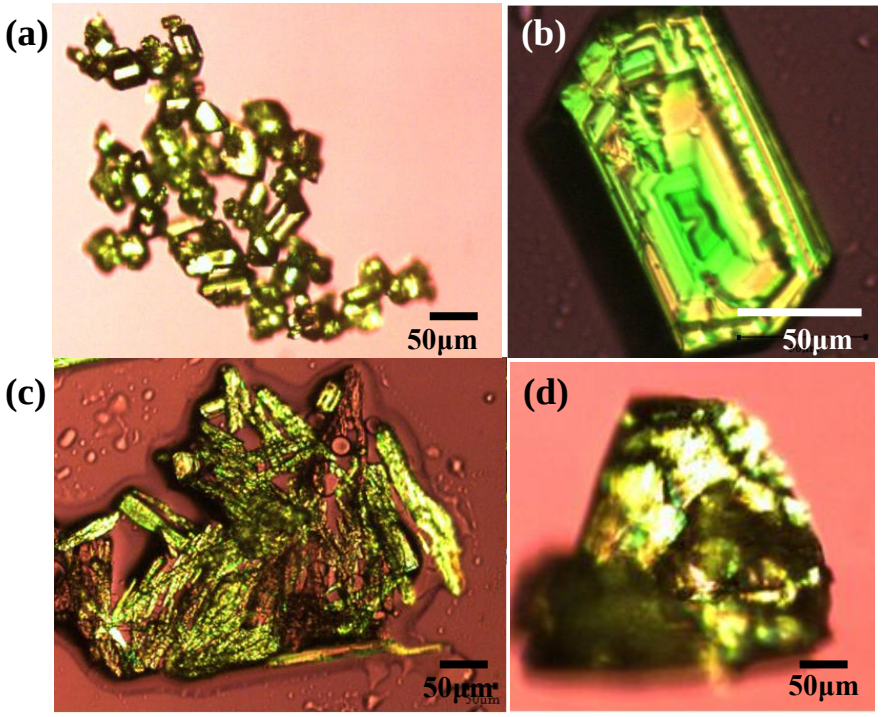

Figure 3.8 Optical microscope images for of the α, β and γ forms. (a) and (b) the α form; (c) the β form;(d) the γ form.

Crystallisation within a microemulsion can only occur at three locations: the interface, the outer water layer that is bound or perturbed by the surfactants or the central water pool. The former two locations are heavily influenced by the surfactants and thus any product crystallised from these two regions are possibly nucleated by heterogeneous nucleation with the surfactants being the foreign surfaces or templates. In contrast, the last location is free from any external disruption and solely controlled by the thermodynamic 3D-nanoconfinement. Since any contribution from the surfactants is ruled out, the γ form crystallisation can thus only take place at the central water pool via homogeneous nucleation.

3.6.2.1 Preliminary experiments on the effect of different antisolvent addition methods

Our preliminary tests demonstrated that for a microemulsion consisting of 6g heptane and 4 g Span 80/Brij 30, the dispersed phase of solely UHP water has to be in the 0.25 – 0.45 g region for stability to be maintained. This region is narrowed to ~0.30 g if 4% (w/w) glycine solution is the dispersed phase. This region corresponds to the red dot indicated in the phase diagram in Figure 3.9. As the region appears on the edge of the single phase microemulsion boundary small perturbations to the system may result in phase separation, so careful control of the aqueous phase volume is required.

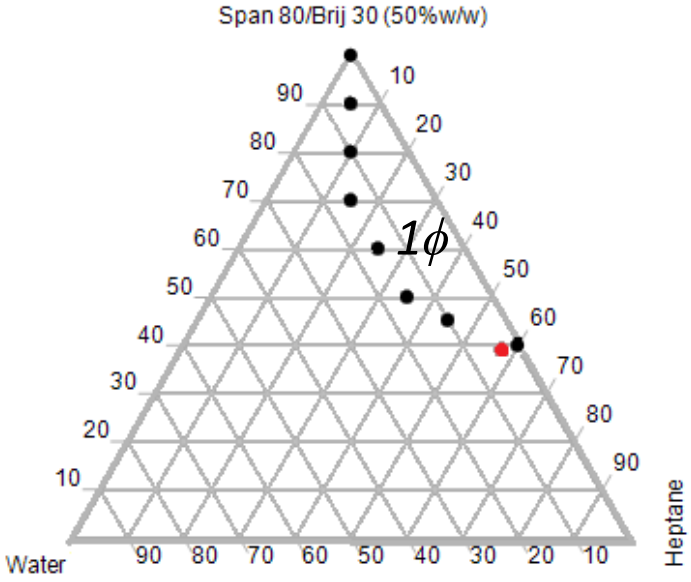

Figure 3.9 Ternary phase diagram of water/Span 80+Brij 30/heptane system (red dot indicates the region of interest)

The reasons to work within this region rather than one of higher stability are: 1) more solute material (glycine) can be doped into the system, thus maximising the yield; and 2) enhancement of the solute exchange rate, due to higher interfacial tensions and the reduced surfactant film rigidity, thus an increased rate of transient dimer formation. From early studies, the latter is highlighted since microemulsions with a smaller amount of inner phase took either a very long period of time (> 1 year) to crystallise or no macroscopic crystals were ever observed.

The addition of methanol was the solution to the above problems because: 1) glycine has very limited solubility in alcohol based solvents: 0.011 M in methanol[31] and 0.0004 M in ethanol[31] (with respect to 3.325 M in water[31]), which makes them effective antisolvents. However ethanol is miscible in both aqueous solutions and heptane whilst methanol is only miscible with aqueous solutions, thus is ideal for this study; 2) methanol is slightly amphiphilic in nature and thus can act as a weak cosurfactant[32] to stabilise the microemulsion. An additional benefit of methanol is its volatile nature, allowing the diffusion of vapour into the microemulsion, thus higher supersaturations can be generated.

The preliminary experimental results using three different methanol addition methods, namely direct addition, vapour diffusion and methanol microemulsion addition, are compared in Table 3.1.

For the direct methanol addition method, the large quantity of methanol addition in a short period of time can lead to α formation with a characteristic FTIR peak at 911 cm^{-1}. This can be explained by the fast addition rate, inducing a high local concentration of methanol and enhancing metastable form nucleation, which is a major drawback of this method.

The vapour diffusion method led to phase separation of the microemulsions after 2 hours, yielding the metastable α form. This is because the antisolvent diffusion rate and overall quantity that participated into the microemulsion are difficult to control. If insufficient antisolvent diffuses into the microemulsion, an adequate supersaturation level will not be achieved and crystallisation will never occur.

Additionally, in some cases, antisolvents with amphiphilic nature are essential components to maintain the stability of the microemulsions and hence insufficient antisolvent can even cause phase separation.

Conversely, if too great an amount of antisolvent presents, the danger of too high a supersaturation could result in the loss of thermodynamic control of crystallisation. In extreme cases, too much methanol vapour addition can also result to phase separation, thus leading to the loss of 3D-confinement and polymorph selectivity.

Table 3.1 Different methods of microemulsion formation and the results.

	Glycine Microemulsion				MeOH addition				
	Glycine solution		Heptane /g	Span 80 / Brij 30 (1:1) /g	MeOH /g	H_2O /g	Heptane /g	Span 80 / Brij 30 (1:1) /g	Result
	Glycine mass %	/g							
Direct MeOH addition	4	0.25	6	4	1	0.25	/	/	γ form but can mixed with α form
Vapour diffusion	4	0.25	6	4	1	0.25	/	/	Phase separation to α form
Mixed Micro-emulsion	4	0.25	4.2	2.8	1	0.25	1.8	1.2	Mostly γ form

In contrast, the mixed microemulsion method (or methanol microemulsion encapsulation) reproducibly obtained mostly the γ form with only a very small amount of the α form produced (Figure 3.10). This method has its advantages over the previous two methods:

- Precise control of the quantity of antisolvent added.
- Maintenance of a uniform microemulsion droplet size range.
- Avoidance of locally high concentrations of methanol.

Thus the mixed microemulsion method is found to be the most reliable and robust method and thus was employed in further studies.

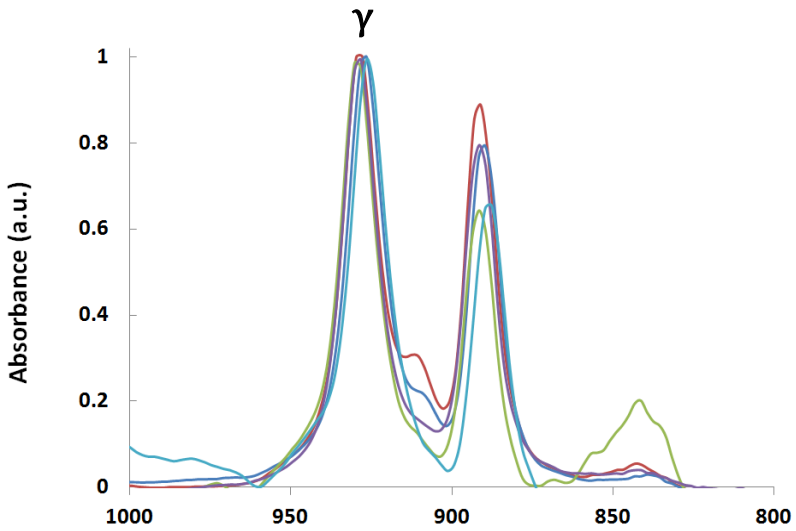

Figure 3.10 Overlaid ATR FTIR spectra from 1000–800 cm^{-1} of γ-glycine obtained from five repeats of the mixed microemulsion method.

3.6.2.2 Effect of glycine solution concentration

The concentrations of glycine solution were varied from 3% to 5% w/w (Table 3.2) where both 3% and 3.5% show no sign of crystallisation after 3 months due to the limited amount of glycine in the microemulsions. The 4%–5% glycine solutions formed ~mm sized crystals, sufficient in size to be analysed after three weeks. FTIR analysis (Figure 3.11) indicated only the 4% glycine solution contained mostly the γ form, while the 4.5% had a majority of the α form with a minority of the γ form and 5% solutions formed a vast majority of the α form.

Table 3.2 Effects of glycine concentrations for the mixed microemulsion method

Glycine Microemulsion				MeOH microemulsion					
Glycine solution		Heptane /g	Span 80 / Brij 30 (1:1) /g	MeOH /g	H_2O /g	Heptane /g	Span 80 / Brij 30 (1:1) /g	Mean initial supersaturation ratio	Result
Glycine mass %	/g								
3	0.25	4.2	2.8	1	0.25	1.8	1.2	1.7	No crystals
3.5	0.25	4.2	2.8	1	0.25	1.8	1.2	2.0	No crystals
4	0.25	4.2	2.8	1	0.25	1.8	1.2	2.3	Mostly γ form
4.5	0.25	4.2	2.8	1	0.25	1.8	1.2	2.6	Mostly α form
5	0.25	4.2	2.8	1	0.25	1.8	1.2	2.9	Mostly α form

These results reveal that small changes (0.5% w/w) in glycine concentration can have a large impact on the polymorphic outcomes (3.5%-no crystal, 4%-γ form, 4.5%-α form). This observation was attributed to the different supersaturation ratios, as thermodynamic control is favoured when crystallisation was just possible, i.e. the case of the 4% glycine solution in this study. Below this concentration at 3.5% glycine solution, insufficient material is present in the microemulsion to form stable nuclei, hence no crystallisation was observed. At a higher concentration of 4.5%, thermodynamic control was lost, as stable nuclei of the α form can also be achieved, so kinetic control took place.

The above observation has previously been illustrated in the study of AOT microemulsions by Allen *et.al.*[2]. He shows that an AOT microemulsion with a low supersaturation ratio (S = 1.1) and a small droplet size < 5 nm favours the formation of γ form. Whilst for higher supersaturation (S > 1.2), the quantity of the α form also increased and at S > 1.5, the product was entirely the α form. However, in the Span 80/Brij 30 microemulsion with a mean droplet size of 3.6 nm, no crystallisation was observed for S < 2.0. The γ form mainly formed at S = 2.3 and for S > 2.6, the α form was the dominant product. The discrepancies between the two systems can be explained by the different nucleation processes. Heterogeneous nucleation was postulated in AOT system where the surfactant template assisted the nucleation, reduced the energy barrier and thus lowered the driving force for nucleation (i.e. supersaturation). In contrast homogeneous nucleation happened in Span 80/Brij 30 case where crystallisation occurred at the free central water pool and the surfactants did not contribute to the nucleation process.

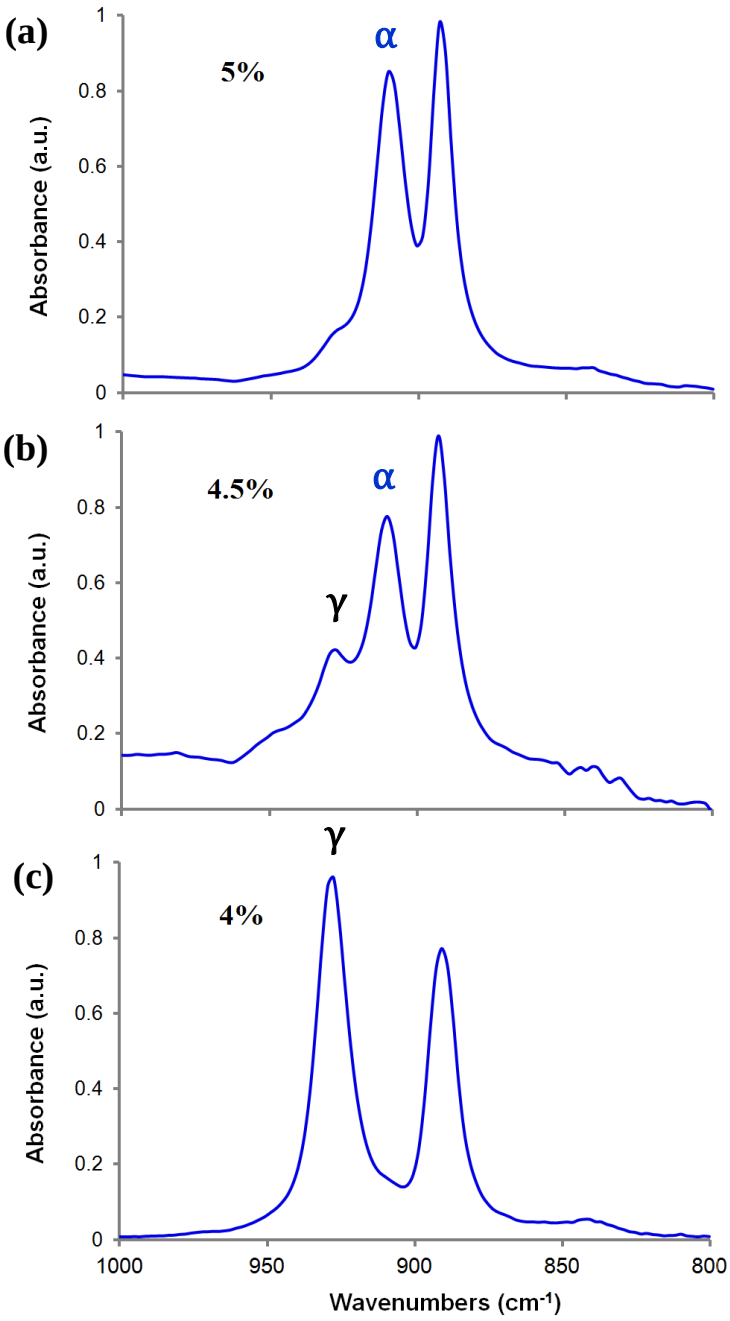

Figure 3.11 FTIR spectra of crystals that obtained from (a) 5%, (b) 4.5% and (c) 4% microemulsions

Overall the glycine encapsulated in the microemulsion to maintain the confinement is limited to a very narrow concentration region (~4% glycine solution). Therefore, this 4% glycine solution microemulsion was employed as the 'optimum formulation' for further investigations in which other conditions, such as antisolvent quantity and crystallisation duration, were studied.

3.6.2.3 Effect of methanol to water ratio

As mentioned in section 3.4, methanol is an antisolvent which is essential to provide the desired supersaturation to induce crystallisation, ideally under thermodynamic control (section 1.5). In addition, it can act as a microemulsion stabiliser (similar to a co-surfactant[33]) owing to its 'slight amphiphilic' nature. This is also supported by the observation that the mixture prepared from 0.5 g of pure water, 6 g heptane and 4 g Span 80/Brij 30 (1:1 by w/w) resulted in immediate phase separation. However, the addition of methanol can significantly improve the stability of the above mixture: the addition of 0.5 g methanol delayed the phase separation by several hours and 0.6 g methanol formed stable microemulsions. These observations were further reflected in the phase diagrams. In the absence of methanol the targeted red dot (Figure 3.12) lay outside the microemulsion boundary. For the addition of 0.5 g methanol the region fell inside the microemulsion region. Thus the methanol amount can be varied widely whilst maintaining stable microemulsions, allowing a comprehensive study on the effect of increased methanol addition to be undertaken.

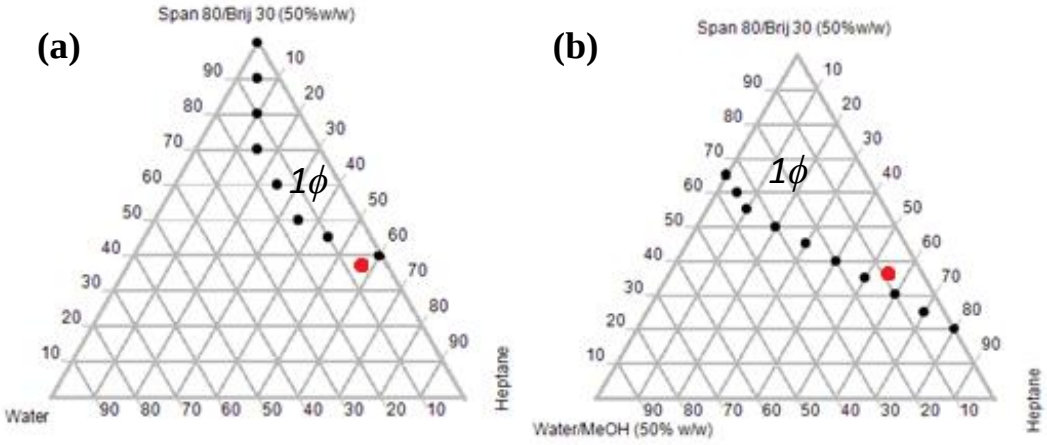

Figure 3.12 Comparison of Span 80+Brij 30/heptane ternary phase diagrams varying dispersed phase: (a) water; (b) water: MeOH of 1:1(w/w)

The methanol quantity was varied from 0.6 g to 2.3 g (Table 3.4) where the overall microemulsion remains stable. Samples with less than 0.7 g of methanol showed no visual sign (confirmed by optical microscope) of crystallisation even after 3 months. From 0.8–1.5 g, mostly the γ form was obtained. As the methanol level increased from 1.6–1.9 g, the yield of β form increased whilst the presence

of the γ form reduced. Above 2.0 g of methanol, the β form dominated. This process is depicted in the FTIR spectra shown in Figure 3.14.

Table 3.3 Span 80/Brij 30 microemulsion systems compositions of varying methanol amount. From 1.1g of methanol onwards, the methanol emulsions started to form but the overall microemulsions remained stable.

Glycine Microemulsion				MeOH microemulsion					
Glycine solution Glycine mass %	Glycine solution /g	Heptane /g	Span 80 / Brij 30 (1:1) /g	MeOH /g	H_2O /g	Heptane /g	Span 80 / Brij 30 (1:1) /g	Result	γ form /%
4	0.25	4.2	2.8	0.6	0.25	1.8	1.2	No crystal	/
4	0.25	4.2	2.8	0.7	0.25	1.8	1.2	No crystal	/
4	0.25	4.2	2.8	0.8	0.25	1.8	1.2	Mostly γ form	95
4	0.25	4.2	2.8	0.9	0.25	1.8	1.2	Mostly γ form	87
4	0.25	4.2	2.8	1.1	0.25	1.8	1.2	Mostly γ form	92
4	0.25	4.2	2.8	1.2	0.25	1.8	1.2	Mostly γ form	85
4	0.25	4.2	2.8	1.3	0.25	1.8	1.2	Mostly γ form	74
4	0.25	4.2	2.8	1.4	0.25	1.8	1.2	Mostly γ form	67
4	0.25	4.2	2.8	1.5	0.25	1.8	1.2	Mostly γ form	69
4	0.25	4.2	2.8	1.6	0.25	1.8	1.2	Mostly γ form with small amount β form	67
4	0.25	4.2	2.8	1.7	0.25	1.8	1.2	Mostly γ form with small amount β form	64
4	0.25	4.2	2.8	1.8	0.25	1.8	1.2	Mostly γ form with small amount β form	45
4	0.25	4.2	2.8	1.9	0.25	1.8	1.2	Mostly β form with small amount γ form	35
4	0.25	4.2	2.8	2.0	0.25	1.8	1.2	Mostly β form	10
4	0.25	4.2	2.8	2.1	0.25	1.8	1.2	Mostly β form	3
4	0.25	4.2	2.8	2.2	0.25	1.8	1.2	Mostly β form	3
4	0.25	4.2	2.8	2.3	0.25	1.8	1.2	Mostly β form	0

Upon an increase in methanol or ethanol, the β form is expected to become predominant due to the increase in supersaturation of glycine and the inhibition of the α and γ forms, by H-bonding of the methanol/ethanol to the fast growing faces.[19] Glycine is much less soluble in methanol than water, thus higher supersaturations are obtained with increasing methanol within the microemulsions. This leads to the loss of thermodynamic control, and hence the faster growing metastable forms are favoured. As the fast growth face of the α and γ forms are poisoned, the β polymorph dominates.

Once the quantity of methanol exceeds 1.1 g, the microemulsion is no longer stable, forming an emulsion. However, after dispersion of the aqueous glycine microemulsion the overall mixed system returns to a clear single-phase microemulsion. This highlights that the microemulsion system is robust with regard to the variation of the quantity of methanol. Hence 3D-confinement was maintained for a broad range of methanol quantities at a constant glycine solution concentration of 4% by mass. The effect of the supersaturation level was also illustrated by the nucleation and crystallisation period for different microemulsion compositions. With samples comprised of 0.8 g or 0.9 g methanol, ~4 months was required for crystallites to grow to ~ μm size. However, for 2.0 – 2.3 g methanol, ~ μm sized crystallites were observed within hours. This is investigated in more detail in section 3.6.2.5.

An estimate of the relative proportion of the γ form obtained at different methanol quantities is listed in Table 3.3 and plotted in Figure 3.13. These values were determined from the relative characteristic peak heights of the FTIR spectrum. This method has previously been used for quantitative analysis of various compounds/mixtures[34-37]. For a mixture of γ and β forms, if the γ peak height is *x* and the β form height is *y*, then the percentage of γ form is *approx.* $\frac{x}{x+y} \times 100\%$.

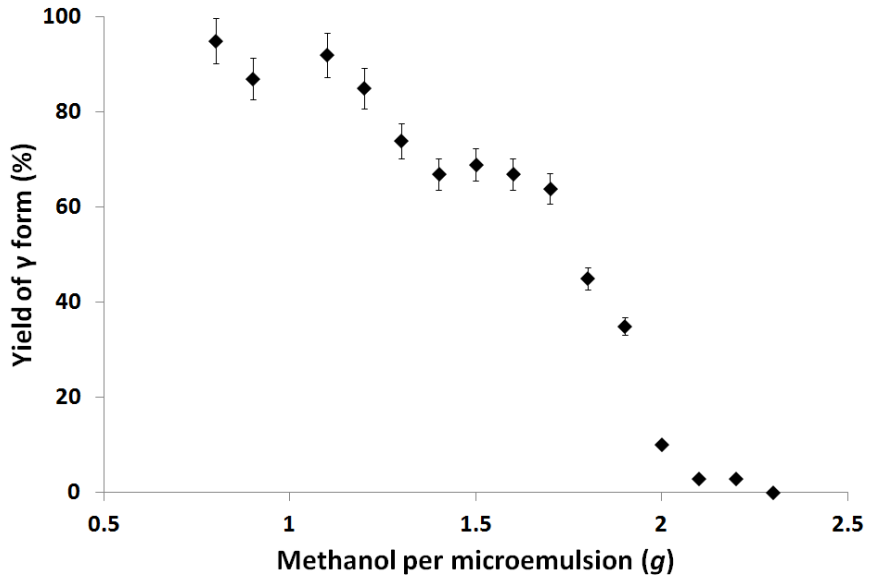

Figure 3.13 Relative yields of the γ form at different methanol concentration.

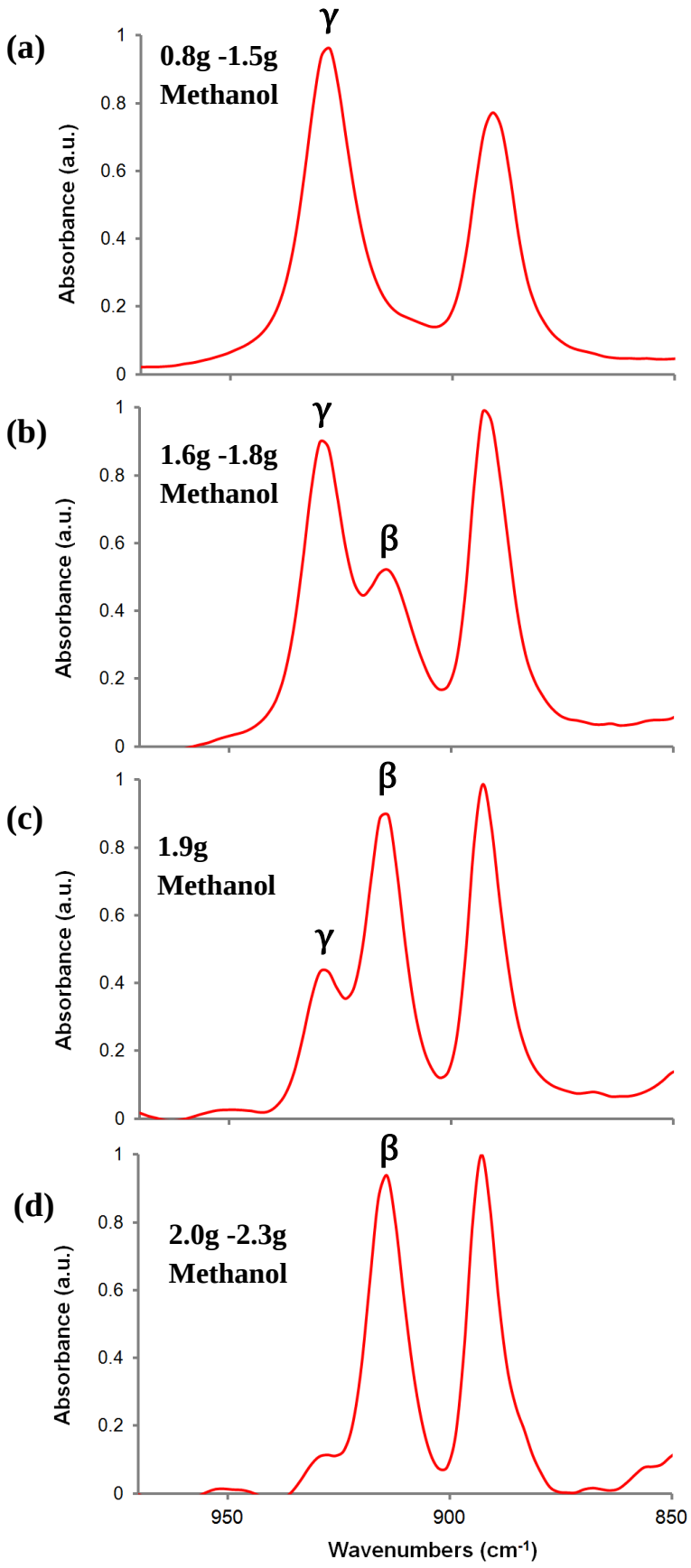

Figure 3.14 FTIR spectra of glycine crystallised from microemulsions with methanol quantity varied: (a) 0.8-1.5g: yielding γ form; (b)1.6-1.8g: yielding mostly γ form with small amount of β; (c) 1.9g: yielding mostly β form with small amount of γ; (d) 2.0-2.3g: yielding β form.

3.6.2.4 Effect of surfactant to heptane ratio

Higher surfactant concentrations can promote bicontinuous microemulsions, lyotropic (liquid crystal) and/or gel phases depending on the nature of the surfactant. In the above cases, 3D-nanoconfinement would no longer be retained and thus the crystallisation outcome would be expected to vary. To investigate such a phenomenon, the Span 80/Brij 30 concentrations were varied between 40% to 90% surfactant-to-solvent mass ratio by reducing the heptane volume (Table 3.4), whilst maintaining the glycine-to-surfactant ratio.

Although the viscosity of the microemulsions increased with increasing surfactant concentration, a bicontinuous phase was not obtained based on the viscosity measurements. In fact, all experiments were found to remain within the clear single phase microemulsion regions of the phase diagram and so majorly exhibited the formation of the γ form.

Table 3.4 shows that the microemulsion stability was maintained upon variation of surfactant concentration from 40% to 90% w/w. Subsequently the nm-sized free 'water pool' is still available for homogeneous nucleation to take place within the 3D-nanoconfinement of the microemulsion droplets. Accordingly, non-ionic surfactants, such as Span 80 and Brij 30, are less likely to be involved in nucleation due to its relatively shorter range interaction with the rigidly held water layer and thus cannot affect the crystal outcome and morphology.

Table 3. 4 Effect of surfactant concentration on crystallisation from microemulsions

Glycine Microemulsion				MeOH microemulsion					
Glycine solution Glycine mass %	/g	Heptane /g	Span 80 / Brij 30 (1:1) /g	MeOH /g	H_2O /g	Heptane /g	Span 80 / Brij 30 (1:1) /g	Surfactant mass /%	Result
4	0.25	4.2	2.8	1.0	0.25	1.8	1.2	40	Mostly γ form
4	0.25	2.8	2.8	1.0	0.25	1.2	1.2	50	Mostly γ form
4	0.25	1.87	2.8	1.0	0.25	0.8	1.2	60	Mostly γ form
4	0.25	1.2	2.8	1.0	0.25	0.51	1.2	70	Mostly γ form
4	0.25	0.7	2.8	1.0	0.25	0.3	1.2	80	Mostly γ form
4	0.25	0.31	2.8	1.0	0.25	0.13	1.2	90	Mostly γ form

The additional benefits of such a finding is that corresponding experiments could be performed at a much higher surfactant concentration, allowing a greater quantity of glycine and a much reduced heptane level to be used, which is beneficial in both environmental and economy senses, favourable for industrial scaling up experiments.

3.6.2.5 Effect of crystallisation duration

Due to the dramatic difference in growth rates for the α and γ forms, their relative yields can be time-dependent. For this reason, the crystallisation outcome of the optimum formulation at various time intervals is investigated. Figure 3.15 shows the FTIR results after 7 days and 45 days of crystallisation. The amount of γ form detected progressively increases as the crystallisation duration increases. On day 7, the relative proportion of γ form was ~20% compared to 80% of the α form, but on day 45 there was ~90% (the relative percentage of yield is calculated from the characteristic peak height for each form).

This observation can be explained by 1) the slow growth of γ form, taking 3 weeks for sufficient sized crystals to grow, whereas the α form grows to this size far more quickly (~1 week) and/or 2) the polymorphic transformation of the meta-stable α form, to the thermodynamically stable γ form by re-dissolution into the microemulsion and re-crystallisation as per Ostwald's Law of stages.

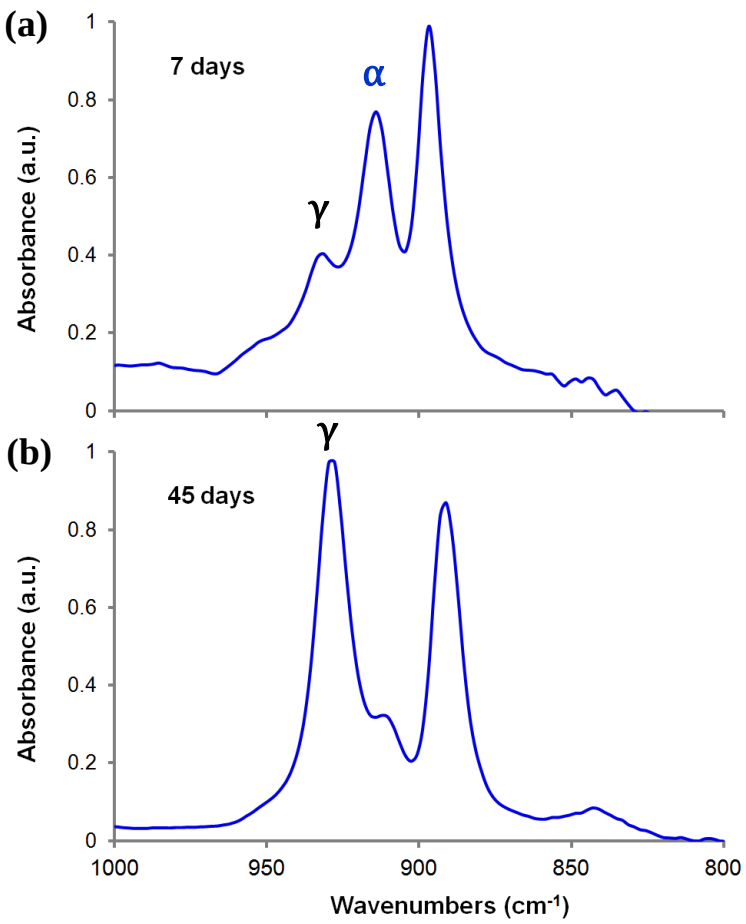

Figure 3.15 FTIR for Optimum formulation at (a) day 7 and (b) day 45

TEM was used to examine the microemulsion systems on the nano-scale after 48 hours. Nanocrystals of γ form were observed with the supporting characteristic hexagonal diffraction pattern shown in Figure 3.16a. It matched to the [001] zone axis via the generated TEM diffraction pattern as illustrated in Figure 3.16c. Figure 3.16b displayed the HREM images of the nanocrystalline aggregates. It can be seen that the nanocrystalline aggregates showed some preferred orientation, indicative of a degree of oriented attachment, as the electron diffraction pattern showed arcs rather than rings. This oriented attachment of the aggregates enables rapid identification of the γ form, as a result of the hexagonal symmetry. However, more frequently the nanocrystals did not aggregate so that the electron diffraction patterns of regions containing several nanocrystals displayed diffraction rings. The hexagonal symmetry of the γ–nanocrystals was, nevertheless, still apparent from fast Fourier transforms (FFTs) of HREM images of the individual nanocrystals (see Figure 3.16b).

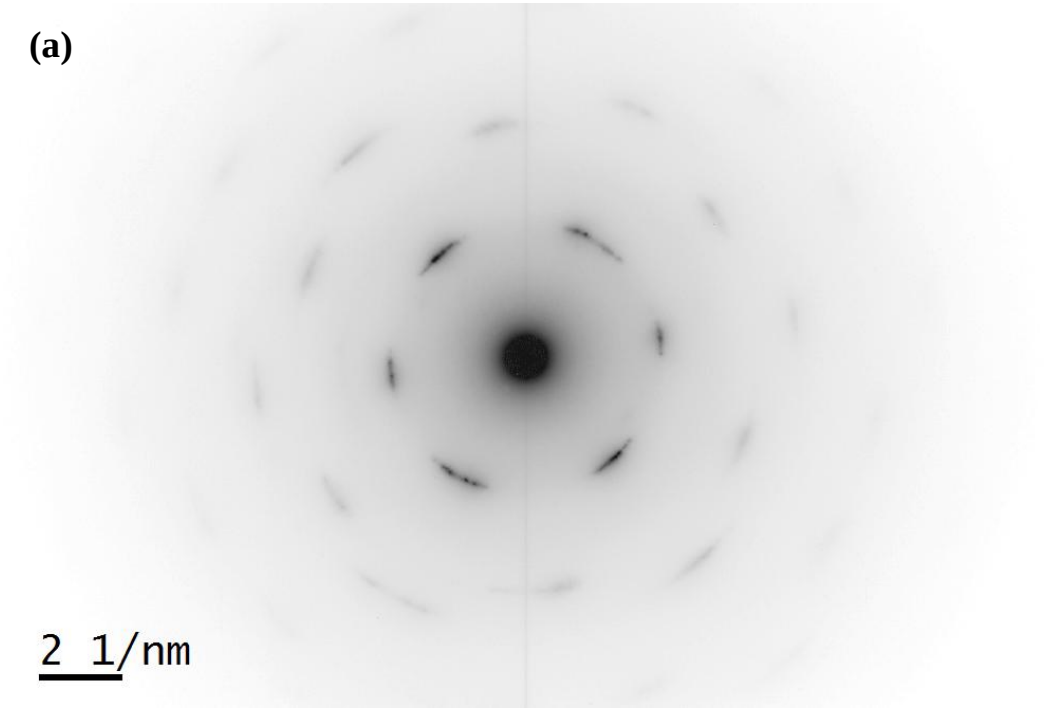
(a)
2 1/nm

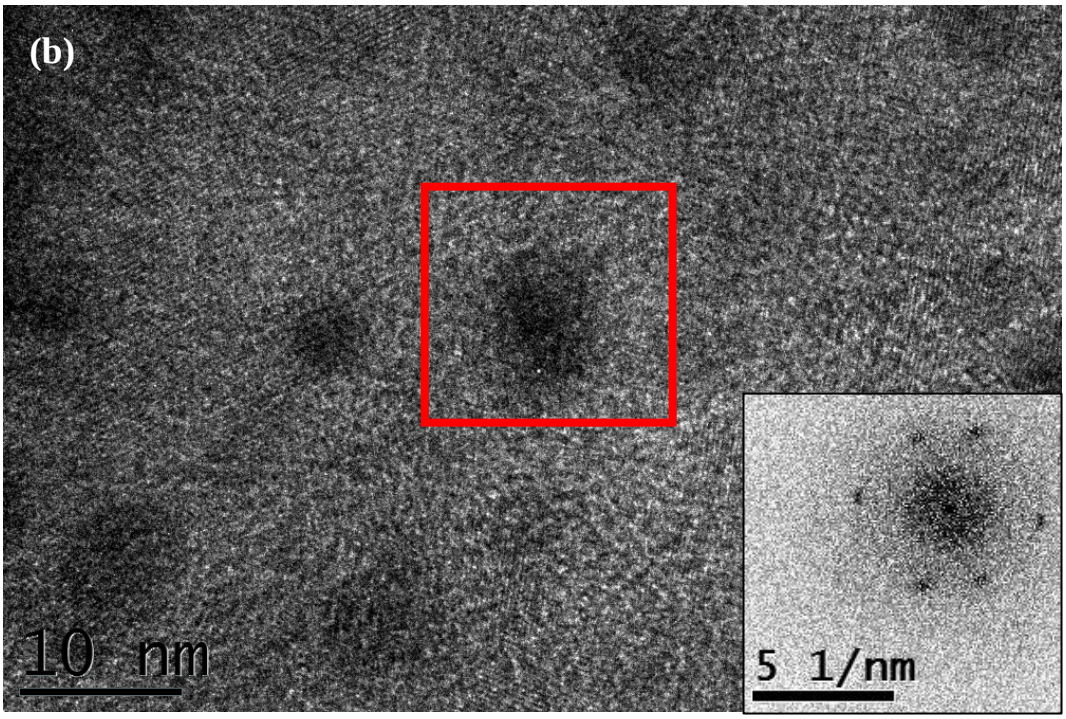
(b)
10 nm
5 1/nm

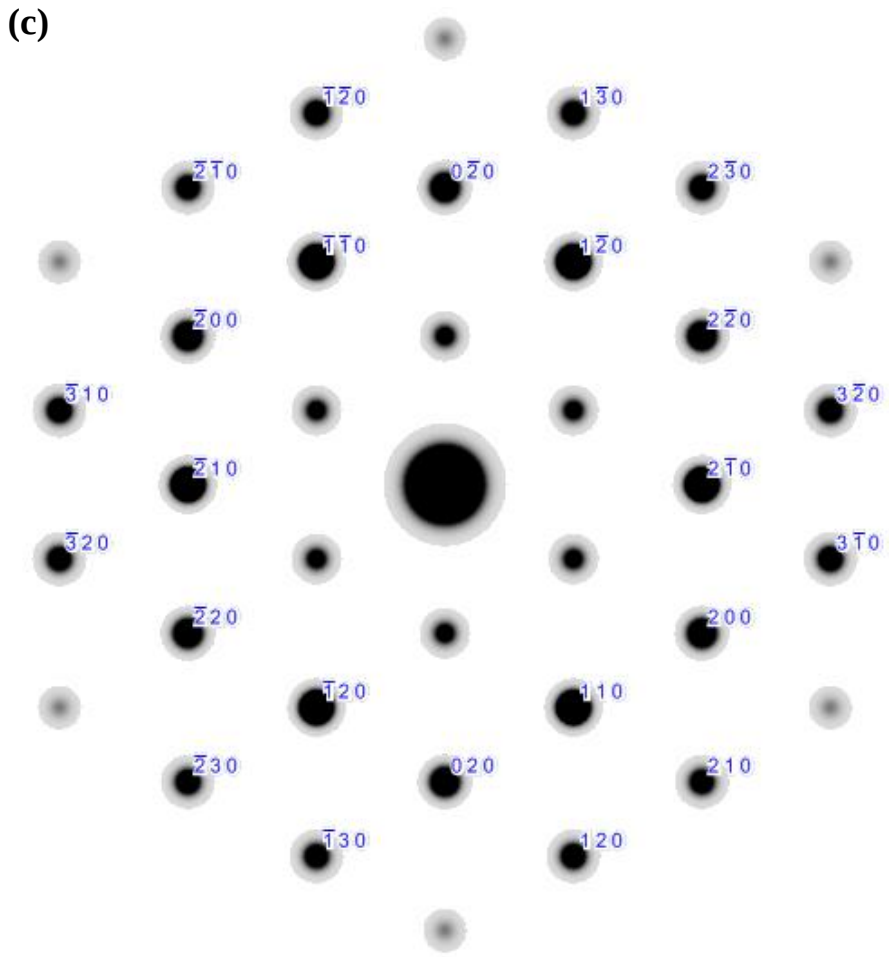

Figure 3.16 TEM images for the nanocrystals within 48hrs of formation: (a) Hexagonal diffraction pattern (inverted) for γ form; (b) the HREM image of the γ form nanoaggregates and the inset is the inverted FFT image of the selected area in (b); (c) generated TEM diffraction pattern from *SingleCrystal* module of *CrystalMaker*®[38]

Sakai *et. al.*[7, 39] previously reported that for a 100% α-crystals containing sample at 40 ℃ and 70% relative humidity (RH), up to 10 days was required for the completely transformation to the γ form. If the sample is dry more than 30 days was required to show significant transformation. This transformation time is expected to be much longer for the microemulsion case if the γ form crystals are the result of α polymorph transformation. This is because microemulsion crystallisation is a time-consuming process limited by the rate of transient dimer formation, and the microemulsion storage temperature at 25 ℃ reduces the droplet collision rate.

Furthermore, a solvent-mediated polymorphic transformation requires the growth of the stable form at the expense of the dissolution of a metastable form. Initially the solution surrounding both forms will be saturated with respect to the stable form, but undersaturated with respect to the metastable form. Hence the dissolution of the metastable form leads to a supersaturated solution for the stable form, which can then grow until the supersaturation is relieved. Under the conditions of thermodynamic control in the 3D-nanoconfinement within microemulsions it is highly unlikely that the α and γ phase nanocrystals will coexist in the same droplet. This is because the glycine concentrations (i.e. the supersaturations) are kept sufficiently low such that crystallisation is only just possible. Consequently, solvent mediated transformation may only occur through repeated transient dimer formation via the exchange of material. Here both the α and γ nanocrystals are surrounded by the same solution.

In addition, the transformation of macroscopic α crystals will also be very slow. A microemulsion sample, that previously gave solely the α form after 4 days, was stored at room temperature for ~4 months. Upon re-examination under FTIR, no polymorphic transformation was observed. The transformation of macroscopic α-phase crystals into the γ-form is severely impeded in microemulsions, due to the minute solubility of glycine in the heptane continuous phase, thus transformation via dissolution in the continuous phase will be an extremely slow process. The alternative process of energetic droplet and crystal collisions, leading to rupture of the droplets and concomitant partial dissolution of the crystal within the contents of the ruptured droplet will also only occur at a slow rate. The glycine purchased from Aldrich contains only the α form, with only undersaturated glycine solutions used to prepare microemulsions. This should eliminate potential seeding effects and hence these γ nano-aggregates are owed to the consequences of thermodynamic control. Sakai *et. al.*[7, 39] also reported that for a sample containing 60% α form and 40% γ form at 40ºC and 70% RH, it took 1 day for a wet sample and 3 days for a dry sample to completely transform into the γ form.

Subsequently, to confirm if the γ form was induced by polymorphic transition, a few γ form crystals of ~μm in size were seeded by direct addition to the

microemulsion comprising 6 g heptane, 4 g Span 80/Brij 30 (1:1 mass ratio), 0.49 g water, 1 g methanol and also 10 mg of the α form powder. After 4 months, the microemulsion sample still had a majority of α form. Our study also shows that the α form produced from bulk experiments of 2:1 methanol to glycine solution (mass ratio) remained as the same form after a two month period. These pieces of evidence strongly suggest; if a large amount of the α form is going to transform to the γ form within a microemulsion, it requires a much longer period of time than the crystallisation time (~3 weeks) to obtain macroscopic γ form. Hence the slow appearance of γ form crystals is majority related to its inherent slow growth.

However, we cannot rule out that polymorphic transformation may occur but if so, at a very slow rate. Given that the solvent-mediated transformation of the γ form will occur at a greater rate if there is a plentiful amount of γ form nanocrystals existing; it is clear that the conditions most likely to promote the α–γ phase transformation are those that favour γ form crystallisation. Consequently, the production of the γ form can certainly not, solely be attributed to the transformation of the α form that was crystallised from the microemulsion initially. Indeed, given the faster growth rate of the α form and the small lattice energy difference between the α and γ forms (~0.2 kJ/mol), it is likely that the faster-growing and thus larger α-form nanocrystals would in fact be more stable than the much slower-growing and so smaller γ-nanocrystals. Using the Gibbs-Thompson equation introduced as Equation (1. 14) in Section 1.5.2a,

$$r^* = \frac{2\sigma v_l}{\Delta\mu} \qquad \text{(recall 1.14)}$$

In combination with the similar solubility (the α form is only ~1.03-1.1 more soluble than the γ form in water at room temperature) and the similar interfacial tension values in the range of 30 $mN.m^{-1}$ to 50 $mN.m^{-1}$ for both forms, only when the γ nanocrystals reach ~10–28 nm in diameter, will they be more stable than the macroscopic α phase crystals (~μm in size).

3.6.2.6 Droplet size measurements

Since microemulsions are volume confined systems, an estimation of the small volume of the microemulsion droplet and the environment of the internal phase, it is essential to both calculate and compare the geometric droplet size from its composition and the actual size using techniques determined via SAXS, SANS, DLS and many others.

The geometric approximation of the microemulsion droplet is predicted from its composition and the interfacial properties, assuming the droplets are spherical and roughly homogeneous in size:

$$r = \frac{3\emptyset}{\Sigma} \tag{3.1}$$

where ∅ is the volume fraction of internal phase and ∑ is the total interfacial area per unit volume. Appendix 4 details the calculation of the geometric droplet radius *r*.

In this calculation, the hydrophilic head group of a surfactant is included in the inner phase of the droplet due to interfacial properties. The results can then be directly compared to the measurements obtained from SAXS and processed by GIFT analysis.

The hydrophobic part of the surfactant is almost undistinguishable, (in terms of electron density), from the heptane phase in the SAXS measurement and so the X-ray scattering is assumed to arise solely from the hydrophilic core of the microemulsion droplets. For the Span 80/Brij 30 microemulsions, this is comprised of the aqueous glycine solution, methanol, and the hydrophilic part of the surfactant molecules (Figure 3.17).

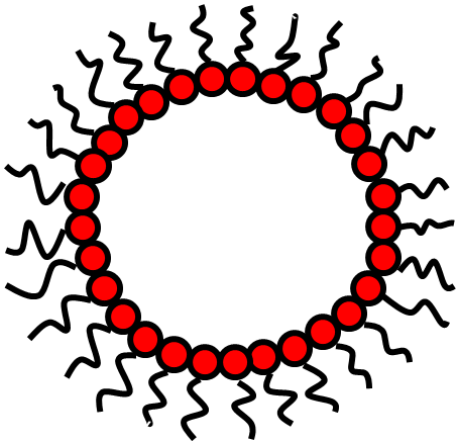

Figure 3.17 an O/W microemulsion model

The scattering function, *I(q)*, from the SAXS measurement is transformed by GIFT[40] analysis, to reveal the pair distance distribution function, *p*(*r*), which provides information on the shape and maximum size of the particle.

GIFT analysis takes into account both the form factor, arising from the intrapaticle contributions and the structure factor determined by the interparticle contributions. To estimate the droplet size, *p*(*r*) is used to find the radius of gyration, r_g. r_g value can then be converted into the spherical hydrophilic droplet radius, *r*, by multiplying a factor of $(5/3)^{0.5}$ for a simple hard sphere model based on the assumptions that all the droplets are perfect spheres and are homogeneous in size.

For a comparative study, the droplet sizes of the same glycine microemulsion composition, i.e. the optimum formulation with 0.25 g of 4% glycine solution, 4.2 g heptane and 2.8 g Span 80/Brij 30 (1:1), but with varying amounts of methanol (0.6 g to 2.3 g) in the methanol microemulsion composition with 0.25 g water, 1.8 g heptane and 1.2 g Span 80/Brij 30 (1:1), have been calculated and listed in Table 3.5.

Table 3.5 Geometric droplet radius and GIFT analysis droplet radius for microemulsion where the methanol quantity varies from 0.6–2.3g

MeOH in microemulsion /g	Geometric R_{core} of confined phase / nm	GIFT R_{core} of confined phase ±0.3 /nm	Difference /%
0.6	3.6	3.3	8
0.7	3.7	3.4	8
0.8	3.9	3.3	15
0.9	4.0	3.6	10
1.0	4.2	3.6	14
1.1	4.4	3.8	14
1.2	4.5	3.9	13
1.3	4.7	4.1	13
1.4	4.8	4.0	17
1.5	5.0	4.2	16
1.6	5.1	4.2	18
1.7	5.3	3.9	26
1.8	5.5	4.0	27
1.9	5.6	4.0	29
2.0	5.8	4.4	24
2.1	5.9	4.4	25
2.2	6.1	4.7	21
2.3	6.2	4.8	23

The percentage difference between the geometric and GIFT analysis estimates of the droplet radius, r is calculated as $\frac{|r_{geometric}-r_{GIFT}|}{r_{geometric}} \times 100\%$, which is within a ~8–30% range. This % difference is larger for microemulsions containing more methanol due to increased partitioning of methanol into the heptane continuous phase.

At high methanol quantities, the microemulsion droplet swells to its maximum possible size, prior to the methanol preferentially partitioning into the heptane phase. Thus this can be expected given the solubility of methanol in heptane has been well studied when varying the temperature and pressure, by a number of groups[41-43]. The $p(r)$ function for the optimum formulation is plotted in Figure 3.18a as a function of the radius and Figure 3.18b shows the overlaid *I(q)* plots as a functions of $q(r)$ for microemulsions with 0.6 g to 1.4 g of added methanol.

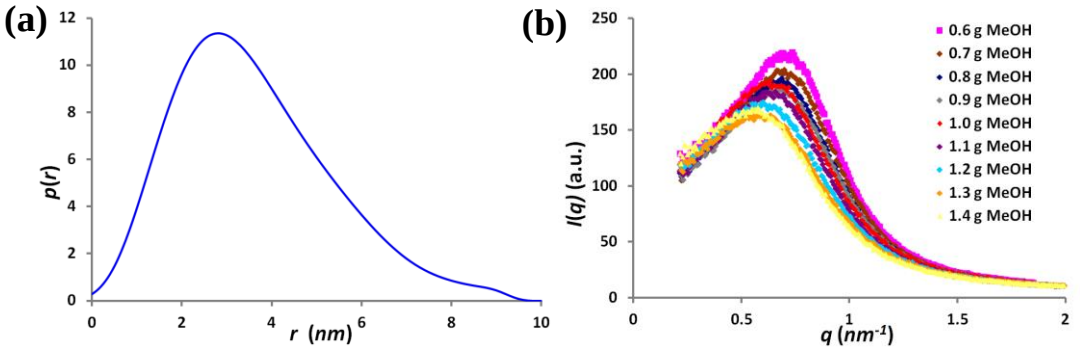

Figure 3.18 GIFT analysis for glycine mixed microemulsions:(a) *p(r)* function versus *r* for optimum formulation; (b) *I(q)* function for methanol quantity varies from 0.6g to 1.4g

Overall good agreement between the hydrophilic core droplet size from GIFT analysis and the geometric calculated radius is observed, suggesting that the structure of the internal phase of the microemulsion is as predicted, i.e. with the dispersed phase and the hydrophilic head groups of Span 80 and Brij 30. The discrepancies between the two values can be rationalised in terms of errors arising from the area per surfactant molecule quoted in the literature (0.37 nm^2)[44] in addition to various assumptions; all of the particles are homogeneous in size and spherical in shape, the approximation of the hard sphere model, and the miscibility of the solvents, for example, at 298K, ~ 5% of the methanol will be readily soluble in heptane[42, 45].

The most influential of these factors is the estimation of the size and shape of the particles. From Figure 3.18b, the *p(r)* functions can be seen as slightly asymmetric, indicating the particles are slightly polydisperse. Noticeably, the partitioning of methanol into the heptane phase increases at higher methanol levels (> 1.7 g in microemulsion), leading to the small variations in the overall droplet sizes.

3.6.2.7 Bulk experiments

The purpose of performing bulk experiments (i.e. under non-confined conditions with the exact composition as in the dispersed phase of the microemulsion) is to clarify the effect of confinement. The results for the bulk experiments are listed in Table 3.6. With the addition of methanol antisolvent, 5%–18% (w/w) glycine solutions exhibit rapid crystallisation giving needle/long plate-like β form crystals after 2 hours, with most undergoing polymorphic transformation to the α form

when left in solution for 4 days. In contrast, 3.5%–4.5% (w/w) glycine solutions nucleated at a much slower rate and hence resulted in α-form crystals. Overall the bulk experiments proved that under non-confined conditions the γ form is not expected to appear.

Table 3.6 Bulk solution tests.

Concentration of glycine (%)	Observation	Results	
		2hrs	4 days
3%	No crystal	/	/
3.5%	Starting to crystallize after 4 days	/	α
4%	Crystallisation overnight	/	α
4.5%	Crystallisation overnight	/	α
5%	Crystallisation after 1-2hrs	β	α
6%	Fast crystallisation	β	α
8%	Immediate crystallisation	β	β*
10%	Immediate crystallisation	β	α
12%	Immediate crystallisation	β	α
14%	Immediate crystallisation	β	α
16%	Immediate crystallisation	β	α
18%	Immediate crystallisation	β	α

*8% turned into α form when re-analysed in 2 month time.

The fast initial β polymorph formation can be rationalised by both Ostwald's rule and the effect of the methanol. The former suggests that the β form, being the least stable polymorph, is likely to have the lowest nucleation energy barrier of the three forms, and so is kinetically favoured. The experiments were carried out in water-methanol solutions, that were previously reported[19] to promote β formation, due to the nature of the crystal structure. It is postulated that methanol forms strong hydrogen bonds with the glycine monomer via a $N\text{-}H_{gly}\ldots O_{met}$ link slowing down the cyclic dimer formation of the α form and poisoning the γ forms fastest growing site via an $O\text{-}H_{met}\ldots O^{-}_{gly}$ and three $O\text{-}H_{met}\ldots O^{-}_{gly}$ interactions[19].

However in the case of the β form, methanol only binds to the slow growing face which affects the crystallisation rate to a much lesser extent, but leads to an acicular morphology. Consequently, the β form can still grow very rapidly. Being the least stable polymorph, the β form[46] tends to undergo solvent-mediated polymorphic transformations via dissolution to the more stable α form.

3.6.2.8 Solubility tests

The solubilities of glycine in the varied methanol microemulsions are listed in Table 3.7, along with the supersaturation ratio for each microemulsion. This solubility is an averaged value calculated from experimental data. For example, for a microemulsion containing 0.6 g methanol and 0.5 g water, 5.5 mg of glycine powder dissolved into this microemulsion, but 6 mg did not. Hence, the average solubility is estimated as (5.5 mg + 6 mg)/2, which equals 5.75 mg. Figure 3.19 plots the solubility curve as a function of the mass of methanol. The solubility generally decreases with an increase in the amount of anti-solvent before plateauing. This is due to the partitioning of the methanol into the continuum as discussed previously, before nanoemulsions and emulsions form.

Table 3.7 Solubility data and supersaturation ratio for methanol quantity carried microemulsions.

MeOH in microemulsion /g	Solubility of glycine /mg per g microemulsion	Solubility of glycine /mg per g dispersed phase	Supersaturation ratio C_{sol}/C_{sat}
0.6	5.75	5.23	1.74
0.7	5.25	4.38	1.90
0.8	4.75	3.65	2.11
0.9	4.25	3.04	2.35
1.0	4.50	3.00	2.22
1.1	4.25	2.66	2.35
1.2	4.50	2.65	2.22
1.3	4.25	2.36	2.35
1.4	3.75	1.97	2.67
1.5	3.75	1.88	2.67
1.6	3.25	1.55	3.08
1.7	3.25	1.48	3.08
1.8	3.75	1.63	2.67
1.9	3.75	1.56	2.67
2.0	3.75	1.50	2.67
2.1	3.75	1.44	2.67
2.2	3.75	1.39	2.67
2.3	3.75	1.34	2.67

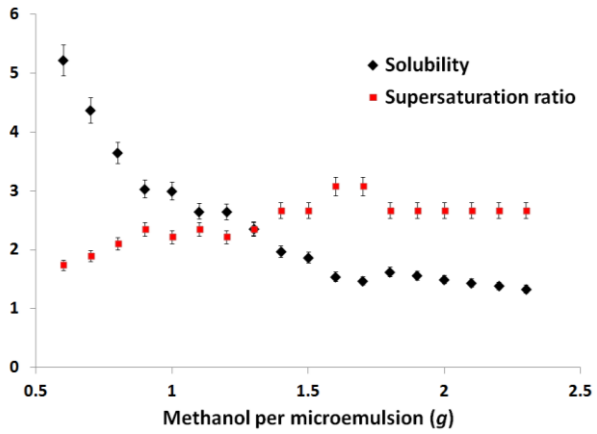

Figure 3.19 Solubility curve as methanol quantity varied

3.7 Conclusions

The polymorphic study of glycine reveals that the selective crystallisation of specific polymorphs can be achieved by careful control of the microemulsions composition, i.e. glycine concentration, surfactant concentration and methanol concentration. The use of confined systems allows direct access to the thermodynamically most stable polymorph, which is less likely to appear under non-confined conditions where kinetic control dominates, leading to the formation of metastable form(s).

The stable γ form of glycine was reproducible within microemulsion systems, employing both AOT and Span 80+Brij 30 surfactants. However, there are two main factors contributing to, and influencing this crystallisation outcome; the choice of surfactant, and the methanol antisolvent addition method. In particular, the known ability of the AOT surfactant to aid γ glycine nucleation, plays an important role in obtaining the γ form. This is evident from both Davey *et. al*'s[2] study and our experiments in Section 3.6.1.

Conversely, for the Span 80/Brij 30 system, the stable γ form was obtained solely due to the thermodynamic control afforded by 3D-nanoconfinement. This can be stated with confidence, given that the Span 80 and Brij 30 surfactants were known to assist the crystallisation of the metastable glycine forms in both bulk solutions and in emulsions. In addition, the supersaturations that are likely to have arisen in droplets forming stable nuclei are in the range of 2.0–2.6. Secondly, the importance of the microemulsion preparation techniques to the crystallisation outcome is highlighted, e.g. in the Span 80/Brij 30 case, a microemulsion mixing method will give more consistent results compared to both the direct methanol antisolvent addition and vapour diffusion. For the direct methanol addition, locally high methanol concentrations can initially arise causing too high supersaturations levels, falling outside the regime of thermodynamic control. Whilst for the methanol vapour diffusion it is difficult to control the exact quantity of methanol added, hence the supersaturation can again rise above that needed to maintain the thermodynamic control.

Furthermore, the duration of crystallisation is also a crucial factor to the polymorphic outcome, due to various polymorphs having different growth rates (i.e. the α form grows 500 times faster than γ form). The γ form crystallites of ~5nm in size were visible by TEM after 48 hours of growth in the microemulsions, whilst after 3 weeks ~mm size crystals could be extracted. This indicates the slow growth rate of γ form. Even if the α-γ polymorphic transformation does occur on a noticeable timescale, it is expected to contribute only a very small part to the γ polymorph formation, i.e. an amount that is beyond the detection limit of FTIR. More importantly, very careful control over the quantity of each of the inner phase components of the microemulsion is required as small changes in glycine concentration or methanol concentration can destroy the thermodynamic control.

3.8 References

1. H. Betz and R. J. Harvey, in *Glycine as a Neurotransmitter*, *eLS*, John Wiley & Sons, Ltd, 2001.
2. K. Allen, R. J. Davey, E. Ferrari, C. Towler, G. J. Tiddy, M. O. Jones and R. G. Pritchard, *Cryst Growth Des*, 2002, **2**, 523-527.
3. K. Chadwick, R. J. Davey, R. Mughal and I. Marziano, *Org. Process Res. Dev.*, 2009, **13**, 1284-1290.
4. C. E. Nicholson, S. J. Cooper and M. J. Jamieson, *J. Am. Chem. Soc.*, 2006, **128**, 7718-7719.
5. J. Yano, H. Füredi-Milhofer, E. Wachtel and N. Garti, *Langmuir*, 2000, **16**, 10005-10014.
6. A. Dawson, D. R. Allan, S. A. Belmonte, S. J. Clark, W. I. F. David, P. A. McGregor, S. Parsons, C. R. Pulham and L. Sawyer, *Cryst Growth Des*, 2005, **5**, 1415-1427.
7. G. He, V. Bhamidi, S. R. Wilson, R. B. H. Tan, P. J. A. Kenis and C. F. Zukoski, *Cryst Growth Des*, 2006, **6**, 1746-1749.
8. K. Srinivasan, *J. Cryst. Growth.*, 2008, **311**, 156-162.
9. A. Dawson, D.R.Allan, S.A.Belmonte, S.J.Clark, W.I.F.David, P.A.McGregor, S.Parsons, C.R.Pulham, and L.Sawyer, *Cryst.Growth Des.*, 2005, **5**, 1415-1427.
10. G. L. Pervolich, L.K. Hansen, and A. Bauer-Brandl, *J.Therm.Anal.Calorim.*, 2001, **66**, 699-715.
11. O. V. Dolomanov, L. J. Bourhis, R. J. Gildea, J. A. K. Howard and H. Puschmann, *J. Appl. Crystallogr.*, 2009, **42**, 339-341.
12. C. F. Macrae, I. J. Bruno, J. A. Chisholm, P. R. Edgington, P. McCabe, E. Pidcock, L. Rodriguez-Monge, R. Taylor, J. van de Streek and P. A. Wood, *J. Appl. Cryst.*, 2008, **41**, 466-470.
13. E. V. Boldyreva, V. A. Drebushchak, T. N. Drebushchak, I. E. Paukov, Y. A. Kovalevskaya, and E. S. Shutova, *J. Therm. Anal. Calorim.*, 2003, **73**, 409-418.
14. J. W. Chew, S. N. Black, P. S. Chow, R. B. H. Tan and K. J. Carpenter, *CrystEngComm*, 2007, **9**, 128-130.
15. C. E. Hughes, S. Hamad, C. R. A. Catlow, K. D. M. Harris and P. C. Griffiths, *Faraday Discuss*, 2007, **136**, 71-89.
16. X. Yang, J. Lu, X. J. Wang and C. B. Ching, *J. Cryst. Growth.*, 2008, **310**, 604-611.
17. J. E. Aber, S. Arnold, B. A. Garetz and A. S. Myerson, *Phys. Rev. Lett.*, 2005, **94**, 145503-145506.
18. J. Zaccaro, J. Matic, A. S. Myerson and B. A. Garetz, *Cryst Growth Des*, 2001, **1**, 5-8.
19. I. Weissbuch, V. Y. Torbeev, L. Leiserowitz and M. Lahav, *Angew. Chem. Int. Ed.*, 2005, **44**, 3226-3229.
20. A. Bouchard, G. W. Hofland and G. Witkamp, *J. Chem. Eng. Data.*, 2007, **52**, 1626-1629.
21. L. P. Dang, H. Y. Yang, S. Black and H. Y. Wei, *Org. Process Res. Dev.*, 2009, **13**, 1301-1306.
22. L. Yu, J. Huang and K. J. Jones, *J. Phys. Chem. B*, 2005, **109**, 19915-19922.
23. G. L. Perlovich, L. K. Hansen and A. Bauer-Brandl, *J. Therm. Anal. Cal.*, 2001, **66**, 699-715.
24. G. B. Chernobai, Y. A. Chesalov, E. B. Burgina, T. N. Drebushchak and E. V. Boldyreva, *J. Struct. Chem.*, 2007, **48**, 332-339.
25. N. V. Surovtsev, S. V. Adichtchev, V. K. Malinovsky, A. G. Ogienko, V. A. Drebushchak, A. Y. Manakov, A. I. Ancharov, A. S. Yunoshev and E. V. Boldyreva, *J. Chem. Phys.*, 2012, **137**, 065103-065110.
26. M. T. Rosado, M. L. T. S. Duarte and R. Fausto, *Vib. Spectrosc.*, 1998, **16**, 35-54.

27. Y. Luan, G. Xu, G. Dai, Z. Sun and H. Liang, *Colloid. Polym. Sci.*, 2003, **282**, 110-118.
28. C. Sekar, and R. Parimaladevi, *Spectrochim. Acta, A*, 2009, **74**, 1160-1164.
29. M. J. Jamieson, Controlling crystallization and the effect of interfacial curvature. PhD thesis, Durham University, 2004.
30. J. W. Chew, S. N. Black, P. S. Chow, R. B. H. Tan and K. J. Carpenter, *CrystEngComm*, 2007, **9**, 128-130.
31. A. Jouyban, *Handbook of Solubility Data for Pharmaceuticals*, CRC PressINC, 2009.
32. D. F. Anghel, M. Balcan and D. Donescu, in *Dispersed Systems*, eds. K. Hummel and J. Schurz, Steinkopff, 1988, vol. 77, pp. 127-130.
33. S. G. Schon and E. A. Hazbun, *Methanol as cosurfactant for microemulsions*, Arco Chemical Technology, Inc., 1991.
34. R. Helmy, G. X. Zhou, Y. W. Chen, L. Crocker, T. Wang, R. M. Wenslow and A. Vailaya, *Anal. Chem.*, 2002, **75**, 605-611.
35. E. Atef, H. Chauhan, D. Prasad, D. Kumari and C. Pidgeon, *ISRN Chromatography*, 2012, **2012**, 1-6.
36. P. J. Skrdla, V. Antonucci, L. S. Crocker, R. M. Wenslow, L. Wright and G. Zhou, *J. Pharmaceut. Biomed.*, 2001, **25**, 731-739.
37. Y. Hu, A. Erxleben, A. G. Ryder and P. McArdle, *J. Pharmaceut. Biomed.*, 2010, **53**, 412-420.
38. *CrystalMaker: a crystal and molecular structures program for Mac and Windows*, CrystalMaker Software Ltd, Oxford, England (www.crystalmaker.com).
39. H. Sakai, H. Hosogai, and T. Kawakita, *J. Cryst. Growth.*, 1992, **116**, 421-426.
40. A. B. G. Fritz, and O. Glatter, *J. Chem. Phys.*, 2000, **113**, 9733.
41. R. W. Kiser, G. D. Johnson and M. D. Shetlar, *J. Chem. Eng. Data.*, 1961, **6**, 338-341.
42. M. Yarrison and W. G. Chapman, *Fluid Phase Equilibr.*, 2004, **226**, 195-205.
43. M. Goral, P. Oracz, A. Skrzecz, A. Bok and A. Maczynski, *J. Phys. Chem. Ref. Data.*, 2002, **31**, 701-748.
44. L. Peltonen, J. Hirvonen and J. Yliruusi, *J. Colloid Interface Sci.* , 2001, **240**, 272-276.
45. P. Setua, D. Seth and N. Sarkar, *Phys. Chem.*, 2009, **11**, 8913-8922.
46. E. S. Ferrari, R. J. Davey, W. I. Cross, A. L. Gillon and C. S. Towler, *Cryst Growth Des*, 2003, **3**, 53-60.

Chapter 4 Dipicolinic acid (I)

4.1 Introduction

It has been demonstrated in the previous chapter and other similar cases[1] that a microemulsion is a suitable vehicle to manage 3D-nanoconfinement for crystallisation and subsequently to achieve thermodynamic control of a polymorphic system. However, the ability to crystallise other forms, e.g. hydrates, salts or co-crystals, from microemulsions has yet to be studied. Therefore, dipicolinic acid (DPA), known to exist as an anhydrous form, a monohydrate form and a dihydrate form under ambient conditions, was chosen as a model compound for such a study.

4.2 Literature review

Dipicolinic acid (DPA), with the structure shown in Figure 4.1, has attracted much interest due to its potential applications in crystal engineering, ligand formation, and biological functions. It was first discovered in 1936[2], and is an essential part of bacterial spores[3]. DPA functionality heavily replies on bond formation via the carboxylic acid group(s); for instance, cocrystallisation with carbamazepine, caffeine[4], isonicotinamide and urea[5], in addition to acting as a chelating agent for metal complexes.

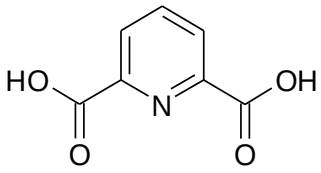

Figure 4.1 Dipicolinic acid

It was reported that the anhydrous form of DPA can lead to both the dihydrate and monohydrate, when recrystallising from aqueous solutions under different conditions. For example, the monohydrate form was obtained upon recrystalling the anhydrous form in an aqueous solution[6]; the dihydrate was obtained from hot methanol/water solution[7]; with the anhydrous form recrystallised from hot water or hot water with HCl[8]. The single crystal structures of all three forms (Figure 4.2) are published in the CSD with high similarity in their crystal packing (analysed using *Materials* Module in *Mercury*[9, 10]), based on their structural features in

Table 4.1. The Crystal Packing Similarity tool[11-13] calculates the level of packing similarity, i.e. the 3D geometry, between structures of the same compound.

Table 4.1 Crystal packing similarity

Similarity /%	Anhydrous	Monohydrate	Dihydrate
Anhydrous	N/A	90.6	90.4
Monohydrate	90.6	N/A	86.8
Dihydrate	90.4	86.8	N/A

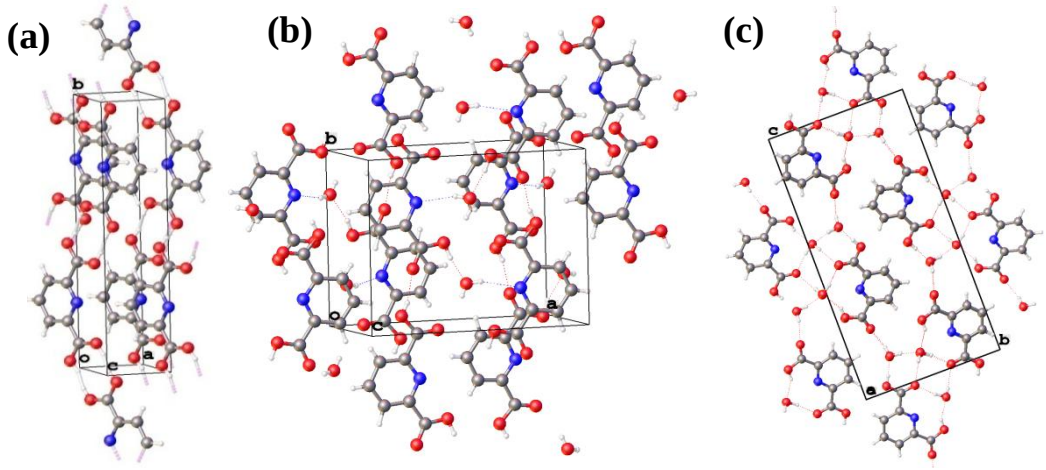

Figure 4.2 Crystal structures of (a) DPA anhydrous (refcode: AFEBUI) in $P2_1/m$ space group, (b) monohydrate (refcode: DIPICA 10) in $P2_12_12_1$ space group and (c) dihydrate (refcode: MEDNIT01) in $P2_1/c$ space group, taken from Olex 2[14].

Figure 4.3 displays the generated powder X-ray diffraction patterns for the anhydrous, monohydrate, and dihydrate forms, with their distinctive peaks inset. The anhydrous form has characteristic 2θ peaks at 16.8 °, 19.4 °, 24.3 °, 27.9 °, and 39.0 °; the monohydrate form at 14.5 °, 27.1 °, and 28.7 °; and the dihydrate form at 11.4 °, 16.0 °, 20.2 °, 26.6 °, 28.8 °, 29.4 ° and 29.9 °.

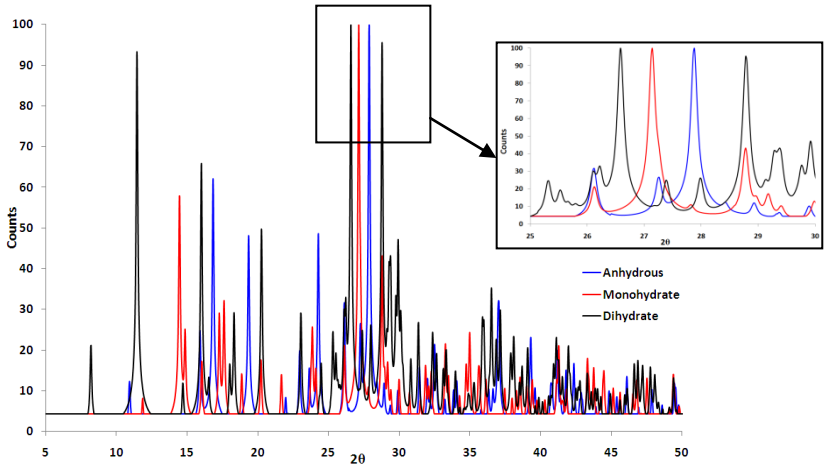

Figure 4.3 Generated PXRD patterns from single crystal structures for anhydrous, monohydrate and dihydrate forms.

The FTIR spectrum of each form (confirmed by PXRD) contains distinctive features in the region 1800 cm^{-1}-900 cm^{-1} and thus was compared in Figure 4.4; where the anhydrous form has peaks at 1693, 1576, 1462, 1416, 1331, 1298, 1261, 1176, 1163, 1082, and 997 cm^{-1}, matching very well with the literature values[15]; the monohydrate has peaks at 1726, 1651, 1585, 1477, 1454, 1435, 1383, 1346, 1271, 1178, 1126, 1157, 1092, 1067, and 1001 cm^{-1}; and the dihydrate has peaks at 1736, 1693, 1640, 1585, 1451, 1363, 1281, 1223, 1182, 1151, 1082, and 1003 cm^{-1}. In particular, the peaks at 1800-1600 cm^{-1} associated with C=O stretching for the monohydrate and dihydrate are shifted to higher wavenumbers due to weaker hydrogen bonding to water molecules in the hydrate crystals in comparison to the anhydrous form due to much stronger hydrogen bonding in the dimer molecules (compared to the hydrates)[15, 16].

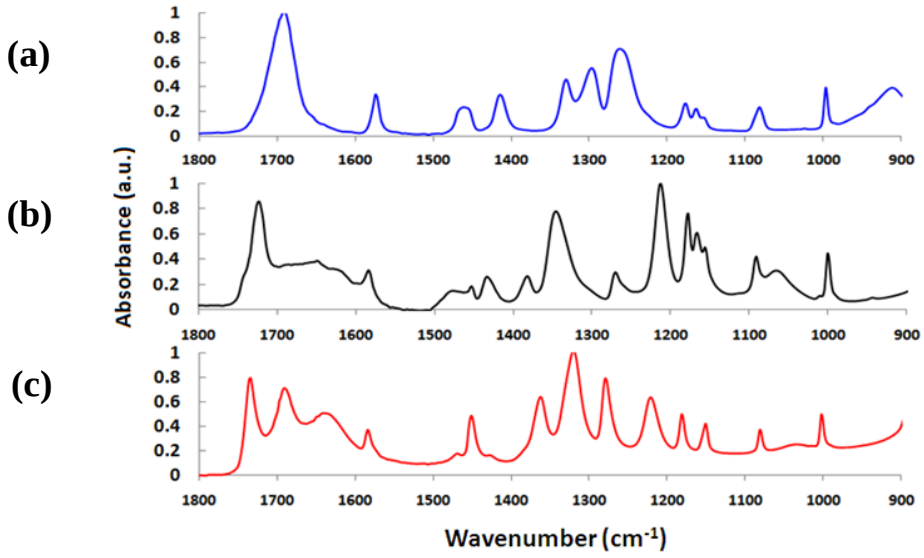

Figure 4.4 FTIR of bulk DPA forms: (a) anhydrous; (b) monohydrate; (c) dihydrate.

4.3 Experimental

4.3.1 Bulk (unconfined) experiments

The DPA anhydrous form was purchased from SigmaAldrich (98%) and used without further purification. It was dissolved in hot water (~70 ℃) at various concentrations (2 mg/ml – 15 mg/ml), before cooling to room temperature.

Crystals were obtained after filtration and analysed by FTIR spectroscopy and WAXS Bruker D8 diffractometer.

4.3.2 Microemulsion preparation

The anhydrous DPA was dissolved in UHP water or methanol at various concentrations (2 mg/ml – 18mg/ml). The aqueous DPA solution was dispersed into the readily prepared surfactant and oil mixture. The microemulsion was left to crystallise at room temperature for 1 day to 5 weeks before being analysed. The microemulsion systems used in this study are water/AOT/heptane, water/Span 80 + Brij 30/heptane, water/Triton X-100 + 1-hexanol/cyclohexane, water/Triton X-114/cyclohexane, and methanol/Triton X-100 + 1-hexanol/cyclohexane.

4.3.2.1 Water/AOT/heptane microemulsion

The concentrations of DPA in water solution were varied between 2 mg/ml to 15 mg/ml, and used as the dispersed phase. The continuous phase was 25% w/w AOT in heptane solution. The dispersed phase was varied from 50 μl/g (50 μl of the DPA solution per gram of the surfactant solution) to 400 μl/g.

4.3.2.2 Water/Span 80 + Brij 30/heptane microemulsion

The concentrations of DPA in water solution were varied from 2 mg/ml to 15 mg/ml, and used as the dispersed phase. The continuous phase was 40% w/w Span 80 and Brij 30 in heptane solution, where Span 80 and Brij 30 were mixed in a 1:1 mass ratio. The dispersed phase was varied from 5 μl/g to 75 μl/g.

4.3.2.3 Water/Triton X-100 + 1-hexanol/cyclohexane microemulsion

The dispersed phase was DPA in water solution with concentrations varying from 2 mg/ml to 15 mg/ml. The continuous phase was 55% w/w Triton X-100 and 1-hexanol in cyclohexane, where Triton X-100 and 1-hexanol were mixed in a 2.2:1 mass ratio. The dispersed phase was varied from 5 μl/g to 300 μl/g.

4.3.2.4 Water/Triton X-114/cyclohexane microemulsion

Aqueous DPA solutions with concentrations varied between 2 mg/ml and 16 mg/ml were employed as the dispersed phase, with a 30% w/w Triton X-114 in

cyclohexane continuous phase. The amount of dispersed phase added to the Triton X-114 in cyclohexane solution was in the range of 20 µl/g -70 µl/g.

4.3.2.5 Methanol/Triton X-100 and 1-hexanol/cyclohexane microemulsion

DPA in methanol solutions were used as the dispersed phase with concentrations ranging from 6 mg/ml-20 mg/ml. The amount of dispersed phase added to the continuous phase was in the range of 10 µl/g - 400 µl/g.

4.4 Results and discussions

4.4.1 Bulk crystallisation

All three DPA polymorphs can be obtained from hot aqueous solution as described earlier. The anhydrous form crystallised as prismatic needles or thin plates. Monohydrates appear prism-like and dihydrates acicular. Their morphologies are shown in Figure 4.5. The images were taken with an optical microscope under an objective lens with magnification x10.

The PXRD pattern of each form, unground, was compared to their simulated pattern, as presented in Figure 4.6. The experimental and simulated powder patterns for both the anhydrous and monohydrate forms agreed reasonably well. In the dihydrate case, 2θ peaks from $25°$ onwards are missing as a result of preferred orientation arising in the experimental patterns due to the crystals' needle morphology, with (002) being the slowest growing face.

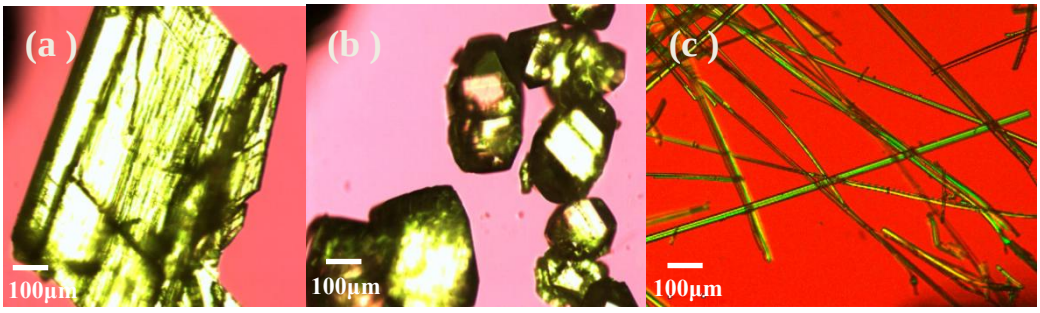

Figure 4.5 DPA crystals obtained from bulk solutions: (a) anhydrous, (b) monohydrate, and (c) dihydrate taken from optical microscope under magnification of x10.

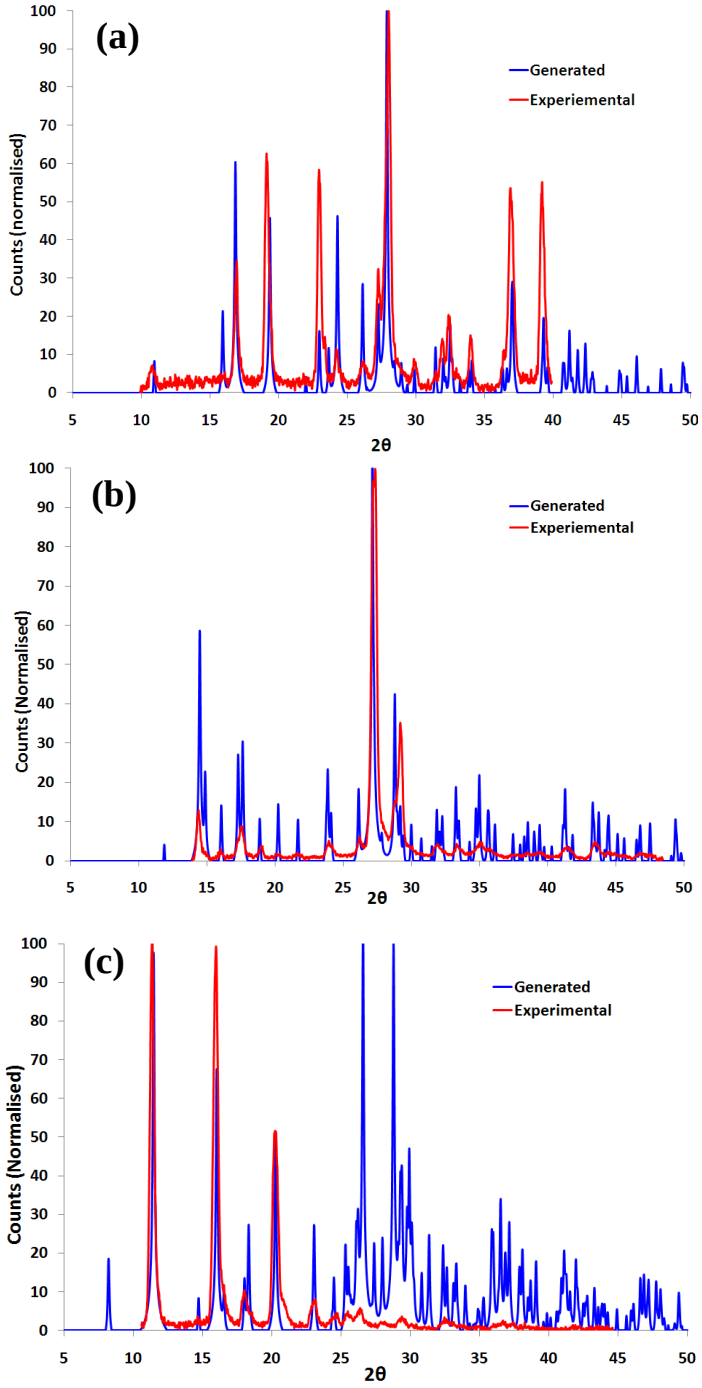

Figure 4.6 DPA bulk crystallisation where the experimental patterns are compared with the generated ones for: (a) anhydrous; (b) monohydrate; (c) dihydrate.

To observe any possible phase transformation, all three bulk forms were heated using a hot stage microscope at 10 ℃/min from room temperature to 300 ℃. For the anhydrous form, no phase transformation was observed until it melted ~250 ℃, as shown in Figure 4.7. For the monohydrate form (Figure 4.8), dehydration was observed at ~50 ℃, confirmed by TGA analysis. The residual

solids were analysed in FTIR and were of the anhydrous form as expected. For the dihydrate form (Figure 4.9), dehydration was observed at a slightly lower temperature (~ 40 ℃). However, thermal analysis could not easily be applied to this form due to its unstable nature. Considering its fast dehydration at room temperature (as Figure 4.10 suggest) and fast transformation upon the application of an external force such as grinding, the dihydrate could readily convert into the anhydrous form in the duration of DSC/TGA sample preparation stage.

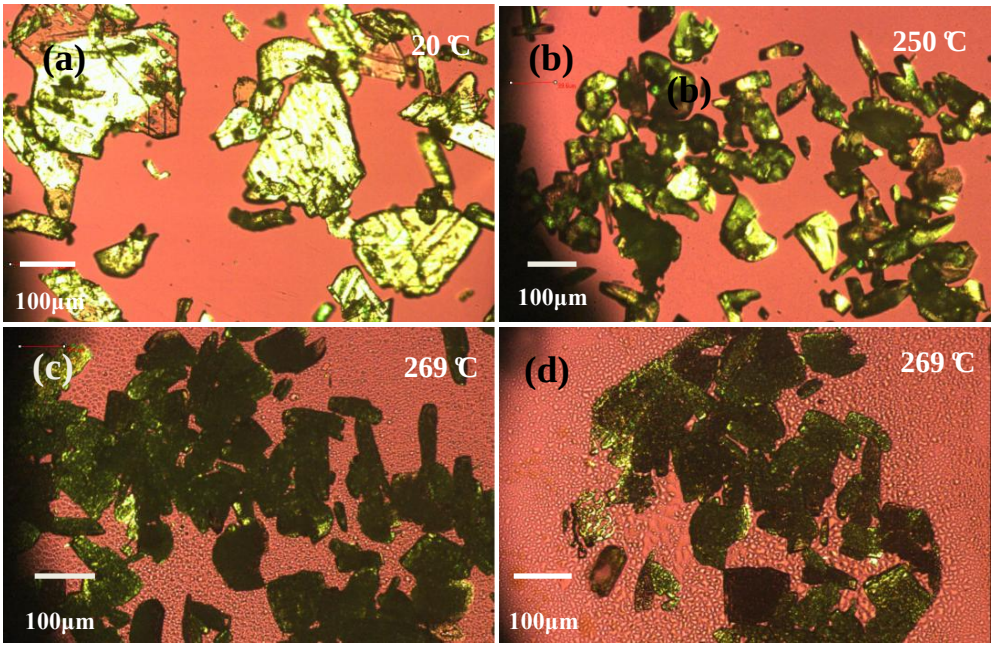

Figure 4.7 The anhydrous form heated on the optical microscope under magnification x10: (a) 20 ℃; (b) 250 ℃; (c) 269 ℃; (d) 269 ℃

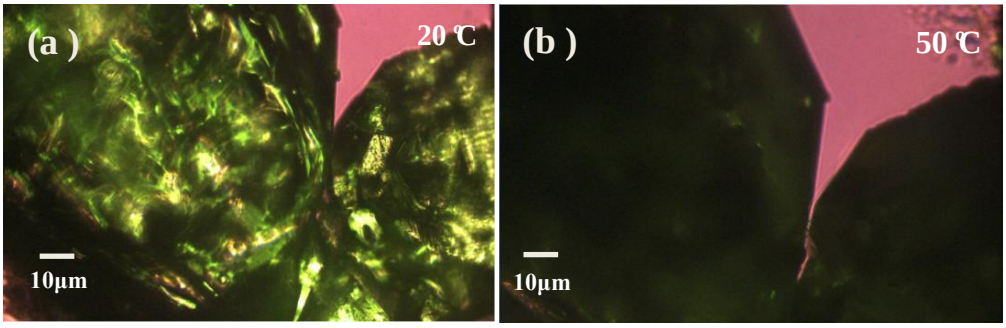

Figure 4.8 DPA monohydrate heated on the optical microscopy under magnification x50: (a) 20 ℃; (b) 50 ℃.

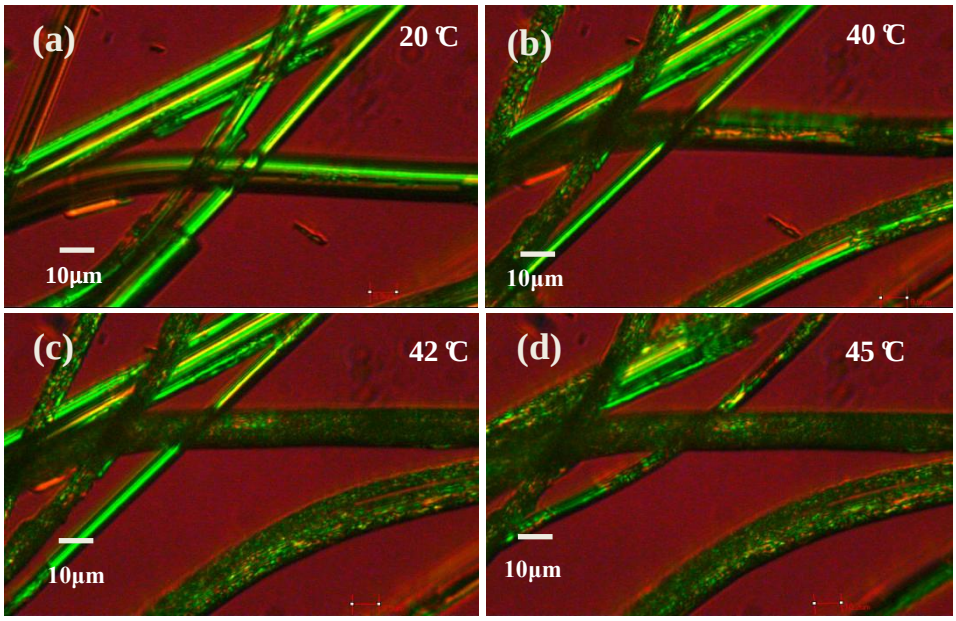

Figure 4.9 DPA dihydrate heated on the optical microscopy under magnification x50: (a) 20 ℃; (b) 40 ℃; (c) 42 ℃; (d) 45 ℃

In terms of the relative stability in water, the anhydrous form can transform into the monohydrate when there is sufficient water in solution; the dihydrate form rapidly crystallises out as 'fluffy' needles and typically transforms into the anhydrous form immediately upon grinding or within a few hours once removed from the mother liquor and left at ambient conditions. It can also transform into the monohydrate when left in the mother liquor over a short period of time. Consequently, the monohydrate is expected to be the most readily obtained form from an aqueous solution. This is in agreement with the fact that the monohydrate crystal structure was the first to be reported in 1973[6], whereas both the anhydrous and the dihydrate structures remained unknown until 2002[8] and 2007[7] respectively. Figure 4.10 illustrates the phase transformation from the dihydrate to the anhydrous form observed in PXRD, where the characteristic 2θ peaks of the dihydrate at 11.2˚, 15.8˚, and 20.0˚ were observed for up to 40 mins. After that, these peaks either disappeared or shifted over time, with new 2θ peaks appearing at 16.7˚, 19.2˚, 24.3˚, and 27.8˚. In addition the broad 'amorphous' background in the 2θ region of 23˚–40˚ for t = 10 min is possibly due to the residual water contained in the sample.

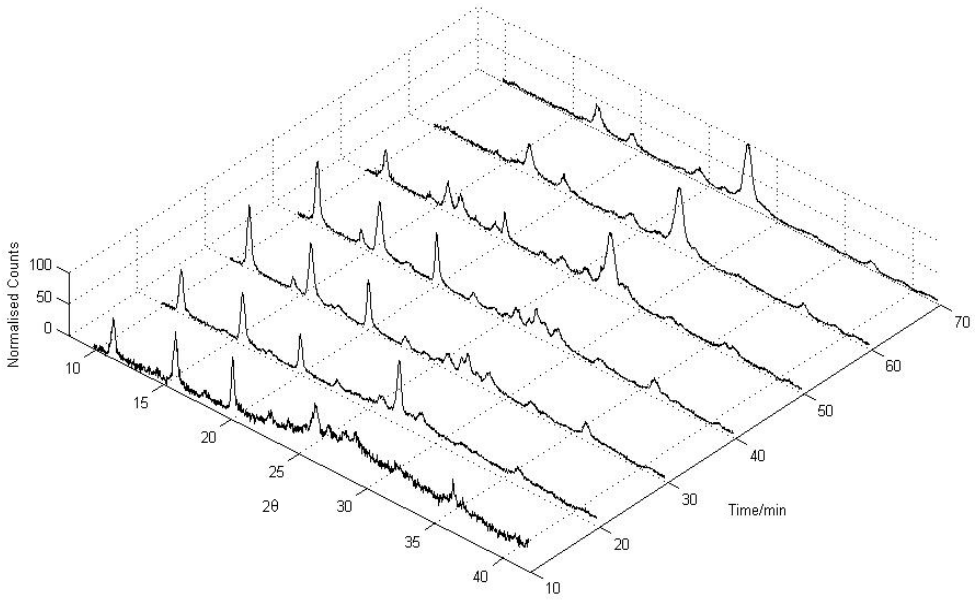

Figure 4.10 DPA dihydrate transformation to the anhydrous from when left in air over time

To examine the water content of the monohydrate, the prismatic crystals were left in an oven for 15 mins at 30 ℃ to remove excess surface water before the TGA analysis was carried out from room temperature to 300˚C at 10˚C/min. The result (Figure 4.11) indicated a 9.75% loss of water from 50˚C to 72˚C. This corresponds to a theoretical calculation of a 1:1 (DPA: water) molar ratio, confirming the monohydrate formation.

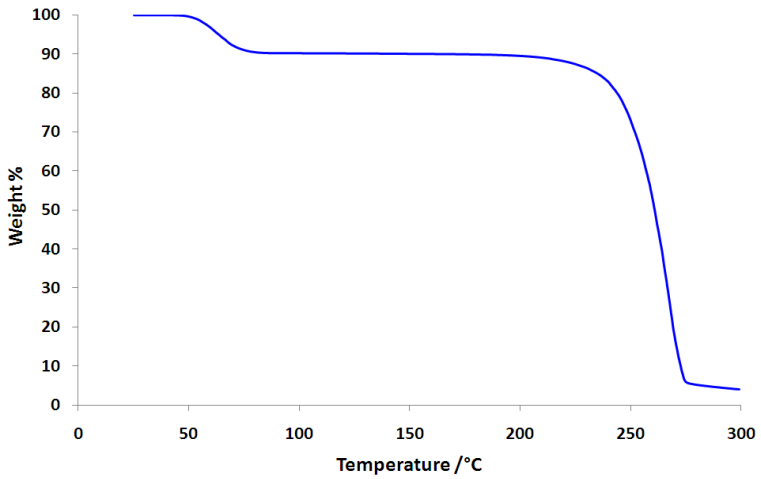

Figure 4.11 TGA trace for DPA monohydrate

4.4.2 Microemulsion crystallisation

4.4.2.1 Water/AOT/heptane microemulsion crystallisation

Two different types of acicular morphologies (Figure 4.12), named the anhydrous needle form I and the long needle form II (later to be found as sodium salt trihydrate), were obtained at different water/AOT/heptane microemulsion compositions, as shown in Figure 4.13. The DPA concentration was varied from 3mg/ml to 15 mg/ml and the dispersed phase from 50 µl to 400 µl per gram of surfactant solution. The anhydrous needle form I was observed on most occasions except at larger droplet sizes (> 200 µl) and high supersaturations (> 8mg/ml) of DPA solution, when a long needle form, subsequently identified as the sodium salt trihydrate of DPA, started to appear.

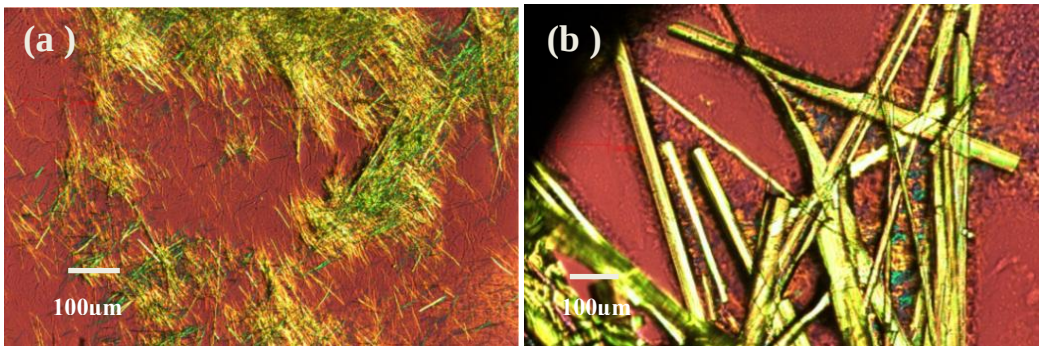

Figure 4.12 DPA crystallised from AOT microemulsion: (a) anhydrous needle form I (fluffy needles); (b) sodium salt trihydrate long needle form

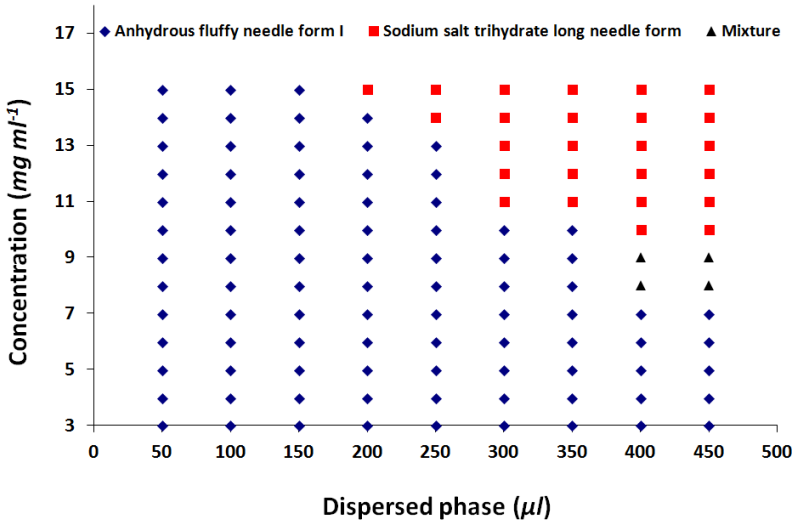

Figure 4.13 AOT microemulsion compositions

The FTIR spectra for both of these forms differ from the three known forms. In particular, the anhydrous needle form I (fluffy needles) FTIR spectrum (Figure 4.14a) has peaks at 1728, 1634, 1578, 1563, 1464, 1431, 1381, 1292, 1225, 1151, 1077, 1046, and 1002 cm^{-1} with the spectra of sodium salt trihydrate form (long needles) (Figure 4.14b) having peaks at 1726, 1699, 1633 (v. weak), 1587, 1565, 1456, 1380, 1312, 1293, 1263, 1178, 1163, 1152, 1079, 1046 and 998 cm^{-1}. There are distinct differences between the two forms at 1699, 1312, 1225, 1178 and 1163 cm^{-1}, whilst the common peaks at 1225 cm^{-1} can be attributed to residual surfactant from the microemulsion.

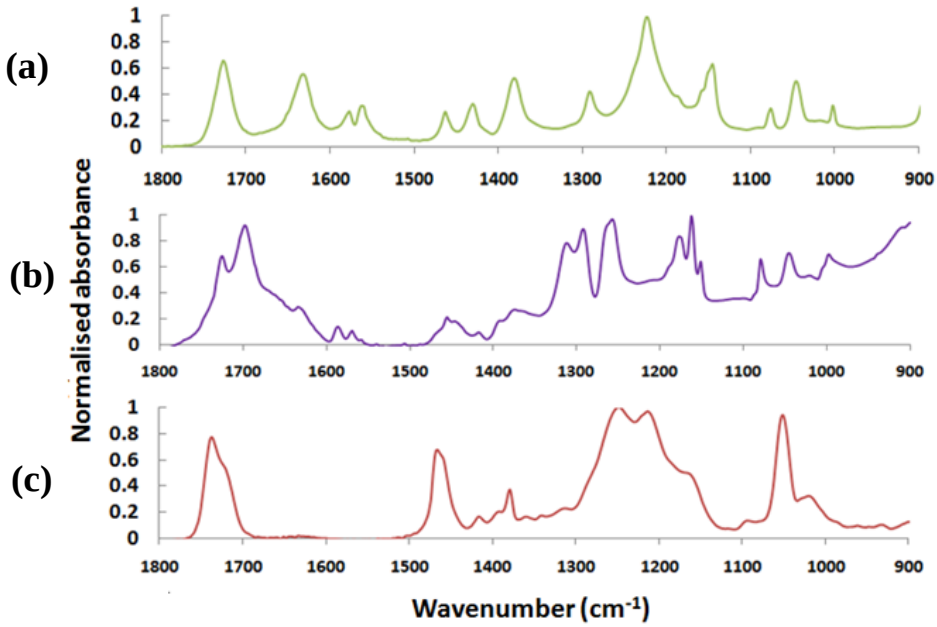

Figure 4.14 FTIR spectra for (a) anhydrous fluffy needle form I, (b) sodium salt trihydrate long needle form, and (c) AOT in heptane

The PXRD patterns for both forms are shown in Figure 4.15. The fluffy form I has characteristic 2θ peaks at 12.16 °, 14.94 °, 18.38 °, 23.42 °, 26.88 °, 28.86 °, 34.04 °, 35.28 °, 36.44 °, and 43.58 °. On comparison, the long needle form II has 2θ peaks at 15.76 °, 17.12 °, 18.22 °, 19.12 °, 19.96 °, 21.7 °, 25.98 °, 26.76 °, 27.86 °, 29.3 °, 32.94 °, 35.44 °, 36.98 °, 42.82 ° and 45.62 °. The major differences between the two forms are at 23.42 °, 25.98 °, and 29.3 °.

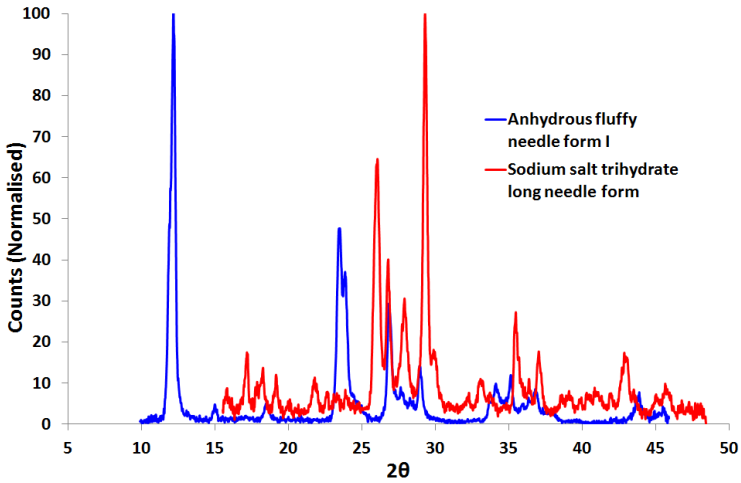

Figure 4.15 PXRD patterns for anhydrous fluffy needle form I and sodium salt trihydrate long needle form of DPA

Both forms were heated on a hot stage equipped optical microscope to investigate possible phase conversion. Figure 4.16 shows no apparent phase transformation for the anhydrous needle form I until crystallinity is lost at 260 ℃. In contrast, the sodium salt hydrate form started to dehydrate at 103 ℃ with this process being completed at 113 ℃. This is also supported by the TGA trace shown in Figure 4.18, where 12–13% of water was lost at ~110 ℃. Theoretically, this provides an approximate DPA: water ratio of ~1.5:1. Furthermore, the ion analysis indicated that the anhydrous needle form I contained 10.77% of Na (with 12.1% expected for a NaDPA salt) and the sodium salt trihydrate form had 5.41% Na.

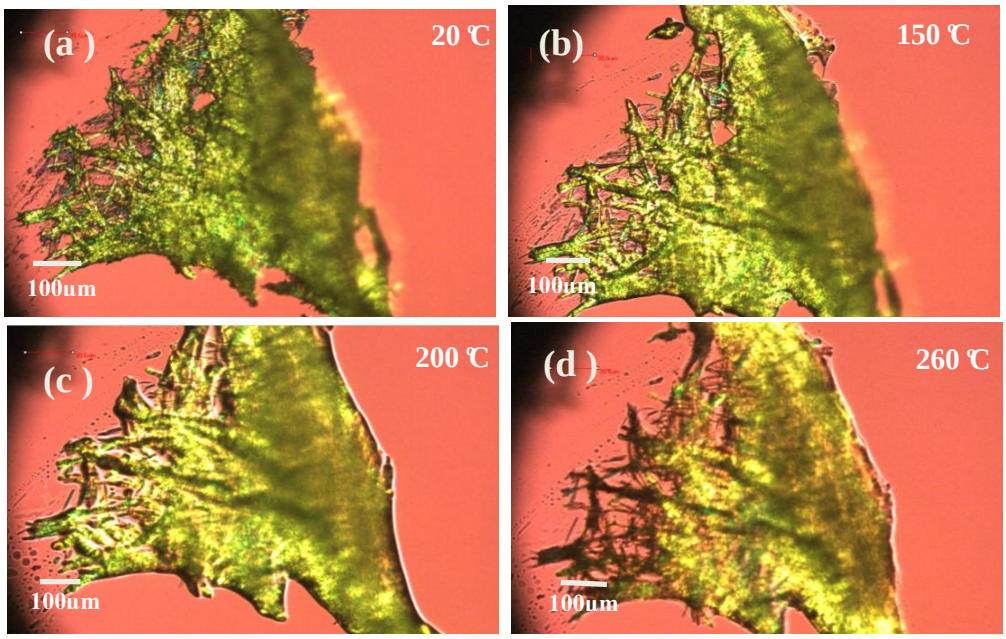

Figure 4.16 DPA anhydrous fluffy needle form heated under optical microscope with magnification x10: (a) 20 ℃; (b) 150 ℃; (c) 200 ℃; (d) 260 ℃

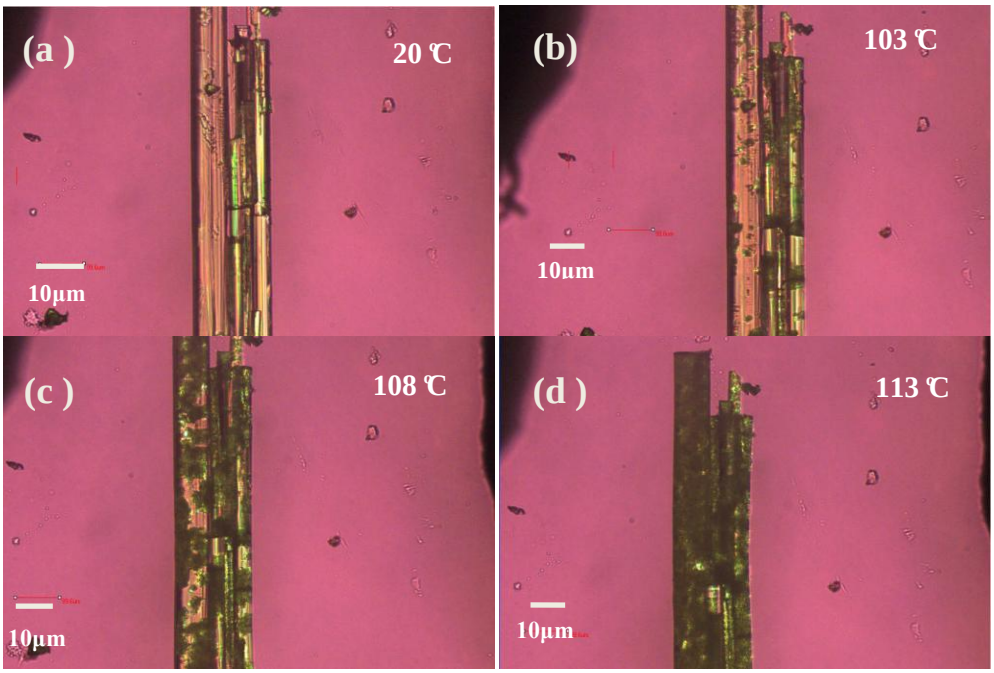

Figure 4.17 Sodium salt trihydrate long needle form heated to dehydration under magnification x10: (a) 20 ℃; (b) 103 ℃; (c) 108 ℃; (d) 113 ℃

After the loss of water, a further weight loss (53–55%) occurred at ~280–300 ℃ which corresponded to the DPA decomposition. At this stage, the residual component was NaOH, which further dehydrated to Na_2O. This process is described in the recently published paper by Santra *et. al.*[17]

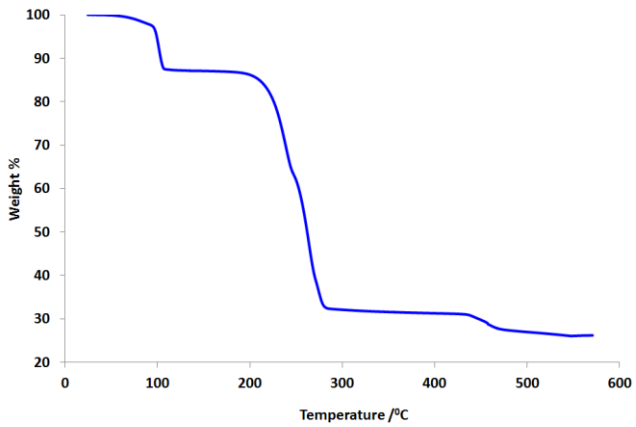

Figure 4.18 TGA of sodium dipicolinate dipicolinic acid trihydrate

The PXRD patterns and FTIR spectra of these two forms did not match any of the bulk forms of DPA, i.e. they are not the anhydrous, monohydrate, or dihydrate form of DPA. Consequently to determine the structure of these two forms, single X-ray diffraction (SXRD) would be ideal. However, only single crystals of the

sodium salt trihydrate form were sufficiently large in size for SXRD. The structure of these crystals were resolved to be sodium hydrogen dipicolinate dipicolinic acid trihydrate[18, 19], or [(dipicH)(dipicH_2)]Na•3H_2O. The crystal structure of this compound was first reported in 1995 by both Lainé *et. al.*[18] and Browning *et. al.*[19] in two separate works. Of these, the former work prepared the compound via neutralising DPA in a water suspension with 5M NaOH followed by pH adjustment to 3.5 using HCl. Finally, slow cooling yielded white crystals of this trihydrate salt. In the latter work, a multistep synthesis was required. An agar solution was first prepared and held at 50 ℃ before the addition of $NaHCO_3$. The mixture was then cooled overnight, followed by the addition of an aqueous solution containing $Al(NO_3)_3$•9H_2O and dipicolinic acid. Further, the mixture was sealed to prevent loss of water and left to crystallise for 24 days. Recently, Santra[17] *et. al.* also reported the synthesis of this form by reacting dipicolinic acid with sodium acetate at a 1: 2 molar ratio, followed by slow evaporation from a methanol/water medium. In comparison to the above methods, the AOT microemulsion method reported in this thesis required only a one step synthesis, yielding crystals suitable for diffraction experiments in ~few days. In this trihydrate sodium salt form, the sodium ion is seven coordinated (Figure 4.19). It is further bound to one water molecule both above and below the plane and in the direction of the plane it is bound to one oxygen atom from each of a carboxylic acid, carboxylate, and a water molecule, as well as binding to a nitrogen atom on the pyridine ring.

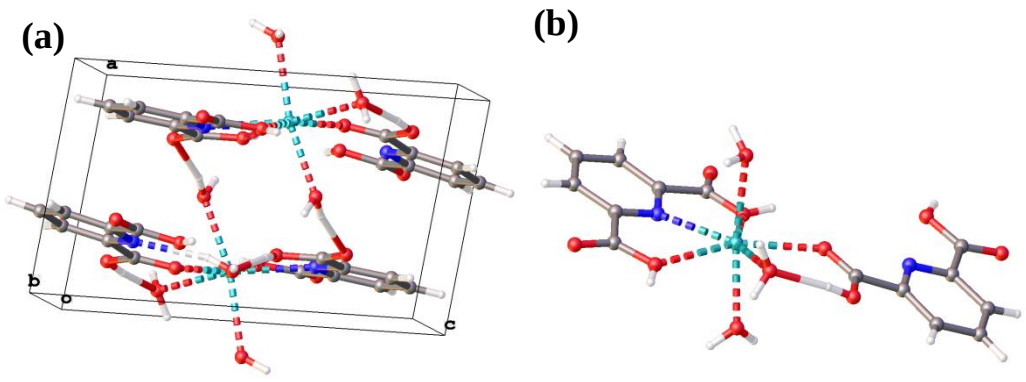

Figure 4.19 Crystal structure of DPA sodium salt trihydrate: (a) Unit Cell and (b) Asymmetric unit.

To assess the Na…O-C bond strength, searches containing Na…O-C(carboxylic group) fragments have been performed in the CSD and the results from which are plotted in Figure 4.20 in the form of bond angle versus bond distance. As can be

seen, the Na…O-C bonds in this structure are within the 2.25–2.70Å and 115–160 °regions which are situated in the middle of the scatter plot, and comparable to mean Na…O-C bond values (~2.50 Å and 121).

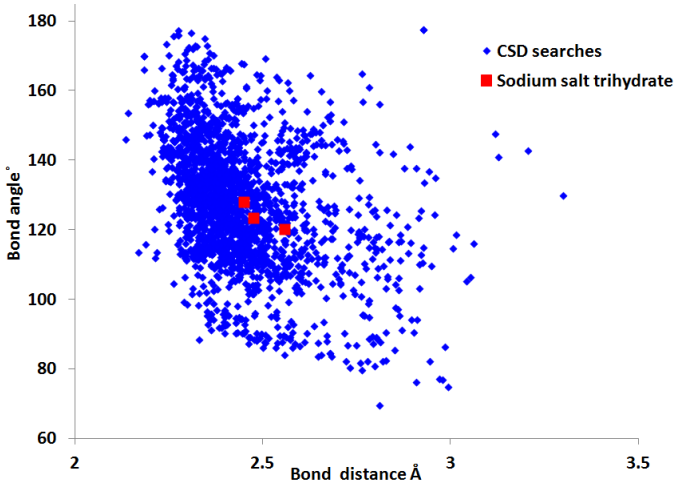

Figure 4.20 Scatter plot of bond angle Vs bond distance for Na-O-C (carboxylic group) in CSD

In this AOT system, the trihydrate sodium salt form only started to appear at higher concentrations (above 8 mg/ml) and larger droplet sizes of ≥ 3.3 nm. At lower values, the anhydrous fluffy needle form I of DPA crystallised out from the microemulsion. This is proposed to be the effect of different water content within the droplets. To investigate this further, the droplet size of various microemulsion compositions was measured using small angle X-ray scattering (SAXS). Figure 4.21 reveals the scattering function and the pair-distance distribution function, *p(r)*, from which the hydrophilic core radius can be determined as a function of the W value, the ratio of the molar concentration of water to surfactant. As the volume of the dispersed phase was increased, the droplets also swelled accordingly.

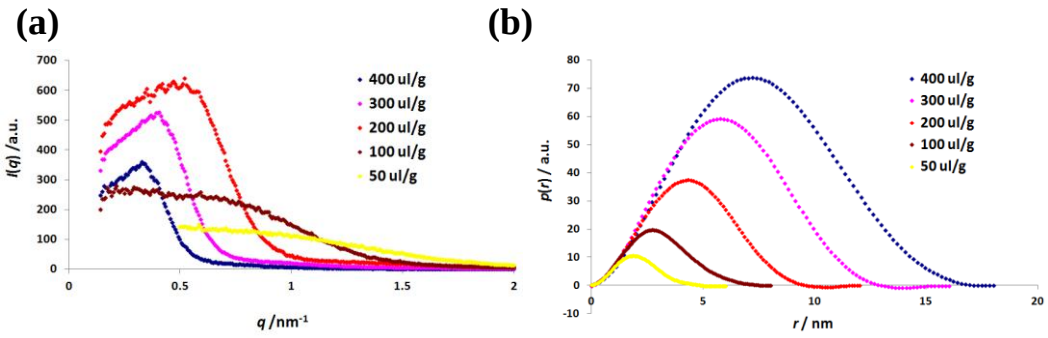

Figure 4.21 AOT microemulsion using 3 mg/ml DPA solution with various dispersed phase: (a) Scattering function *I(q)* versus *q*, the length of scattering factor; (b) pair-distance distribution function *p(r)* of the microemulsion from GIFT analysis.

Table 4.2 displays the information regarding the volume of dispersed phase, the droplet size and the calculated number of droplets in the system, the number of water molecules per droplet, the number of AOT molecules per droplet, and the number of water molecules bounded to the AOT per droplet. The latter parameter enables the fraction of water bound to AOT per droplet to be determined.

These calculations were carried out for both the geometric radius, $r_{c(geometric)}$, and the experimental radius obtained from GIFT analysis, $r_{c(gift)}$. Both radial values agree reasonably well with each other given the assumptions made in the geometric calculation, namely: a) the droplets are spherical in shape and homogenous in size; and b) the surface area per molecule values of the surfactants are taken from literature.

Table 4.2 Estimation of the free water pool size from the geometric and the GIFT radii

Dispersed phase /μl per gram surfactant solution	50	100	200	300	400
$r_{c(geometric)}$ /±0.3 nm	1.4	2.2	3.8	5.4	7.1
$r_{c(gift)}$/ ±0.3 nm	2.0	2.7	4.3	5.9	7.5
$V_{c\ (gift)}$/nm^3	33.5	82.4	333.0	860.3	1767.1
Approx. No. of droplets /x10^{17}	25.9	16.6	7.11	3.92	2.47
Mean No. of water molecules per droplet	645	2015	9406	25629	54128
Mean No. of AOT molecules per droplet	131	204	476	865	1370
Mean Water taken by AOT per droplet	783	1224	2856	5188	8217
Theoretical fraction of Water bound to AOT	1.21	0.61	0.30	0.20	0.15

*The calculations are detailed in Appendix 5.

As the AOT molecule can strongly bond to 6 water molecules per SO_3^- group and may structurally perturb 10-15 water molecules[20], the smaller droplets will be influenced by the AOT to a greater extent than the larger droplet sizes. For instance, with 10 μl/g (of surfactant solution), the fraction of water bound to AOT per droplet is 0.61, meaning only 39% of the freely moving water is left in the microemulsion core. In contrast, the 400 μl/g sample has a fraction of 0.15 water molecules bound to the AOT, and therefore a greater amount of free water molecules (i.e. 85% of the water) in the droplet, able to orientate around the dipicolinic acid and participate in the formation of hydrated crystal structures. Additionally, for a dispersed phase of 50 μl/g, the nominal calculated water fraction is 1.21, meaning AOT would be able to structurally influence 1.21 times more water than the number of existing water molecules in a droplet. As a result,

at 50 µl/g, the system is more accurately described as a swollen micelle with virtually no unperturbed water in its hydrophilic core.

The estimation of droplet sizes for various volumes of dispersed phase enabled the average number of DPA molecules in each droplet to be determined. These values are listed in Table 4.3. Relating this table to the microemulsion composition caption (Figure 4.13), for less than 4-6 DPA molecules per droplet, only anhydrous needle form I is formed. Once above this threshold, the Na salt trihydrate of DPA was seen. This is expected, since in the unit cell of the trihydrate Na salt form, there was one dipicolinate and one DPA neutral molecule. Therefore the neutral acid form of DPA will crystallise preferentially when there are more DPA molecules existing. Otherwise, the DPA molecules are more likely to crystallise as the sodium salts.

Table 4.3 Estimation of average number of DPA molecules per droplet at various dispersed phases

Dispersed phase /µl g^{-1}		50	100	200	300	400
Mean $r_{c(gift)}$/nm		2.0	2.7	4.3	5.9	7.5
No. of droplets in the system (x 10^{17})		25.9	16.6	7.11	3.92	2.47
Mean no. of DPA molecules per droplet	15 mg/ml	1.0	1.6	3.8	6.9	10.9
	13 mg/ml	0.9	1.4	3.3	6.0	9.5
	11 mg/ml	0.8	1.2	2.8	5.1	8.0
	9 mg/ml	0.6	1.0	2.3	4.1	6.6
	7 mg/ml	0.5	0.8	1.8	3.2	5.1
	5 mg/ml	0.3	0.5	1.3	2.3	3.6

The participation of sodium ions into the DPA lattice structure was not expected initially. However, considering the anionic surfactant, AOT has a sodium counterion, this is a likely source of the sodium ions that participates in the DPA crystallisation. In order to investigate the DPA behaviour in reversed microemulsions without the influence of sodium counterions, non-ionic surfactants were employed for further studies.

4.4.2.2 Water/Span 80+Brij 30/heptane systems

In this system, no crystallisation was observed for DPA concentrations lower than 4 mg/ml (Figure 4.22) and all of the yielded crystals were the anhydrous needle form I, with an identical FTIR spectrum and PXRD powder pattern to the anhydrous needle form obtained in the AOT microemulsion.

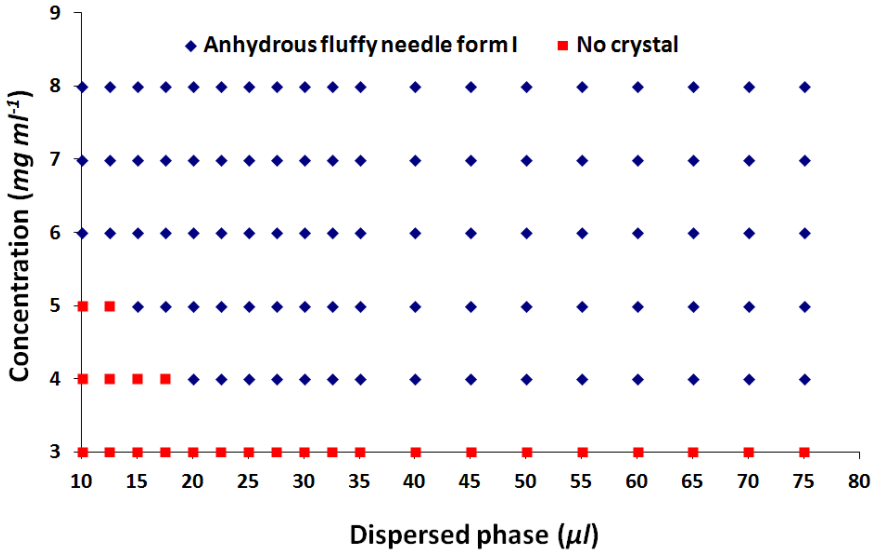

Figure 4.22 Crystallisation outcome for the Span 80+Brij 30 system at various microemulsion compositions.

Ion analysis revealed there was 10.34% Na^+ in the crystals (12% expected for NaDPA) and the elemental analysis (CHN) showed 40.38% C, 3.17% H, and 6.28% N. In comparison to the calculated mass percentage of each element for NaDPA (C: 44%; H: 2.6%; and N: 7.5%), the experimental analysis agrees to the calculated values within the boundary of experimental errors. Consequently, it appears that a sodium salt of DPA has again crystallised, with the same structure as the anhydrous fluffy needle form I obtained from the AOT system. To confirm and further clarify this, it would be ideal to obtain a single crystal structure.

The microscope images of the fluffy needles obtained from this system, taken under an objective lens magnification of x50, are shown in Figure 4.23. No phase transformation was observed until the crystals started to melt at ~260 ℃.

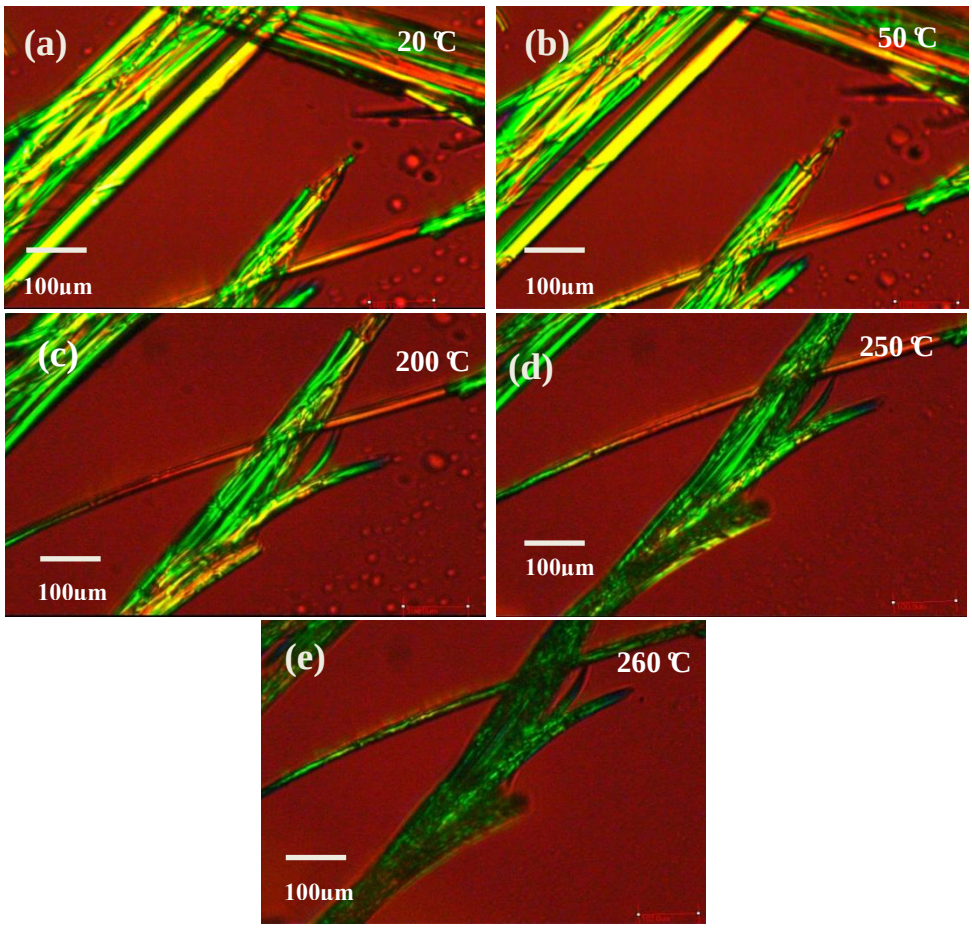

Figure 4.23 DPA fluff needle from Span 80+Brij 30 was heated until melt: a) 20 ℃; b) 50 ℃; c) 200 ℃; d) 250 ℃; e) 260 ℃.

Additionally, as the fluffy needles obtained in this system also contained a large amount of sodium, this suggests that the source of sodium ions may be impurities in the purchased chemicals. However, the dispersed phase and heptane continuous phase were ruled out as the source of the sodium as ion analysis indicated that 5 mg/ml DPA solution contains < 5 ppm of sodium, and the specification of heptane specifies only a trace amount of sodium (< 5 ppm). In contrast, it is expected that Span 80 is likely to contain residual sodium from its precursor. As a consequence, a second non-ionic surfactant system, which is a mixture of Triton X-100 and 1-hexanol, was used for microemulsion crystallisation.

4.4.2.3 Water/Triton X-100+1-hexanol/cyclohexane system

Two types of needle forms were formed from this system, named as anhydrous form needle I and anhydrous needle form II, where anhydrous needle form II is only observable at relatively low concentrations and small droplets sizes as labelled in blue in Figure 4.24. Both forms are very similar in shape apart from the anhydrous needle form I being slightly more aggregated. However, crystals of both forms are not SXRD standard. Therefore, various other techniques, including FTIR, PXRD, Ion/Elemental analysis, and thermal analysis, have been carried out to provide physical/structural information regarding these forms. The FTIR spectra (Figure 4.25) and the PXRD patterns (Figure 4.26) for both forms are drastically different.

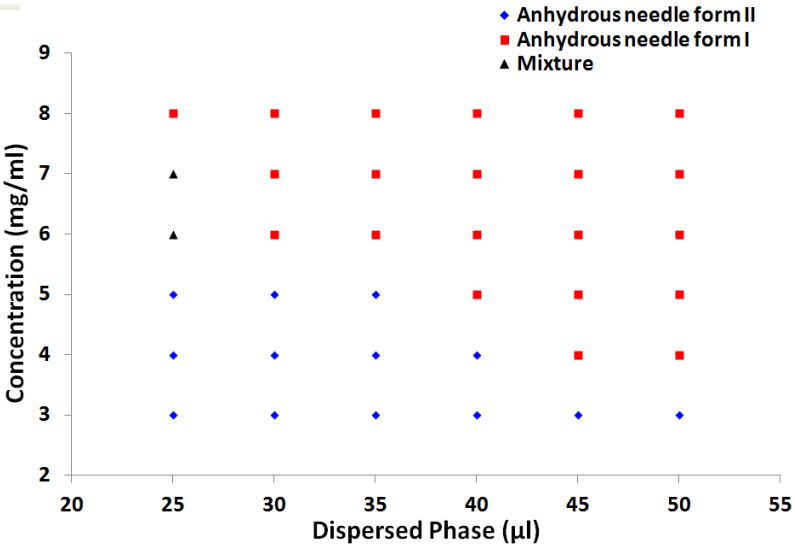

Figure 4.24 DPA Triton X-100+1-Hexanol microemulsion composition

Anhydrous needle form II, has major peaks in the region of 1800-900 cm^{-1} in the FTIR spectrum at: 1676, 1615, 1576, 1437, 1380, 1273, 1189, 1077, 1006, and 909 cm^{-1}. Anhydrous needle form I has characteristic peaks at 1727, 1632, 1578, 1563, 1464, 1431, 1382, 1292, 1225, 1145, 1076, and 1002 cm^{-1}. The distinct differences between the two forms are at 1727 (anhydrous needle form I), 1676 (anhydrous form II), and 1464 cm^{-1} (anhydrous needle form I).

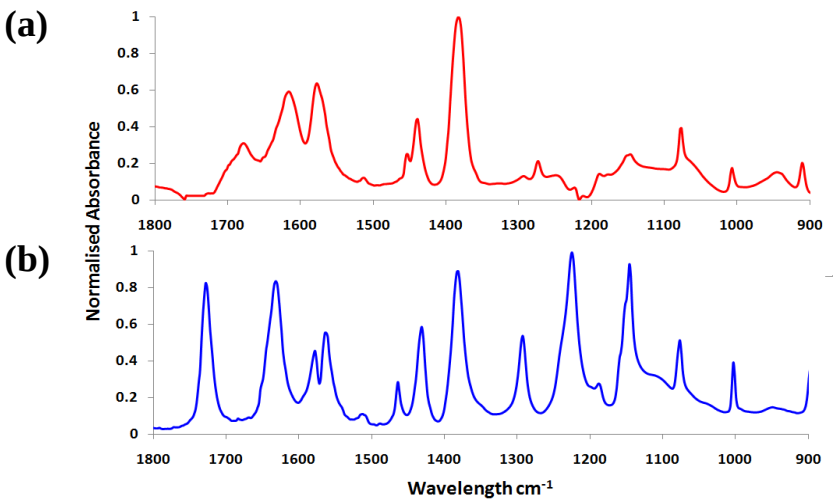

Figure 4.25 FTIR spectra for a) anhydrous needle form II and b) anhydrous needle form I

From the PXRD patterns, anhydrous form II has 2θ peaks at 10.46 °, 14.42 °, 24.08 °, 26.8 °, 29.22 °, 32.82 °, 35.72 °, 37.56 °, 39 °, and 40.14 °. Form II has 2θ peaks are seen at 12.10 °, 14.90 °, 17.04 °, 18.72 °, 23.88 °, 27.00 °, 28.84 °, 34.36 °, 36.60 °, 38.16 °, 39.98 ° and 43.88 °. The most noticeable differences between the two forms are at 10.46 °(II), 12.10 °(I) and 14.42 °(II).

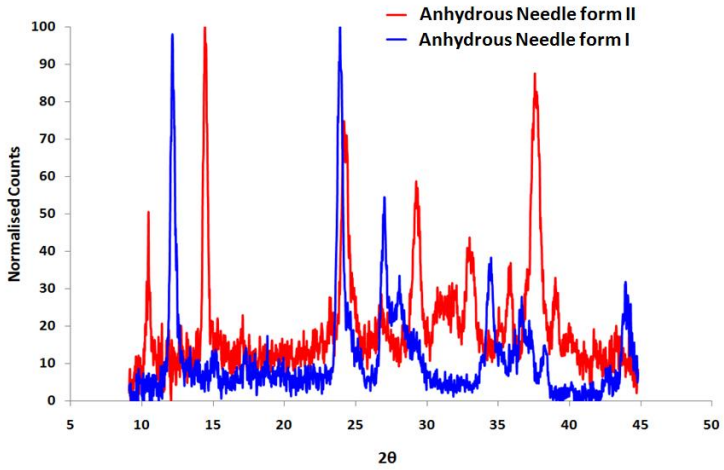

Figure 4.26 PXRD patterns of anhydrous form II and form I of DPA

Anhydrous form II was observed under the optical microscope under an objective lens magnification of x10 and then heated on an attached hot stage to study any phase transitions. As we can see from Figure 4.27 (a)-(g), no phase transformation or dehydration was observed until the needles started to melt at 260 ℃.

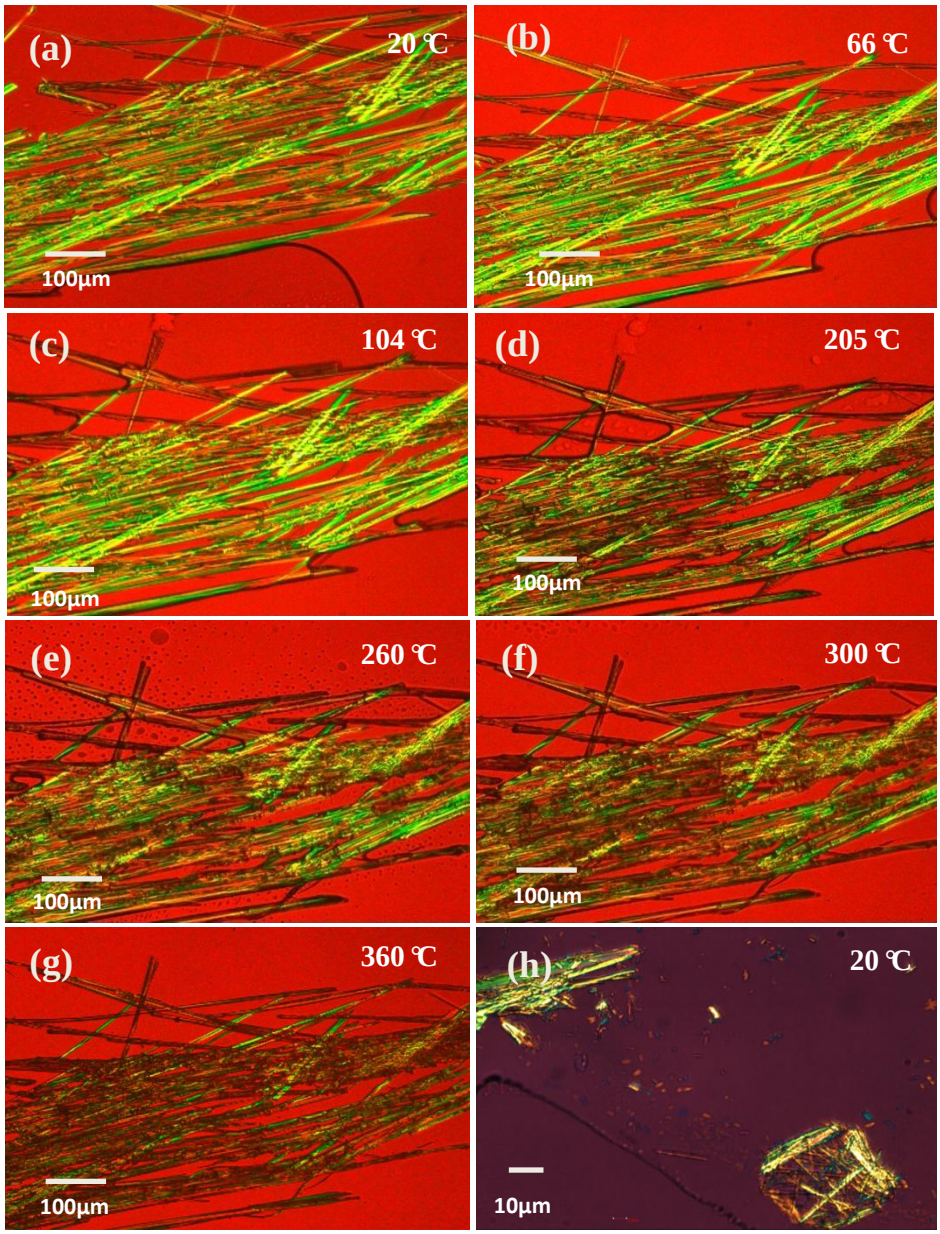

Figure 4.27 DPA crystallisation from Triton X-100 microemulsions: (a)-(g) anhydrous form II heated up to melting point; (h) anhydrous form I form at 20 ℃.

Interestingly, the comparison between the various forms revealed that the anhydrous forms II and I did not match any of the bulk forms obtained from pure water but agreed reasonably well with the two different forms obtained from aqueous NaOH solution. In particular, both the FTIR and PXRD of anhydrous form II overlapped with the corresponding spectra obtained from DPA crystallised from aqueous NaOH over a 4 week period via slow evaporation, as indicated in Figure 4.28 and Figure 4.29. This DPA form contained 22.66% of Na ions, which

is close to the 22% value expected for Na_2DPA. In addition, the FTIR spectrum of this form is in agreement with the reference FTIR of Na_2DPA[15].

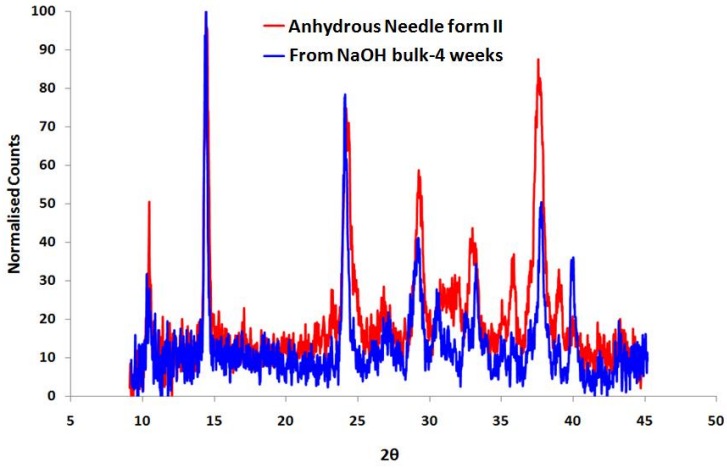

Figure 4.28 PXRD patterns for anhydrous form II and DPA crystallised from NaOH in 4 weeks

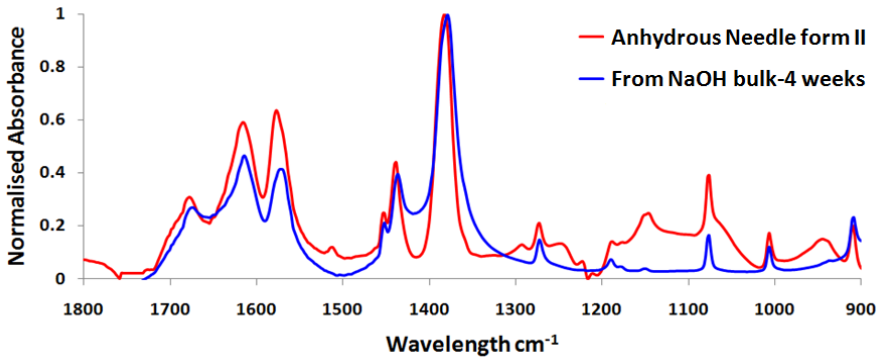

Figure 4.29 FTIR spectra for anhydrous form II and DPA crystallised from NaOH in 4 weeks

In contrast to the anhydrous form II case, form I has almost identical FTIR (Figure 4.30) and PXRD spectra (Figure 4.31) to the anhydrous fluffy needle form I from AOT, the same form from Span 80+Brij 30, and also the DPA salt form crystallised from 5M NaOH overnight. Ion analysis indicated they have similar quantity of sodium ion contents, ranging from 9.56% – 10.89%, with 39.82% C, 2.82% H, and 7.11% N. These results are comparable with each other and indicated that the form that had crystallised in each case is postulated to be NaDPA, which is expected to contain 44% C, 2.6% H, 7.5% N, and 12.2% Na from the empirical formula.

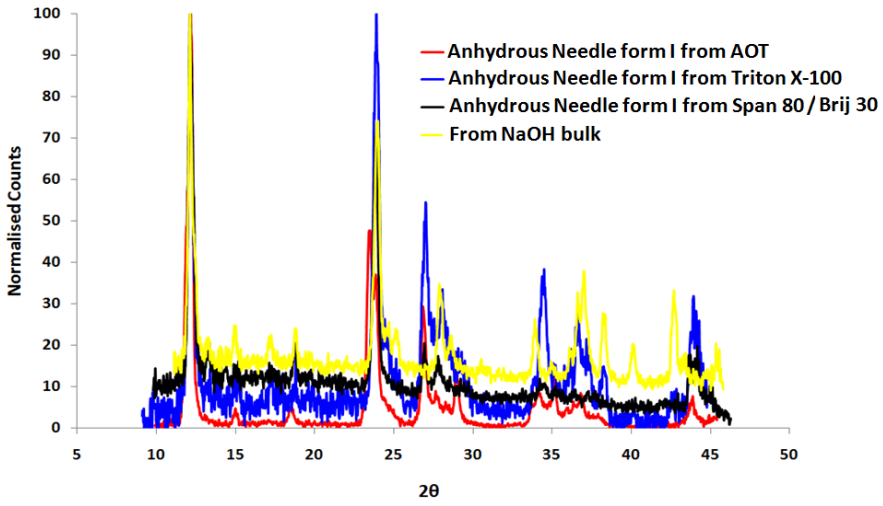

Figure 4.30 PXRD patterns for anhydrous needle form I from Triton X-100, AOT, Span 80/Brij 30, and 5M NaOH bulk solution.

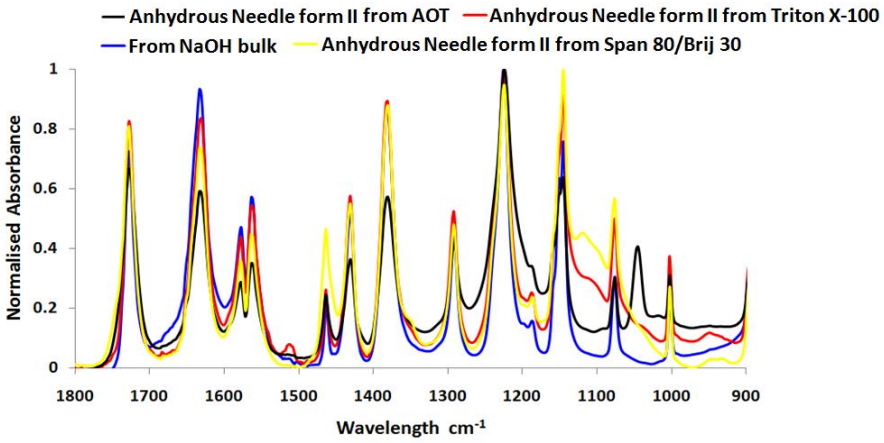

Figure 4.31 FTIR spectra for anhydrous needle form I, fluffy forms from AOT and Span 80/Brij 30, and 5M NaOH bulk solution.

In this Triton X-100 system, it was noticed that with increasing droplet size, crystallisation slowed dramatically. For instance, with DPA solutions 8 mg/ml (a bulk supersaturation ratio of 1.5), the 100– 300 µl/g samples did not show any sign of crystallisation after being left for 1–2 months. In contrast, the 25 µl/g sample with a DPA solution of 2 mg/ml, crystallised out in the duration of days to a week. To investigate this further the droplet size for different microemulsion compositions was measured and presented in Figure 4.32. The droplet shape and size at different volumes of dispersed phase were also simulated from GIFT analysis (Figure 4.32b).

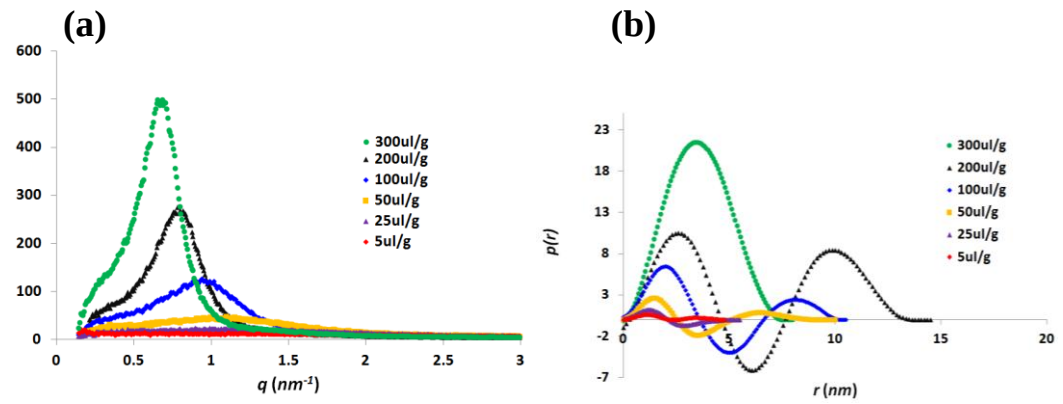

Figure 4.32 Triton X-100/1-Hexanol microemulsion systems with various dispersed phase at 5 µl/g, 25 µl/g, 50 µl/g, 100 µl/g, 200 µl/g, and 300 µl/g with a) Scattering function *I(q;)* b) *p(r)* function obtained from GIFT analysis.

Between 5 µl/g and 200 µl /g of dispersed phase, GIFT analysis showed that the droplet was well described by a core shell model. Beyond 300 µl /g of dispersed phase, a hard sphere model was more appropriate. This is attributed to the degree of continuum (cyclohexane) participating at the interface. The core shell model contains a higher electron density region containing dispersed phase and hydrophilic part of Triton X-100, in addition to a relatively low electron density region comprising a portion of the hydrophobic tail groups of Triton X-100 and 1-hexanol. Up to 300 µl/g, such a core shell model fitted the scattering data best as the 1-hexanol, in particularly, has a lower electron density (0.28 e $Å^{-3}$) compared to the dispersed phase, 0.33 e $Å^{-3}$. Once the droplets are swollen to a certain size with > 300 µl/g dispersed phase, the cyclohexane becomes more incorporated into the surfactant tail groups and thus the tail group region becomes less distinguishable from the surrounding continuous phase. The resulting scattering appears to emanate simply from a sphere model, comprised of the inner phase and the hydrophilic head groups of the surfactants and cosurfactants. The electron density, ρ_e, is estimated using the following equation and listed in Table 4.4:

$$\rho_e = \frac{\rho N_A N_e^-}{M_r} \qquad (4.1)$$

Where ρ is the density, N_e^- is the number of electrons in the molecule, N_A is Avogadro's number, and M_r is the molecular weight.

Table 4. 4 Electron density per A^3 for each of the microemulsion component

	H_2O	Cyclohexane	TX-100	1-hexanol
Density/g ml^{-1}	1	0.78	1.07	0.81
No. of e^-	10	48	342	58
M_r /g mol^{-1}	18	84	625	102
Electron Density /A^{-3}	0.33	0.27	0.35	0.28

The GIFT analysis estimate of the hydrophilic core droplet size (experimental) was compared with geometric calculations with small discrepancies. This is due to a different level of cosurfactant participating at the interface. As a result, it is highly possible that some of the 1-hexanol migrates to the outer shell of the surfactant layer as well as partitioning into the cyclohexane continuous phase. Therefore geometric calculations were also performed with a reduced amount of, or no 1-hexanol (Table 4.5), for comparison and the results were also plotted in Figure 4.33.

Table 4. 5 Geometric radius calculated from different mass fraction of hexanol vs the experimental radius obtained from GIFT analysis

Dispersed Phase / ulg^{-1}	Mass fraction of hexanol at the interface			R_{gift}/nm
	No	0.11	0.17	
300	11.28	5.32	4.16	4.01
200	8.45	4.00	3.14	3.73
100	5.94	2.84	2.24	3.65
50	4.81	2.31	1.83	3.56
25	4.28	2.06	1.63	3.15
5	3.86	1.87	1.49	3.14

When the mass fraction of 1-hexanol is reduced from 0.17 to 0.11 per unit of surfactant solution, the plot was much closer to the ideal value. However, if hexanol is not taken into account in the calculation, the droplet becomes much larger and further deviates from the ideal. This was expected since the addition of a cosurfactant tends to reduce the droplet size owing to their ability to decrease the bending elasticity of the interfacial film. This has already been reported by Farago *et. al.*[21] for the effect of butanol addition and Kitchens *et. al.*[22] on the addition of octanol to AOT reversed microemulsions. They found that the cosurfactant can reduce the bending elasticity and therefore the micelle rigidity, leading to an increased material exchange rate between the droplets.

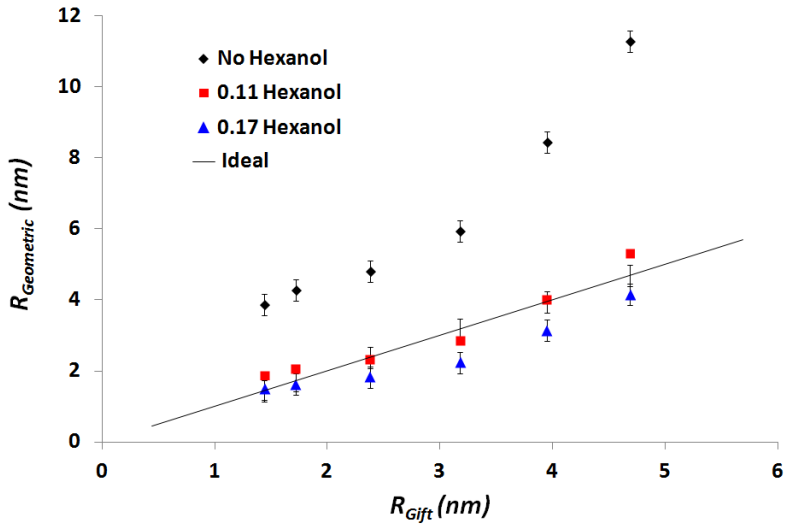

Figure 4.33 Geometric droplet sizes calculated with various 1-hexanol amount (0.17, 0.11 or no 1-hexanol) comparing to the GIFT droplet size.

The different crystallisation outcome at various compositions could possibly be attributed to the amount of water bound by Triton X-100, which has a greater influence on the small droplet size microemulsions. This is similar to the effect of AOT. Several values have been reported for the number of water molecules per Triton X-100 molecule that can be structurally bound/perturbed due to the ~9.5 ethylene oxide groups on the Triton X-100 backbone. In Zhu *et. al.*'s work[23], a Triton X-100 molecule was found to potentially perturb up to 16 water molecules. Sarkar *et. al*'s research[24] revealed the appearance of a free water pool once the W value is ~ 5.3, suggesting a Triton X-100 molecule can bind to ~5.3 water molecules. The calculation of the hydration layer depth in our study was based on Sarkar's value since his study also employed Triton X-100 and hexanol to form microemulsions with aqueous solutions as dispersed phase and cyclohexane as the continuous phase. As shown in Table 4.6, this hydration effect is more significant for small droplets from 5 µl/g to 50 µl/g, where the Triton X-100 can nominally bind to more water molecules than the amount actually existing in a droplet since the bound water fraction values are greater than 1. So all of the water molecules have been used up to solvate the EO groups. Hence solutions used to prepare the microemulsions that were initially undersaturated become rapidly supersaturated, and hence crystallisation is promoted. This is evidenced by their solubility data where for per gram of the microemulsion comprising 25 µl of water, the solubility

of Na_2DPA is ≤ 0.025 mg while for 50 μl of water, the solubility is ≤ 0.05 mg. In contrast, the solubility of Na_2DPA in bulk water is ~11mg/ml.

Table 4. 6 Droplet size and water content calculations from the GIFT radii

Dispersed phase /μl g^{-1}	5	25	50	100	200	300
$r_{c(gift)}$ /nm	1.44	1.72	2.38	3.18	3.95	4.69
$V_{c\ (gift)}$/nm^3	12.20	21.31	56.12	134.07	179.59	258.40
Approx. No. of droplets (x 10^{17})	4.10	11.70	8.91	7.46	7.74	6.95
Approx. No. of water molecules per droplet (x 10^3)	0.41	0.71	1.88	4.49	8.64	14.43
Approx. No. of Triton X-100 molecules per droplet (x 10^3)	0.89	0.31	0.41	0.49	0.47	0.53
Approx. Water theoretically taken by Triton X-100 per droplet (x 10^3)	4.73	1.65	2.18	2.60	2.51	2.79
Theoretical fraction of Water theoretically bound to Triton X-100	11.6	2.3	1.2	0.6	0.3	0.2

The different crystal form outcome at different compositions was attributed to a combination of the uptake of water by Triton X-100 and a pH shift effect of the microemulsion.[25-27] In particular it has been previously found that microemulsions can shift the pH of the dispersed phase towards neutrality (by selectively bind to H^+/OH^- ions). Sedgwick's study[28] on decavanadate revealed that non-ionic reversed micelles can assist the deprotonation of the probing compound and generate a pH neutral environment, in weakly acidic/basic bulk solutions.

DPA itself can undergo self-association to various ionic species depending on the pK_a values. Below pK_a of -1.0, DPA exists in its cation form; between -1.0 and 2.2, the neutral forms (the Zwitterion and uncharged forms) dominate; between 2.2 and 5.2, monoanion forms play the key role; once above 5.2, dianion form exists. Thus these forms are interconvertible by varying the pH of the solutions. Therefore depending on the local pH environment of the microemulsion, different forms of DPA can then bind to the surrounding sodium ions and form different salts, which will be discussed in greater detail in section 4.4.3.

Furthermore, the available DPA molecules may contribute to the crystallisation of different forms. Accordingly the average number of DPA molecules per droplet at various compositions was estimated (Table 4.7). Macroscopic crystals (> μm) were observed solely in the dispersed phase region of 25–50 μl/g. With droplets

from < 25 μl/g, insufficient material and a limited number of droplets might limit the crystal growth. At larger droplet sizes (> 50 μl/g), the viscosity noticeably increased which would be expected to slow down the droplet collision rate and thus the rate of crystal growth (See Chapter 5 section 5.3.2e for further discussion). Despite the small average number of molecules existing in each droplet, crystallisation was possible since a large fraction of the water has hydrated the surfactant head group, leading to a much higher concentration of DPA in the droplets' hydrophilic core compared to in the bulk. Furthermore, monoanion anhydrous form I was observed to crystallise at 8 mg/ml in the case of a 25 μl/g sample but at ≥ 4 mg/ml for a 50 μl/g sample. This revealed an average number of ~0.6-0.8 DPA molecules per droplet when the anhydrous form I crystallises.

Table 4. 7 Estimation of the average number of DPA molecules in each microemulsion droplet when varying the microemulsion composition

Dispersed phase /μl g^{-1}		5	25	50	100	200	300
Mean $r_{c(gift)}$/nm		1.44	1.72	2.38	3.18	3.95	4.69
No. of droplets in the system (x 10^{17})		4.1	11.7	8.91	7.46	7.74	6.95
Mean no. of DPA molecules per droplet at various DPA concentration	8 mg/ml	0.4	0.6	1.6	3.9	7.4	12.4
	7 mg/ml	0.3	0.5	1.4	3.4	6.5	10.9
	6 mg/ml	0.3	0.5	1.2	2.9	5.6	9.3
	5 mg/ml	0.2	0.4	1.0	2.4	4.7	7.8
	4 mg/ml	0.2	0.3	0.8	1.9	3.7	6.2
	3 mg/ml	0.1	0.2	0.6	1.4	2.8	4.7
	2 mg/ml	0.1	0.2	0.4	1.0	1.7	3.1

Overall, sodium ion contamination is still a problem existing in this system. As stated earlier, DPA aqueous solutions have negligible sodium ion content. The specification for cyclohexane indicates it has < 5 ppm of sodium ions, which leaves Triton X-100 and/or 1-hexanol (cosurfactant) as the possible source of sodium. Thus to eliminate the effect of cosurfactant, Triton X-114, a similar surfactant to Triton X-100 but can form stable microemulsions without the assistant of a cosurfactant, was employed.

4.4.2.4 Water/Triton X-114/cyclohexane microemulsion preparation

Similar to the previous two systems, two forms were produced in this system with the anhydrous form I (NaDPA) being the product at low DPA concentrations and smaller droplet sizes (Figure 4.34). With the increase of both the DPA concentration and the dispersed phase volume fraction, a new form was obtained, later proven to be a potassium salt hydrate form with the empirical formula $[(dipicH)(dipicH_2)]K•3H_2O$. This was first reported last year by Santra *et. al*.[17] However, the quality of the crystals obtained from our microemulsion is much improved than those crystallised by Santra *et. al* [17] (Table 4.8). Details of the crystal structure, e.g. bond length, bond distance, are attached in Appendix 6.

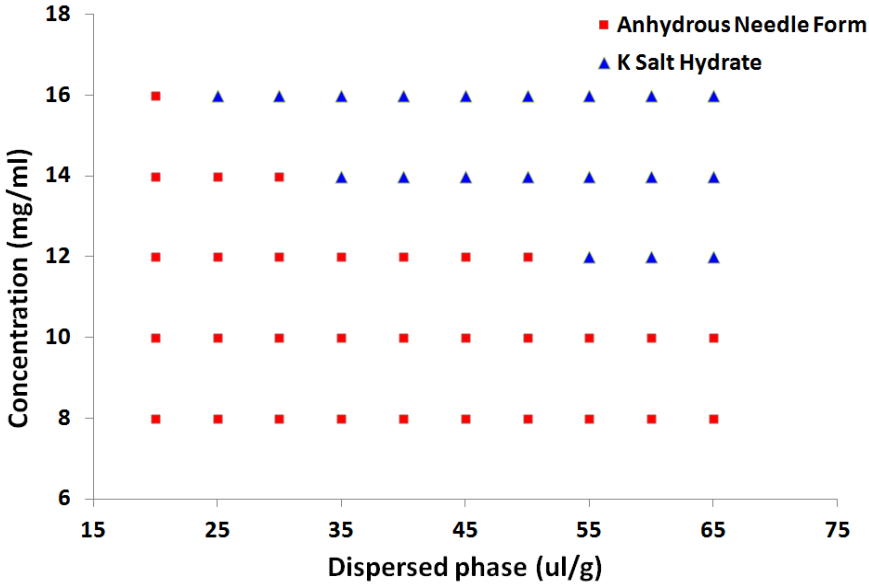

Figure 4.34 DPA in Triton X-114 microemulsion composition

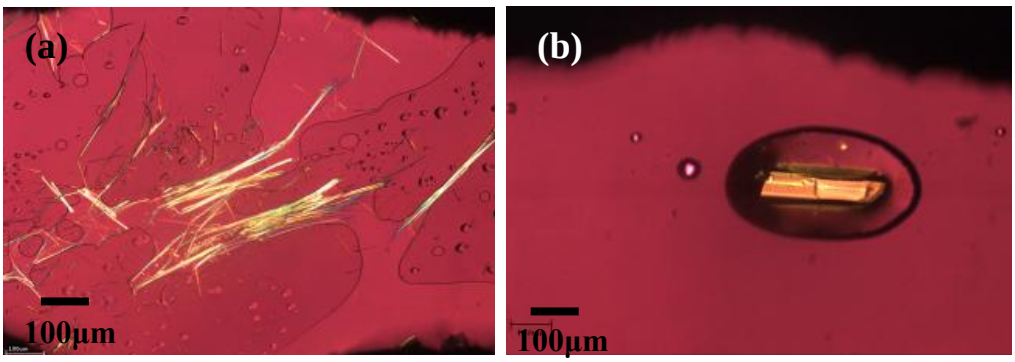

Figure 4.35 DPA crystallisation from Triton X-114 microemulsions:
(a) Anhydrous form I heated up to melting point; (b) potassium salt hydrate form at 20 ℃.

Table 4.8 Comparison of structures with Santra *et.al.*'s[17] study

	Santra *et. al.*	This study
Empirical formula	$C_{28}H_{30}K_2N_4O_{22}$	$[C_7H_5NO_4]$ x $[C_7H_4NO_4]$ x K x $3H_2O$
Formula weight	852.76	426.38
Temperature/K	/	120
Crystal system	Triclinic	Triclinic
Space group	$P_{\bar{1}}$	$P_{\bar{1}}$
a/Å	7.0937(4)	6.9649(3)
b/Å	11.0034(5)	10.9834(5)
c/Å	11.2732(6)	11.2246(6)
α/°	91.603(3)	91.635(2)
β/°	96.088(3)	96.001(2)
γ/°	97.207(4)	97.585(2)
Volume/$Å^3$	867.29(8)	845.70(7)
Z	1	2
$\rho_{calc}mg/mm^3$	1.633	1.674
m/mm^{-1}	0.373	0.382
F(000)	440.0	440.0
Crystal size/mm^3	/	0.15 × 0.12 × 0.06
2Θ range for data collection	< 48 °	3.66 to 59 °
Index ranges	-8,8; -12,12; -12, 12	$-9 \leq h \leq 9$, $-15 \leq k \leq 15$, $-15 \leq l \leq 15$
Reflections collected	7204	9753
Independent reflections	2592	4655[R(int) = 0.0365]
Data/restraints/parameters	2532/0/274	4655/0/313
Goodness-of-fit on F^2	0.941	1.020
Final R indexes [I>=2σ (I)]	0.0410	R_1 = 0.0466, wR_2 = 0.1123
Final R indexes [all data]	0.0517	R_1 = 0.0768, wR_2 = 0.1289
Largest diff. peak/hole / e $Å^{-3}$	/	0.52/-0.52

This new form is triclinic with space group P-$_1$ and 4 asymmetric units in the unit cell. This form is similar to the trihydrate sodium salt except the sodium salt is mononuclear whereas the potassium salt is binuclear. The core potassium is eight coordinated by 3 water molecules, 4 oxygen atoms from the carboxylic acid groups and the nitrogen of the pyridine ring (Figure 4.36). This means two of the carboxylic acid oxygen atoms are effectively shared by 2 neighbouring potassium ions. To assess the K-O-C bond strength, searches containing K-O-C(carboxylic group) fragments have been performed in the CSD and the results from which are plotted in Figure 4.37 in the form of bond angle versus bond distance. As can be seen, the K-O-C bonds in this structure are within the 2.71-2.81Å and 121-130 º regions which are situated in the middle of the scatter plot, and comparable to mean K-O-C bond values (~2.81 Å and 123 º).

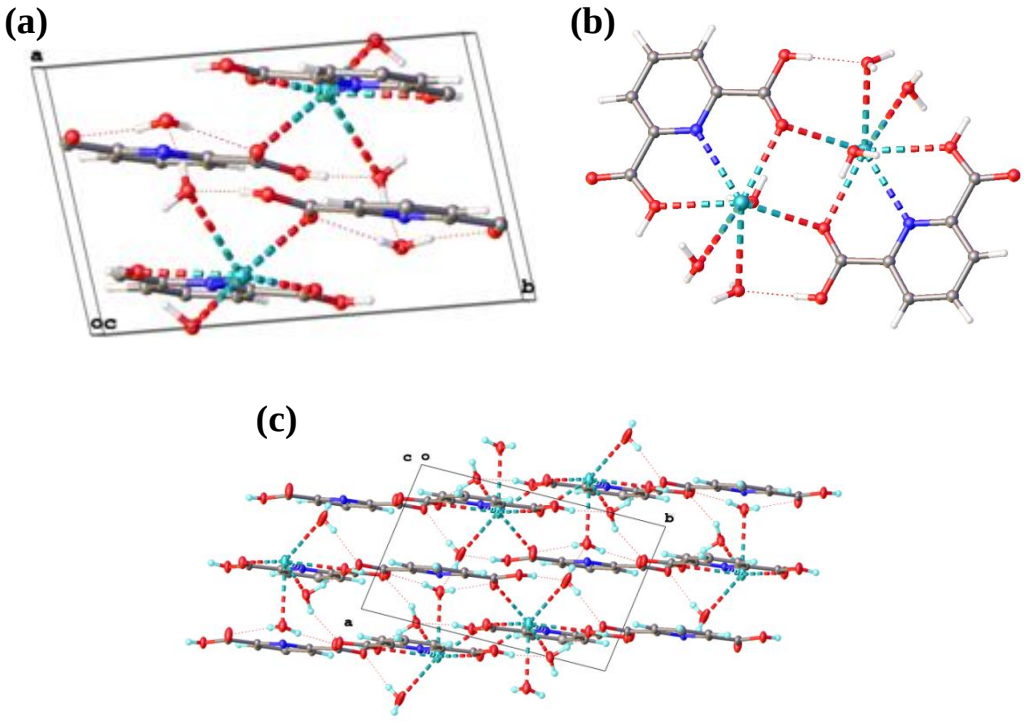

Figure 4.36 Crystal structure of potassium salt hydrate form obtained from Olex-2[14]: (a) Unit cell; (b) dimer (dinulear); (c) Layered structure

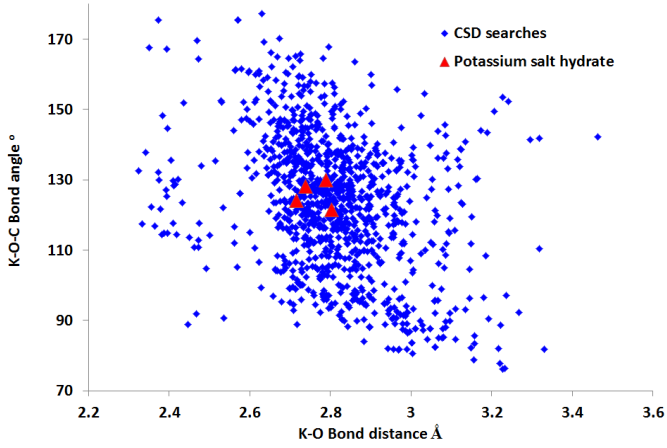

Figure 4.37 Scatter plot of bond angle versus bond distance for K-O-C(carboxylic group)

SAXS measurements and GIFT analysis were employed to rationalise the different crystallisation outcome at various microemulsion compositions. Unlike the Triton X-100 system, the *p(r)* function stayed solely as a simple sphere model, suggesting the reduced electronegative region in the core shell model of Triton X-100 system was 1-hexanol. The droplet radius from the GIFT analysis value matched adequately with the geometric calculation values; within the boundary of ±0.3 nm experimental error.

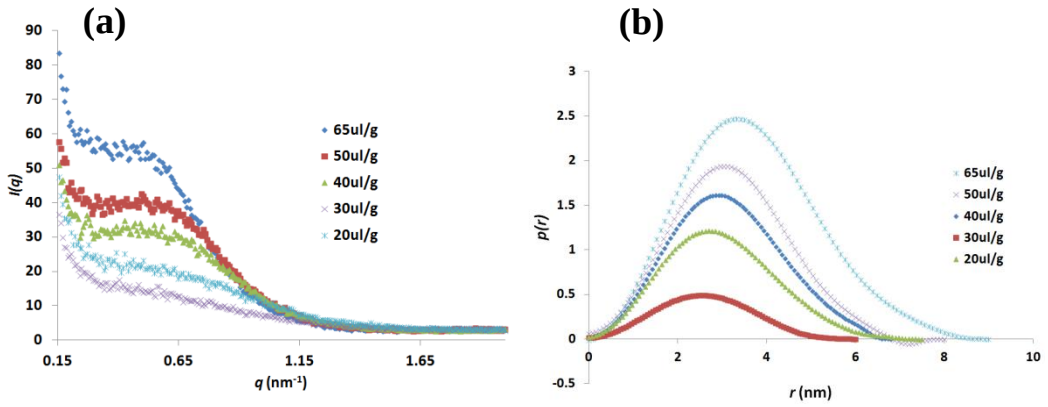

Figure 4.38 Droplet size measurement obtained from SAXS and GIFT analysis:(a) Scattering function *I(q)* Vs *q*; (b) pair distance distribution function *p(r) vs r*

From Figure 4.38, larger droplet sizes are observed from an increase in the volume of dispersed phase. The specifics are displayed in Table 4.9. Free water is expected to be available in the droplets with dispersed phases greater than 50 µl/g. This explains the appearance of the hydrates from larger droplets, owing to the freely moving water molecules that are available for DPA bonding.

Table 4. 9 Droplet size calculation from both GIFT analysis and geometric estimation.

Dispersed phase /µl g^{-1}	20	30	40	50	65
Mean $r_{c(geometric)}$/nm	3.34	3.52	3.7	3.88	4.14
Mean $r_{c(gift)}$/nm	3.29	3.55	3.73	3.98	4.36
Mean $V_{c\,(gift)}$/nm^3	149.4	187.4	217.5	263.3	384.0
Approx. No. of droplets in the system (x 10^{17})	12.6	10.5	9.55	8.28	6.04
Approx. Mean no. of H_2O molecules per droplet (x 10^2)	5.33	9.52	14.01	20.2	36
Approx. Mean no. of Triton X-114 molecules per droplet (x 10^2)	2.68	3.19	3.52	4.06	5.57
Approx. Mean H_2O can be taken by Triton X-114* per droplet (x 10^3)	1.42	1.69	1.87	2.15	2.95
Theoretical fraction of H_2O can be bound to Triton X-114	2.8	1.8	1.4	1.1	0.8

The average number of DPA molecules at different microemulsion composition was also estimated to provide an insight into the system. When the average number of DPA molecules was < 0.8–1 per droplet, crystallisation was not observed. 1–4 DPA molecules per droplet tended to produce the anhydrous salt form I (expected to be the monoanion sodium salt form NaDPA). Exceeding 4-5 molecules, a potassium salt hydrate, $[(dipicH)(dipicH_2)]K{\bullet}3H_2O$, was observed. Similar to the AOT microemulsion systems, the increase in the number of DPA

molecules per droplet led to an increase in the ratio of DPA: impurity ion. Combined with an increase in the free water pool within the droplets, the potassium salt hydrate form, [(dipicH)(dipicH_2)]K•3H_2O, which contains an anion and a neutral molecule was obtained.

Table 4.10 Estimation of DPA molecules per droplet at various microemulsion compositions.

Dispersed phase /µl g^{-1}		20	30	40	50	65
Mean $r_{c(gift)}$/nm		3.29	3.55	3.73	3.98	4.36
No. of droplets in the system (x 10^{17})		12.6	10.5	9.55	8.28	6.04
Mean no. of DPA molecules per droplet	16 mg/ml	0.9	1.6	2.4	3.5	6.2
	12 mg/ml	0.7	1.2	1.8	2.6	4.7
	10 mg/ml	0.6	1.0	1.5	2.2	3.9
	8 mg/ml	0.5	0.8	1.2	1.7	3.1
	2 mg/ml	0.1	0.2	0.3	0.4	0.8

4.4.2.5 Methanol/Triton X-100+1-hexanol/cyclohexane system

Due to alkali metal participation being observed in the previous systems, methanol, also a polar solvent, was used as a replacement of water to minimise/eliminate this problem. However, two forms were still obtained at different microemulsion compositions; the anhydrous needle form I, NaDPA, from smaller droplet samples and a new form, later confirmed as the methanol solvate of sodium dipicolinate, $C_{14}H_{11}N_2NaO_8$ • 0.5CH_3OH, crystallising at larger droplet sizes. The methanol sodium salt of DPA desolvates ~150 ℃ onwards with complete crystallinity lost at 200 ℃. This process is illustrated in Figure 4.39.

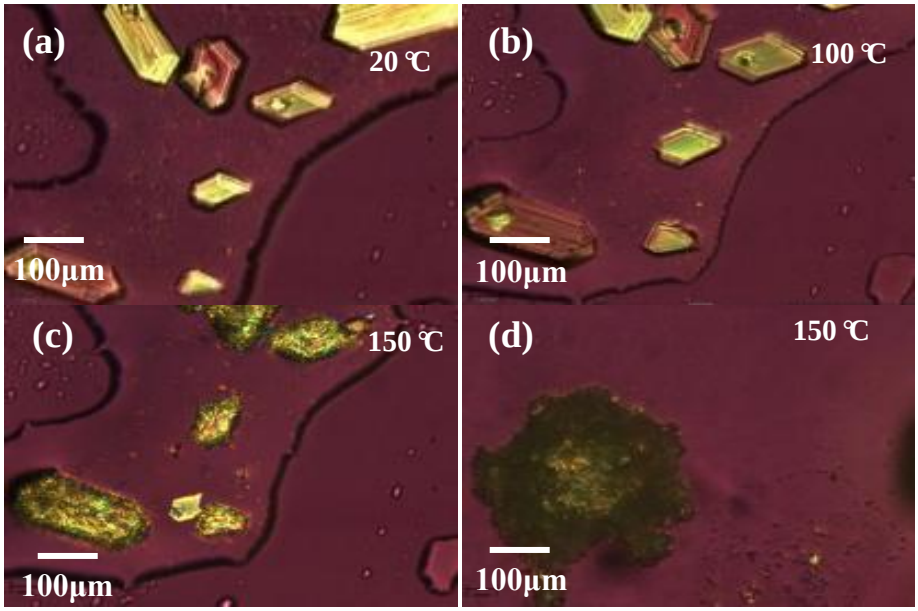

Figure 4.39 Desolvation process of the methanol solvate of sodium dipicolinate.

Figure 4.40 is the composition chart, where the concentration of the DPA solutions is plotted against the dispersed phase volume.

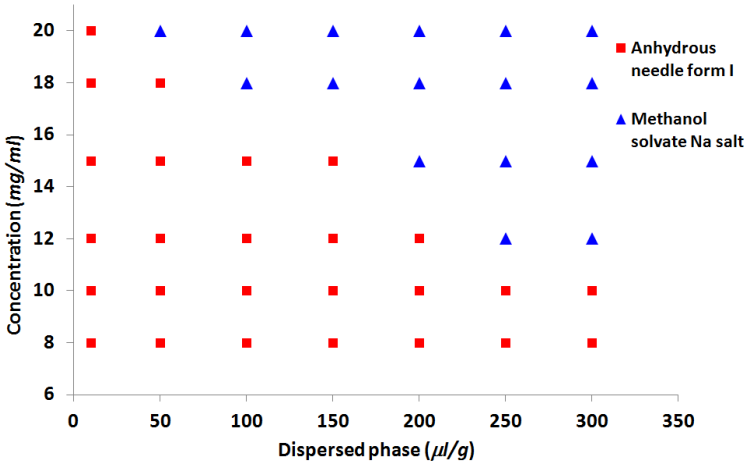

Figure 4.40 Variation in crystallisation outcome with the microemulsion composition

4.4.2.5.1 Structural Study

The crystal structure of the methanol solvate of sodium dipicolinate form is shown in Figure 4.41, where the unit cell is made of 4 asymmetric units with each of the asymmetric units being comprised of 1 dipicolinic acid, 1 dipicolinate, 1 sodium ion and ½ a methanol molecule (shared with the neighbouring unit). These 4 asymmetric units are arranged into 2 layers and each layer contains 2 units which are linked via Na…O bonds to form a binuclear block. Such Na…O bridges also exist between the layers and construct a Zig-Zag Na…O framework (4 Na with 8 O) with each Na being 7-coordinated. Such a Na…O network is a rare occurrence with < 50 cases present in the CSD. The detailed crystal structural information is included in Appendix 7.

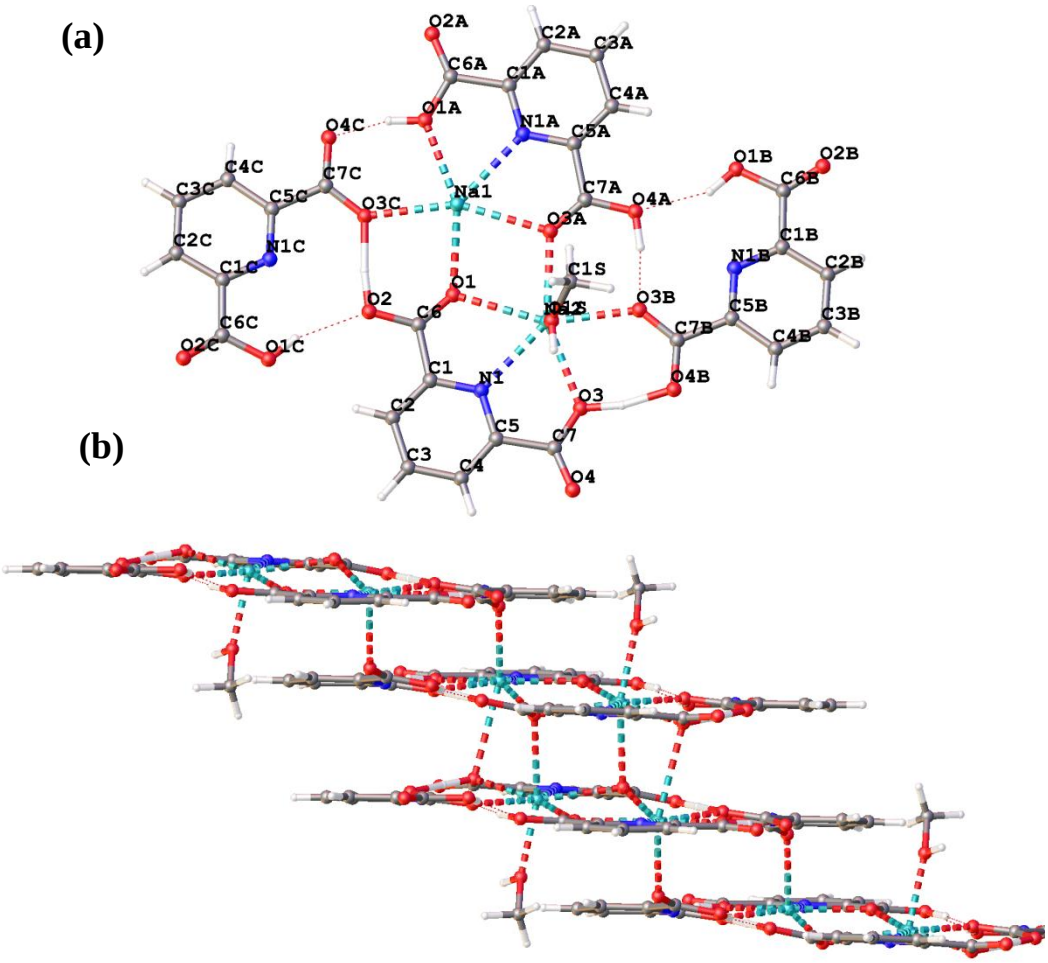

Figure 4.41 Crystal structure of the methanol solvate of sodium dipicolinate: (a) Dimer unit; (b) complete framework

The description of this network was finally completed with the assistance of CSD searches. From the initial inspection of the structure, it was hard to determine the coordination number of Na (i.e. 5, 6 or 7) due to the large variations in the Na-O bond distances and where to define the cut-off distance of a Na…O interaction.

Table 4.11 Na…O bond length in the methanol solvate of DPA sodium salt structure

		Å			Å
Na1	O1	2.375	Na2	O3A	2.336
	O1A	2.386		O1S	2.348
	O3C	2.416		O3	2.389
	N1A	2.496		O3B	2.400
	O3A	2.503		N1	2.451
	O2C	2.578		O1	2.594
	O3	3.007		O1(2)	2.675

Depending on the charge and the coordination number (CN) of the species, the average Na…O distance can vary by *ca.* 0.5 Å. There are several parameters that can quantify this variation; including the crystal and ionic radii defined by Pauling[29] and Fumi and Tosi[30] but updated by Shannon in 1976[31], considered to be the most accurate data set and thus most commonly used. Using this criterion to distinguish an actual metal-ligand interaction from other contacts, the inter-planar Na1…O3 of 3.007 Å in this structure is *ca.* 0.2 Å outside the crystal radius range (2.34-2.81 Å where 2.34 Å is for a Na with 4 ligands and O^{2-} with a CN of 2, and 2.81 Å for 12 coordinated Na and 8 coordinated O^{2-}) so should be discarded. In addition, Na1…O2C, Na2…O1, and Na2…O1(2) distances are 2.578 Å, 2.594 Å and 2.675 Å, respectively. These are slightly longer than the average values.

Table 4.12 Na and O radii, and Na…O bond length defined by VDW, Covalent bond, Ionic radii and crystal radii.

	Na /Å	O /Å	Na…O /Å
VDW	2.27	1.52	3.79
Covalent	1.66	0.68	2.34
Ionic radii	0.99-1.39	1.35-1.42	2.34-2.81
Crystal radii	1.13-1.53	1.21-1.28	2.34-2.81

However, solely using the ionic/crystal radii to assess the bond/intermolecular/VDWs interactions can be misleading and thus miss important features of the structure being discounted. As a consequence, CSD searches to define a typical bond length of Na…O measured by X-ray/Neutron diffraction and to obtain a statistical evaluation of the Na…O interactions in this structure with respect to the reported structures was carried out.

4.4.2.5.2 Database Study

In recent years, employing a data mining method to study the distance, geometry and local environment[32-37] of metal-ligand interactions has attracted many interests. The common metals, include Na, Mg, K, Ca, Mn, Fe, Co, Ni, Cu, Cd, Zn have been investigated so far as many of these metals can form complexes with bio-macromolecules and thus offer a wide range of functionalities[38], such as providing structural rigidity, stability, and UV/thermal resistance. Harding[33] Zheng[34] and Kuppuraj[32] reported Na…O distances obtained from CSD searches to be 2.42(9) Å for any Na…O, 2.40(10) Å for Na…$O_{carboxylate}$, 2.41(9) Å for

Na…OH_2, 2.41(9) Å for Na…OH_2/2.46(14) for Na…O=C, and 2.30±0.13(38) Å for Na with a CN of 6 and O with a CN of 3, respectively. However, discrepancies were noticed among these literature values which might be due to the following factors: 1) the searches were performed with an older version of the CSD, and the total number of structures in the CSD has significantly increased during the last decade; 2) various search criteria were adopted, for example, a R factor of 0.065 was used in Harding's study, which is no longer applicable; the cut-off distances were 2.70 Å for Harding[33], 3.00 Å for Zheng[34], and the CSD default radii used by Kuppuraj[32]; 3) the fragment used in the search can also have a huge impact, for example, both Harding and Zheng grouped the metals depending on the coordinating atom but did not investigate the influence of the metal CN. Additionally, other factors such as the CN of the ligand and the charge of the metal/ligand[32] may also contribute to the M-L interaction distance and geometry.

Preliminary searches have been performed to investigate any change in the coordination sphere limit applied to the literature searches. CSD version 5.33 (Nov 2011 with 586977 structures) and ConQuest version 1.14 were used to search for complexes containing Na…O interactions (any) satisfying the following conditions: 1) R factor ≤ 0.05; 2) No disorder, powder and error were allowed in the structures; 3) ≥ 25 CSD structures are available for statistical analysis.

Table 4.13 shows the number of overall Na containing structures (hits), the Na…O hits (Na…O interaction existing in the structures), observations (the number of Na…O interactions), mean bond length with S.E.(standard error), sample S.D.(standard deviation), and the observed distance range (inspected from the histogram of the data) for the Na…O interaction with various CNs.

Table 4.13 The number of hits, number of observed structures, mean bond length and its sample standard deviation and the observed range obtained from Na…O bond searching with various CNs. Structures are refined with R value of < 0.05.

CN of Na (R<0.05)	Na…O				
	Hits	Observations	Mean (S.E) /Å	Sample S.D. /Å	Observed Range /Å
any	1380	8899	2.44(2)	0.13	2.00-3.34
8	126	848	2.57(2)	0.12	2.17-3.21
7	174	1122	2.49(2)	0.14	2.13-3.25
6	760	4737	2.43(1)	0.10	2.09-3.02
5	265	1418	2.38(1)	0.09	2.03-2.87
4	151	627	2.38(2)	0.13	2.16-2.99
3	231	773	2.42(2)	0.12	2.01-2.99
2	477	1456	2.45(1)	0.12	2.12-2.98
1	441	810	2.41(1)	0.10	2.15-2.87

Na…O bonds are the predominant interaction in Na containing structures (for a total of 2207 Na containing structures, 1380 have Na…O interactions). Despite the fact that the CN of Na ion can vary from 1 to 10+, nearly half of these structures are six-coordinated. CNs of 9 and above are not listed since there are too few hits (≤ 25 CSD hits) to be statistically valid.

Compared to the literature values, a slightly longer mean Na…O bond distance of 2.44(2) Å was observed for any Na…O interaction (i.e. no CN restriction). The histogram shown in Figure 4.42, shows most of the Na…O interactions were in the range of 2.20-2.88 Å, while there was a substantial number of Na…O bonds below 2.20 Å and above 2.88 Å. The mean bond distance and the observed range varied with the CN, where values of 7 and 8 had particularly long bonds and CNs of 4 and 5 were much shorter. This was expected as higher metal CN typically prefer longer metal-ligand distances to minimise the repulsion between the ligands[39]. When focusing only on the Na…O interactions with CN 7, the vast majority of them were within 2.18-3.03 Å, with an elongated mean bond length of 2.49(2) Å. In our structure, the inter-planar Na1…O3 is still in the observed range for a 7 coordinated Na…O bond as are the other three Na…O bonds. Consequently it is reasonable to consider that the structure is comprised of a 7-coordinated binuclear Na…O network.

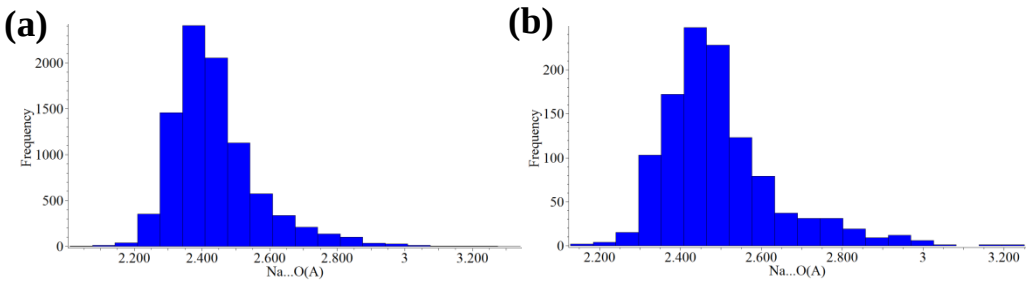

Figure 4.42 Histograms of the bond length for (a) any Na…O interaction and (b) Na…O with Na 7 coordinated

The prelimimary search considered the metal CN but the properties/neighbouring groups of the ligand can also affect the bond distance. In this structure, the M-L interactions we are concerned with are either Na…O=C or Na…O-$H_{(non\text{-}wat)}$. As a consequence, a search for an overall structure and CN of 7 case was performed (Table 4.14). Na…O=C with no CN restriction exihibited a much shorter mean distance of 2.40(1) Å while Na…O-$H_{(non\text{-}wat)}$ was the same as the average Na…O distance. For CN = 7, few hits were observed and the Na…O=C was elongated by ~0.1 Å with Na…O-$H_{(non\text{-}wat)}$ of 0.02 Å. The range of the interaction distances can be visualised (Figure 4.43). For the Na…O=C bond, the most common distances lay ~2.10–2.70 Å with < 5% of the bonds in the range of 2.70–2.95 Å. A similar trend was observed for the Na…O-$H_{(non\text{-}wat)}$ distance, but here overall interactions can exist up to 3 Å.

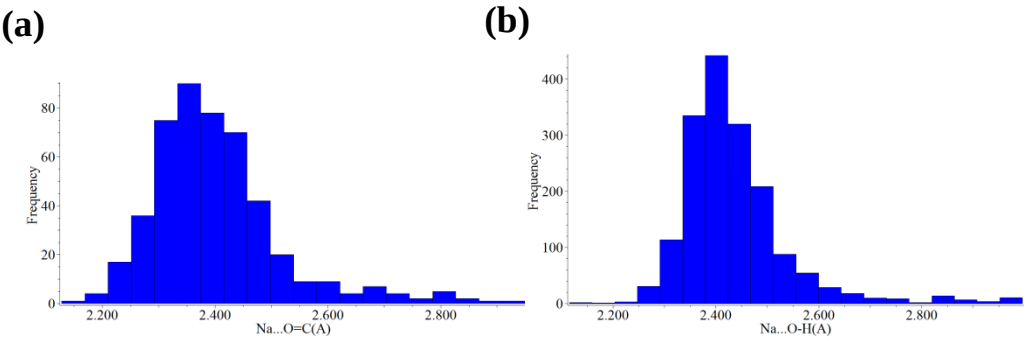

Figure 4.43 Histograms of a) Na…O=C bond length and b) Na…O-H bond length

Table 4.14 Comparison of Na…O bond parameters with the literature data

	CN	Ligand	R factor	No. of Hits	No. of observations	Mean Na…O (Å)	Sample S.D.	Range for evaluation (Å)
Harding 2002	any	O	0.065	/	4315	2.42(9)	/	2.01-2.70
		OH_2			1149	2.41(9)		2.13-2.76
		$O_{carboxylate}$			178	2.41(10)		2.23-2.74
This study	any	O	0.05	1380	8899	2.44(1)	0.13	2.00-3.34
		O=C		216	477	2.40(1)	0.12	2.13-2.95
		$OH_{(non-wat)}$		451	1704	2.44(1)	0.11	2.12-3.00
	7	O		174	1122	2.49(2)	0.14	2.13-3.25
		O=C		26	64	2.50(3)	0.17	/
		$OH_{(non-wat)}$		30	69	2.46(1)	0.11	/
Zheng 2008	any	O=C	0.05	/	8398	2.46(14)	/	≤ 3.0
		OH_2			1917	2.41(9)		≤ 3.0
Kuppuraj	6	0	0.05	/	/	2.30(38)	0.13	/

Statistically all of the four interactions of interest in the methanol solvate of the DPA Na salt were assigned to be real M-L interactions and therefore it can be confirmed to exist as a 7 coordinated binuclear complex. Structurally speaking, such a binuclear Na structure is an unusual occurrence. Without a restriction on the CN, only 606 structures exhibit binuclear Na…X features (27% of the total Na containing structures) in the database with 606 of these structures, 508 of them are Na…O networked. However, limiting the CN to be 7, only 14 structures were found to have binuclear bridging via a Na…O bond. For this reason, the ligand molecule, dipicolinate, often multidentate, has been investigated. There are 802 structures containing metal-dipicolinate ligand interactions in the entire database, with most being tridentate (734 structures). However, only 31 of these structures comprise a 7 coordinated binuclear metal centre with M…O bridges (<5%) with the metals typically having a valence number of 2 or above (Ca, Mn, Ti, Cd, Sn, and Bi).

4.4.2.5.3 Visualisation of the structure

In this methanol solvate of sodium dipicolinate structure, each Na has a distorted pentagonal bipyramidal geometry with two types of chemical environments surrounding the central Na, as illustrated in Figure 4.44. Since the complete framework contains 2 sets of each Na centre, these 4 distorted pentagonal bipyramids share an O-O edge with each other as Figure 4.44 reveals also in addition to links between the layers of dipicolinate/DPA together. Such a network

did not exist for previously reported structures comprising both dipicolinate/DPA ligands and binuclear CN7 metal centres to date.

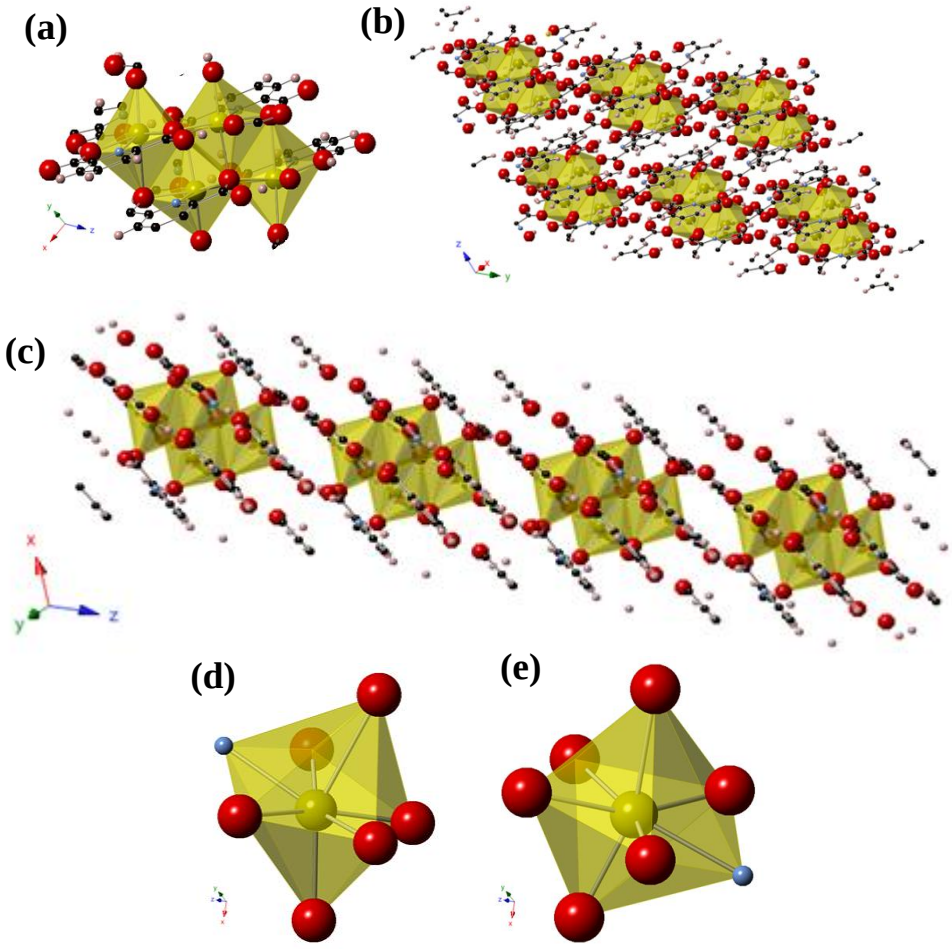

Figure 4.44 Layer view of the methanol solvate of sodium dipicolinate with the 7-coordianted Na plotted in the centre of the distorted pentagonal bipyramid (a-c) and (d-e) pentagon bipyramids with Na centres. Images produced from CrystalMaker®[40]

The formation mechanism of this rare structure is not fully understood. However the hypothesis is that due to the rigid packing geometry of the ligand molecules and their multiple binding sites (carboxylic groups and pyridine nitrogen), Na ions are more likely to be forced into the less favoured 7 coordination position. Such metal-ligand interactions have been observed in many organometallic compounds and even proteins[41]. The solvent molecule, i.e. methanol, can easily occupy pockets created from the organisation of ligands, increasing the packing efficiency, density, and structural rigidity, leaving no voids in the structure for other molecules to access.

4.4.3 Further discussion

The participation of the sodium ion into the DPA lattice structure was not expected and has been a persistent problem in the systems reported so far. The likely sources of sodium in this microemulsion system is thought to be 1) from the surfactant e.g. the AOT counterion or an impurity in the Span 80 from the unfiltered precursor; 2) from further impurities in the system e.g. from UHP water, cyclohexane, or purchased dipicolinic acid. Replacing either the surfactant or cosurfactant did not resolve the issue, with various tests revealing only trace amounts of sodium present in the system (e.g. < 1 ppm for UHP water, < 5ppm for cyclohexane, and 99% pure DPA). Thus impurity participation from the surfactant and/or cosurfactant is the most likely source of the sodium.

Initially the ability of DPA to chelate metals was expected to be irrelevant to the process of crystallisation from microemulsions. However considering the use and applications of DPA, it becomes clear that: 1) biologically pyridine carboxylic acids has been used to transport and scavenge metals ions within the body. For instance, very high concentrations of DPA (approx. 15% by dry weight) can be found in bacillus spores to form DPA-Ca(II) complexes that have high thermal and UV stability to defend against damage by nucleic acid and thus increasing the spore survival rate[42]; 2) chromatographically it has been used in many eluent formulations to detect the existence of small amounts of ions such as Mn, Co, Ni, La, Fe and U[43]. As a consequence, when crystallisation was occurring under confined conditions on such a small scale, the impurities might be expected to become significantly incorporated in the outcome.

Additionally DPA itself can undergo self-association to various ionic species depending on the pK_a values, as shown in Figure 4.45. Therefore variations in the pH of the solution,[25] e.g. by the addition of an acid or base, can alter the pK_a and hence influence the anionic form adopted by DPA.

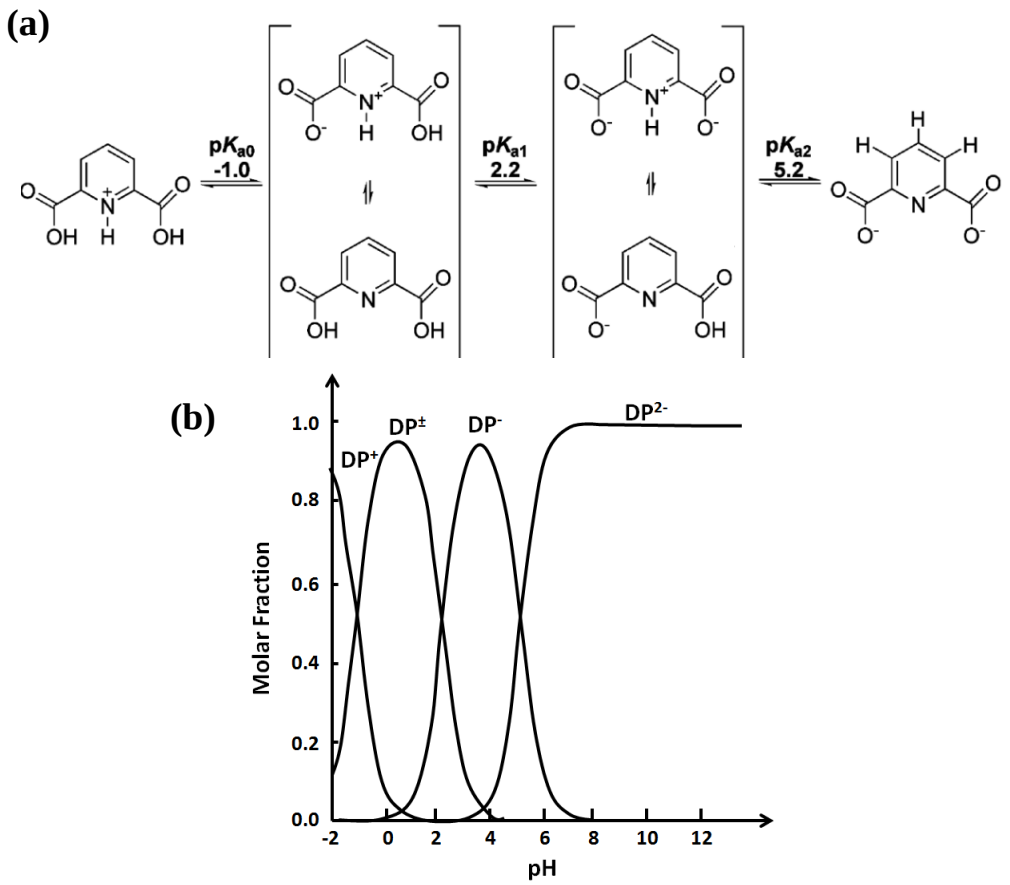

Figure 4.45[25, 26] Self association of DPA forms with different pK_a values (a) and the pH dependent ionic form of DPA (b). (Reproduced with permission from ref 24, Copyright © 2000, Elsevier)

Furthermore, the pH shift of microemulsions could explain the observations in the Triton X-100 system, where (Chapter 4.4.2.3) smaller droplet sizes and lower concentrations yielded the dianionic form that normally appear from pH 7 upwards in bulk solution. The monoanionic form that was expected to dominate in the pH 2–6 range was only observed at larger droplet sizes and higher concentrations, despite the pH of the dispersed phase (before microemulsion preparation) being in the range of 1.69–2, which should favour the zwitterion form. This is because at smaller droplet sizes, a greater level of perturbation of the water molecules occurred due to increased contact with the surfactant. Thus this may be the cause of the pH shift towards neutrality, promoting the dianionic form. At larger droplet sizes, more water molecules ensures the existence of a free central water pool, hence the pH level is perturbed less, so the acidic favoured monoanionic form is observed. Such a decrease in pH with increasing dispersed aqueous phase was also demonstrated by Mcllwaine *et. al.*'s study[27] via acid-autocatalytic bromated-sulfide reactions using water/Triton X-100/toluene

microemulsions. Both the initial and final pH values of the microemulsion (before and after the reaction) were higher than the aqueous solutions used as the control of experiments.

Additionally, it has been proven by Crans *et. al.*[26] that the deprotonated dipicolinate can penetrate negatively charged lipid interfaces, i.e. they can travel through the charged hydrophilic core of AOT into its hydrophobic tail group and reside in the more hydrophobic interface. As a result, any free sodium that is in contact with the dipicolinates with might be embedded in the structure. Therefore it would be worthwhile to investigate the pH and pK_a values of the bulk DPA solutions in order to possibly predict the behaviour of DPA in the microemulsions. Further work regarding the pH issue has been performed, and is reported in Chapter 5.

4.5 Conclusions

Three DPA forms, namely anhydrous, monohydrate and dihydrate, were obtained from the bulk solutions. Regarding the stability of each form, the dihydrate can rapidly transform to the anhydrous form in air or to the monohydrate in solution (~ a few hours). It is therefore the least stable form of the three. The stability of the anhydrous form and monohydrate is interchangeable, since the monohydrate can dehydrate into the anhydrous form if left in air (~1–2 months) and the anhydrous form can slowly transform into the monohydrate in aqueous solution (≥ 3 months).

The crystals obtained from the microemulsions, were not any of these three forms. Instead the DPA crystallised as sodium or potassium salts, raising suspicion of the source of the Na/K. Initially AOT, containing one Na ion per molecule, was used as a surfactant for microemulsion preparation. Consequently, AOT was thought to be the origin of the sodium, as the UHP water used during the experiments was found to contain a negligible amount of Na (0.997 ppm). Subsequently, Span 80 and Brij 30, two non-ionic surfactants, were used to replace AOT. However, only an anhydrous fluffy needle form was crystallised from the Span 80/Brij 30 system. This had a very similar FTIR, PXRD and ion analysis result to the sodium salt

crystallised from AOT. This was not expected as the DPA used in the experiment was 98% pure, the Span 80/Brij 30 system was non-ionic and the bulk crystallisation in aqueous solution never produced any sodium salts. However, Span 80 uses Na containing precursors, thus residual sodium might arise from this, hence a second non-ionic system; Triton X-100/1-hexanol was employed for clarification. Surprisingly, two different needle forms were obtained (NaDPA and Na_2DPA), although both are accepted to be anhydrous sodium salts. These differing behaviours were attributed to the variation in the pH state, affected by the droplet size of the reversed microemulsions. To eliminate/minimise the contribution of cosurfactants to the source of the ion impurities, a third non-ionic surfactant, Triton X-114, with a very similar structure to Triton X-100 but which can form stable microemulsions without cosurfactant was employed. Here, the anhydrous sodium salt form and a potassium hydrated salt form were yielded. For further investigation, a final system, replacing the aqueous inner phase with methanol was studied. Again this produced the anhydrous sodium salt form and a new methanol solvate of sodium dipicolinate. This new form contained a very rare 7 coordinated binuclear sodium centre, sharing an O-O bond with the next binuclear centre and forming a network based on 4 edge-sharing pentagonal bipyramids.

In the AOT system, at larger droplet sizes and high DPA concentrations, sodium dipicolinate dipicolinic acid trihydrate was obtained from a one step crystallisation. Similarly in the TX-114 system, potassium dipicolinate dipicolinic acid trihydrate was also obtained at larger droplets. The trihydrate formed possibly due to the large number of ‘free water molecules’ in the hydrophilic core.

Given time for further investigation a more detailed study on the effect of water pool size upon the form of the dipicolinic anion would provide additional insight into the mechanism; however this is beyond the scope of this work. Additionally, obtaining a crystal structure of the anhydrous fluffy needles forms would provide further insight. Also the effect of microemulsions on the dipicolinic acid anion forms at different water pool sizes would also be very intriguing. These planning for future work will be discussed in Chapter 6.2.

4.6 References

1. C. E. Nicholson, C. Chen, B. Mendis and S. J. Cooper, *Cryst Growth Des*, 2011, **11**, 363-366.
2. S. Udo., *J. Agr. Chem. Soc. Jpn.*, 1936, **12**, 386.
3. K. E. Edgecombe, D. F. Weaver and V. H. Smith-Jr, *Can. J. Chem.*, 1994, **72**, 1388-1403.
4. B. Das and J. B. Baruah, *Cryst Growth Des*, 2011, **11**, 278-286.
5. G. Smith, K. E. Baldry, K. A. Byriel and C. H. L. Kennard, *Aust. J. Chem.*, 1997, **50**, 727-736.
6. F. Takusagawa, F. Hirotsu and A. Shimada, *Bull. Chem. Soc. Jpn.*, 1973, **46**, 2020-2027.
7. M. C. Grossel, A. N. Dwyer, M. B. Hursthouse and J. B. Orton, *CrystEngComm*, 2007, **9**, 207-210.
8. V. Carranza Tellez, B. Sanchez Gaytan, S. Bernes and E. Gonzalez Vergara, *Acta Crystallogr C*, 2002, **58**, O228-230.
9. F. H. Allen, *Acta Cryst. B*, 2002, **58**, 380-388.
10. J. Chisholm, E. Pidcock, J. van de Streek, L. Infantes, S. Motherwell and F. H. Allen, *CrystEngComm*, 2006, **8**, 11-28.
11. A. R. Kennedy, C. A. Morrison, N. E. B. Briggs and W. Arbuckle, *Cryst Growth Des*, 2011, **11**, 1821-1834.
12. C. R. Groom, T. S. G. Olsson, J. W. Liebeschuetz, D. A. Bardwell, I. J. Bruno and F. H. Allen, in *Bioisosteres in Medicinal Chemistry*, Wiley-VCH Verlag GmbH & Co. KGaA, 2012, pp. 75-101.
13. S. L. Childs, P. A. Wood, N. r. Rodríguez-Hornedo, L. S. Reddy and K. I. Hardcastle, *Cryst Growth Des*, 2009, **9**, 1869-1888.
14. O. V. Dolomanov, L. J. Bourhis, R. J. Gildea, J. A. K. Howard and H. Puschmann, *J. Appl. Crystallogr.*, 2009, **42**, 339-341.
15. K. McCann and J. Laane, *J. Mol. Struct.*, 2008, **890**, 346-358.
16. L. Kong, P. Setlow and Y.-q. Li, *Analyst*, 2012, **137**, 3683-3689.
17. S. Santra, B. Das and J. Baruah, *J Chem Crystallogr*, 2011, **41**, 1981-1987.
18. K. Browning, K. A. Abboud and G. J. Palenik, *J Chem Crystallogr*, 1995, **25**, 851-855.
19. P. Lainé, A. Gourdon and J.-P. Launay, *Inorg. Chem.*, 1995, **34**, 5129-5137.
20. S. P. Moulik and B. K. Paul, *Adv. Colloid Interface Sci.*, 1998, **78**, 99-195.
21. B. Farago, D. Richter, J. S. Huang, S. A. Safran and S. T. Milner, *Phys. Rev. Lett.*, 1990, **65**, 3348-3351.
22. C. L. Kitchens, D. P. Bossev and C. B. Roberts, *J. Phys. Chem. B*, 2006, **110**, 20392-20400.
23. D.-M. Zhu, X. Wu and Z. A. Schelly, *J. Phys. Chem.*, 1992, **96**, 7121-7126.
24. D. Sarkar, K. C. Khilar, G. Begum and P. V. SubbaRao, *Colloids Surf., A*, 2005, **268**, 73-77.
25. F. Peral and E. Gallego, *Spectrochim. Acta, A*, 2000, **56**, 2149-2155.
26. D. C. Crans, A. M. Trujillo, S. Bonetti, C. D. Rithner, B. Baruah and N. E. Levinger, *The Journal of organic chemistry*, 2008, **73**, 9633-9640.
27. R. E. McIlwaine, H. Fenton, S. K. Scott and A. F. Taylor, *J. Phys. Chem. C.*, 2008, **112**, 2499-2505.
28. M. A. Sedgwick, D. C. Crans and N. E. Levinger, *Langmuir*, 2009, **25**, 5496-5503.
29. L. Pauling, *The nature of the chemical bond*, Cornell University Press, Ithaca, New York, 1960.
30. F. G. Fumi and M. P. Tosi, *J. Phys. Chem. Solids*, 1964, **25**, 31-43.
31. R. D. Shannon, *Acta Cryst. A*, 1976, **32**, 751-767.

32. M. D. G. Kuppuraj, and C. Lim, *J. Phys. Chem. B*, 2009, **113**, 2952-2960.
33. M. M. Harding, *Acta Cryst. D*, 2002, **58**, 872-874.
34. M. C. H. Zheng, P. Lasota, L. Lebioda, and W. Minor, *J. Inorg. Biochem.*, 2008, **102**, 1765-1766.
35. M. M. Harding, *Acta Cryst. D*, 2001, **57**, 401-411.
36. M. M. Harding, *Acta Cryst. D*, 1999, **55**, 1432-1443.
37. R. K. Hocking and T. Hambley, *Organometallics*, 2007, **26**, 2815-2823.
38. H. Sigel, *Metal Ions in Biological Systems*, Marcel Dekker, New York, 1974.
39. J. E. Huheey, E. A. Keiter and R. L. Keiter, *Inorganic Chemistry: Principles of Structure and ReactiVity*, 4th ed edn., Harper Collins, New York, 1993.
40. *CrystalMaker: a crystal and molecular structures program for Mac and Windows*, CrystalMaker Software Ltd, Oxford, England (www.crystalmaker.com).
41. M. M. Harding, *Acta Cryst. D*, 2000, **56**, 857-867.
42. B. Setlow, S. Atluri, R. Kitchel, K. Koziol-Dube and P. Setlow, *J. Bacteriol.*, 2006, **188**, 3740-3747.
43. P. N. Nesterenko and P. Jones, *J. Sep. Sci.*, 2007, **30**, 1773-1793.

Chapter 5 Dipicolinic acid (II)

5.1 Introduction

5.1.1 Previous experimental findings

As described in Chapter 4, the participation of metal cations was unexpected during the crystallisation of DPA from the microemulsion. This was postulated to be a result of the effect of the pH dependent self-association combined with the metal binding ability of DPA. Several measures have been employed to resolve this issue. Firstly, 15-Crown-5, known for its ability to selectively chelate Na and K ions, has been applied to each of the microemulsion components individually. However, this method failed since the binding affinity of 15-Crown-5 was poorer than DPA. Our previous experimental work indicated that upon doping the microemulsion with solid anhydrous DPA, the salt form of DPA was produced. Thus, it was hypothesised that upon filtration, a salt-free DPA microemulsion could be achieved. However, the dilemma with this approach is that any crystals smaller than the pore size of the filter paper would remain within the system, possibly acting as templates or seeds. Consequently, a third attempt was employed; variation of the pH. Metals such as Cu and Zn are documented to favour binding to specific ligands at certain pH levels. For example, the retention efficiency of metal binding for poly(2-acrylamido glycolic acid), a water-soluble polymer used for waste water treatment, largely relies on pH[1]. Hence, the crystallisation of DPA with added hydrochloric acid has been investigated, to ensure a sufficiently acidic environment in the microemulsion (confined) phases.

5.2 Experimental

5.2.1 Bulk experiments

To investigate the outcome of crystallisation under acidic conditions, 2M HCl solution was added to various concentrations of DPA from 2 mg/ml to 18 mg/ml. A given amount of DPA solid was weighed out, followed by the addition of 2M HCl and then sonicated at 70–80 ℃ for ~30 mins to ensure complete dissolution, before adding this to the surfactant solution to make the microemulsion. Sonication at elevated temperature ensured that no nuclei exist in the solutions

before the solution was confined in the microemulsions. To further test the effect of metal cations, NaCl was added to the above solutions at a molar ratio of 1:1, 1:1.5 and 1:2 of NaCl: DPA. Additionally, to illustrate the effect of 2M HCl on pH, methyl red was added to the microemulsions.

5.2.2 Crystallisation from bulk surfactant solutions (non-confined)

0.5% to 20% w/w of surfactants was added to 8–12 mg/ml DPA solutions, both with and without 2M HCl solutions. The mixture was heated to ensure complete dissolution before leaving at room temperature for crystallisation.

5.2.3 Microemulsion preparation

The same method as described in chapter 4 was followed to prepare the microemulsions. However, here the dispersed phase was 2.0 M HCl solution rather than an aqueous solution. The surfactant systems adopted in this study were Triton X-100+1-hexanol and Triton X-114. The concentration of dipicolinic acid was varied between 2–18 mg/ml in 2.0 M HCl solution. The volume of dispersed phase was varied in the range of 50–225 µl of DPA solution per gram of the surfactant/oil component. Either a Triton X-100: 1-hexanol: cyclohexane ratio of 2.2: 1: 2.6 w/w or a Triton X-114: cyclohexane ratio of 3:7 w/w was used in this system.

5.2.3 Phase diagrams

With the addition of 2M HCl, only the Triton systems were able to form stable microemulsions. The surfactant to cosurfactant ratio was fixed at 2:1 w/w as this ratio has been shown to form the largest single phase region[2] for a pure water confined phase. The single phase region in the respective phase diagrams for the HCl acidified aqueous systems was determined and compared with the pure water versions, as shown in Figure 5.1a-d. It is clear that in the Triton X-100+1-hexanol system, 2M HCl has enlarged the single phase microemulsion region. In particular, the high surfactant concentration region now displays microemulsions, compared to nanoemulsions with the pure water dispersed phase. In comparison, the addition of 2M HCl to Triton X-114 system did not significantly change the area of the microemulsion region on the phase diagram.

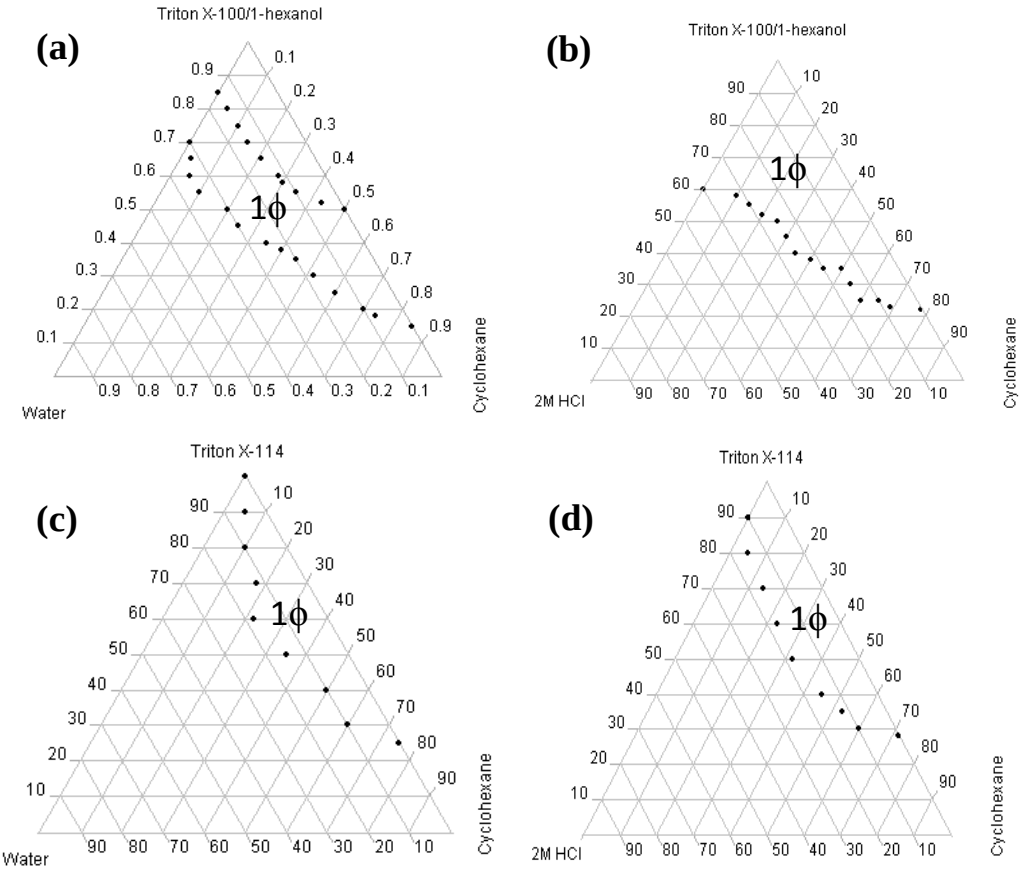

Figure 5.1 Ternary phase diagrams determined from experimental: (a) Water/Triton X-100 +1-hexanol/cyclohexane system; (b) 2M HCl/Triton X-100 +1-hexanol/cyclohexane system; (c) Water/Triton X-114/cyclohexane system; (d) 2M HCl/Triton X-114/cyclohexane system

The impact of HCl depends largely on the type of surfactants[3, 4]. For example, certain zwitterionic surfactants are insensitive to salt/acid addition since they can behave as electroneutral in a range of pHs, thus the phase diagram is not greatly affected. However for other types (both ionic and non-ionic) the effect can be considerable. In this study HCl is postulated to be at the rigid water region that is in close proximity to the interface, which might affect the packing of surfactant molecules and thus the phase diagram.[5]

5.3 Results and Discussion

5.3.1 Bulk experiments

In the bulk experiments, aqueous solutions of DPA produce sodium dipicolinate trihydrates at a molar ratio of 1:2 DPA to NaCl. Upon the addition of 2M HCl solutions, no salt form was observed, even in the presence of NaCl. This suggests the 2M HCl solution may inhibit the binding of metals. Consequently HCl was added during the microemulsion preparation process. With the addition of methyl red indicator, the effect of HCl in acidifying the microemulsion can be observed, as Figure 5.2 shows. Without HCl, no/little colour change was observed as the dispersed phase was increased in the microemulsion. After acidifying, a red/pink colour resulted as the concentration of methyl-red increased within the dispersed phase. This coincided with the previous findings that microemulsions can shift the pH towards neutrality at smaller droplets. Further discussion is detailed in section 5.3.2.6.

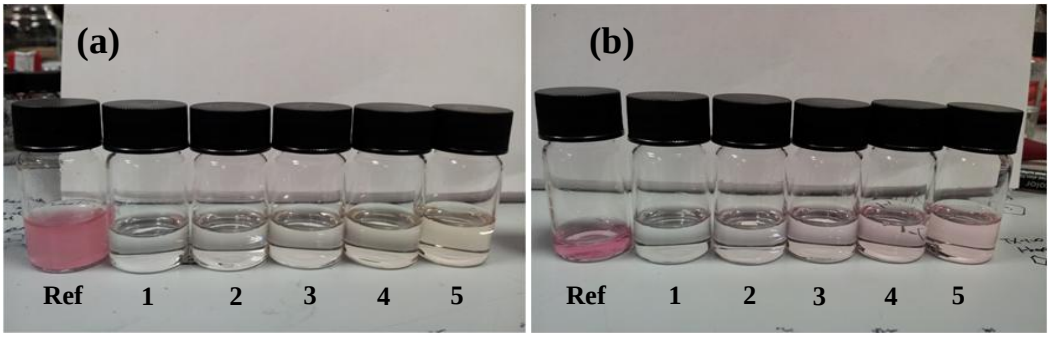

Figure 5.2 Addition of methyl red indicator into microemulsions: (a) 2 mg/ml DPA solution as dispersed phase; (b) 2M HCl solution as dispersed phase. The labels below the vials denote the contents/concentrations of the solutions/microemulsions. **Ref**: reference methyl red indicator solution; **1**: 10 µl reference solution per gram of microemulsion (i.e. 10 µl/g); **2**: 50 µl/g; **3**: 100 µl/g; **4**: 200 µl/g; **5**: 250 µl/g.

5.3.2 Triton X-100/1-hexanol system

As the Triton X-100/1-hexanol system is able to stabilise a microemulsion under acidic conditions, it was chosen for further studies. Other surfactant systems (AOT and Span 80/Brij 30) tend to phase separate within hours of preparation and can only take up a very limited amount of dispersed phase under acidic conditions.

5.3.2.1 Initial observations

Unlike in the previous systems, macroscopic sized crystals were not produced even after 6 months. Consequently TEM was employed to visualise the Triton X-100 sample at the nanoscale. Square shaped nanocrystals of ~30–100 nm in dimension were observed (Figure 5.3), with each nanocrystal being composed of spherical subunits. Despite the HREM images indicating regions of different electron densities, both the FFT and the selected area DPs reveal single crystal-like properties. Such aggregates would typically be expected to be polycrystalline. Instead this remarkable, single crystal-like scattering from the whole particle was observed despite it appears to be composed of small subunits and so these crystals have similar features to iso-oriented crystals/mesocrystals.

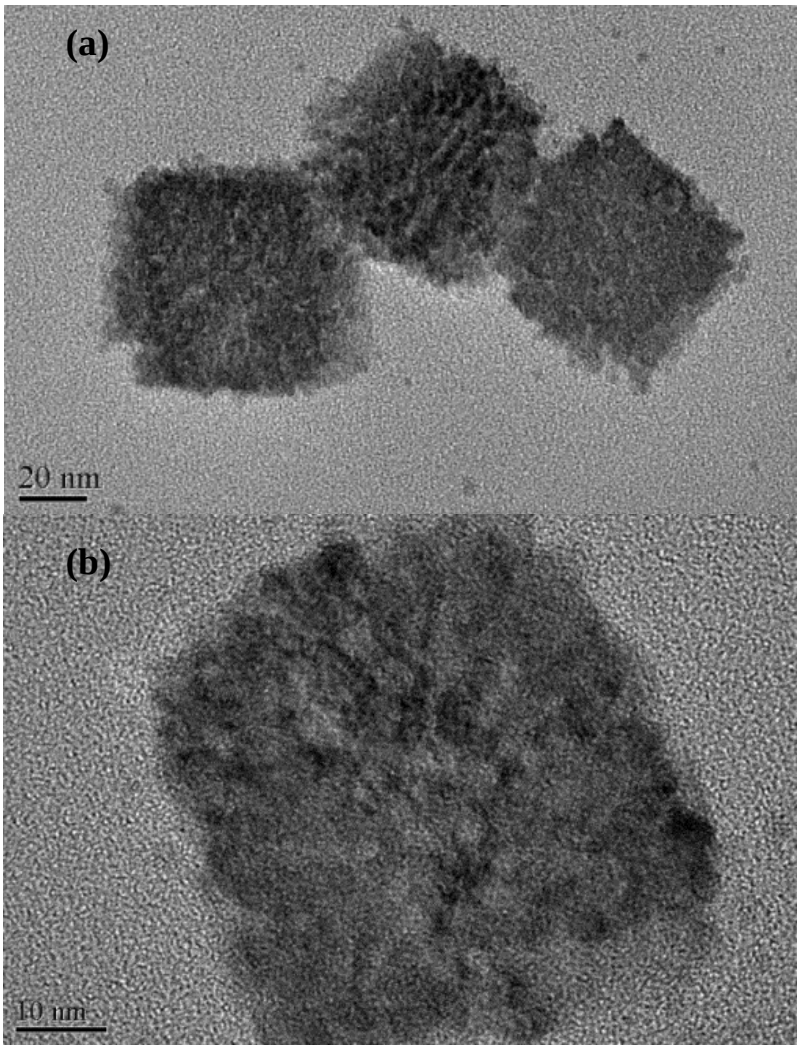

Figure 5.3 An overview of the square shaped nanocrystals: (a) microemulsions prepared from 225 µl/g (of surfactant solution) of 18 mg/ml DPA in 2M HCl solution; (b) microemulsions prepared from 225 µl/g (of surfactant solution) of 12 mg/ml DPA in 2M HCl solution.

5.3.2.2 Indexing

We need to determine whether the participation of alkaline metals in three DPA crystals had been prevented by the addition of an acid. Due to the limited size of these nanocrystals and the difficulty in extracting, ion analysis was impractical. However, EDX, running parallel with the TEM, can characterise the components of these aggregates. Clearly from Figure 5.4, no alkaline metals are present in the sample, which is a good indication of their total elimination. The high intensity for C and Cu comes from the copper coated carbon grid, whilst the chlorine may possibly be due to the residual HCl. Impurities such as Si, S, and Fe were also present but at negligible amounts within the noise of instrument. Given alkaline salts formation could be ruled out, the primary objective became the identification of these square-plate shaped crystals.

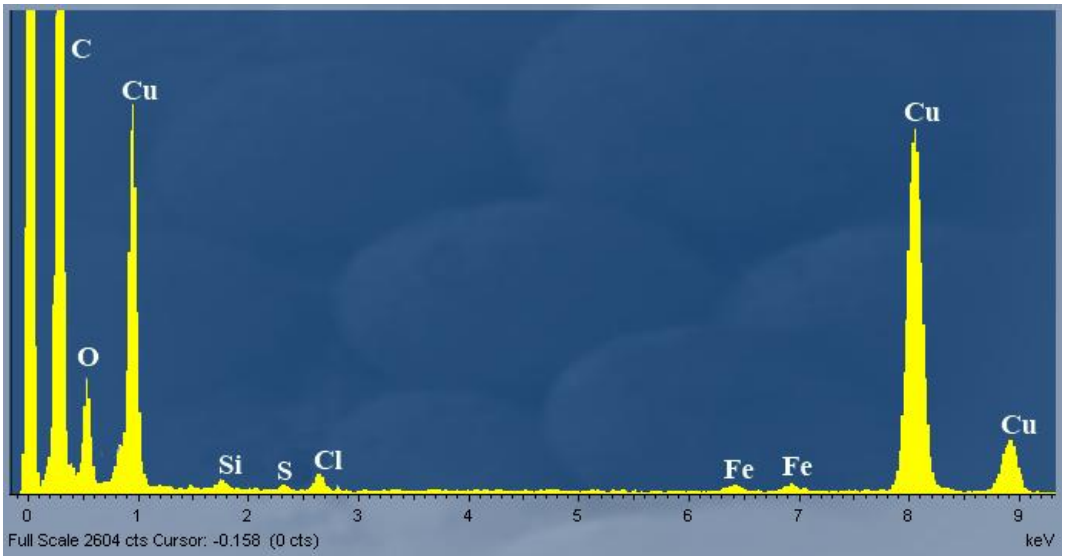

Figure 5.4 EDX spectrum of square-plate nanoaggregates (NAs)

The DP (Figure 5.5) of the 50 nm nanocrystal was indexed and compared with the generated electron diffraction patterns of DPA and the hydrate forms. These nanocrystals were characterised as the monohydrate form due to the good agreement between the DP and the [102] zone axis of the DPA monohydrate and the absence of any good agreement between the DP and the zone axes of the anhydrous DPA or the DPA dihydrate. The different faces of the nanocrystals were thus determined as shown in Figure 5.6a. The slowest growing face with the largest exposure area is determined (101) with both the (010) and $(\bar{2}01)$ growing

at competing speeds. When visualising this plane at the molecular level, the (101) plane does not cut through any of the hydrogen bonds that bridge two DPA molecules together (Figure 5.6b) and hence it would be expected that this would be a slow growing face, since the attachment energy to this face will be lower in magnitude.

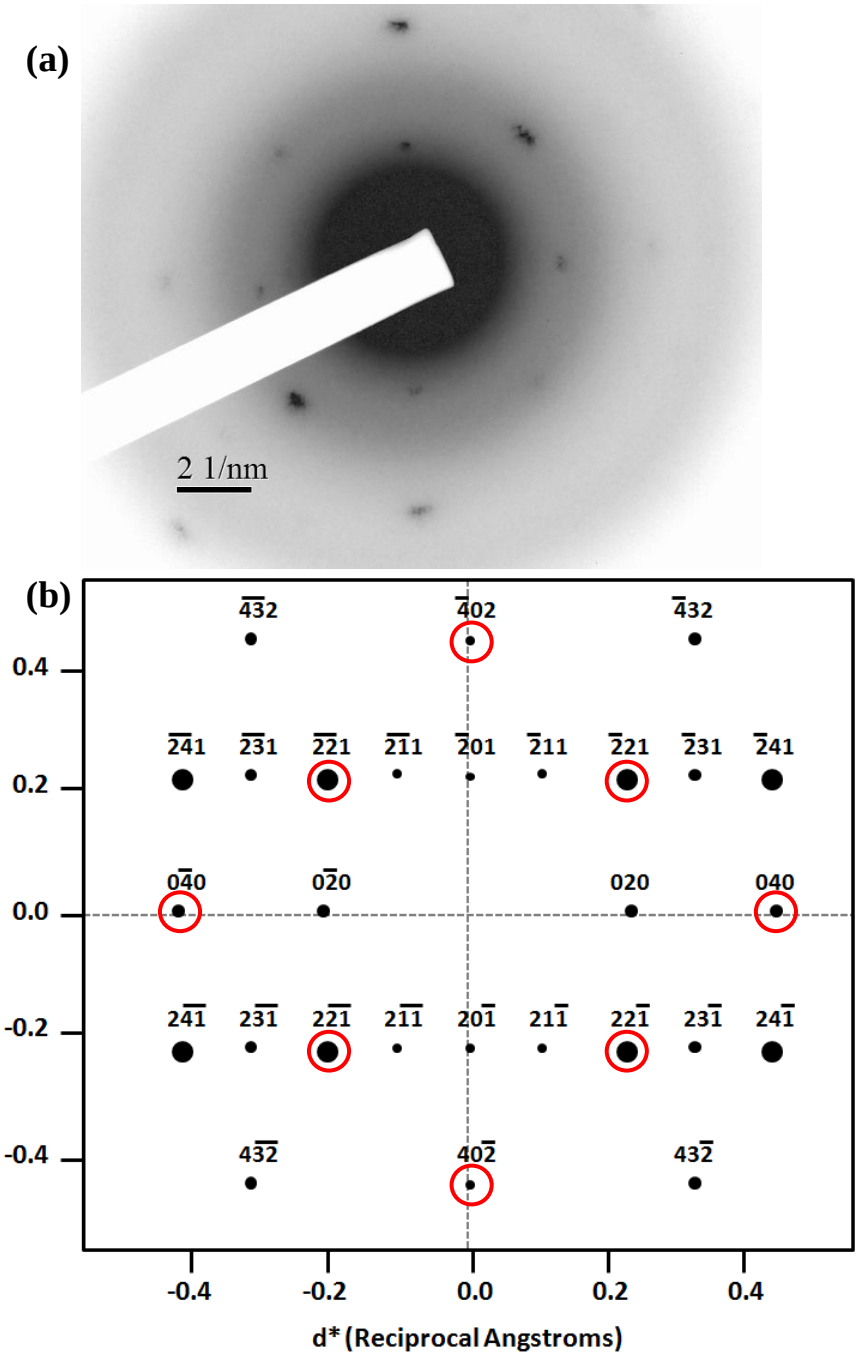

Figure 5.5 DP of (a) the square plate shaped nanocrystal from microemulsions containing 225 µl/g (of surfactant solution) of 18 mg/ml DPA in 2M HCl solution and (b) the generated electron diffraction pattern of DPA monohydrate along [102] zone axis, from *Cerius2*®[6], rotated anticlockwise, i.e.($\bar{2}$01) at vertical axis, by 45 °angle to the DP in (a) and the BF in Figure 5.6 (a).

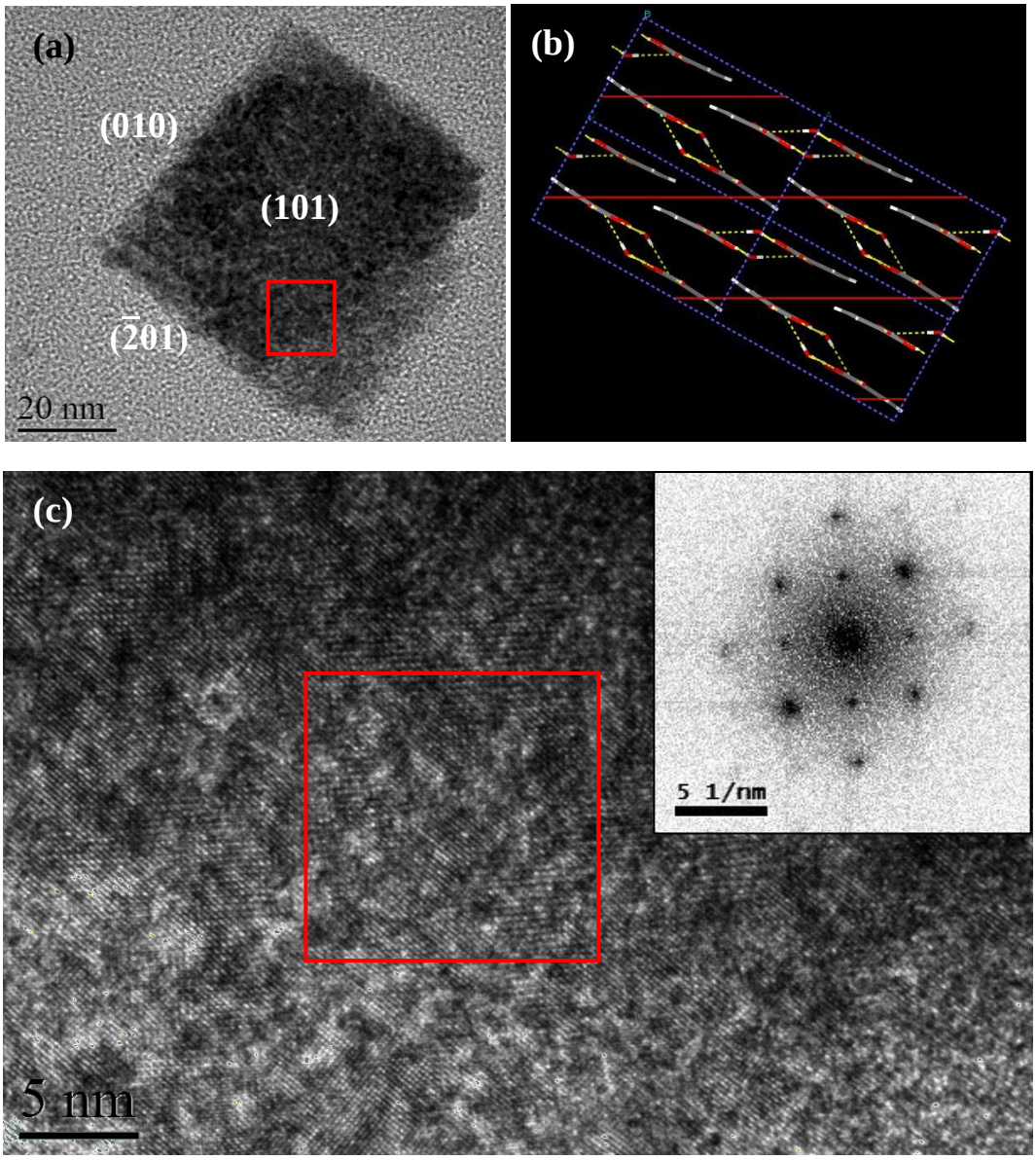

Figure 5.6 Determination of the growing faces and Miller planes: (a) the BF image of the growing faces of an aggregated nanocrystal; (b) Miller plane of (101) at the molecular view, generated in Cerius2[7]; (c) the HREM image of the selected region in (a) and the inset shows the FFT image of the selected area in (c).

5.3.2.3 Effect of dispersed phase variation (SAXS and droplet size calculation)

The crystallisation outcome of this Triton X-100+1-hexanol/cyclohexane microemulsion system is dependent on both the DPA concentrations and the volumes of dispersed phase, as shown in Figure 5.7. Thus the effect of each factor will be discussed separately.

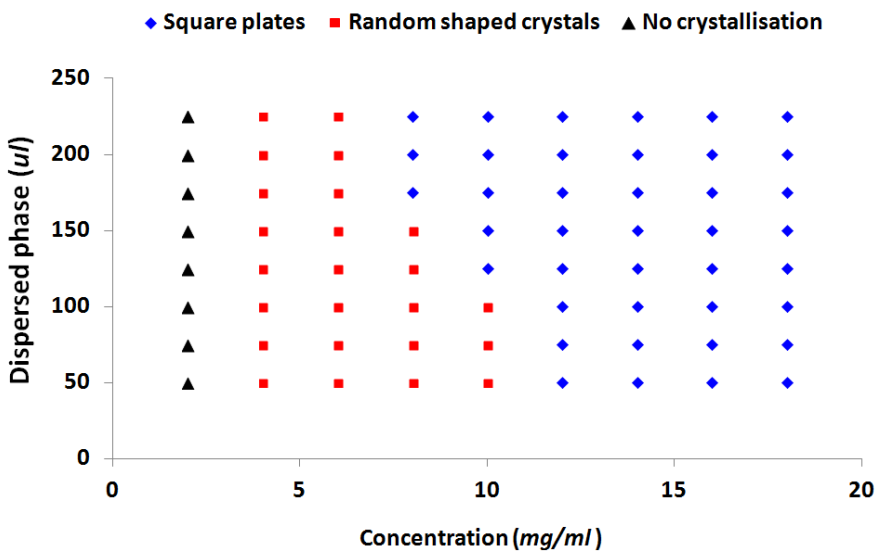

Figure 5.7 A composition Table of Triton X-100+1-hexanol/cyclohexane microemulsions employing various concentrations of DPA in 2M HCl solutions as dispersed phases

The effect of varying the droplet size of the dispersed phase has been illustrated in the previous chapters which typically led to different polymorphic outcomes. In this system, the scenario was slightly different. Instead of different polymorphs, the variation of the dispersed phase led to different levels of nanoparticle aggregation. Figure 5.8, reveals TEM data obtained from the three microemulsion samples with 12 mg/ml DPA solution, differing volumes of dispersed phase from 50 µl/g, 100 µl/g to 225 µl/g. The 225 µl/g sample produced more organised square shaped nanocrystals from 2–4 nm nanopaticles. However, both the 50 µl/g and 100 µl/g samples exhibited only partial agglomeration. For the latter case the alignment of these nanoparticles was not as organised as the former case, resulting in arcing in the DP and FFT images.

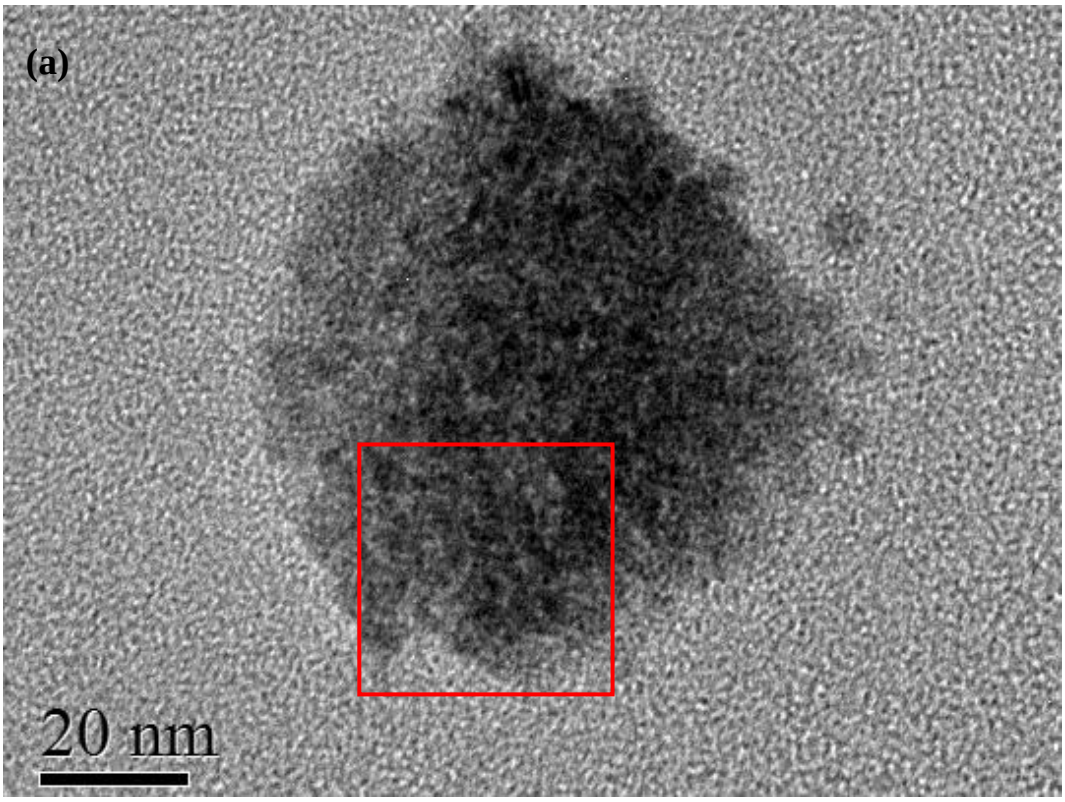
(a)
20 nm

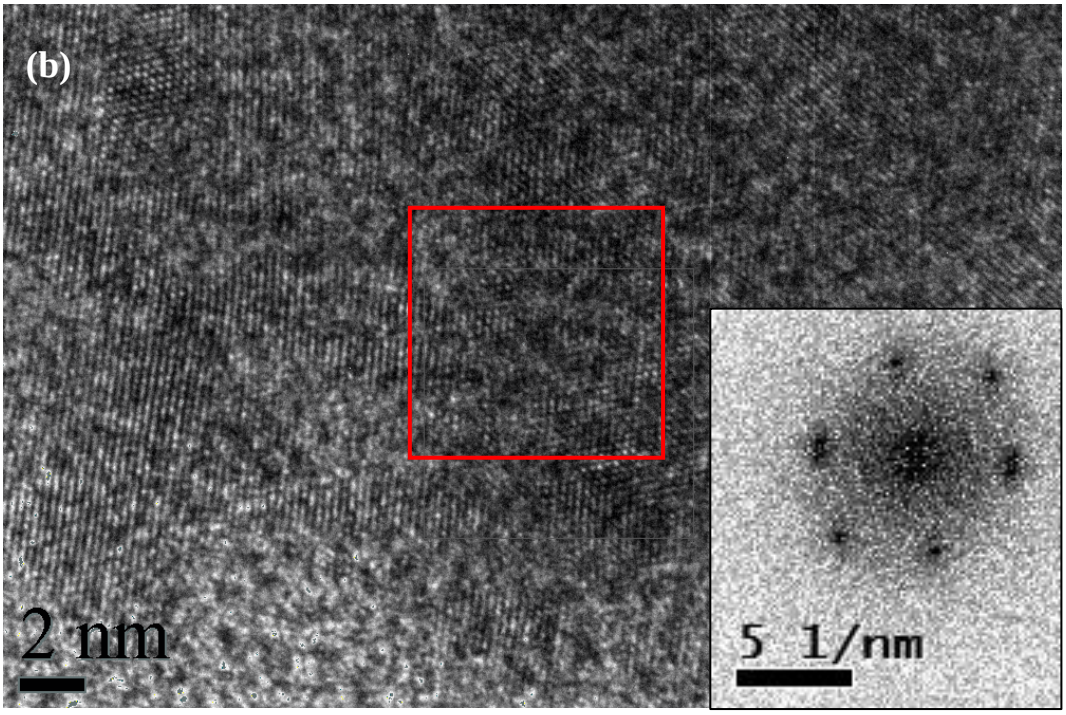
(b)
2 nm
5 1/nm

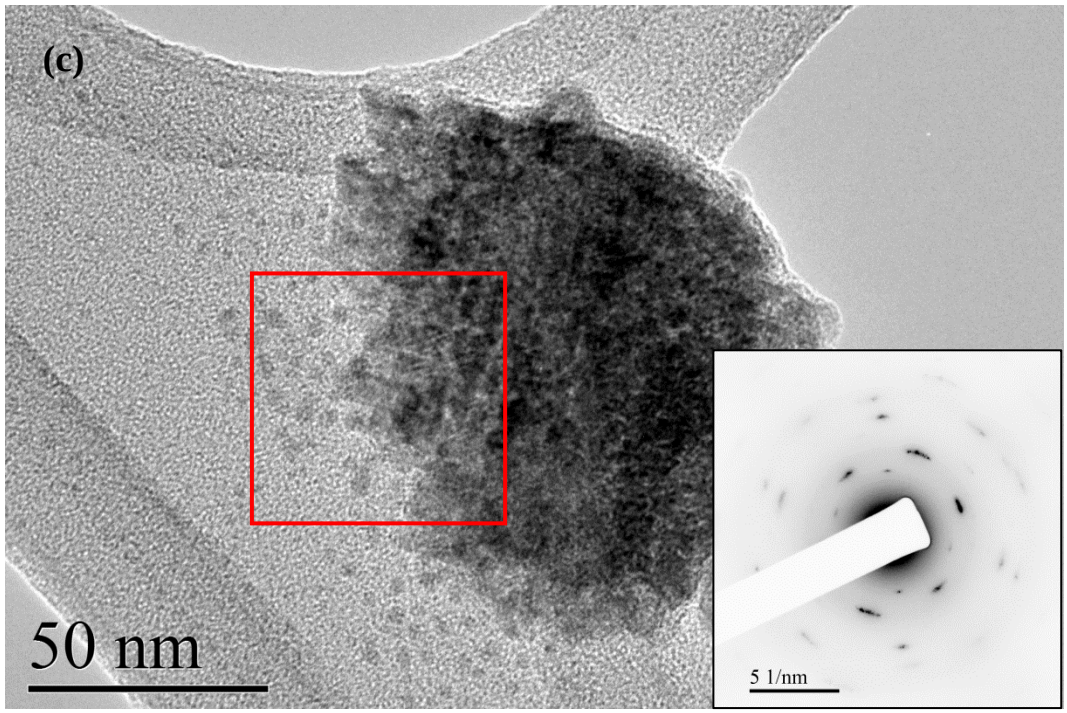
(c)
50 nm
5 1/nm

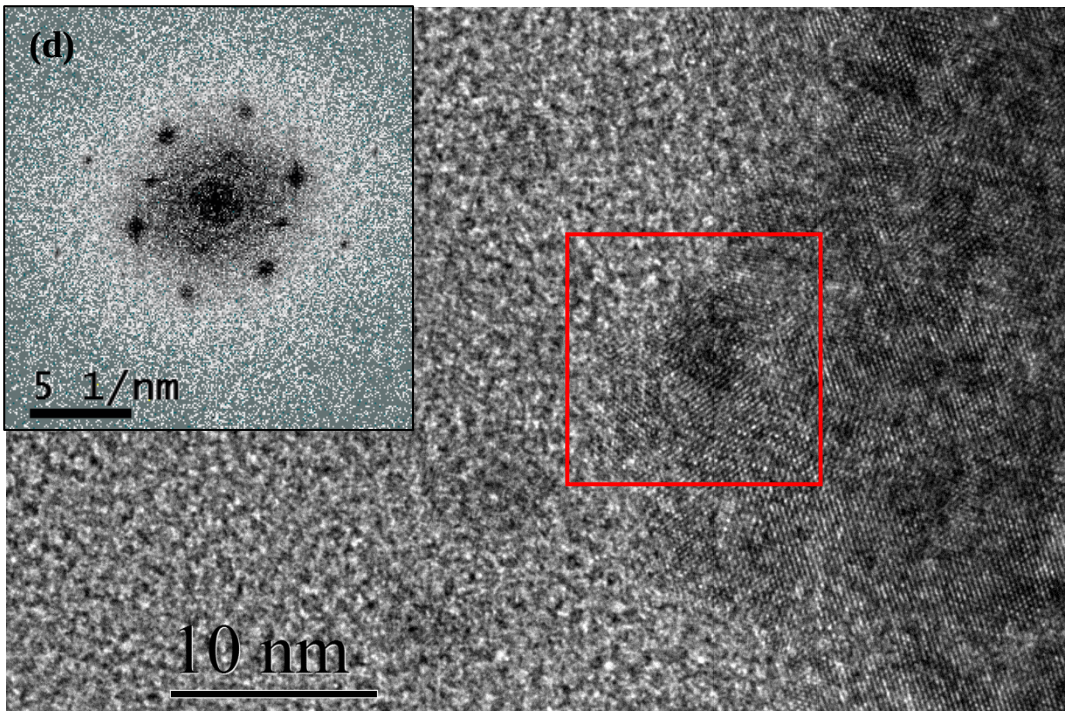
(d)
5 1/nm
10 nm

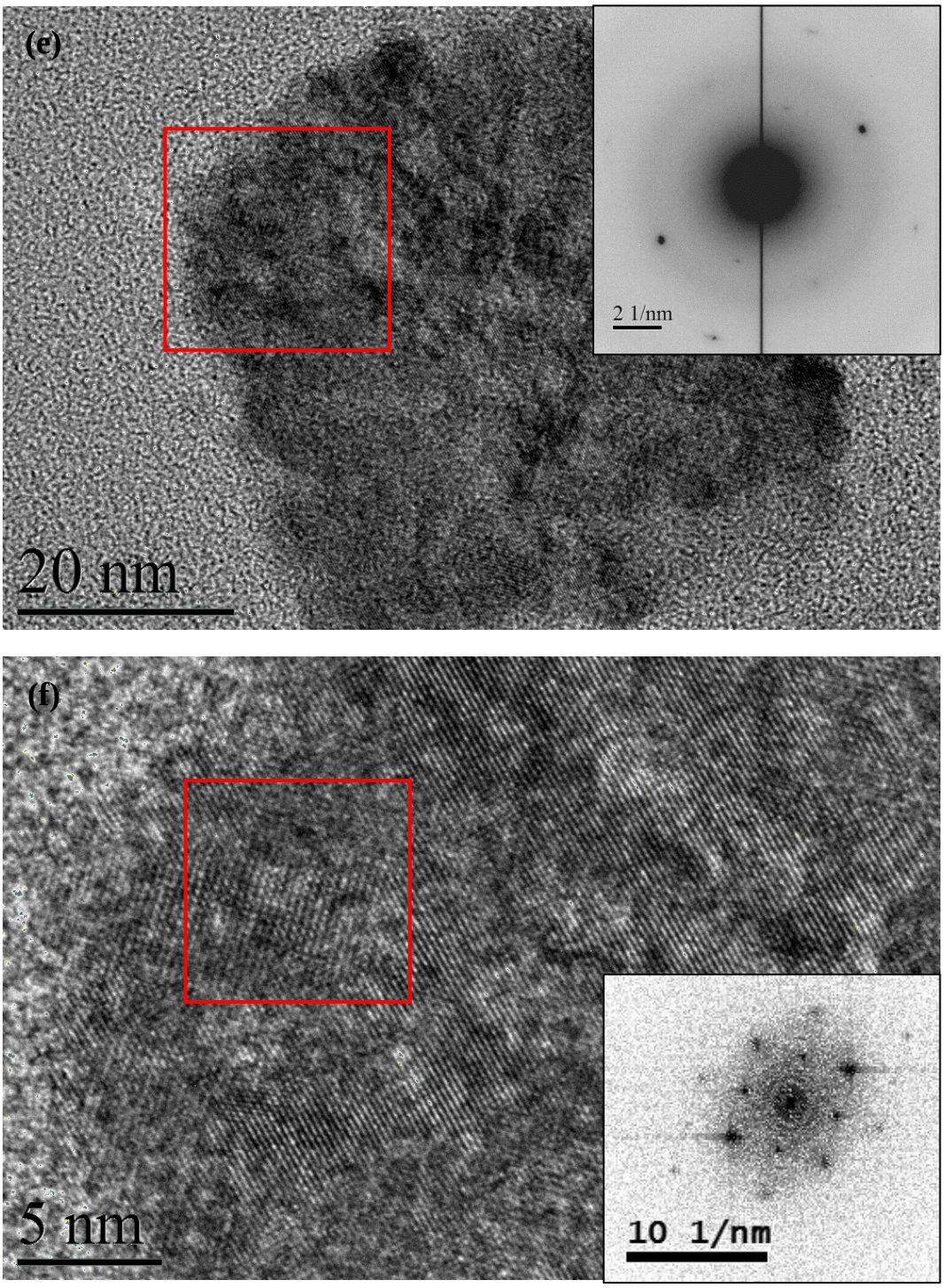

Figure 5.8 BF, DP, HREM, and FFT images of DPA crystals from Triton X-100/1-hexanol microemulsions with 12mg/ml DPA in 2M HCl solution at (a-b) 50ul/g where (a) is the BF image, (b) is the HREM image of the selected area in (a), and the inset in (b) is the FFT image of the selected region in (b), (c-d) 100ul/g where (c) is the BF image with the inset showing the DP of the nanocrystal, (d) is the HREM image of the selected area in (c), and the inset in (d) is the FFT image of the selected region in (d), and (e-f) 225ul/g, where (e) is the BF image with the inset showing the DP of the nanocrystal, (f) is the HREM image of the selected area in (e), and the inset in (f) is the FFT image of the selected region in (f).

In order to rationalise these observation, SAXS measurements have been carried out on comparable samples. The resulting *I(q)* functions (Figure 5.9a) have been further processed using the GIFT package to produce the pair distance distribution functions *p(r)* as shown in Figure 5.9b. With an increased volume of dispersed phase, both the diffraction intensity and the droplet radius increased proportionally.

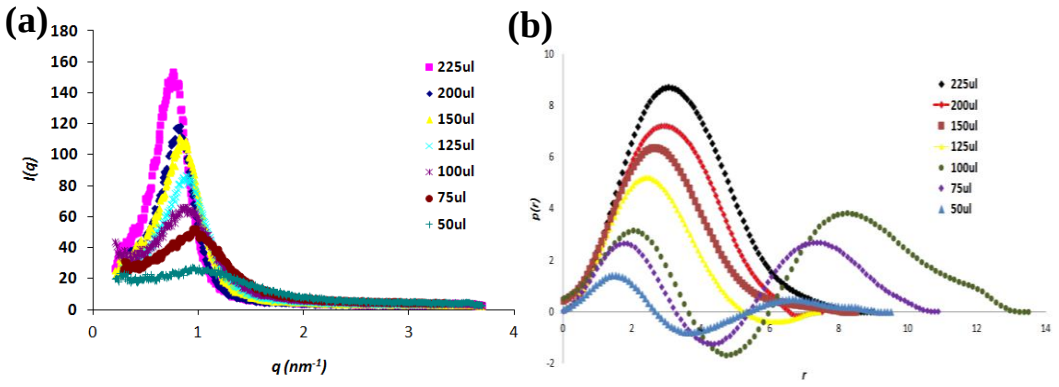

Figure 5.9 SAXS measurements: (a) scattering function *I(q)* vs *q* and (b) Pair distance distribution function *p(r)* vs *r* processed by GIFT package.

Inspecting the *p(r)* functions, the best fit for a dispersed phase up to 100 µl/g was a core-shell model, with a high electron density core region comprising of the dispersed phase and the hydrophilic head of surfactant, a slightly lower electron density region due to the benzene within the Triton X-100 and the 1-hexanol cosurfactant.

Table 5.1 Electron density per A^3 for each of the microemulsion components

	DPA in 2M HCl	H_2O	Cyclohexane	Triton X-100	1-hexanol
Density/g ml^{-1}	1.04	1	0.78	1.07	0.81
No. of e^-	86	10	48	342	58
M_r /g mol^{-1}	167	18	84	625	102
Electron Density /A^{-3}	0.32	0.33	0.27	0.35	0.28

However, for a dispersed phase above 125 µl/g, the best fit changed to an approximately homogeneous hard-sphere, modelled as a hard sphere, due to the enhanced participation of the high electron density dispersed phase into the continuum (Figure 5.9b). As a consequence, the electron density contrast between the surfactant tail groups and cyclohexane is reduced to a negligible level. In

addition, the electron density of 1-hexanol is very similar to cyclohexane, reducing the contrast between the surfactant tails and the continuum further.

As mentioned in Chapters 3 and 4, the outcome of crystallisation can depend on the water pool size of the microemulsion. If it is too small or negligible, crystallisation may occur in the water layer that is rigidly held by the surfactant and thus templating effects might take over and the water may be hard to incorporate into the crystal structure. By calculating the quantity of dispersed phase that is bound or structurally perturbed by the surfactants, the dimensions of the central free water pool, where homogeneous nucleation occurs, can be estimated. In addition, the surfactant to water ratio will influence the level of supersaturation; too high a supersaturation would normally lead to fast nucleation and less organised nanoaggregates (NAs). As shown in Table 5.2, when the dispersed phase is increased from 50 μl/g to 225 μl/g (*r* from 2.4–4 nm), the amount of water molecules that are bound to the surfactants layer is reduced to 30%. This reveals an increased free water pool, possibly resulting in an increased level of self-organisation and aggregation of DPA molecules. Thus the shape and size of the DPA crystals were more regular and uniform as the droplet size increased.

Table 5.2 Estimation of free central water pool proportion from the GIFT radii

Dispersed phase /μl g^{-1}	50	75	100	125	150	175	200	225
Mean $r_{c(gift)}$/nm	2.40	2.91	3.14	3.23	3.56	3.65	3.73	4.01
Mean $V_{c\,(gift)}$/nm^3	58	103	130	140	189	204	218	271
Approx. No. of droplets in the system (x 10^{18})	5.15	3.18	2.68	2.65	2.10	2.07	2.06	1.74
Approx. no. of H_2O molecules per droplet (x 10^3)	0.31	0.76	1.21	1.53	2.31	2.74	3.14	4.17
*Approx.*no. of Triton X-100 molecules per droplet	71	115	137	138	174	177	178	210
Approx. H_2O can be taken by Triton X-100* per droplet (x 10^3)	0.38	0.61	0.72	0.73	0.92	0.94	0.94	1.11
Theoretical fraction of H_2O can be bound to Triton X-100	1.2	0.8	0.6	0.5	0.4	0.3	0.3	0.3

*calculated based on free water pool formation threshold at W=5.3[8]

As in previous chapters, the droplet sizes obtained from GIFT analysis is compared directly with a calculated geometric droplet size to provide further insight into the structure of the microemulsion. However, as can be seen from Table 5.3, large discrepancies were noticed between these two radial estimates, when assuming all of the 1-hexanol (with a mass fraction of 0.17) is acting as cosurfactant at the interface. This assumption underestimates the level of 1-hexanol partitioning into the continuous phase, owing to its long alkyl chain. Therefore the geometric calculations have been redefined with both zero and a reduced amount (mass fraction of 0.11) of 1-hexanol.

Table 5.3 Geometric radius calculated from different mass fraction of hexanol vs the experimental radius obtained from GIFT analysis

Dispersed Phase / ulg^{-1}	Mass fraction of hexanol at the interface			R_{gift}/nm
	No	0.11	0.17	
225	9.19	4.35	3.41	4.01
200	8.50	4.03	3.16	3.73
175	7.83	3.72	2.92	3.65
150	7.19	3.42	2.69	3.56
125	6.56	3.13	2.46	3.15
100	5.96	3.01	2.24	3.14
75	5.38	2.85	2.03	2.91
50	4.82	2.32	1.83	2.40

For straightforward visualisation, the geometric droplet sizes calculated based on zero hexanol, 0.11 and 0.17 of hexanol were plotted against Gift analysis droplet radius. The black dashed line is the ideal scenario where both the geometric and Gift analysis values are in agreement. In reality only the estimations for the 0.11 hexanol case agree within the boundary of experimental errors, whilst both the case of zero and 0.17 hexanol deviate from ideal. This suggests that either the hexanol is partitioning significantly into the continuous phase and/or the area per molecule value of 48 $Å^2$ used for the Triton X-100[9] is inaccurate. In particular, if this area per molecule value is increased by 10% and 25%, then the required partitioning of hexanol into the continuous phase to give good agreement with the GIFT analysis radius values would increase to 0.07 (i.e. mass fraction of 0.10 hexanol at the interface) and 0.09 (i.e. 0.08 at the interface), respectively.

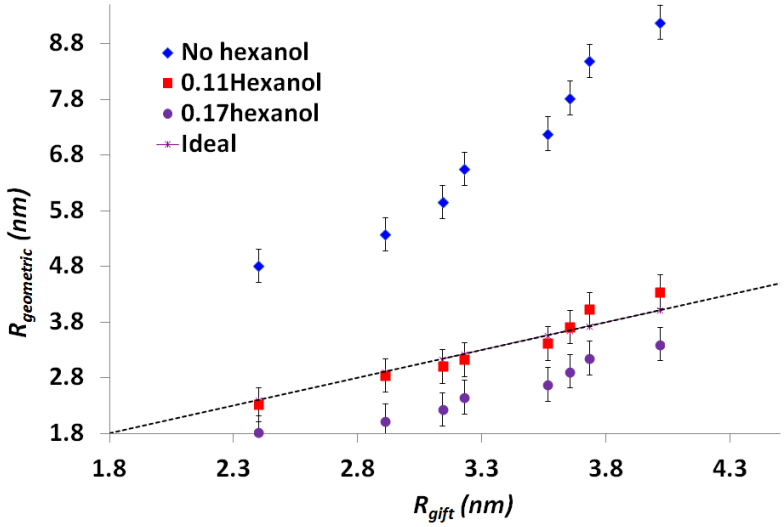

Figure 5.10 Geometric radii plotted as a function of Gift analysis radii

Additives and the pH can greatly influence the phase behaviour of a surfactant system. Thus to clarify further, the effect on droplet size was investigated by comparing the radius of microemulsions made from pure aqueous phase and 2M HCl. The droplet radii of the pure water and 2M HCl dispersed phases are in agreement with each other, within the boundary of experimental error (±0.3 nm). This illustrates that the effect of 2M HCl on droplet size is negligible in Triton X-100 system.

Table 5.4 Gift analysis mean droplet size of Triton X-100 microemulsion with aqueous and 2M HCl dispersed phase at various dispersed quantity

Dispersed phase /μl g^{-1}		50	100	200
Mean $r_{c(gift)}$/nm	Aqueous phase	2.38	3.18	3.95
	2M HCl	2.40	3.14	3.65

5.3.2.4 Effect of DPA concentration variation

At lower concentrations (< 2 mg/ml), no macroscopic crystalline particles were observed. With 2–8 mg/ml DPA solution, small particles ~3–10 nm in size existed. These small particles are believed to be the primary building unit of the square shaped NAs obtained in the higher concentration samples as both samples exhibit identical DP/FFT (Figure 5.11). The size of these small particles (~3–10 nm) are comparable to the size of the droplets (~5–8 nm in diameter) hence they can be

postulated to be the early stage product, nucleated within the droplets or formed during transient droplet dimer formation as described in Chapter 1.

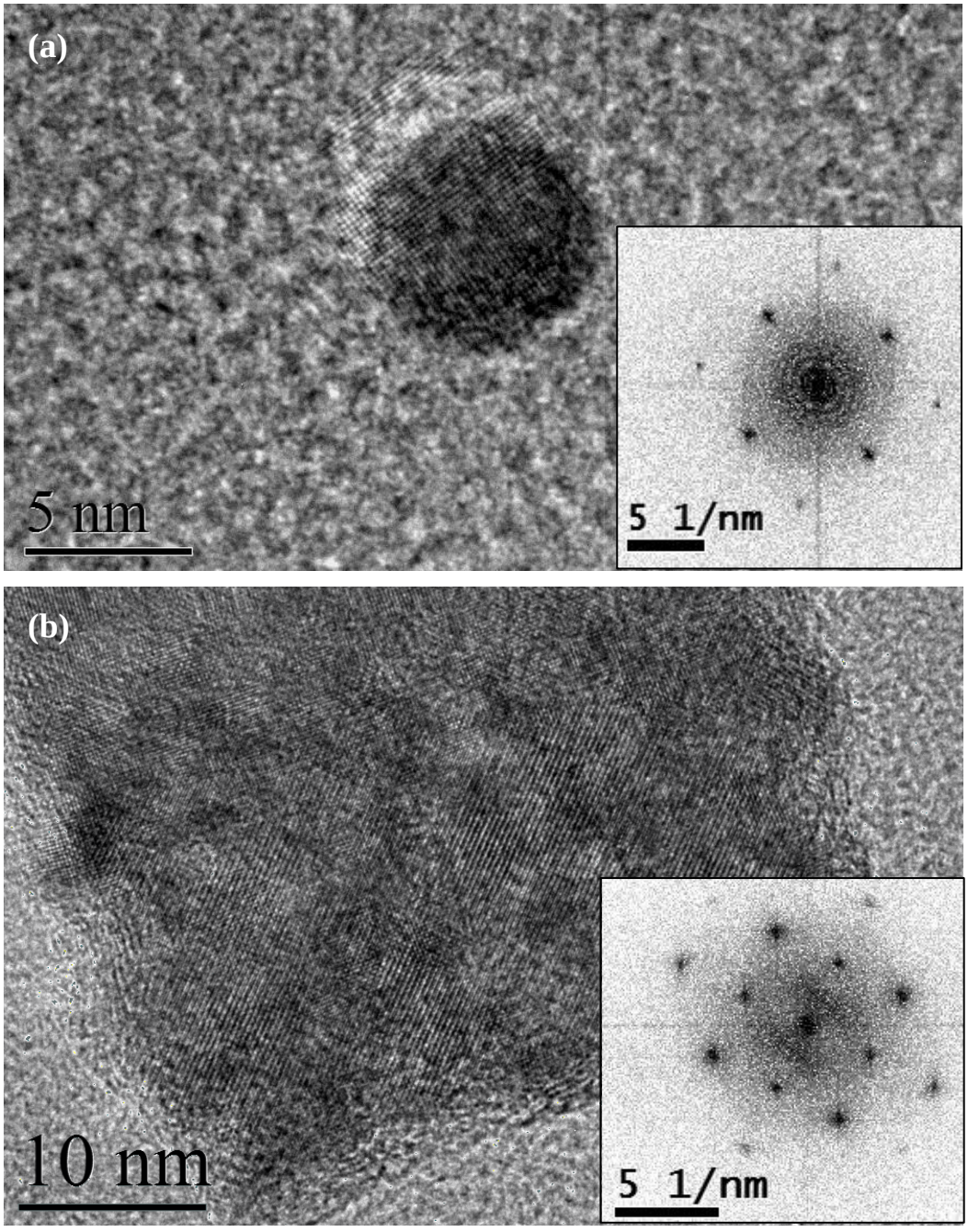

Figure 5.11 The HREM and inverted FFT (as the inset) images of microemulsions containing 225 μl/g of (a) 8 mg/ml DPA sample; (b) 18 mg/ml DPA sample

Above 8 mg/ml, NAs of 20–100 nm in size were seen. The level of aggregation and organisation of these nanoparticles still depend on the quantity of DPA in each sample. A strong contrast can be observed between the 10 mg/ml samples that exhibit partially aggregated nanocrystals of ~20–50 nm in diameter and the

18 mg/ml samples, which contains well organised square-plate shaped nanocrystals of ~50–100 nm in diameter, as seen in Figure 5.12. Furthermore, the partially aggregated nanocrystals typically have misalignments in the structure with either different FFTs for different regions of the nanocrystals or arcs in the FFTs. While the well-organised aggregates tend to have a single crystal-like diffraction pattern with uniform FFTs across the whole crystal surface.

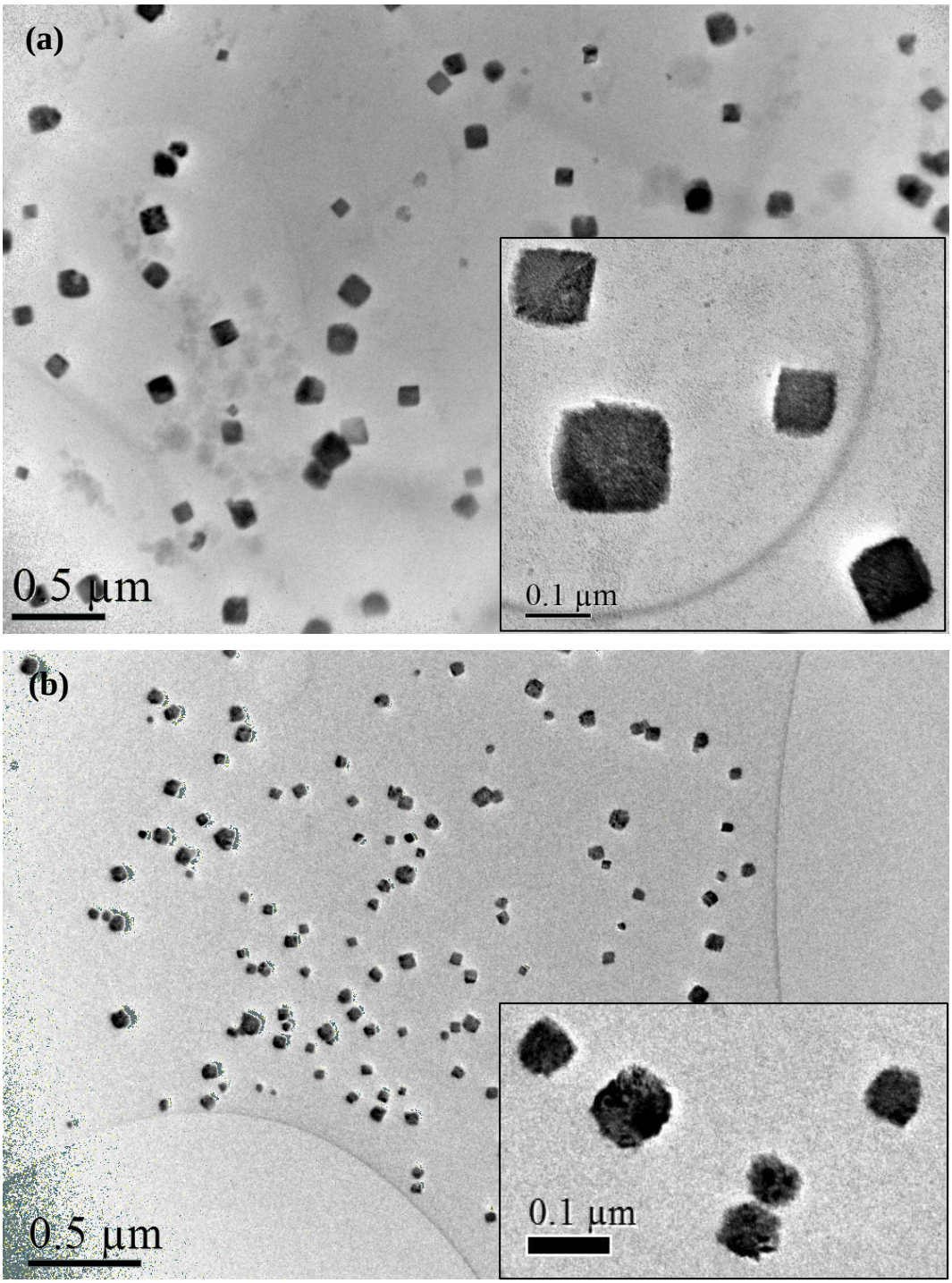

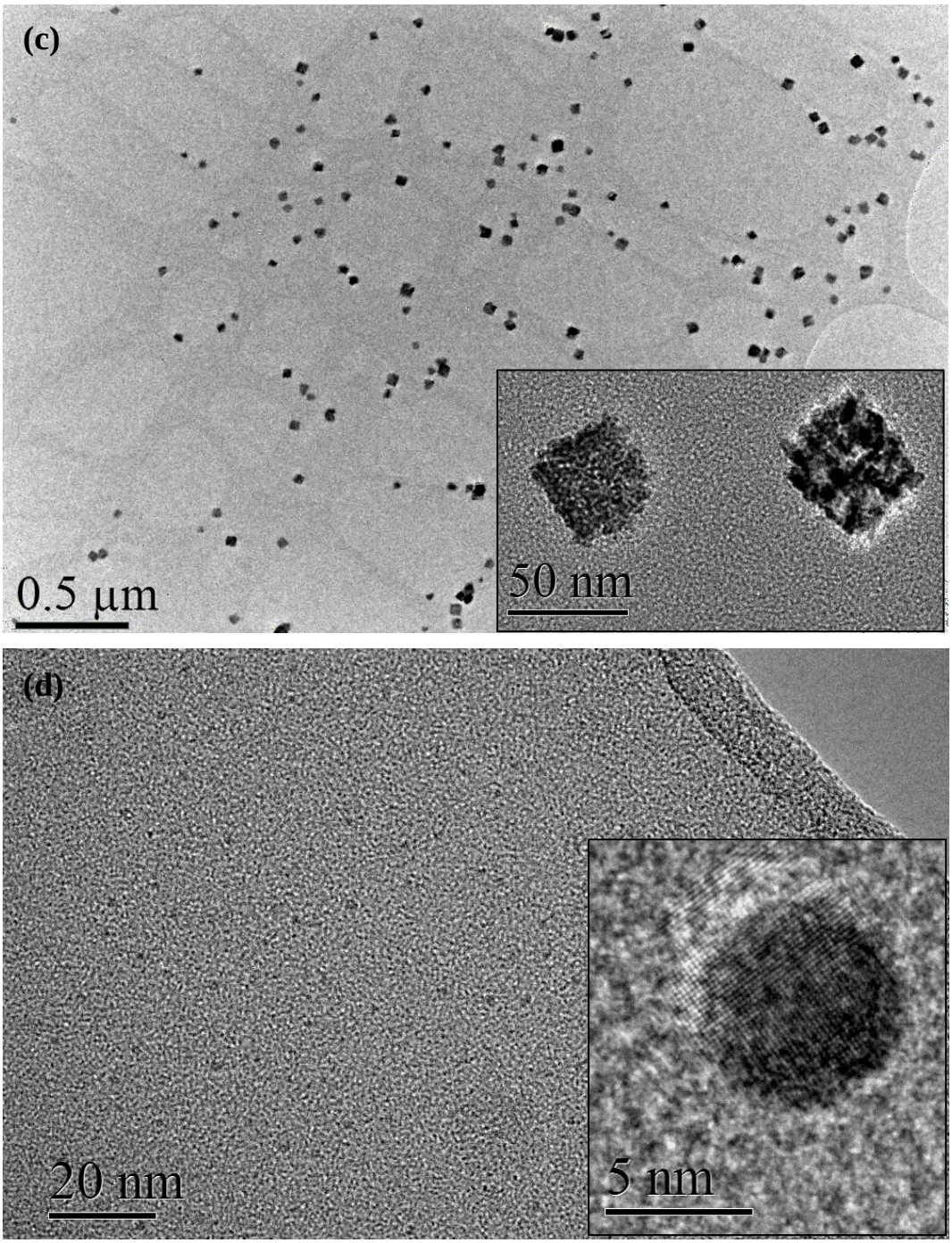

Figure 5.12 Morphology change as the DPA concentration varies in the microemulsion at fixed disperse phase (225 μl/g), with the insets showing the representative image at a higher magnification: (a) 18 mg/ml; (b) 12 mg/ml; (c) 10 mg/ml; and (d) 8mg/ml

It is expected[10] that the primary building unit would be comparable in size to the microemulsion droplets, since particles formed by aggregation are normally constrained by their confinement. Bandyopadhyaya *et. al.* reported a decrease in the aggregation rate as the particle size of CdS approached that of the droplet size, thus providing evidence to support the existence of droplet size barrier. Once the

particles exceed the droplet diameter (in any dimension), the head group of the surfactant will begin to adsorb onto the particle surface and slow down its growth. Consequently these surfactant coated particles often remain in the system. Sato and others have previously investigated the adsorption process. Moreover the ability of a surfactant to control the morphology during crystallisation has been demonstrated in a number of studies, e.g. MOFs like zeoliticimidazolate framework[11], minerals such as $CaCO_3$[12], magnetic compounds such as α-Fe_2O_3[13]. Due to interactions between the primary particles/surfactant/droplets, e.g. hydrogen bonding/π-π stacking/hydrophobic interactions, the particles were able to attach to each other in a particular orientation, (i.e. the fastest growing face with the smallest area in this case) which led to the final formation of the square aggregated structures. However, we cannot at present give a more quantitative evaluation for the preferred choice of crystal face attachment and the oriented attachment mechanism albeit a proposed growth mechanism is detailed in Section 5.3.2.7. Increasing the DPA concentrations to $\geq$ 8 mg/ml, further aggregation of the small particles into organised nanocrystals was evident.

Crystallising DPA from bulk aqueous solutions at 8 mg/ml and above, the product was often a mixture of prism shaped monohydrate and plate/needle anhydrous forms. In contrast, in 2M HCl solutions at 8 mg/ml and above, only needle/rod-like anhydrous crystals were obtained.

With the addition of surfactants to the DPA aqueous solutions, thin plates of the monohydrate form were obtained from the surfactant solutions/emulsions, as shown in Figure 5.13d. Since monohydrate has a prismatic morphology when crystallising from bulk aqueous solution, these thin plates were attributed to the surfactant adsorption onto the monohydrate slowest growing (101) face and thus prevent its further growth.

In contrast, with the addition of surfactants to the acidified DPA solutions, dendritic anhydrous crystals were the sole product. Such a dramatic morphology change (Figure 5.13b) can be associated with the effect of surfactant control. Dendritic growth is often a result of a difference in solute concentration at the tips and surface of the crystals, but here it is expected that the surfactants are adsorbed

on/attached to the fast growing crystal face and thus block the site from further growth. Therefore subsequent crystal growth proceeds via deposition of materials onto the readily available crystal surface by means of a lower energy barrier through heterogeneous nucleation. There are a few reported cases of surfactant assisted dendritic growth describing such an effect[14-16].

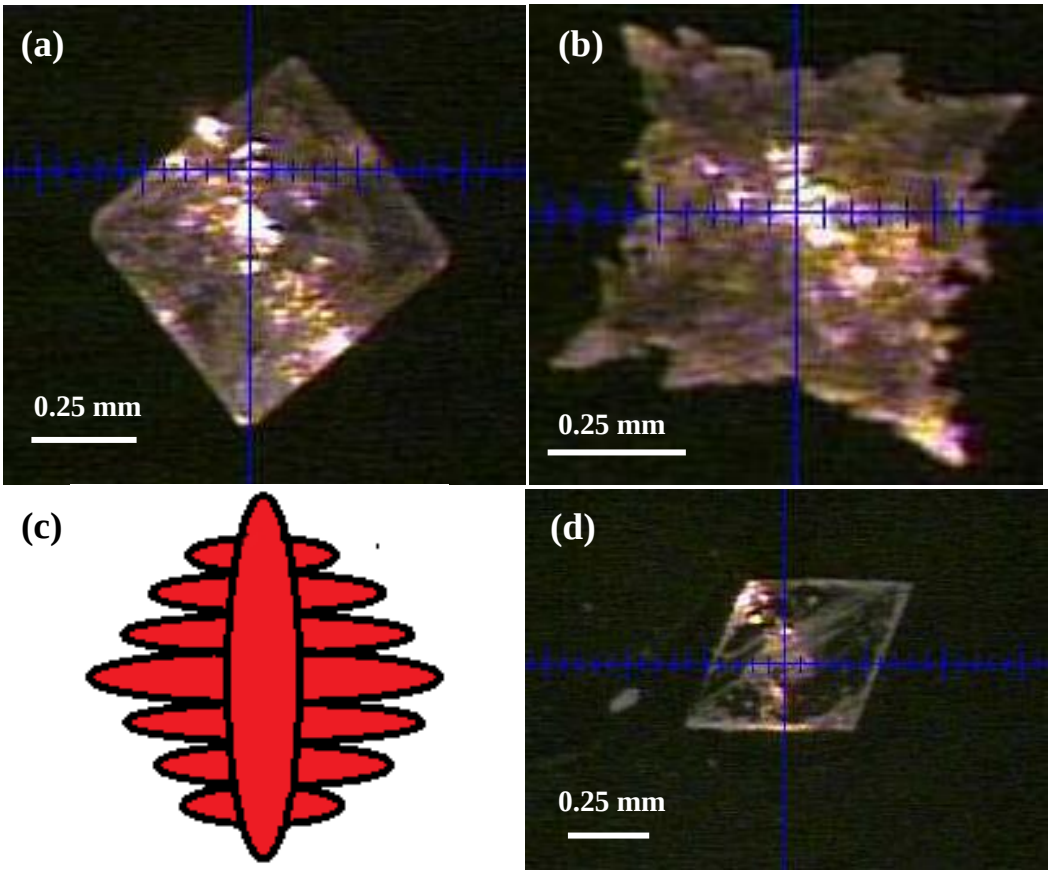

Figure 5.13 Crystals obtained from non-confined conditions: (a) aqueous solution at 5 mg/ml of DPA; (b) from emulsions containing 2M HCl solution of 8 mg/ml of DPA; (c) schematic diagram of the dendritic growth; and (d) thin plate monohydrate crystals obtained from surfactant solutions

To conclude, in the non-confined acidic conditions describing above, the DPA anhydrous form is the sole product at 8 mg/ml and above. Within the confinement of a Triton X-100+1-hexanol/cyclohexane based microemulsion, from DPA solutions only the square plate crystals of the most stable polymorph, the DPA monohydrate, were obtained. Hence the monohydrate NAs obtained can be attributed to a combination of the effect of its 3D-nanoconfinement and the ability to shift the pH back to neutrality. The morphology of the monohydrate is a result of the surfactant adsorption effect similar to the emulsion experiments.

5.3.2.5 Effect on viscosity with dispersed phase variation

Viscosity is an important feature of microemulsions that can provide structural information of the system.[17] It heavily relies on the components and additives within the system. At a small fraction of dispersed phase, microemulsions are often dilute and thus can be described by Einstein's well-known viscosity relationship:

$$\eta_r = 1 + 2.5\phi \tag{5.1}$$

where η_r is the relative viscosity of the solution or dispersion and ϕ is the volume fraction of the solute or dispersed phase.

However at a high fraction of dispersed phase this relationship does not hold, due to the increasing droplet interactions in the system. Consequently a non-linear change in viscosity with dispersed phase volume can be one result of percolation and thus is characteristic of such behaviour. Percolation is the phenomenon used to describe the start of clustering of microemulsion droplets into networked channel structures (also known as bicontinuous microemulsion), as illustrated in Figure 5.14.

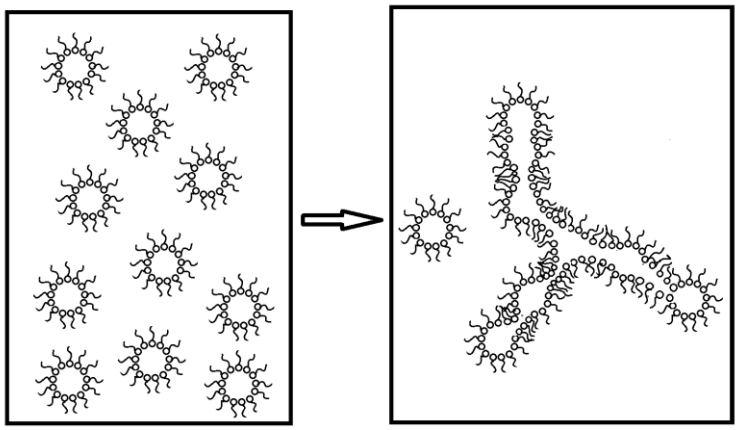

Figure 5.14 Illustration of percolation

Typically, upon reaching a threshold level of water in a w/o microemulsion at a constant temperature, sharp increases in conductance and viscosity are observed. Conversely, similar effects are observed upon maintaining the water level and reaching a threshold temperature. The temperature or concentration that percolation occurs is termed the 'percolation threshold'. Furthermore, addition of

certain additives such as NaCl can increase the viscosity of the microemulsion prepared from ionic surfactants by modifying the packing at the interface, thus decreasing the rigidity of the interface. Therefore these additives can assist and stabilise the channel formation between microemulsion droplets. However, to date, there is not an empirical rule/theory completely describing the viscosity of microemulsions, but several studies have attempted to provide an insight to the systems.

With the Triton X-100 system, the viscosity of the microemulsion samples was noticeably greater with an increased volume of inner phase. However, due to the restrictions of the viscometer, i.e. a stainless steel spindle can be damaged by 2M HCl, only measurements for the aqueous DPA microemulsions were recorded.

The viscosity was measured as a function of shear velocity, plotted in Figure 5.15. A typical trend can be observed: with increasing shear velocity. There is an initial sharp rise in the viscosity followed by a plateau region after *approx.* 30 RPM.

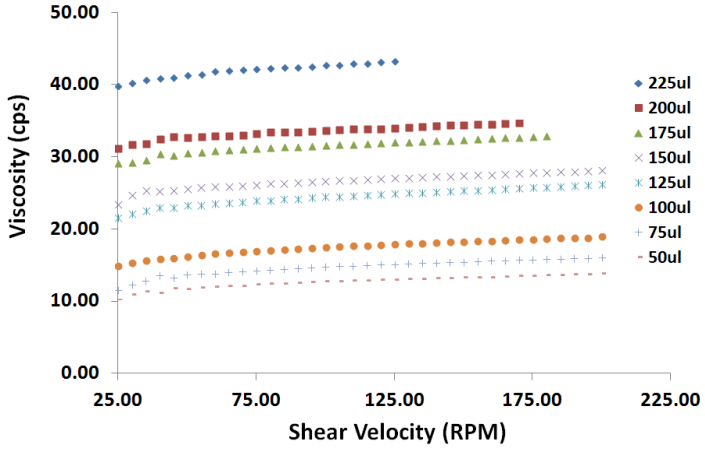

Figure 5.15 Experimental determined viscosity measurements plotted against shear velocity

Consequently, only the plateau region was used for analysis. The plateau region was extrapolated to intersect the y-axis and thus provide the viscosity value at zero shear rate. Prior to measurements being taken, calibration of the viscometer was necessary. In addition to the calibration, experimental readings were processed (Table 5.5) allowing replotting as a function of dispersed phase volume for further study (Figure 5.16).

Table 5.5 Experimental, calibrated viscosities and their errors for different dispersed phase volume

Dispersed phase /ul	50	75	100	125	150	175	200	225
η (cps)	11.49	12.92	15.47	22.46	24.85	29.82	32.01	40.56
η_{cal} (cps)	6.40	7.54	9.58	15.15	17.06	21.02	22.77	29.09
Error	0.47	0.41	0.77	0.91	0.75	0.59	1.33	3.06

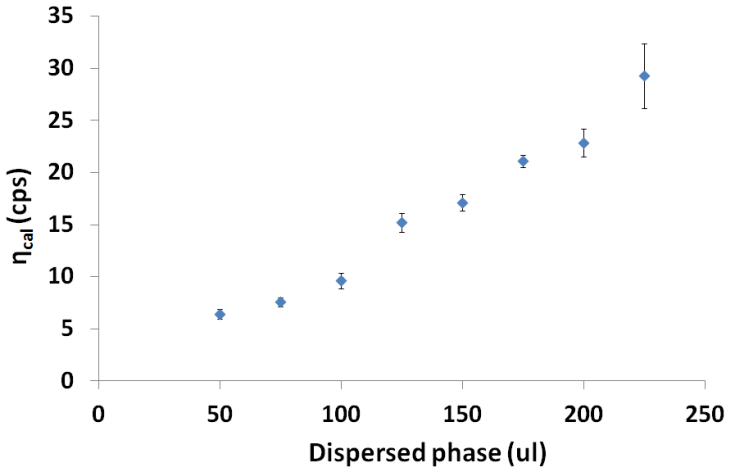

Figure 5.16 Calibrated viscosity, η_{cal}, as a function as dispersed phase volume

The viscosity increased considerably with an increase in the volume of dispersed phase. This is postulated to be the effect of the cosurfactant, 1-hexanol. It is relatively hydrophobic and has been reported to significantly increase the viscosity when compared to other short/middle chain cosurfactants[18], such as ethanol and butanol. However, the latter are expected to promote the phase transition from o/w microemulsion to a bicontinuous microemulsion. This is related to their superior ability to penetrate into the amphiphilic layer, than 1-hexanol. Thus, upon increasing the dispersed phase, the w/o microemulsion droplets swell until either entering emulsion regions or phase separating into multi-phase regions. Systems employing mid-length chain alcohol, such as 1-butanol, can experience a transition from w/o to o/w microemulsions via a bicontinuous zone, upon increased addition of the inner phase. This bicontinuous zone can be determined by several techniques[19, 20], including SAXS(SANS), TEM, FTIR, viscometry and conductivity measurements. In particular, the viscosity is expected to increase significantly from a microemulsion to a percolating system, but then suddenly drop once entering the bicontinuous zone. This is owing to the ability of the cosurfactant, in enhancing the dynamics of the bicontinuous region,

which contains interconnected channels. In our measurements, no decrease in viscosity was observed, thus the formation of a bicontinuous zone did not occur. Our studies were consistent with the reported trend; systems containing 1-hexanol are more likely to contain discontinuous domains in the phase diagram rather than having a smooth transformation from w/o to o/w via bicontinuous microemulsion without phase separation.

With the support of SAXS analysis, percolation was not observed even at high volume fractions of dispersed phase. This coincides with Clausse *et. al's.* [18, 21] study on level of the percolation affected by the chain length of cosurfactant[22]. Here conductivity measurements were carried out, proving that long chain cosurfactants e.g. hexanol and heptanol do not promote percolation, at high volume fractions of water. Further the viscosity data can be applied to estimate the droplet collision rate and time from the Smoluchowsky equation (5.2), thus providing an insight into the kinetics of a microemulsion system:

$$k_D = \frac{8k_B T}{3\eta} \tag{5.2}$$

where k_D is the collision frequency, k_B is the Boltzmann constant, T is temperature and η is the viscosity.

Once the collision frequency, $k_{D,}$ is determined and the droplet size is known, the encounter rate, k_{en}, of the droplets and the average collision time τ_{en} can be systematically resolved, using the following relation:

$$k_{en} = k_D\, C \tag{5.3}$$

Where C is the concentration of microemulsion droplets. The average collision time τ_{en} is calculated as follows, which is typically in the order of μs:

$$\tau_{en} = \frac{1}{k_{en}} \tag{5.4}$$

Table 5.6 Encounter rate of droplets and the average collision time calculation

Dispersed phase	50	75	100	125	150	175	200	225
ŋ /cp	6.40	7.54	9.58	15.15	17.06	21.02	22.77	29.09
k_D / x10^8 M^{-1} s^{-1}	10.20	8.61	6.78	4.29	3.81	3.09	2.85	2.23
Φ / x10^{-2}	4.20	6.20	8.10	9.90	11.60	13.30	14.90	16.50
r /nm	2.40	2.80	3.20	3.30	3.50	3.65	3.80	4.20
V / x10^{-26} m^3	5.79	9.20	13.73	15.05	17.96	20.37	22.98	31.03
[Droplet] / x10^{-3} M^{-1}	1.20	1.12	0.98	1.09	1.07	1.08	1.08	0.88
k_{en} / x10^5 s^{-1}	12.22	9.64	6.64	4.68	4.08	3.35	3.07	1.97
τ_{en} / x10^{-6} s	0.82	1.04	1.51	2.14	2.45	2.99	3.26	5.07

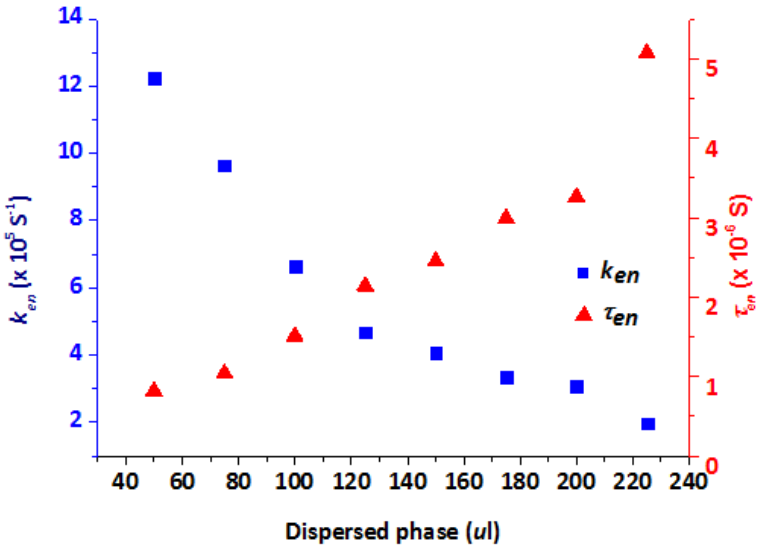

Figure 5.17 Encounter rate of the droplets and the average time of collision as a function of dispersed phase volume.

From Figure 5.17 the collision rate can be seen to decrease, whilst conversely the collision time increase with the volume of the dispersed phase. Only a small fraction of the aforementioned collisions (i.e. usually the most energetic ones) can form transient dimers to allow material exchange. Therefore knowing only the collision rate is insufficient to provide an estimate for the material exchange rate. Consequently, a further parameter, termed the encounter rate factor[23], D, which describes the statistical population of material exchange, is required. Hence the material exchange rate, k_{ex}, can be expressed as:

$$k_{ex} = Dk_{en} \tag{5.5}$$

The magnitude of D is also dependent on the film flexibility. In the case of AOT, which can form very rigid films; D = ~0.001[24]. This can be interpreted as roughly 1 in 1000 collisions are going to form a dimer. For other surfactants, D can

approach 0.1[25]. However the value of D in this system was not measured mainly due to the difficulty in finding a desirable probing molecule that is suitable in size for microemulsion work and will reside in the central water pool rather than at the interface.

5.3.2.6 Effect of pH

The environment inside the microemulsion droplets and its effect on solute molecule are still not fully understood. In particular, the pH-shift inside the microemulsion has been reported on a number of occasions[26] with these studies covering a variety of techniques, ranging from a simple pH probe (potentiometric measurements)[26, 27] to observing peak shifts in NMR, UV and Raman spectra. There are both advantages and drawbacks with each method; for instance, the pH probe allows fast assessment of samples. However, the pH of reversed microemulsions always appeared to have a 'buffer' effect comparing to the pH of the solutions added into the microemulsions[26, 28], and although this effect may be real, because it is seen more for the small droplet sizes, it may also be related to the ability of the probe to access the interior of the droplets at small droplet sizes. Previous studies were performed on the pH of buffered solutions in water/AOT/heptane reversed microemulsions[27]. It revealed that at high volumes of dispersed phase the electrical response was similar to that of the pure aqueous solution. However such measurements were not applicable for small volumes of dispersed phase. Furthermore, the interfacial interaction between the probe and the microemulsion was not fully understood, which increased the difficulty in interpreting the observed pH values. On comparison, spectroscopy methods, e.g. UV[8, 29-32], NMR[31, 33, 34] and FTIR[31, 35], often require doping of probe molecules into the dispersed phase of the microemulsion. An advantage is the avoidance of the issue as to whether the pH probe is reliable at small droplet sizes; however a careful choice of the probe dopant is required. This is a result of some probe molecules preferring to reside at the interface, rather than in the central pool of the microemulsion. Different positioning of the probe molecules[29] can affect the spectroscopic peak positions (e.g. NMR chemical shift, FTIR or Raman wavenumber). Recently, Halliday *et. al.*[33] attempted to measure the pH of microemulsions, using NMR without a probe molecule. Instead T2 relaxation time

of water molecules in the reversed microemulsion was evaluated. This work has relegated the prerequisite of a probe molecule, but how to quantify the pH in the central pool is still a question to be addressed.

In this thesis, the pH values of the Triton X-100 microemulsions were measured by both the pH probe and UV-Vis spectrometer using methyl red as the probe molecule. The purpose of measuring the pH is to provide indications for the level of pH variations at different amounts of dispersed phase and with different dispersed phases rather than define the precise value. The spectroscopy methods were first employed to microemulsions doped with equimolar methyl red solutions. When keeping the volume of the dispersed phase constant at 150 µl/g but varying this phase from pure aqueous water to 4 mg/ml DPA in water solution, the absorption peak shifts from 410 nm to 520 nm. The acidity of the solution is distinguishable from the absorbance values. The UV spectra of microemulsions (Figure 5.18), using 2M HCl solution as the dispersed phase, illustrated increasing absorbance with the volume of dispersed phase, but gave a single peak at 520 nm in all cases, i.e. similar to that found for the 4 mg/ml DPA.

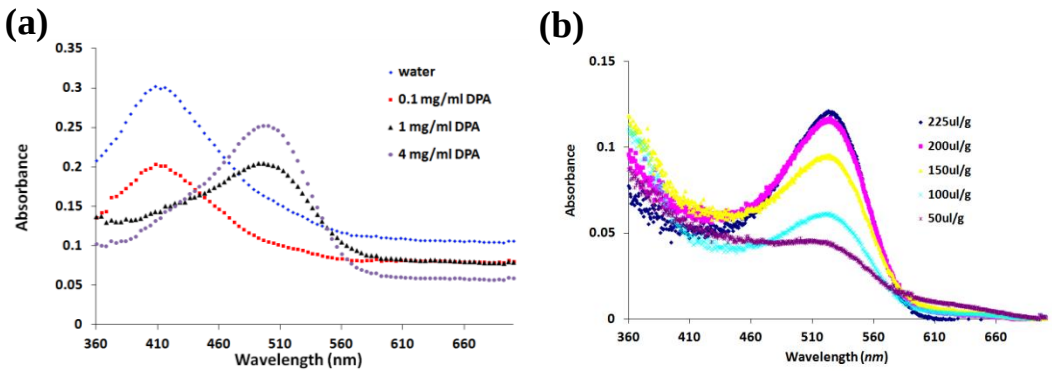

Figure 5.18 UV spectra of microemulsions doped with methyl red: (a) a comparison of water, 0.1mg/ml, 1mg/ml and 4mg/ml DPA solutions as dispersed phase at 225 µl/g; (b) UV spectrum of 2M HCl dispersed phase with its volume increase

The pH meter method was also employed on this Triton X-100 microemulsion system. As depicted in Figure 5.19, using pure water as the dispersed phase, the pH of microemulsions decreased only[32] very slightly from 7.50 at 50 µl/g to 6.99 at 225 µl/g. With DPA solutions of different concentrations (4 mg/ml or 2 mg/ml), a dramatic increase in pH was observed with decreasing DPA solution volume. At the low dispersed phase volume of 25 µl/g, the pH values of both 4 mg/ml and 2

mg/ml solution were comparable with the reading of the microemulsions having pure water as dispersed phases. At higher disperses volumes, the pH readings were in the range of 4–5 which are much lower than the readings at small droplet sizes, and more similar to the values of 2–3 expected from bulk DPA solutions at these concentrations. These findings were possibly due to the different levels of pH shifting when differing dispersed phase amounts. The greater ratio of surfactant to water at smaller dispersed phase can thus have a bigger influence to the overall pH. However these pH values even at the larger dispersed phases are still higher than the pH of comparable concentration bulk DPA solution, and this explains why the DPA crystallised out in its salt form rather than its acid form from the microemulsions discussed in Chapter 4.

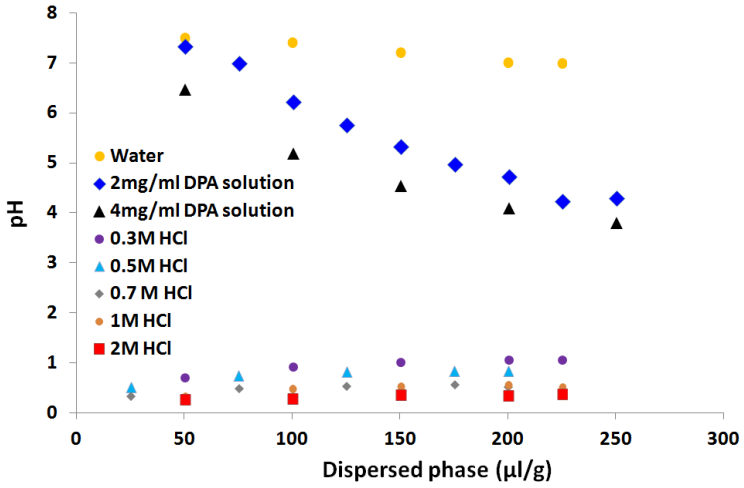

Figure 5.19 pH measurements as a function of dispersed phase

When the dispersed phase is 2M HCl solution, the pH became very acidic but only varied from 0.26 to 0.37 with increasing dispersed phase volume. This slight increase in pH with increasing dispersed phase volume was the opposite trend of the DPA solution cases, which was not expected. Table 5.7 calculated the $[H^+]$ per droplet based on the experimental pH, and a decrease in $[H^+]$ was observed with the increase of the dispersed phase volume. However this can be rationalised in terms of the strong acidity of HCl that overwhelms the pH shift of the microemulsion. This trend was observed for all of the microemulsions prepared from HCl solutions, with HCl concentration ranging from 0.3M to 2M (Figure 5.20a). Such a low range of pH values could explain the absence of the salt form

even at small volumes of dispersed phase, since the DPA molecule will exist predominantly in its acid form when the pH is less than 2.

Table 5.7 Mean [H^+] per droplet based on experimental pH in the acidic microemulsions

Dispersed phase /µl g^{-1}		50	100	150	200	225
Mean $r_{c(gift)}$/nm		2.40	3.14	3.56	3.73	4.01
No. of droplets in the system (x 10^{18})		5.15	3.18	2.68	2.65	2.10
Mean [H^+] per droplet/ M	0.3M HCl	0.20	0.12	0.10	0.09	0.09
	0.5M HCl	0.31	0.18	0.15	0.14	0.14
	0.7M HCl	0.33	0.21	0.19	0.18	0.19
	1M HCl	0.46	0.32	0.29	0.27	0.30
	2M HCl	0.55	0.52	0.45	0.46	0.43

An attempt to correlate the pH of the bulk HCl solutions with that of their microemulsions was carried out as plotted in Figure 5.20b. The pH readings of the microemulsions with the largest dispersed phase, i.e. at 225 µl/g, were used for comparison. The plot of the two pHs followed a linear relationship with the pH values of the microemulsion being much higher than the HCl solutions at high HCl concentrations. With the decrease of HCl concentration, the pH of the microemulsion becomes comparable to that of the bulk solution.

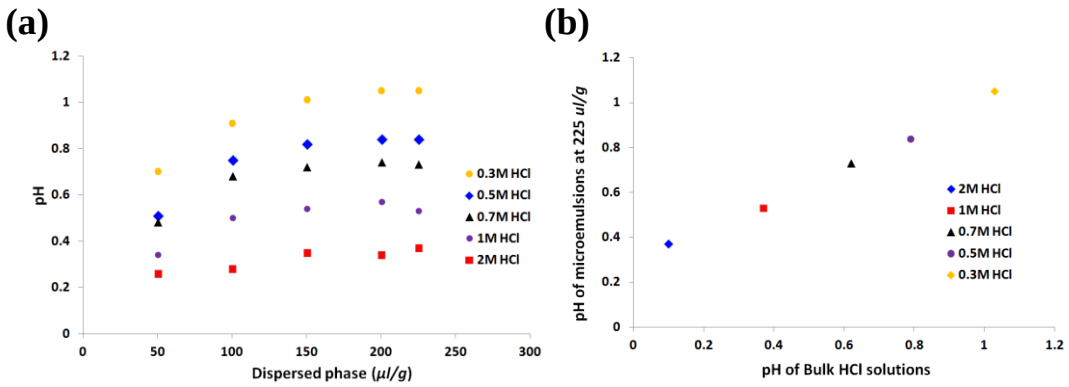

Figure 5.20 The pH values against the dispersed phase for the HCl containing microemulsion, as plotted in (a) and the correlation plot between the pH of the bulk HCl solutions and the pH of HCl microemulsions at 225 µl/g, as plotted in (b).

5.3.2.7 Proposed formation mechanism

The growth of the nanoparticles up to the droplet diameter could be explained by transient dimer formation and material exchange. However, the aggregation and orientated attachment of these primary nanoparticles into the larger square-plate nanocrystals is not fully understood. At this stage, the hypothesis is that as the particles move around and collide with each other, the fast growing (010) and ($\bar{2}$01) faces can thus be selectively attached via hydrogen bonding, eventually forming the square plate shape of the nanocrystals. Hydrogen bonding is probably the dominating interaction in this system and consequently both the (010) and ($\bar{2}$01) faces have the fastest growing rates than the (101) face.

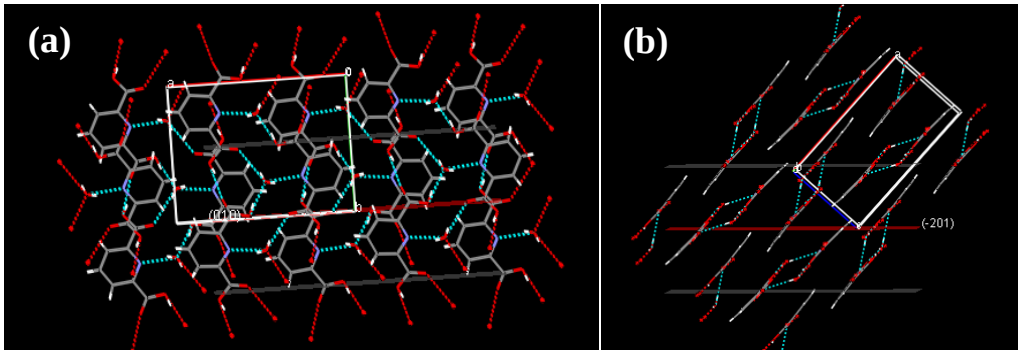

Figure 5.21 Structure and bonding geometry for the different growing face: a) 010; b) $\bar{2}$01

Thickness-wise, π-π stacking of the DPA benzene ring might have contributed to the growth in the vertical direction, perpendicular to the (010) and ($\bar{2}$01) faces. However π-π stacking is a much weaker force than hydrogen bonding and the largest (101) face is possibly covered by surfactants, illustrated by the surfactant altered (101) thin plate morphology of DPA grown from aqueous solutions containing these surfactants. Consequently the stacking of the nanoparticles in this direction is reduced. The organisation in the vertical dimension is much weaker and therefore misalignments can sometimes occur when the primary particles on the upper layers slightly shifted and didn't overlap with the bottom layers completely, leading to the arcing in the DP.

Arcing is more noticeable in diluter samples or with smaller droplet sizes. Increasing the DPA concentration, misalignment was reduced and the size of particles increased. This was postulated to be due to a combination of the reduced

surfactant adsorption and the significant primary nanoparticle population increase with the DPA concentration increase since the probability of 'finding another particle' is greater, i.e. to the increased primary nanoparticle collision and attachment.

As stated earlier, residual surfactants adsorbed on the primary particle surface might have assisted this process. This is because hydrophobic interactions can occur between the surfactant tail groups and enhance the attachment of the primary particles. However hydrophobic surfactant tail group interactions would not be orientation selective if the surfactant adsorbed on all faces and consequently the agglomerates would be expected to be polycrystalline. Oriented attachment could possibly arise if the surfactant adsorbed only on specific faces, which then attached to one another via surfactant hydrophobic tail group interactions. This is unlikely in the DPA systems though, as it is the faster growing faces that show the oriented attachment, and growth of these faces would have been expected to be slowed significantly, if surfactant adsorption occurred on only these faces. A degree of surfactant adsorption on all faces may explain the polycrystallinity arising from microemulsions with a smaller droplet size at constant DPA concentration, because these microemulsions have a higher surfactant to DPA ratio. As a result, the surfactant would be adsorbed onto the particle surface and slow down or prevent the further aggregation. The effect of strong surfactant adsorption can be illustrated by the enhanced hydrophobic interactions, leading to an increase in the DP arcing due to the increased polycrystallinity of the sample.

Viscosity may also contribute to the oriented attachment of the nanoparticles. Since the viscosity increases dramatically with the increase of dispersed phase, the microemulsion droplets in samples with larger dispersed phases have slower collision rate and longer collision duration. Therefore, the lifetime of a transient dimer is longer, proving sufficient time for the primary nanoparticles to orientate to their preferred geometry or face before aggregating further. The slower collision rate also slows down the random attachment of the nanoparticles. Consequently, the NAs produced are better self-organised and thus are single-crystal like. For microemulsions with smaller dispersed phases, the relatively low

viscosity and fast collision rate would thus lead to less organised NAs and arcing in the DP due to the nanoparticle misalignment.

Estimating the average number of DPA molecules existing in the droplet could provide further understanding of the system at the molecular level. From Table 5.8, the well organised particles that arise from DPA concentrations of >10 mg/ml appear to require at least a mean value of ~ 1–2 molecules per droplet for the initial primary particles to aggregate. The primary particle size and the final crystal distribution were increasing from 20–50 nm when droplets contained on average ~3–5 molecules to 50–100 nm when each had on average ~5–10 molecules.

Table 5.8 Estimation of DPA number in each droplet

Dispersed phase /μl g^{-1}		50	75	100	125	150	175	200	225
Mean $r_{c(gift)}$/nm		2.40	2.91	3.14	3.23	3.56	3.65	3.73	4.01
No. of droplets in the system (x 10^{18})		5.15	3.18	2.68	2.65	2.10	2.07	2.06	1.74
Mean no. of DPA molecules per droplet	18 mg/ml	0.6	1.5	2.4	3.1	4.6	5.5	6.3	8.4
	12 mg/ml	0.4	1.0	1.6	2.0	3.1	3.7	4.2	5.6
	10 mg/ml	0.4	0.8	1.3	1.7	2.6	3.0	3.5	4.6
	8 mg/ml	0.3	0.7	1.1	1.4	2.1	2.4	2.8	3.7
	2 mg/ml	0.1	0.2	0.3	0.3	0.5	0.6	0.7	0.9

The lower concentration and smaller droplet size samples had fewer molecules in each sample. Due to the microemulsion polydispersity and the (assumed) Poisson variation in the distribution of solute molecules amongst droplets, some of the larger droplets will contain significantly more DPA molecules so that the formation of (near) stable DPA nuclei within these droplets is likely. The subsequent dimer formation and material exchange can encourage the growth to the primary particles, which are available for orientated attachment at a later stage. How large the final crystals were, would depend on the number of such events occurring. However, such events are statistically fewer compared to more concentrated DPA solutions and thus observed smaller extent of oriented attachment and smaller aggregate sizes were obtained. Once each droplet contained less than on average ~1-2 molecules there were insufficient DPA molecules to form a (near) stable nucleus, then the system would not be able to form the primary particles and thus would never crystallise.

5.3.3 Triton X-114 systems

A similar procedure has been carried out with the Triton X-114 system to investigate the microemulsion system similar to Triton X-110 but without the influence of co-surfactant(s). On comparison to the Triton X-100 microemulsion system, the amount of dispersed phase (≤ 65 µl of dispersed phase in per gram of surfactant solution) that Triton X-114 can stabilise is reduced due to the relatively low composition of surfactants (~30% w/w) used in the microemulsion preparation.

5.3.3.1 Initial observations

No sign of macroscopic crystals were seen after several months of microemulsion formation. Consequently Triton X-114 samples were inspected by TEM and unsurprisingly NAs of 30–100 nm were observed. However, these aggregates were far less organised compared to the Triton X-100 samples. The individual nanoparticles were more distinct but the FFTs and DPs indicated they're more randomly orientated (or much less ordered) polycrystalline samples.

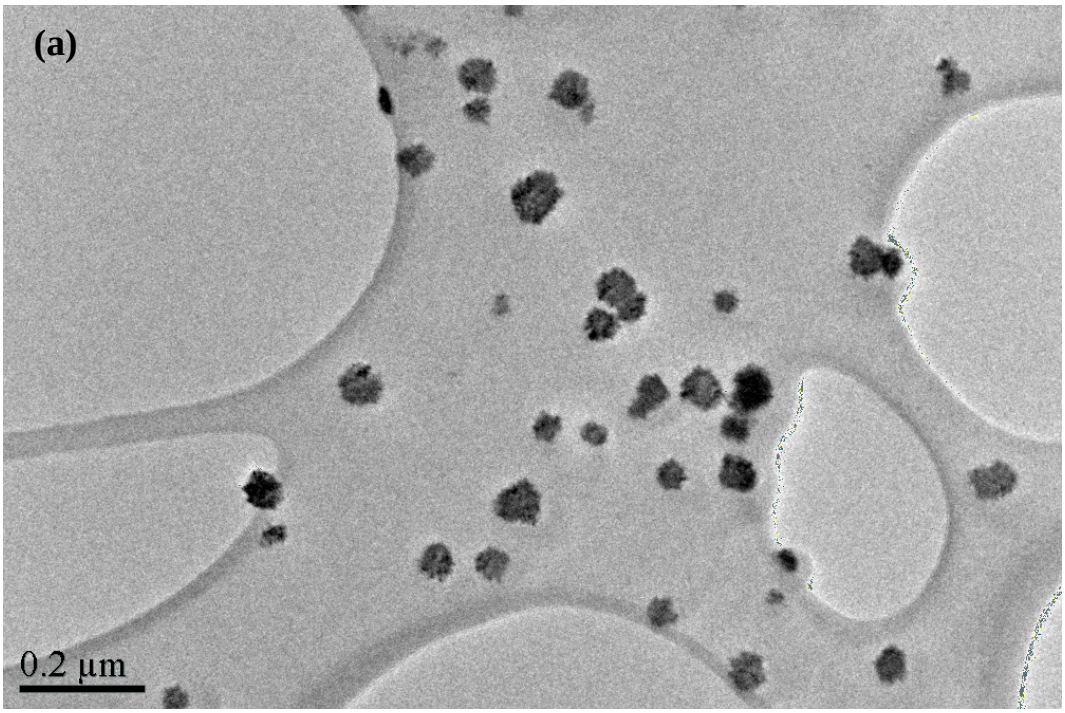

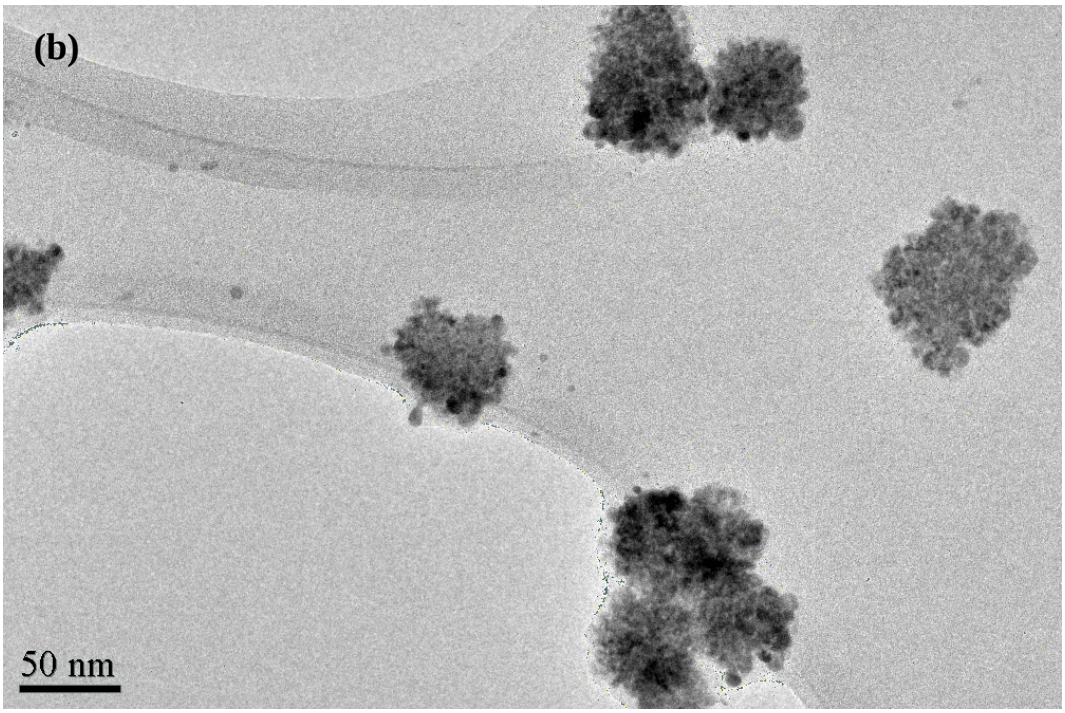
(b)
50 nm

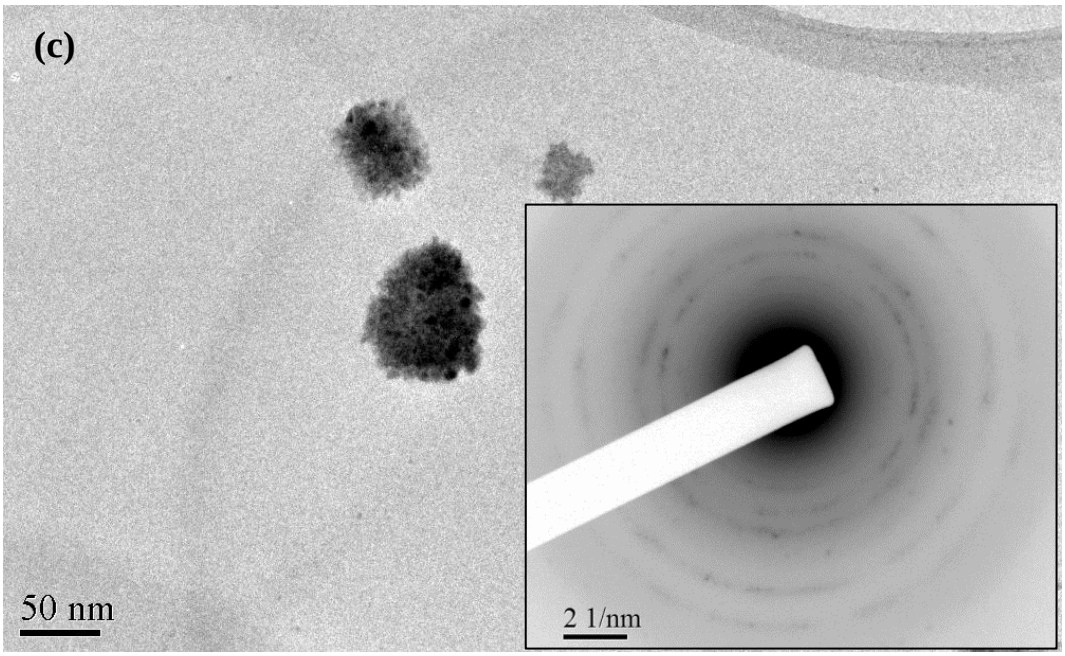
(c)
50 nm
2 1/nm

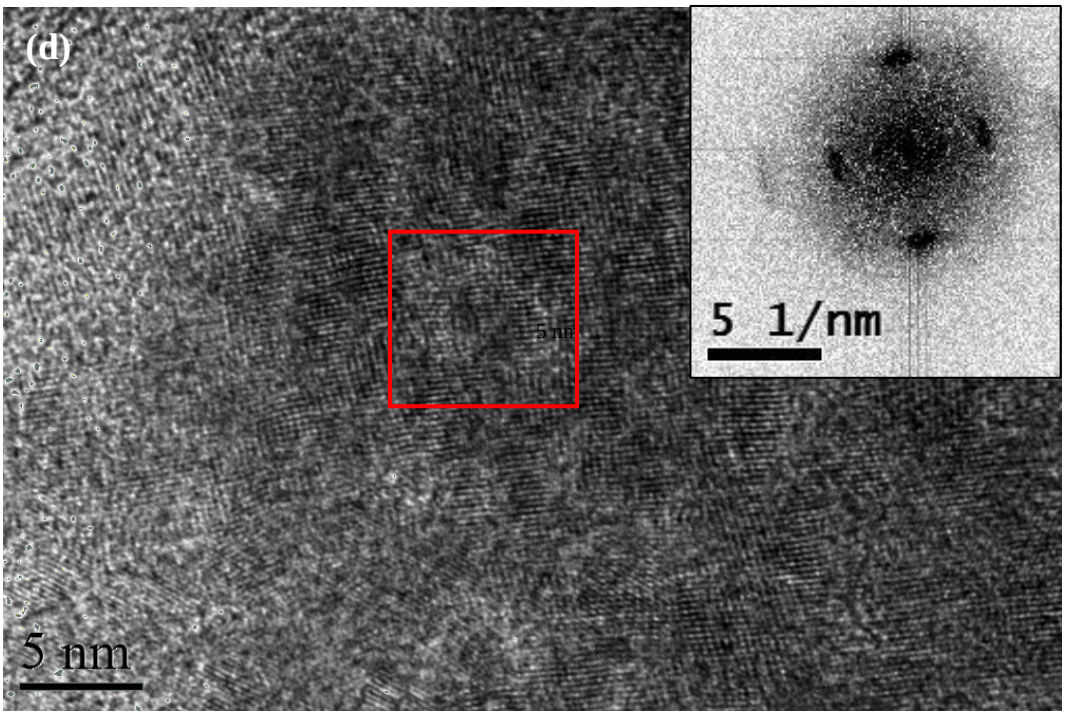

Figure 5.22 Nanoparticles obtained from Triton X-114 microemulsion system: (a) the BF image from 20 µl/g of 12 mg/ml DPA in 2M HCl sample; (b-d) from the sample containing 65 µl/g of 12 mg/ml DPA in 2M HCl solution: (b) the BF image of the area; (c) the BF image with its inlaid DP image (inverted); (d) the HREM with inlaid FFT images (inverted).

Triton X-114 and X-100 are very similar in structure, where Triton X-114 only has a slightly shorter hydrophilic head group (~7.5 alkyl groups) compared to Triton X-100 (~9.5). Therefore Triton X-114 is slightly more hydrophobic with a HLB value of 12.4, whereas Triton X-100's HLB value is 13.5. Such small differences in their HLB values and structures are not sufficient to cause the nanoparticle size variation. Studies[23, 36] on silica-coated iron oxide nanoparticles have shown that non-ionic surfactants with similar structural and physical properties, i.e. Triton X-100 and Igepal CO-720, did not greatly influence the microstructure of the nanoparticles, formed from these microemulsions, which also contained cyclohexane and hexanol. Consequently, in our study, the surfactants are less likely to contribute to this morphology and size variation.

One major difference between the two systems is that Triton X-114 did not employ any cosurfactant. In general, consurfactant has been found to enhance the rate of transient dimer formation and material exchange as it can increase the 'fluidity' of the interfacial film. However, cosurfactant also leads to an increase in the surfactant film curvature, thus giving smaller particles[37, 38]. This effect can be

illustrated by ZnS nanoparticle[39] formation. With the addition of cosurfactants, quantum dots with diameter less than 5 nm in size were obtained. Despite the quantum dots can further agglomerate into secondary particles of 40–100 nm in size, they are still much smaller than those obtained from microemulsions without cosurfactants, which were of size ~μm. Therefore, cosurfactant could heavily influence the particles' size and morphology.

Furthermore ultrasound sonication is also an essential requirement to prepare Triton X-114 microemulsion. The thermal energy introduced by ultrasound could also lead to structural changes in the nanoparticles. This thought is based on the study that ultrasonic cavitation can generate local temperature up to 5000 K and local pressure of up to 500 atm[40]. This process would speed up the cooling and heating rate to at least 10^9 K/s, allowing process/reactions that would not occur under normal conditions to take place. In our case, ultrasound sonication might have enhanced the nanoparticle formation.

5.3.3.2 Indexing

To identify the form of these nanoparticles, their DPs were indexed against the known forms of DPAs. Due to the severe misalignment in the nanoparticles, their DPs were mostly ring patterns so were missing information regarding the angles between the scattering planes. Figure 5.23 is an example with d-spacings of 3.041Å, 2.529Å, 2.207Å, 1.580Å and 1.355Å. However, the d-spacing values between different forms are very comparable and this increases the difficulty in identifying the exact form, as listed in Table 5.9. For the above reasons, the HREM image of a region of interest has been analysed, which revealed the same FFT pattern as the Triton X-100 sample, i.e. it is consistent with the monohydrate form of DPA.

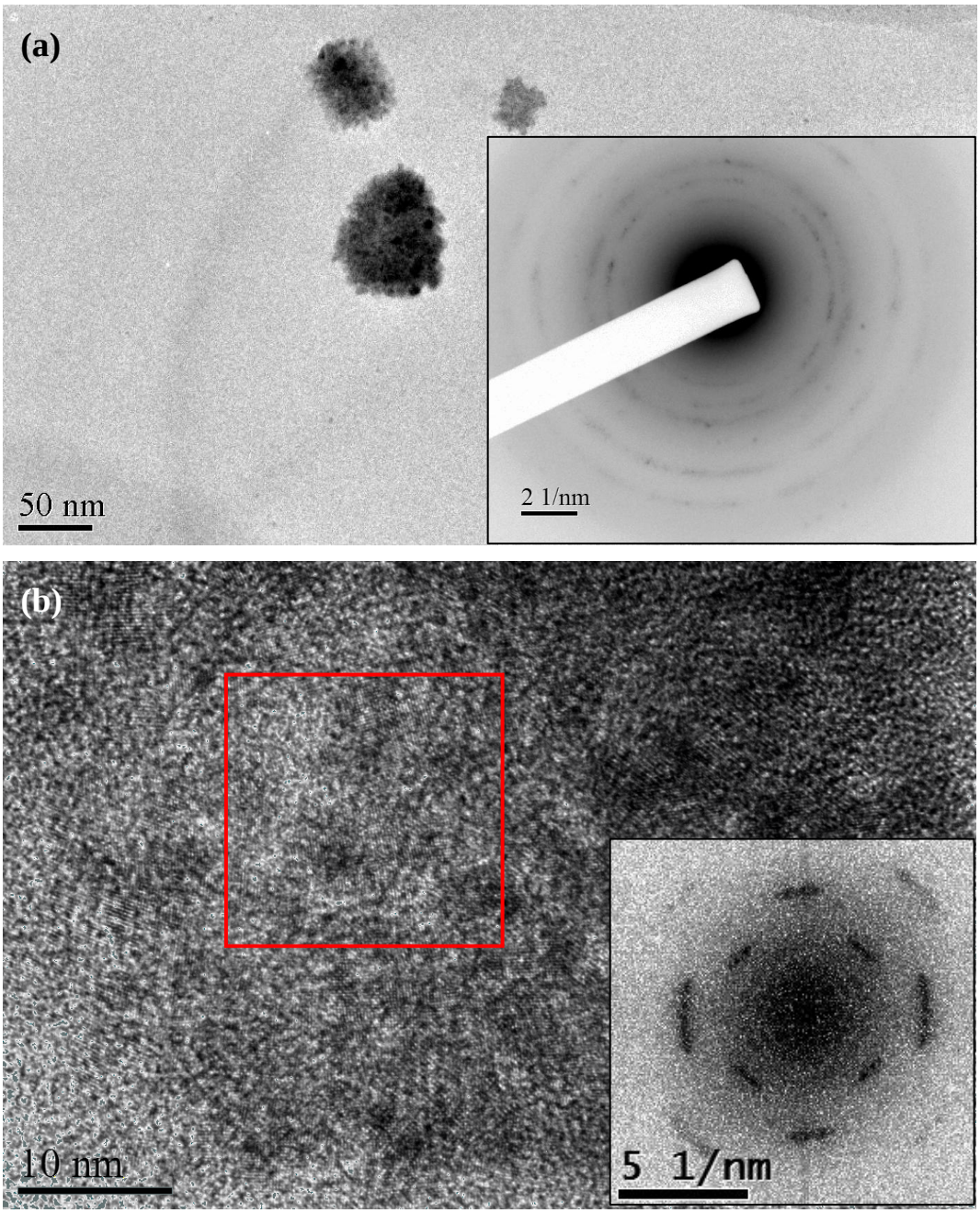

Figure 5.23 Microemulsion sample containing 65µl/g of 12 mg/ml DPA in 2M HCl solution: (a) the BF with the inlaid DP images (inverted); (b) the HREM with inlaid (inverted) FFT images

Table 5.9 Comparison of d-spacing values from Triton X-114 polycrystalline samples and other DPA forms

Nanoparticles	**Monohydrate**		**Dihydrate**		**Anhydrous**	
d-spacing	d-spacing	*hkl*	d-spacing	*hkl*	d-spacing	*hkl*
3.041	3.058	400	3.048	120	3.039	101
2.529	2.519	312	2.501	132	2.508	$14\bar{1}$
2.207	2.209	013	2.204	140	2.210	$12\bar{2}$

5.3.3.3 Effect of dispersed phase variation

The dispersed phase volume was varied from 20 µl/g to 65 µl/g which was a much smaller range compared to Triton X-100, due to smaller microemulsion region of this system. As a result, the differences between 20 µl/g and 65 µl/g samples of 12 mg/ml DPA solution were not as distinct as in the 50 µl/g to 225 µl/g regions for the Triton X-100 case. The 65 µl/g sample was slightly more organised in morphology and the size of the overall aggregate was slightly larger (~30–50 nm) while the 20 µl/g sample was ~15–40 nm. In addition the primary particles (that are the building units of the aggregates) were more visible in the 65 µl/g sample with diameter of ~5–10 nm whereas the 20 µl/g sample contained particles of ~2–5 nm, as shown in Figure 5.24.

To investigate the slight difference between these samples, SAXS and GIFT analysis were employed to measure and model the droplet size. Also geometric calculations on the droplet sizes were performed for comparison. During the geometric calculation, the surface area of Triton X-100 was adopted as a good estimation for Triton X-114 since their structures only differ by 2 polyethylene oxide groups.

Large discrepancies in radii values were observed between the Geometric calculations and GIFT analysis, see Table 5.11. As the dispersed phase volume increased, the droplet sizes were larger. The *p(r)* distribution remained as the simple hard sphere model which was postulated to be due to both the lack of 1-hexanol and so the weaker electron contrast between the surfactant tail groups and the cyclohexane dispersed phase.

Table 5.10 Electron density per A^3 for Triton X-114 and its EO head group

	Triton X-114	EO group
Density/g ml^{-1}	1.06	1.06
No. of e^-	294	24
M_r /g mol^{-1}	537	44
Electron Density /A^{-3}	0.35	0.34

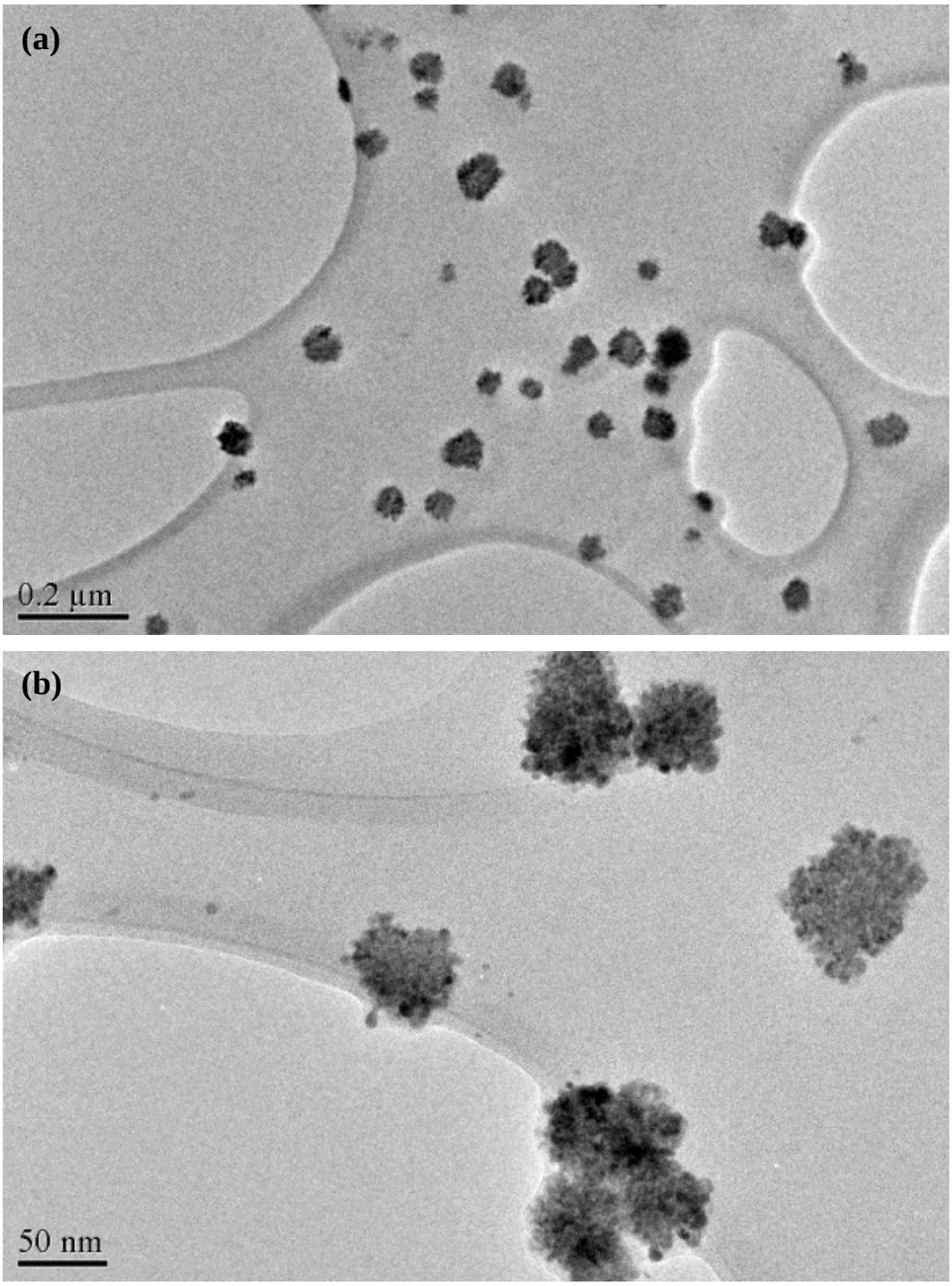

Figure 5.24 BF images of microemulsion samples with (a) 20 µl/g of 12 mg/ml DPA in 2M HCl sample; (b) 65 µl/g of 12 mg/ml DPA in 2M HCl sample

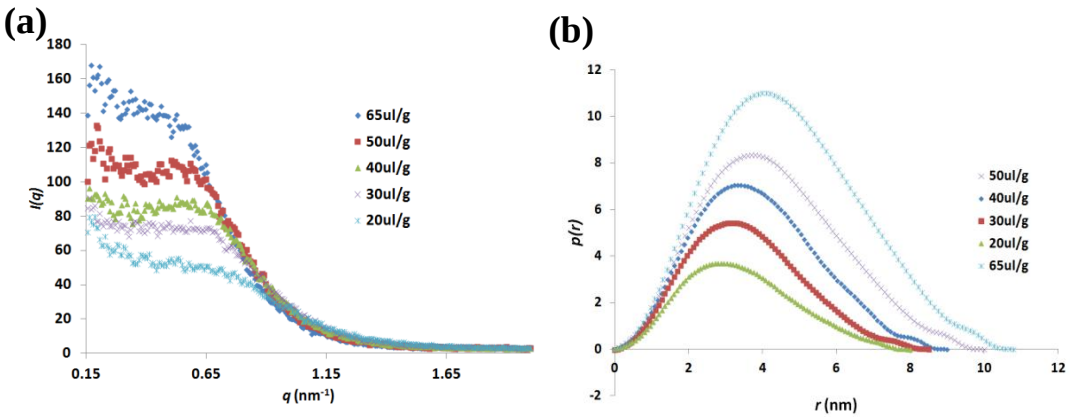

Figure 5.25 Droplet size measurements obtained from SAXS: (a) *I(q)* vs *q*; (b) *p(r)* vs *r*.

Calculation of the water molecules that can be bound to the surfactants per droplet was done based on the GIFT analysis droplet radius. Similar to the Triton X-114 microemulsion with aqueous inner phase, free water molecules only existed with dispersed phase volumes greater than 50 µl/g. The increase in droplet size with the dispersed phase was consistent with the primary particle size observed. For smaller droplets at 20 µl/g, the mean diameter for these droplets is ~6–6.6 nm. Since microemulsions always have a degree of polydispersity[41, 42] (up to 20% for a moderate level), the actual droplet size could deviate [4] from the mean values for ±0.3 nm of the droplet, assuming a Gaussian distribution of the droplet size is followed. Thus the size distribution of the primary particle can be rationalised in terms of the fluctuation in microemulsion droplet size. With larger droplets (65 µl/g), the mean droplet diameter increased to ~10–11 nm, and hence the primary nanoparticles are larger.

The GIFT droplet radius in this system was much larger that the geometric estimation. Particularly, at 65 µl/g the difference can be as large as 20%. This was postulated to the preferred location of HCl within the microemulsion. The HCl might set at the rigidly water region that is in close proximity to the surfactant interface and thus affect the surfactant packing. Table 5.12 has compared the droplet sizes of the microemulsions with pure aqueous water and 2M HCl solutions as dispersed phases. The latter was found to be much bigger, suggesting the swelling effect of HCl.

Table 5.11 Calculation from the droplet radius obtained from GIFT analysis to the theoretical fraction of water bound to Triton X-114

Dispersed phase /μl g^{-1}	20	30	40	50	65
Mean $r_{c(geometric)}$/nm	3.34	3.52	3.7	3.88	4.14
Mean $r_{c(gift)}$/nm	3.33	4.12	4.36	4.84	5.22
Mean $V_{c\ (gift)}$/nm^3	154.8	292.6	348.0	475.3	598.7
Approx. no. of droplets in the system (x 10^{18})	1.21	0.68	0.60	0.46	0.39
Mean no. of H_2O molecules per droplet (x 10^3)	0.53	1.39	2.08	3.35	5.07
Mean no. of Triton X-114 molecules per droplet (x 10^3)	0.28	0.48	0.54	0.70	0.81
Mean H_2O can be taken by Triton X-114 per droplet (x 10^3)	1.44	2.56	2.87	3.69	4.30
Theoretical fraction of H_2O can be bound to Triton X-114	2.8	1.8	1.4	1.1	0.8

Table 5.12 Comparison of the droplet sizes of microemulsions constructed from pure aqueous water and 2M HCl solutions as dispersed phase.

Dispersed phase /μl g^{-1}		20	30	40	50	65
Mean $r_{c(gift)}$/nm	Aqueous phase	3.29	3.55	3.73	3.98	4.36
	2M HCl	3.33	4.12	4.36	4.84	5.22

The number of DPA molecules per droplet is estimated as listed in Table 5.13. Only if the average number of DPA molecules exceeds ~1–2 per droplet, do primary nanoparticles of 2–10 nm in diameter start to form. Once the DPA molecules approach ~2–3 molecules per droplet on average, NAs of the primary particles with a diameter of 20–100 nm would appear.

Table 5.13 Estimation of average number of DPA molecules per droplet at various microemulsion compositions

Dispersed phase /μl g^{-1}		20	30	40	50	65
Mean $r_{c(gift)}$/nm		3.33	4.12	4.36	4.84	5.22
No. of droplets in the system (x 10^{18})		1.21	0.68	0.60	0.46	0.39
Mean no. of DPA molecules per droplet	18 mg/ml	1.1	2.9	4.4	7.1	10.9
	12 mg/ml	0.7	1.9	2.9	4.7	7.2
	10 mg/ml	0.6	1.6	2.4	3.9	6.0
	8 mg/ml	0.5	1.3	1.9	3.1	4.8
	2 mg/ml	0.1	0.3	0.5	0.8	1.2

5.3.3.4 Effect of concentration

A similar trend to Triton X-100 was observed in this system in that higher concentration samples tend to have more organised nanoparticles. At concentrations less than 8 mg/ml, only nanoparticles between 3–10 nm in size were seen, while at 10 mg/ml, aggregates of these nanoparticles with diameters of *approx.* 20–100 nm were formed from these particles. In contrast to the Triton X-100 case, the nanoparticles grown from the Triton X-114 microemulsions were often polycrystalline, rather than iso-oriented crystals/mesocrystal like.

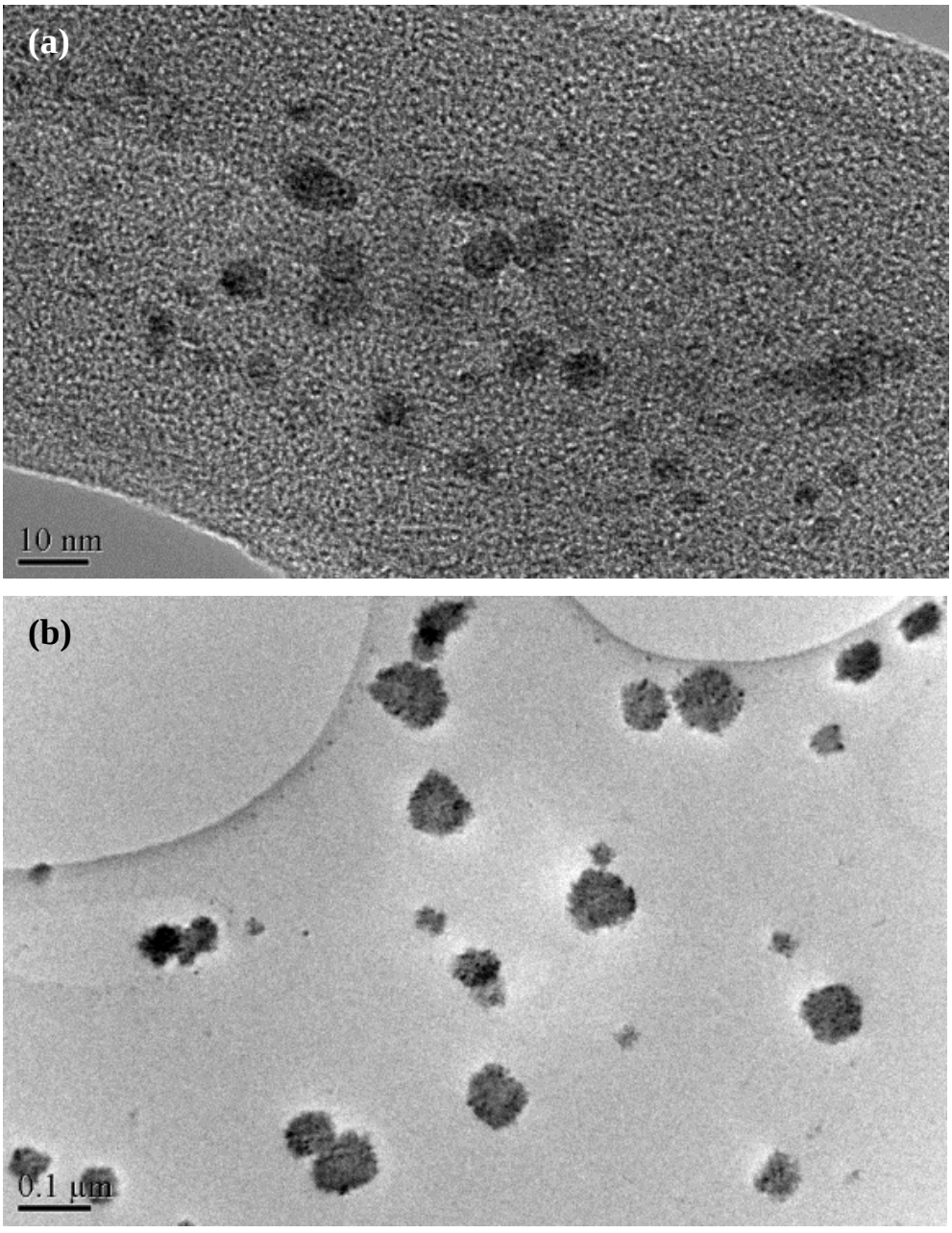

Figure 5.26 BF images of DPA NAs with a DPA concentration of (a) 8 mg/ml; (b) 12 mg/ml

5.4 Conclusions

This chapter concluded the work carried out with Triton X-100/1-hexanol/cyclohexane and Triton X-114/cyclohexane microemulsions employing DPA in 2M HCl solutions as the dispersed phases. The purpose of this was to ensure the DPA was predominantly in its acid form and so eliminate the metal cation participation and thus form the acid crystals rather than metal salts.

Both microemulsion systems can produce NAs of the DPA monohydrate forms with diameters in the range of 20–100 nm, when the DPA in 2M HCl solution concentration is greater than 8 mg/ml. These NAs are agglomerated via oriented attachment of primary nanoparticles of size 2–10 nm in diameter. When the concentration of DPA in 2M HCl solution is below 2 mg/ml, no crystallisation of the primary nanoparticle was observed. In general, Triton X-100 microemulsions can produce more organised NAs. The DPs and the FFT images of the best organised NAs were single-crystal like, despite the fact that they comprise the primary nanoparticles, demonstrated by their non-uniform densities across the nanocrystal surface. Hence these may be considered as DPA iso-oriented crystals/mesocrystals. These single-crystal like NA were produced at the largest disperse phase volumes (225 μl/g) and the highest DPA concentrations (18 mg/ml). At lower dispersed phases and concentrations, slightly less organised NAs were obtained, giving ‘arcing’ in the DPs rather than the single-crystal like spot DPs. This is due to the misalignment in the NAs. The level of misalignment increased with the decrease of dispersed phase and DPA concentration, resulting in ring DPs for polycrystalline NAs.

In contrast, the NAs of Triton X-114 were much less organised and sometimes polycrystalline, producing mostly ‘arcing’ or ‘ring’ DPs. However, the individual primary particles were more distinct compared to the Triton X-100 system due to their less organised packing. The less organised packing was postulated to be due to the lack of cosurfactant.

Further investigations, e.g. droplet size analysis from SAXS data, viscosity measurements, and pH of microemulsions, were performed with the Triton X-100

microemulsions. SAXS data were analysed using GIFT analysis to work out the droplet sizes of microemulsions, r_{gift}, with difference volumes of dispersed phases. r_{gift} can then be used to rationalise the crystallisation outcome by estimating the average number of surfactant water and DPA molecules per droplet.

Due to the significant increase in viscosity observed with the dispersed phase, the viscosity data were collected to provide an insight into the structural information of the microemulsions and also the kinetics of the systems. Although the viscosity increased by almost a factor of 5, percolation was not observed. The kinetics, i.e. the droplet collision rate and the average collision time, were thus calculated based on the viscosity data. The collision rate was found to be ~5 times lower at 225 µl/g than that of 50 µl/g, while the average collision time was ~5 times longer for 225 µl/g microemulsions.

The pH values of microemulsions with water, DPA and HCl solutions were measured as a function of dispersed phase, to illustrate the effect of acidifying the microemulsions. The most dramatic change was observed for DPA solutions, with nearly neutral pH at the small dispersed phases and acidic (~3–4) at the larger volumes. In contrast the pH changes in microemulsions comprising pure water and aqueous HCl were much smaller. In the 2M HCl microemulsions, the measured pH values were maintained at a very acidic level (≤1) in the entire dispersed phase range. At smaller dispersed phases the pH values were slightly more acidic than at larger dispersed phases. This was not expected since $[H^+]$ per droplet decreased with the dispersed phase but the effect is not large and may be related to the ability of the probe to provide accurate pH values for microemulsions.

5.5 References

1. B. L. Rivas and A. Maureira, *Inorg. Chem. Commun.*, 2007, **10**, 151-154.
2. Y. Bayrak and M. Iscan, *Colloids Surf., A*, 2005, **268**, 99-103.
3. J. L. Chai, J. Liu and H. L. Li, *Colloid J*, 2009, **71**, 257-262.
4. S. Kosmella and J. Koetz, *Curr. Opin. Colloid Interface Sci.*, 2012, **17**, 261-265.
5. X.-q. Li, J.-l. Chai, S.-c. Shang, H.-l. Li, J.-j. Lu, B. Yang and Y.-t. Wu, *J. Chem. Eng. Data.*, 2010, **55**, 3224-3228.
6. B. M. S. Inc, *Cerius2: Materials Science : Tutorial Guide : Release 2.0*, BIOSYM/Molecular Simulations, 1995.
7. S. L. Childs, P. A. Wood, N. r. Rodríguez-Hornedo, L. S. Reddy and K. I. Hardcastle, *Cryst Growth Des*, 2009, **9**, 1869-1888.
8. L. Qi and J. Ma, *J. Colloid Interface Sci.* , 1998, **197**, 36-42.
9. R. Porcel, A. B. Jódar, M. A. Cabrerizo, R. Hidalgo-Álvarez, Martı, amp, x, R. n, amp, x and A. guez, *J. Colloid Interface Sci.* , 2001, **239**, 568-576.
10. M. Ethayaraja, K. Dutta, D. Muthukunmaran and R. Bandyopadhyaya, *Langmuir*, 2007, **23**, 3418-3423.
11. Y. Pan, D. Heryadi, F. Zhou, L. Zhao, G. Lestari, H. Su and Z. Lai, *CrystEngComm*, 2011, **13**, 6937-6940.
12. Z. Chen and Z. Nan, *J. Colloid Interface Sci.* , 2011, **358**, 416-422.
13. S. Bharathi, D. Nataraj, M. Seetha, D. Mangalaraj, N. Ponpandian, Y. Masuda, K. Senthil and K. Yong, *CrystEngComm*, 2010, **12**, 373-382.
14. Z. Kang, E. Wang, S. Lian, B. Mao, L. Chen and L. Xu, *Mater. Lett.*, 2005, **59**, 2289-2291.
15. D. Kuang, A. Xu, Y. Fang, H. Liu, C. Frommen and D. Fenske, *Adv. Mater.*, 2003, **15**, 1747-1750.
16. N. Zhang, W. Bu, Y. Xu, D. Jiang and J. Shi, *J. Nanosci. Nanotechno.*, 2008, **8**, 1468-1472.
17. D. P. Acharya and P. G. Hartley, *Curr. Opin. Colloid Interface Sci.*, 2012, **17**, 274-280.
18. G. Kaur, L. Chiappisi, S. Prévost, R. Schweins, M. Gradzielski and S. K. Mehta, *Langmuir*, 2012, **28**, 10640-10652.
19. A. Kogan, D. E. Shalev, U. Raviv, A. Aserin and N. Garti, *The Journal of Physical Chemistry B*, 2009, **113**, 10669-10678.
20. A. Kogan, D. E. Shalev, U. Raviv, A. Aserin and N. Garti, *J. Phys. Chem. B*, 2009, **113**, 10669-10678.
21. M. Clausse, L. Nicolas-Morgantini, A. Zradba and D. Touraud, in *Microemulsion Systems*, eds. H. L. Rosano and M. Clausse, M. Dekker, New York, 1988.
22. D. S. Mathew and R.-S. Juang, *Sep. Purif. Technol.*, 2007, **53**, 199-215.
23. M. A. López-Quintela, C. Tojo, M. C. Blanco, L. García Rio and J. R. Leis, *Curr. Opin. Colloid Interface Sci.*, 2004, **9**, 264-278.
24. P. D. I. Fletcher, A. M. Howe and B. H. Robinson, *J. Chem. Soc. Faraday Trans. 1*, 1987, **83**, 985-1006.
25. M. A. López-Quintela, J. Rivas, M. C. Blanco and C. Tojo, in *Nanoscale Materials*, eds. L. Liz-Marzán and P. Kamat, Springer US, New York, 2004, pp. 135-155.
26. R. E. McIlwaine, H. Fenton, S. K. Scott and A. F. Taylor, *J. Phys. Chem. C.*, 2008, **112**, 2499-2505.
27. F. M. Menger and K. Yamada, *J. Am. Chem. Soc.*, 1979, **101**, 6731-6734.
28. M. da Graca Miguel, H. D. Burrows, M. A. Escaroupa Pereira and A. P. Varela, *Colloids Surf., A*, 2001, **176**, 85-99.
29. R. K. Dutta and S. N. Bhat, *Colloids Surf., A*, 1996, **106**, 127-134.

30. N. Li, Y. Gao, L. Zheng, J. Zhang, L. Yu and X. Li, *Langmuir*, 2006, **23**, 1091-1097.
31. N. Li, S. Zhang, H. Ma and L. Zheng, *Langmuir*, 2010, **26**, 9315-9320.
32. T. Kumar, A. Bera and A. Mandal, *WASET*, 2012, **64**, 1114-1119.
33. N. A. Halliday, A. C. Peet and M. M. Britton, *J. Phys. Chem. B*, 2010, **114**, 13745-13751.
34. H. Christenson, S. E. Friberg and D. W. Larsen, *J. Phys. Chem.*, 1980, **84**, 3633-3638.
35. D. J. Christopher, J. Yarwood, P. S. Belton and B. P. Hills, *J. Colloid Interface Sci.* , 1992, **152**, 465-472.
36. S. Santra, R. Tapec, N. Theodoropoulou, J. Dobson, A. Hebard and W. Tan, *Langmuir*, 2001, **17**, 2900-2906.
37. J. Eastoe, M. J. Hollamby and L. Hudson, *Adv. Colloid Interface Sci.*, 2006, **128–130**, 5-15.
38. A. Zielińska-Jurek, J. Reszczyńska, E. Grabowska and A. Zaleska, in *Microemulsions - An Introduction to Properties and Applications*, ed. R. Najjar, InTech, 2012.
39. C. Tawatchai, C. Amornsak, D. Joydeep, R. Uracha and T. Wiwut, *Sci. Technol. Adv. Mat.*, 2005, **6**, 266.
40. C. Zhang, Q. Wang, H. Xia and G. Qiu, *Eur. Polym. J.*, 2002, **38**, 1769-1776.
41. F. Sicoli, D. Langevin and L. T. Lee, *J. Chem. Phys.*, 1993, **99**, 4759-4765.
42. L. Arleth and J. S. Pedersen, *Phys. Rev. E*, 2001, **63**, 061406.

Chapter 6 Conclusions and Further work

6.1 Overview of this project

The aim of this project was to investigate the possibility of thermodynamic control of polymorphic systems within the 3D-nanoconfinement of a microemulsion droplet, using glycine and DPA as the model compounds.

The study of glycine was detailed in Chapter 3, with the purpose to test the effect of 3D-nanoconfinement under conditions, which in bulk solution would be preferential for the formation of metastable forms. The most stable γ form of glycine was obtained from an 'optimum' microemulsion composition of 6 g heptane, 4 g Span 80+Brij 30 (1:1 w/w), 0.25 g of 4% (w/w) glycine solution, 0.25 g of pure water and 1 g of methanol antisolvent. Further, variations to the optimal system were also investigated: microemulsion preparation methods, glycine concentration, methanol volume, surfactant-to-heptane ratio, and the length of crystallisation.

- For the incorporation of an antisolvent, a mixed microemulsion method was found to be the most reliable, robust, and reproducible technique, hence it was employed in the study.
- Glycine concentration had a huge impact on the crystallisation outcome; only 4% (w/w) glycine solution yielded the γ form. No crystallisation was observed from ≤ 3.5% (w/w) glycine solution, with the metastable forms being dominant for glycine solutions ≥ 4.5% (w/w). This illustrates the 4% (w/w) solution had just sufficient crystallisable material. Hence as the metastable forms had sufficient material to form stable nuclei, thermodynamic control was achieved with predominantly the most stable γ form crystallising.
- An increase of methanol is noted to increase the supersaturation of a glycine solution, thus leading to the loss of thermodynamic control, resulting in the crystallisation of the metastable forms. With very high methanol content, the least stable β form is the sole product, due to the

solvent specific interactions between methanol and glycine molecules that poisoned other forms.

- The surfactant-to-heptane ratio did not affect the polymorphic outcome since a microemulsion was maintained even at a 9:1 surfactant-to-heptane ratio.
- The 'age' of the microemulsion sample is crucial to the polymorph which is observed, due to the vastly different growth rates of the glycine polymorphs (i.e. the α form grows ~500 times faster than the γ form). This explains the following observations; on day 7 the majority of the macroscopic visible crystals were of α form, whilst on day 45, the γ form dominated. The increased yield of the γ form with time is mainly attributed to its extremely slow growth, with the nanocrystals of the γ form detected after 48 hrs of microemulsion preparation. The α to γ form transformation is significantly delayed in the microemulsion, and so this is not expected to contribute to γ form formation (or only contribute to a very small part).

Thus the thermodynamic control of glycine crystallisation within the 3D-nanoconfinement was evidenced, with careful control of the microemulsion composition.

DPA was chosen as an target to study the thermodynamic control of hydrates within 3D-nanoconfinement. From bulk solutions (non-confined), 2 hydrates (monohydrate and dihydrate) and 1 anhydrous form of DPA were obtained. However, within the microemulsion metal salts formation occurred, which was unexpected. The main crystallisation outcome in these systems are summarised in Table 6.1.

Table 6.1 Crystallisation outcome from various microemulsion compositions

Surfactant	Lower DPA concentration Smaller dispersed phase	Higher DPA concentration Lower dispersed phase
AOT	Anhydrous needle form I (Na salt)	Sodium salt trihydrate
Span 80/Brij 30	Anhydrous needle form I (Na salt)	
Triton X-100/hexanol	Anhydrous needle form II (Na salt)	Anhydrous needle form I (Na salt)
Triton X-114	Anhydrous needle form I (Na salt)	Potassium salt hydrate

Upon changing the solvent from UHP water to methanol, a new methanol solvate of a sodium salt form of DPA was obtained. At larger dispersed phase volumes, the hydrate/solvate formation was demonstrated, which was attributed to a larger central water pool with more freely moving water available for binding within the microemulsion droplets. However, the formation of a salt form again showed that the metal ion participation in the DPA crystallisation was not resolved, despite the confined phase being non-aqueous. The metal salt formation was attributed to the salt chelating behaviour of DPA, known previously in biological and chromatographic systems, in addition to the observed shift in pH within the microemulsion and the self-association of DPA ionic forms under the influence of pH. As an attempt to prevent the metal ion incorporation, 2M HCl was added to the microemulsion to influence the pH level. This had a significant effect on the crystallisation with only square plate-shaped NAs (30-100 nm in dimension) of nanoparticles with diameter of 2-10 nm being obtained. These NAs were shown by TEM to be consistent with the most stable DPA monohydrate form, indicating that the microemulsions exerted thermodynamic control over the crystallisation process again. However, the morphology of these crystals suggested that their formation arose from a nanocrystal oriented attachment mechanism, rather than a classical molecule by molecule growth route. The effects of DPA concentration and dispersed phase volume on the size and morphology of the NAs were investigated. Further, measurements of the viscosity and pH were taken to provide a rationale for the crystal formation mechanism. The findings can be summarised as follows.

- In both the Triton X-100 and Triton X-114 systems, no macroscopic crystals were obtained. Instead NAs of ~20-100 nm were observed via

TEM. In general, the NAs from Triton X-100 were more organised than those from Triton X-114.

- For Triton X-100 microemulsions, with an increase in both the DPA concentration and the dispersed phase volume, an improvement in the ordering of the NAs was found, shown by their single-crystal like DP's.
- For Triton X-114 microemulsions, the nanoparticles (~2-10 nm) aggregate better into nanocrystals (~20-100 nm) with an increase in both the DPA concentration and the dispersed phase volume. However, the NAs are significantly more misaligned than in the Triton X-100 system, giving rise to arcing and rings in the DP and FFT, respectively.
- The viscosity of the microemulsions experienced a dramatic increase with the addition of dispersed phase. Microemulsions with a larger dispersed phase are expected to have much slower droplet collision rates but much longer droplet collision times. It was postulated that the longer droplet collision times, provided sufficient time for the oriented attachment of the nanoparticles to occur, because it allowed nanocrystals to transfer from one droplet to another during the longer transient dimer formation.
- pH measurements in Triton X-100 indicated a pH shift with variation of the dispersed phase volume within the microemulsion (i.e. pH ~6 at 50 µl/g and pH ~3 at 225 µl/g). With reference to the work of Crans *et. al.*[1] and Peral *et. al.*[2], this provides a rationale to the observed metal salt formation. The addition of 2M HCl maintained the pH at 0.3-0.6, even at small dispersed phases, eliminating the metal ion participation and yielding the iso-oriented crystal/mesocrystal-like NAs.

To conclude, Chapter 3 demonstrated that thermodynamic control is achievable within 3D-nanoconfined volumes, with Chapter 4 extending the concept to hydrates and solvents. Metal salt participation in DPA crystallisation can be prevented by the addition of 2M HCl in the microemulsions. More importantly, controlled crystallisation to allow the oriented attachment of nanoparticles was

also explored, with NAs similar to iso-oriented crystals being obtained and stabilised by the microemulsions.

6.2 Future work

The work described in Chapter 3 is reasonably complete, however, if time allowed, further work could be performed to study the kinetics of transient dimer formation, also known as the 'fusion-mass transport-fission' process, by Moulik *et. al.* and others[3-5]. Further studies on the early stage of crystallisation may be of interest since this would provide us an insight into the relative stability and yield of the α and γ forms at nanoscopic sizes.

In contrast, Chapter 4 explored the area of hydrate/solvate formation, and also raised the issue of impurity participation during crystallisation. The crystallisation of DPA, due to its chelating ability, provides an extreme case of metal salt impurity participation. Precautions and suitable treatments, e.g. the use of additives, may be required to inhibit impurity binding, such as using 2M HCl in DPA solution to prevent metal ion incorporation. UHP solvent could be an alternative to avoid any undesirable impurities, or chelators such as EDTA, crown ethers (e.g. 15-Crown-5, and 18-Crown-6), cryptand and DPA, could be used to eliminate unwanted metal prior to sample preparation. However, any interaction between the target compound and the above chelators should be accounted for, e.g. whether these complexes induce heterogeneous nucleation or participate in the crystal growth via adsorption.

Furthermore, Chapter 5 revealed the capabilities of microemulsions to control both the morphology and structure of NAs via the non-classical crystallisation route of oriented attachment of nanocrystals. This study may pave the way for improving both the organisation and stabilisation of nanoparticles. At present, we have only a preliminary understanding of the formation mechanism, and so future work to answer the following may provide further insight:

- Is the formation of these orientated NAs primarily dependent on the viscosity of the microemulsion? This could be tested by performing

crystallisation from a much less viscous system while maintaining the microemulsion composition, in particular, with a similar supersaturation ratio of DPA.

- The cause of polycrystallinity of the NAs from the Triton X-114 needs to be verified.
- The encounter rate factor, *D*, could be studied; clarifying the process of transient dimer formation rate and further information about the motion of the microemulsion droplets. Similar approaches to the AOT studies could be adopted after modification. Mays *et. al.*[6] used Tb(pyridine-2,6-dicarboxylic acid)$_3^{3-}$ and its quencher bromophenol blue to study the material exchange in the reversed microemulsions of AOT. Thus, by mixing the microemulsion doped with a suitable dye molecule with another microemulsion containing its quencher, their quenching rate could be monitored. Other reactions, e.g. proton/electron transfer and metal-ligand complexation[7], are also suitable to study the microemulsion kinetics.
- The scale-up of these NAs is essential for their extraction to allow for further analysis, using techniques, such as WAXS, to verify that they are indeed iso-oriented crystals or mesocrystals of the most stable monohydrate form of DPA. This may be achieved by employing a bicontinuous microemulsion as the reaction medium, which can possibly enhance the nanoparticle attachment rate by overcoming the viscosity problem.

Overall thermodynamic control of crystallisation via 3D-nanoconfinement was demonstrated with two model compounds: glycine and DPA. For glycine, careful control of the microemulsion composition is key to achieving the thermodynamic control. With DPA, the participation of metal impurities is unexpected; however with the incorporation of 2M HCl, the issue was overcome. Further studies on the formation mechanism of the NAs could enhance our knowledge and understanding of the oriented attachment process (non-classical crystallisation) within the microemulsions; possibly highlighting future applications via the employment of these high surface area materials.

6.3 References

1. D. C. Crans, A. M. Trujillo, S. Bonetti, C. D. Rithner, B. Baruah and N. E. Levinger, *The Journal of organic chemistry*, 2008, **73**, 9633-9640.
2. F. Peral, and E. Gallego, *Spectrochimica Acta Part A*, 2000, **56**, 2149.
3. S. Ray, S. Paul and S. P. Moulik, *Journal of Colloid and Interface Science*, 1996, **183**, 6-12.
4. P. Alexandridis, J. F. Holzwarth and T. A. Hatton, *The Journal of Physical Chemistry*, 1995, **99**, 8222-8232.
5. S. P. Moulik and A. K. Rakshit, in *Microemulsions*, ed. M. Fanun, CRC Press, Taylor & Francis Group, Boca Raton, London, New York, 2008, vol. 144.
6. H. Mays and G. Ilgenfritz, *Journal of the Chemical Society, Faraday Transactions*, 1996, **92**, 3145-3150.
7. P. D. I. Fletcher, A. M. Howe and B. H. Robinson, *Journal of the Chemical Society, Faraday Transactions 1: Physical Chemistry in Condensed Phases*, 1987, **83**, 985-1006.

Appendix 1 List of surfactants used in this thesis

Type	Name	Full name	Formula	Structure	HLB
Non-ionic	Span 80	Sorbitan monooleate	$C_{24}H_{44}O_6$	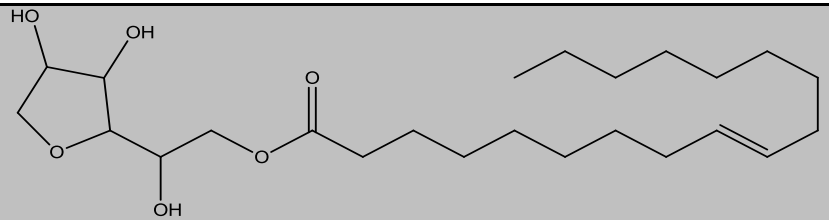	4.3
	Brij 30 (Now Brij L4)	Polyethylene glycol dodecyl ether	$C_{20}H_{42}O_5$	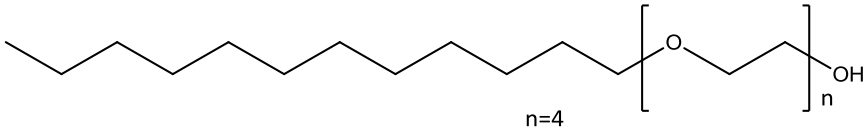	9.7
	Triton X-100	Polyethylene glycol *tert*-octylphenyl ether	$C_{14}H_{22}O(C_2H_4O)_n$ n = 9-10	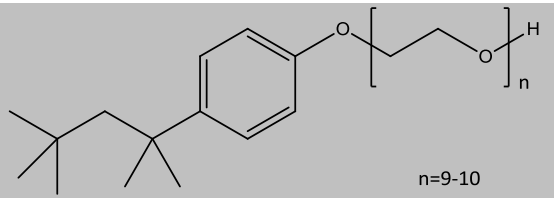	13.5
	Triton X-114	Polyethylene glycol *tert*-octylphenyl ether	$C_{14}H_{22}O(C_2H_4O)_n$ n = 7-8	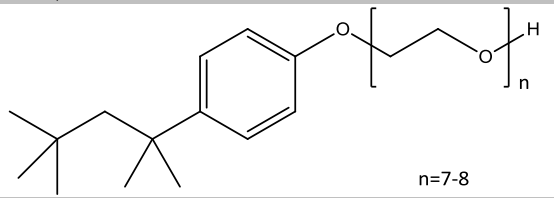	12.4
Ionic	AOT	Dioctyl sodium sulfosuccinate	$C_{20}H_{37}NaO_7S$	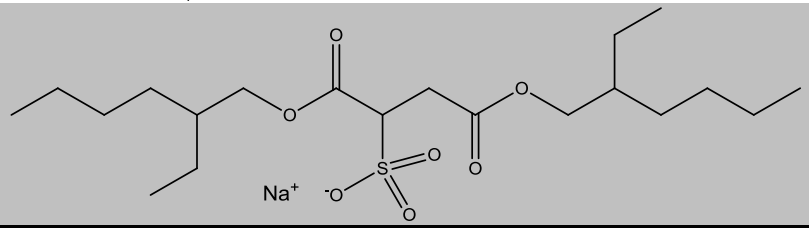	N/A

Appendix 2 Homogeneous nucleation

In the simplest case of the liquid nuclei formation in a bulk vapour phase, the thermodynamic potential, G_v, is defined as

$$G_v = n_v \mu_v \tag{A2.1}$$

where n_v is the number of molecules in a volume and μ_v is the chemical potential.

A liquid droplet with chemical potential μ_l is formed from n molecules in the vapour phase; the thermodynamic potential of the vapour-liquid droplet, G_l, is thus:

$$G_l = (n_v - n)\mu_v + G_{(n)} \tag{A2.2}$$

where $G_{(n)}$ is the thermodynamic potential of a cluster containing n molecules.

The work of formation of a cluster containing n atoms is given by the difference of G_v and G_l,

$$\Delta G_{(n)} = G_l - G_v = G_{(n)} - n\mu_v \tag{A2.3}$$

This is the simplest form of nucleation work.

The thermodynamic potential of the liquid droplet is also given by the sum of chemical potential of the constituent molecules in the liquid phase $n\mu_l$ and the surface energy $4nr^2\sigma$ where σ is the isotropic surface tension in liquid and $4nr^2$ is the surface area of a spherical droplet:

$$G_{(n)} = n\mu_l + 4\pi r^2\sigma \tag{A2.4}$$

The change in Gibbs free energy, ΔG, upon the formation of a droplet is therefore:

$$\Delta G = -n(\mu_v - \mu_l) + 4\pi r^2\sigma \tag{A2.5}$$

The number of molecules, n, in a cluster can be worked out, providing the volume of a spherical cluster, V, and the molecular volume of the molecule, v_l, is known

$$n = \frac{V}{v_l} = \frac{4\pi r^3}{3v_l} \tag{A2.6}$$

Hence by substituting (A2.6) into Equation (A2.5), the Gibbs free energy, ΔG, is

$$\Delta G_{Homo} = -\frac{4\pi r^3}{3v_l}\Delta\mu + 4\pi r^2\sigma \qquad \text{(recall 1.13)}$$

Appendix 3 Heterogeneous nucleation

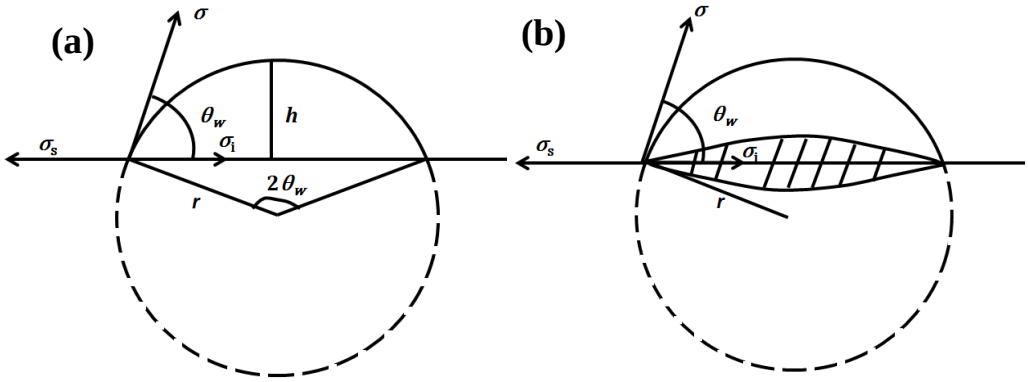

Figure A3.1 Heterogeneous nucleation of a droplet on substrate surface: (a) diagram illustrating the height of the spherical cap of the droplet; (b) contact surface area of the droplet on the surface; where the surface energies of free surfaces of substrate, droplet and the substrate-liquid interface are σ_s, σ, and σ_l respectively. h is the height of the spherical cap.

This system is in equilibrium and given by the equation:

$$\sigma_s = \sigma_l + \sigma\cos(\theta_w) \tag{A3.1}$$

For the spherical cap, the volume is

$$V = \frac{\pi h^2(3r-h)}{3} \tag{A3.2}$$

and its area is

$$A = 2\pi rh \tag{A3.3}$$

As the height of the spherical cap is

$$h = r - r\cos(\theta_w) \tag{A3.4}$$

then the volume is

$$V_l = \frac{\pi r^3(1-cos\theta_w)^2(2+\cos\theta_w)}{3} \tag{A3.5}$$

and the free surface area is

$$A_{\text{free}} = 2\pi r^2(1-\cos\theta_w) \tag{A3.6}$$

The contact surface area between the droplet and solid surface is

$$A_{\text{cont}} = \pi(r\sin\theta_w)^2 = \pi r^2\sin^2\theta_w \tag{A3.7}$$

The surface energy of the droplet, σ_d, is the sum of the contact surface energy and the free spherical cap surface energy.

$$\begin{aligned}\sigma_d &= A_{\text{free}}\sigma + A_{\text{cont}}(\sigma_l - \sigma_s)\\ &= 2\pi r^2(1-\cos\theta_w)\sigma + \pi r^2\sin^2\theta_w(\sigma_l - \sigma_s)\end{aligned} \tag{A3.8}$$

The change of thermodynamic potential upon the formation of droplet is:

$$\Delta G_{Hete} = -\frac{V_l}{v_l}\Delta\mu + \sigma_d$$

$$= -\frac{4}{3}\pi r^3\frac{(1-\cos\theta_w)^2(2+\cos\theta_w)}{4}\frac{\Delta\mu}{v_l} + 2\pi r^2\sigma(1-\cos\theta_w) - \pi r^2\sigma\sin^2\theta_w\cos\theta_w \tag{A3.9}$$

Appendix 4 Geometric droplet size calculation

To estimate the droplet size of the microemulsion, it is assumed the droplets are spherical and the vast majority of the surfactant resides at the droplet interface. Then the droplet radius, *r*, is defined as:

$$r = \frac{3\phi}{\Sigma} = 3 \times \frac{Volume\ fraction\ of\ internal\ phase}{total\ interfacial\ area\ per\ unit\ volume} \quad \text{(A4.1)}$$

When substituting the volume and the surface area of a sphere from Equation (1.13) into (A6.1), the droplet radius, *R* is therefore:

$$r = \frac{3V_{internal}}{A_{total}} \quad \text{(A4.2)}$$

A sample calculation for the optimal formulation of glycine microemulsion, comprising 6 g heptane, 4 g Span 80/Brij 30 (1:1 w/w), 0.50 g 2% glycine solution, and 1 g methanol, is shown below.

Step 1: Construct a microemulsion composition table

Table A6.1 Compositions of the microemulsion and relative calculations:

	Heptane	Span 80/Brij 30	Aqueous 2% glycine	MeOH	Total
Mass /g	6	4	0.5	1	11.5
Mass fraction	0.52	0.35	0.04	0.09	1
Volume /cm^{-3}	8.82	4.12	0.50	1.27	14.71
Density/g cm^{-3}	0.68	0.97*	1.00	0.79	0.78*
Volume fraction	0.60	0.28	0.03	0.09	1
Molecular weight/ g mol^{-1}	100.2	395.5	18	32	/

*Mass fraction $= \frac{\text{Mass of the component}}{\text{Total mass of the microemulsion}}$; Volume fraction $= \frac{\text{Volume of the component}}{\text{Total Volume}}$

*Density of Span 80/Brij 30 $= \frac{\text{Total mass of Span 80 +Brij 30}}{\text{volume of the mixture}} = \frac{2g+2g}{\frac{2g}{0.99\ g\ cm^{-3}}+\frac{2g}{0.95\ g\ cm^{-3}}} = 0.97\ g\ cm^{-3}$

where the density of Span 80 is 0.99 cm^{-3}, and the density for Brij 30 is 0.95 g cm^{-3}.

*Density of overall microemulsion $= \frac{\text{Total mass of microemulsion}}{\text{Total volume}} = \frac{11.5g}{14.71cm^3} = 0.78\ g\ cm^{-3}$

Step 2: To work out the volume fraction of the internal phase, ϕ

1) The hydrophobic part (C17H33) of a Span 80 molecule contains 14 CH_2 group, 1 terminal CH_3 group, and 1 CH=CH goup. The hydrophobic part (C12H25) for a Brij 30 molecule contains 11 CH_2 group and 1 terminal CH_3 group. Providing the volume for a CH_2 group is 27$Å^3$, for a CH_3 group is 55$Å^3$, and for a CH=CH group is 40$Å^3$, the volume of the hydrophobic part can be calculated as:

$\underline{V_{\text{hydrophobic of Span 80}}} = 14 \times 27\ \text{Å}^3 + 1 \times 55\ \text{Å}^3 + 1 \times 40\ \text{Å}^3 = 473\ \text{Å}^3$

$\underline{V_{\text{hydrophobic of Brij 30}}} = 11 \times 27\ \text{Å}^3 + 1 \times 55\ \text{Å}^3 = 352\text{Å}^3$

2) The molecular weight for Span 80 is 429 g mol^{-1}, and for Brij 30 is 362 g mol^{-1}. Therefore, the total volume of Span 80 and Brij 30 can be found as:

$$\underline{V_{\text{Span 80}}} = \frac{\text{Mass of one Span 80 molecule}}{\text{Density of Span 80}} = \frac{\text{Molecular weight of Span 80} \times N_A}{\text{Density of Span}}$$

$$= \frac{429\text{g mol}^{-1}}{0.99\text{g cm}^{-3} \times 6.023 \times 10^{23}\text{mol}^{-1}} = 7.19 \times 10^{-22}\text{cm}^3 = 719\text{Å}^3$$

Similarly,

$$\underline{V_{\text{Brij 30}}} = \frac{\text{Molecular weight of Span 80} \times N_A}{\text{Density of Span}} = \frac{362\text{g mol}^{-1}}{0.95\text{g cm}^{-3} \times 6.023 \times 10^{23}\text{mol}^{-1}}$$

$$= 6.33 \times 10^{-22} cm^3 = 633\text{Å}^3$$

Where N_A is the Avogadro's number, 6.023 x 10^{23} molecules per mole.

3) The volume fraction of the hydrophobic part in a surfactant molecule can be found as:

$$\underline{\text{Vol frac}_{\text{ hydrophobic of Span 80}}} = \frac{\text{Volume of hydrophobic part}}{\text{Total Volume of Span 80}} = \frac{473\text{Å}^3}{719\text{Å}^3} = 0.66$$

$$\underline{\text{Vol frac}_{\text{ hydrophobic of Brij 30}}} = \frac{\text{Volume of hydrophobic part}}{\text{Total Volume of Brij 30}} = \frac{352\text{Å}^3}{633\text{Å}^3} = 0.56$$

4) In a 1:1 (mass ratio) Span 80/Brij 30 mixture, due to the different density their volume ratio are:

$$V_{\text{ Span 80}} : V_{\text{ Brij 30}} = \frac{\text{Mass of Span 80}}{\text{Density of Span 80}} : \frac{\text{Mass of Brij 30}}{\text{Density of Brij 30}}$$

$$= \frac{1}{0.99\text{g cm}^{-3}} : \frac{1}{0.95\text{g cm}^{-3}} = 1.01 : 1.05$$

So: $\underline{\text{Vol frac}_{\text{ Span 80 in 1:1 mixture}}} = \frac{1.01}{1.01+1.05} = 0.49$,

$\underline{\text{Vol frac}_{\text{ Brij 30 in 1:1 mixture}}} = \frac{1.05}{1.01+1.05} = 0.51$

5) To calculate the volume fraction for the total hydrophobic part in the 1:1 Span80/Brij 30 mixture:

$\underline{\text{Vol frac}_{\text{hydrophobic in 1:1 mixture}}}$

$$= \text{Vol frac}_{\text{hydrophobic of Span 80}} \times \text{Vol frac}_{\text{Span 80 in 1:1 mxiture}} + \text{Vol frac}_{\text{hydrophobic of Brij 30}} \times \text{Vol frac}_{\text{Brij 30 in 1:1 mxiture}}$$

$$= 0.66 \times 0.49 + 0.56 \times 0.51 = 0.61$$

6) Hence the volume fraction for the hydrophilic part in the 1:1 mixture is:

$$\underline{\text{Vol frac}}_{\text{hydrophilic in 1:1 mixture}} = 1 - \text{Vol frac}_{\text{hydrophobic in 1:1 mixture}} = 1 - 0.61 = 0.39$$

7) The volume fraction combined hydrophilic in the overall microemulsion is:

$$\text{Vol frac}_{\underline{\text{hydrophobic}}} = \text{Vol frac}_{\text{hydrophilic in 1:1 mixture}} \times \text{Vol frac}_{\text{Span 80+Brij 30}}$$
$$= 0.39 \times 0.28 = 0.11$$

8) Finally, the volume fraction of the total internal phase is :

$$\text{Vol frac}_{\text{total internal}} = \text{Vol frac}_{\text{hydrophilic}} + \text{Vol frac}_{\text{aqueous}} + \text{Vol frac}_{\text{MeOH}}$$
$$= 0.11 + 0.03 + 0.09 = 0.23$$

Step 3: To work out the total interfacial area per unit volume

1) The molecular fractions of Span 80 and Brij 30 in 1:1 mixture (by mass ratio) can be found as :

$$\text{Mol frac}_{\text{Span 80}} = \frac{\frac{1}{\text{Molecular weight of Span 80}} \times N_A}{\left(\frac{1}{\text{Molecular weight of Span 80}} + \frac{1}{\text{Molecular weight of Brij 30}}\right) \times N_A}$$

$$= \frac{\frac{1}{429\text{g mol}^{-1}} \times N_A}{\left(\frac{1}{429\text{g mol}^{-1}} + \frac{1}{362\text{g mol}^{-1}}\right) \times N_A} = \frac{362}{429+362} = 0.46$$

Similarly, $\text{Mol frac}_{\text{Brij 30}} = \frac{\frac{1}{362\text{g mol}^{-1}} \times N_A}{\left(\frac{1}{429\text{g mol}^{-1}} + \frac{1}{362\text{g mol}^{-1}}\right) \times N_A} = \frac{429}{429+362} = 0.54$

2) Then the surface area (SA) per molecule (for the 1:1 Span80/Brij 30 mixture) per nm^2 can be calculated providing the surface area for Span 80 is[55] 0.37 nm^2 and for Brij 30 is 0.396 nm^2.

SA per molecule

$$= \text{SA of Span 80} \times \text{Molecular frac}_{\text{Span 80}} + \text{SA of Brij 30} \times \text{Molecular frac}_{\text{Brij 30}}$$
$$= 0.37\ nm^2 \times 0.46 + 0.396\ nm^2 \times 0.54 = 0.38\ nm^2$$

3) The number of surfactant molecules in 1g microemulsion can be found as:

$$N_{\text{surfactant molecules/g microemulsion}} = \frac{N_A}{\text{Molecular Weight}} \times \text{Mass fraction}$$
$$= \frac{6.023 \times 10^{23}\ \text{mol}^{-1}}{395.5\ \text{g mol}^{-1}} \times 0.35 = 5.33 \times 10^{20}$$

4) Then the number of surfactant molecules per nm^3 is :

$$N_{\text{surfactant molecules/nm3}}$$

$$= N_{\frac{\text{surfactantmolecules}}{\text{gram microemulsion}}} \times \text{Density of overall microemulsion}$$

$$= 5.33 \times 10^{20} \times 0.78\ \text{g cm}^{-3} = 0.42$$

5) Finally the total interface surface area per unit volume is:

$$SA_{\text{total}} = N_{\text{surfactant molecules/nm}^3} \times \text{SA per molecule} = 0.42 \times 0.38\ \text{nm}^2 = 0.159\ \text{nm}^2$$

Step 4: Droplet size calculation

According to equation 3.1, droplet size,

$$R = 3 \times \frac{\text{Volume fraction of internal phase}}{\text{total interfacial area per unit volume}} = 3 \times \frac{0.23}{0.159} = 4.34\ \text{nm}.$$

Appendix 5 Estimation of water pool size from geometric and GIFT radii

Recall Table 4.2 as an example:

Dispersed phase /μl g^{-1} surfactant solution	50	100	200	300	400
$r_{c(geometric)}$ /±0.3 nm	1.4	2.2	3.8	5.4	7.1
$r_{c(gift)}$/ ±0.3 nm	2.0	2.7	4.3	5.9	7.5
$V_{c\ (gift)}$/nm^3	33.5	82.4	333.0	860.3	1767.1
Approx. No. of droplets /$x10^{17}$	25.9	16.6	7.11	3.92	2.47
Mean No. of water molecules per droplet	645	2015	9406	25629	54128
Mean No. of AOT molecules per droplet	131	204	476	865	1370
Mean Water taken by AOT per droplet	783	1224	2856	5188	8217
Theoretical fraction of Water bound to AOT	1.21	0.61	0.30	0.20	0.15

1. r_g is the radius of Gyration obtained from the GIFT analysis;
2. $r_{c(gift)}$ is the droplet radius calculated from the radius of gyration,

$$r_{c(gift)} = \sqrt{\frac{5}{3}} r_g \qquad \text{(A5.1)}$$

3. $r_{c(geometric)}$ is the calculated geometric radius for a hard sphere,

$$r_{c(geometric)} = \frac{3\phi}{\Sigma} \qquad \text{(Recall Equation 5.1)}$$

where ϕ is the volume fraction of the internal phase and Σ is the total interfacial area per unit volume.

4. $V_{c(gift)}$ is the volume of sphere,

$$V_{c(gift)} = \frac{4\pi r_{c(gift)}^3}{3} \qquad \text{(A5.1)}$$

5. No. of droplet in the system = $\frac{\text{Volume of total dispersed phase}}{\text{Volume of a droplet}}$

where the volume of total dispersed phase includes water and hydrophilic part of the AOT

6. No. of molecules per droplet = $\frac{\text{Total no.of molecules per unit volume}}{\text{No.of droplets in the above volume}}$
7. Water taken by AOT per droplet = No. of AOT per droplet x No. of water molecules each AOT molecule bound to
8. Fraction of water bound to AOT = $\frac{\text{Water molecules bound to AOT per droplet}}{\text{Total no.of water molecules per droplet}}$

Appendix 6 Crystal structural information on DPA potassium salt trihydrate

Table A6.1 Crystal data and structure refinement	
Empirical formula	$[C_7H_5NO_4]$ x $[C_7H_4NO_4]$ x K x $3H_2O$
Formula weight	426.38
Temperature/K	120
Crystal system	triclinic
Space group	P-1
a/Å	6.9649(3)
b/Å	10.9834(5)
c/Å	11.2246(6)
α/°	91.635(2)
β/°	96.001(2)
γ/°	97.585(2)
Volume/$Å^3$	845.70(7)
Z	2
ρ_{calc}mg/mm^3	1.674
m/mm^{-1}	0.382
F(000)	440.0
Crystal size/mm^3	0.15 × 0.12 × 0.06
2Θ range for data collection	3.66 to 59 °
Index ranges	$-9 \leq h \leq 9$, $-15 \leq k \leq 15$, $-15 \leq l \leq 15$
Reflections collected	9753
Independent reflections	4655[R(int) = 0.0365]
Data/restraints/parameters	4655/0/313
Goodness-of-fit on F^2	1.020
Final R indexes [I>=2σ (I)]	R_1 = 0.0466, wR_2 = 0.1123
Final R indexes [all data]	R_1 = 0.0768, wR_2 = 0.1289
Largest diff. peak/hole / e $Å^{-3}$	0.52/-0.52

Table A6.2 Fractional Atomic Coordinates ($\times 10^4$) and Equivalent Isotropic Displacement Parameters ($Å^2 \times 10^3$). U_{eq} is defined as 1/3 of the trace of the orthogonalised U_{IJ} tensor.

Atom	*x*	*y*	*z*	U(eq)
K1	1753.0(7)	3571.4(4)	4712.5(4)	22.34(14)
O1	1003(2)	5118.6(13)	6483.0(13)	22.2(3)
O2	500(2)	5595.2(14)	8364.2(13)	21.4(3)
O3	2461(2)	-272.3(13)	6643.2(13)	23.2(3)
O4	2209(2)	1228.3(13)	5347.4(13)	21.7(3)
N1	1574(2)	2809.7(15)	7072.4(15)	15.8(3)
C1	1201(3)	3587.3(17)	7938.1(17)	15.1(4)
C2	1066(3)	3270.3(19)	9118.1(18)	18.7(4)
C3	1290(3)	2075.8(19)	9421.3(19)	19.6(4)
C4	1639(3)	1251.6(18)	8531.3(18)	18.5(4)
C5	1778(3)	1660.0(17)	7384.5(18)	15.9(4)
C6	911(3)	4839.6(18)	7508.0(18)	16.7(4)
C7	2187(3)	772.4(17)	6411.6(18)	17.2(4)
O5	2636(2)	-396.2(13)	3788.3(13)	22.8(3)
O6	2737(2)	770.7(12)	2184.4(13)	21.4(3)
O7	3734(3)	-4510.8(13)	3559.7(14)	28.3(4)
O8	4638(2)	-5326.9(13)	1893.6(14)	21.2(3)
N2	3454(2)	-2349.5(15)	2495.3(15)	16.0(3)
C11	3272(3)	-1301.8(17)	1948.5(18)	15.9(4)
C12	3426(3)	-1174.4(18)	728.1(19)	18.5(4)
C13	3759(3)	-2179.3(19)	40.7(18)	19.7(4)
C14	3953(3)	-3274.7(19)	603.2(18)	18.1(4)
C15	3815(3)	-3308.6(17)	1827.8(18)	15.8(4)
C16	2849(3)	-220.0(18)	2710.6(18)	17.2(4)
C17	4050(3)	-4439.7(17)	2518.3(19)	18.4(4)
O3W	5034(3)	2835.3(17)	3138(2)	46.8(6)
O2W	5(3)	2261.7(14)	2539.1(15)	24.7(4)
O1W	-2330(2)	2647.0(15)	4981.9(14)	23.1(3)

Table A6.3 Anisotropic Displacement Parameters ($Å^2 \times 10^3$). The Anisotropic displacement factor exponent takes the form: $-2\pi^2[h^2a^{*2}U_{11}+...+2hka \times b \times U_{12}]$

Atom	U_{11}	U_{22}	U_{33}	U_{23}	U_{13}	U_{12}
K1	35.6(3)	16.4(2)	17.5(2)	2.58(16)	5.99(19)	10.12(18)
O1	34.2(9)	16.5(7)	17.8(7)	1.4(5)	4.1(6)	9.4(6)
O2	31.5(9)	14.4(7)	20.7(7)	-1.9(6)	5.8(6)	9.5(6)
O3	31.8(9)	13.0(7)	27.0(8)	1.7(6)	5.9(7)	8.1(6)
O4	35.3(9)	14.8(7)	17.1(7)	-0.1(5)	5.7(6)	9.1(6)
N1	16.4(8)	13.5(7)	18.0(8)	-0.6(6)	1.9(7)	4.3(6)
C1	14.3(9)	14.9(9)	16.1(9)	0.0(7)	-0.2(7)	3.1(7)
C2	18.7(10)	21(1)	17.2(10)	-1.9(8)	1.6(8)	6.4(8)
C3	23.1(11)	21.3(10)	15.0(9)	3.0(8)	3.1(8)	3.7(8)
C4	20.4(10)	16.3(9)	18.8(10)	2.8(7)	0.1(8)	3.2(8)
C5	14.7(10)	14.0(9)	19.1(10)	-0.2(7)	1.1(8)	3.4(7)
C6	17.8(10)	14.2(9)	18.5(10)	-2.0(7)	1.0(8)	5.7(7)
C7	20.2(10)	11.9(9)	19(1)	-0.9(7)	0.4(8)	2.4(7)
O5	36.4(9)	14.4(7)	19.3(7)	-1.5(5)	6.5(6)	7.6(6)
O6	27.7(8)	13.3(7)	24.6(8)	0.4(6)	3.0(6)	8.1(6)
O7	48(1)	16.0(7)	25.5(8)	4.4(6)	14.5(7)	11.6(7)
O8	29.9(9)	12.6(7)	22.6(8)	-0.4(6)	4.1(6)	8.3(6)
N2	17.7(8)	13.9(8)	17.3(8)	-1.7(6)	2.7(6)	5.4(6)
C11	14.8(9)	15.0(9)	18.5(9)	-0.3(7)	1.7(7)	4.7(7)
C12	20.8(10)	14.8(9)	20.8(10)	1.6(8)	2.6(8)	5.6(8)
C13	22.7(11)	22.2(10)	15.4(10)	0.8(8)	3.9(8)	6.2(8)
C14	18.7(10)	17.3(9)	19.2(10)	-2.2(7)	2.4(8)	6.0(8)
C15	15.3(10)	13.0(9)	19.4(10)	-0.2(7)	1.9(8)	3.6(7)
C16	18.3(10)	12.9(9)	20.9(10)	-1.6(7)	1.9(8)	4.6(7)
C17	18.8(10)	12.3(9)	24.2(11)	-2.6(7)	3.6(8)	2.6(7)
O3W	63.1(14)	13.0(8)	54.7(13)	4.1(8)	-31.7(11)	-1.3(8)
O2W	27.4(9)	17.1(7)	32.7(9)	4.2(6)	8.7(7)	8.8(7)
O1W	32.5(9)	16.9(8)	21.6(8)	2.5(6)	5.9(7)	7.0(7)

Table A6.4 Bond Lengths.					
Atom	**Atom**	**Length/Å**	**Atom**	**Atom**	**Length/Å**
K1	O1	2.7145(14)	C2	C3	1.389(3)
K1	O1[1]	2.8030(15)	C3	C4	1.391(3)
K1	O4	2.7394(15)	C4	C5	1.384(3)
K1	N1	2.8108(17)	C5	C7	1.517(3)
K1	O7[2]	2.7887(17)	O5	C16	1.251(2)
K1	O3W	3.201(3)	O6	C16	1.260(2)
K1	O2W	2.8668(17)	O7	K1[3]	2.7887(16)
K1	O1W	2.9402(18)	O7	C17	1.214(2)
O1	K1[1]	2.8030(15)	O8	C17	1.317(2)
O1	C6	1.205(2)	N2	C11	1.334(2)
O2	C6	1.330(2)	N2	C15	1.341(2)
O3	C7	1.219(2)	C11	C12	1.395(3)
O4	C7	1.309(2)	C11	C16	1.522(3)
N1	C1	1.344(2)	C12	C13	1.387(3)
N1	C5	1.342(2)	C13	C14	1.390(3)
C1	C2	1.388(3)	C14	C15	1.389(3)
C1	C6	1.502(3)	C15	C17	1.501(3)

[1]-X,1-Y,1-Z; [2]+X,1+Y,+Z; [3]+X,-1+Y,+Z

Table A6.5 Hydrogen Bonds.						
D	**H**	**A**	**d(D-H)/Å**	**d(H-A)/Å**	**d(D-A)/Å**	**D-H-A/ °**
O4	H4	O5	0.97(3)	1.57(3)	2.5310(19)	176(3)
O2	H2	O2W[1]	0.81(3)	1.84(3)	2.641(2)	170(3)
O8	H8	O3W[2]	0.84(3)	1.68(3)	2.516(2)	169(3)
O3W	H3WA	O1W[3]	0.86(3)	1.79(3)	2.651(3)	173(3)
O3W	H3WB	O6	0.73(4)	1.99(4)	2.719(2)	173(4)
O2W	H2WA	O3[4]	0.85(3)	2.04(3)	2.832(2)	155(3)
O2W	H2WB	O6	0.87(4)	1.85(4)	2.721(2)	179(4)
O1W	H1WA	O7[4]	0.82(4)	2.13(4)	2.915(2)	160(4)
O1W	H1WB	O5[4]	0.83(4)	2.03(4)	2.860(2)	171(4)

[1]-X,1-Y,1-Z; [2]+X,-1+Y,+Z; [3]1+X,+Y,+Z; [4]-X,-Y,1-Z

Table A6.6 Bond Angles.							
Atom	**Atom**	**Atom**	**Angle/°**	**Atom**	**Atom**	**Atom**	**Angle/°**
O1	K1	O1[1]	77.71(5)	N1	C1	C2	123.72(18)
O1	K1	O4	116.23(5)	N1	C1	C6	113.63(17)
O1[1]	K1	N1	123.37(5)	C2	C1	C6	122.64(17)
O1	K1	N1	58.67(4)	C1	C2	C3	118.43(18)
O1	K1	O7[2]	92.20(5)	C2	C3	C4	118.62(19)
O1[1]	K1	O3W	115.12(5)	C5	C4	C3	118.65(18)
O1	K1	O3W	144.64(5)	N1	C5	C4	123.75(17)
O1	K1	O2W	142.38(5)	N1	C5	C7	117.22(17)
O1[1]	K1	O2W	69.67(4)	C4	C5	C7	119.04(17)
O1	K1	O1W	78.59(5)	O1	C6	K1	39.55(9)
O1[1]	K1	O1W	64.98(5)	O1	C6	O2	123.62(18)
O4	K1	O1[1]	140.45(5)	O1	C6	C1	123.11(17)
O4	K1	N1	57.59(4)	O2	C6	K1	163.13(13)
O4	K1	O7[2]	138.51(5)	O2	C6	C1	113.26(17)
O4	K1	O3W	75.94(5)	C1	C6	K1	83.56(10)
O4	K1	O2W	80.87(5)	O3	C7	O4	124.87(18)
O4	K1	O1W	81.09(5)	O3	C7	C5	120.64(18)
N1	K1	O3W	121.40(5)	O4	C7	C5	114.49(16)
N1	K1	O2W	127.54(5)	C17	O7	K1[3]	129.98(13)
N1	K1	O1W	72.03(5)	C11	N2	C15	117.55(17)
O7[2]	K1	O1[1]	71.68(5)	N2	C11	C12	122.90(17)
O7[2]	K1	N1	137.34(5)	N2	C11	C16	117.23(17)
O7[2]	K1	O3W	64.17(5)	C12	C11	C16	119.86(17)
O7[2]	K1	O2W	94.82(5)	C13	C12	C11	119.09(19)
O7[2]	K1	O1W	136.65(5)	C12	C13	C14	118.41(19)
O2W	K1	O3W	69.42(5)	C15	C14	C13	118.44(18)
O2W	K1	O1W	71.06(5)	N2	C15	C14	123.58(18)
O1W	K1	O3W	136.70(5)	N2	C15	C17	114.11(17)
K1	O1	K1[1]	102.29(5)	C14	C15	C17	122.32(17)
C6	O1	K1[1]	121.47(13)	O5	C16	O6	126.33(17)
C6	O1	K1	124.03(12)	O5	C16	C11	117.46(17)
C7	O4	K1	128.05(11)	O6	C16	C11	116.21(17)
C1	N1	K1	120.57(12)	O7	C17	O8	123.92(19)
C5	N1	K1	122.58(12)	O7	C17	C15	122.29(17)
C5	N1	C1	116.80(17)	O8	C17	C15	113.80(17)

[1]-X,1-Y,1-Z; [2]+X,1+Y,+Z; [3]+X,-1+Y,+Z

Table A6.7 Hydrogen Atom Coordinates (Å×10^4) and Isotropic Displacement Parameters (Å^2×10^3).

Atom	*x*	*y*	*z*	U(eq)
H4	2310(40)	590(30)	4760(30)	56(9)
H2	480(50)	6270(30)	8100(30)	48(9)
H2A	800(40)	3820(20)	9710(20)	25(6)
H4A	1730(30)	400(20)	8700(20)	17(6)
H3	1260(40)	1770(20)	10210(20)	24(6)
H8	4820(50)	-5880(30)	2390(30)	49(9)
H13	3860(30)	-2090(20)	-820(20)	16(6)
H14	4200(30)	-3980(20)	130(20)	24(6)
H12	3390(30)	-420(20)	360(20)	21(6)
H3WA	5940(40)	2830(30)	3720(30)	43(8)
H3WB	4480(50)	2250(30)	2910(30)	55(10)
H2WA	-950(40)	1840(30)	2810(30)	34(8)
H2WB	870(60)	1780(40)	2420(40)	85(13)
H1WA	-2610(60)	3070(40)	5530(40)	90(14)
H1WB	-2540(50)	1970(40)	5300(30)	64(11)

Appendix 7 Crystal Structural information of DPA sodium salt methanol solvate

Table A7.1 Crystal data and structure refinement	
Empirical formula	$C_{14}H_{11}N_2NaO_8$ x $0.5CH_3OH$
Formula weight	372.24
Temperature/K	120
Crystal system	triclinic
Space group	P-1
a/Å	10.9883(6)
b/Å	12.4796(7)
c/Å	12.6891(7)
α/°	105.284(5)
β/°	113.374(5)
γ/°	95.980(4)
Volume/$Å^3$	1497.34(14)
Z	4
$\rho_{calc}mg/mm^3$	1.651
m/mm^{-1}	0.162
F(000)	764.0
Crystal size/mm^3	0.4789 ×0.1906 ×0.059
2Θ range for data collection	5.26 to 56 °
Index ranges	$-14 \leq h \leq 14$, $-16 \leq k \leq 16$, $-16 \leq l \leq 16$
Reflections collected	25663
Independent reflections	7229[R(int) = 0.0800]
Data/restraints/parameters	7229/0/557
Goodness-of-fit on F^2	0.971
Final R indexes [I>=2σ (I)]	R_1 = 0.0549, wR_2 = 0.0991
Final R indexes [all data]	R_1 = 0.1110, wR_2 = 0.1245
Largest diff. peak/hole / e $Å^{-3}$	0.34/-0.38

Table A7.2 Fractional Atomic Coordinates ($\times 10^4$) and Equivalent Isotropic Displacement Parameters ($Å^2 \times 10^3$). U_{eq} is defined as 1/3 of of the trace of the orthogonalised U_{IJ} tensor.

Atom	*x*	*y*	*z*	U(eq)
Na1	-390.5(10)	8798.4(9)	6894.3(9)	26.6(3)
Na2	1902.9(10)	10378.1(8)	5911.3(9)	22.8(2)
O1A	-1986.8(18)	8418.6(16)	7665.8(17)	23.8(4)
O2A	-2951.5(17)	8850.6(15)	8950.9(16)	27.8(5)
O3A	1187.3(16)	10666.9(14)	7448.1(16)	21.8(4)
O4A	1948.5(17)	12548.4(15)	8487.2(17)	23.8(4)
N1A	-478.2(18)	10436.4(17)	8471.6(18)	16.9(4)
C1A	-1310(2)	10307(2)	8984(2)	18.5(5)
C2A	-1375(3)	11183(2)	9880(2)	21.4(6)
C3A	-517(3)	12250(2)	10278(2)	23.0(6)
C4A	357(3)	12401(2)	9749(2)	21.6(6)
C5A	333(2)	11473(2)	8852(2)	18.3(5)
C6A	-2192(2)	9110(2)	8531(2)	20.4(6)
C7A	1202(2)	11520(2)	8194(2)	19.5(6)
O1	-11.5(16)	8560.6(14)	5138.1(16)	21.4(4)
O2	-493.5(16)	6646.6(14)	4340.6(15)	19.9(4)
O3	3054.4(18)	10884.3(15)	4799.7(16)	24.5(4)
O4	4309.8(16)	10372.7(15)	3800.6(16)	24.1(4)
N1	1767.4(19)	8788.0(17)	4219.4(18)	17.8(5)
C1	1034(2)	7734(2)	3897(2)	17.5(5)
C2	1118(2)	6789(2)	3076(2)	21.0(6)
C3	2017(3)	6945(2)	2585(2)	22.1(6)
C4	2801(2)	8032(2)	2925(2)	20.1(6)
C5	2642(2)	8933(2)	3739(2)	18.9(5)
C6	114(2)	7680(2)	4511(2)	16.8(5)
C7	3427(2)	10145(2)	4123(2)	19.8(6)
O1C	-730.8(18)	4258.8(16)	3002.0(17)	24.7(4)
O2C	-1405.1(18)	2375.4(15)	2473.4(17)	28.1(4)
O3C	-1662.7(16)	6851.6(14)	5682.3(16)	21.5(4)
O4C	-2928.0(17)	6309.3(15)	6543.4(16)	24.5(4)
N1C	-2079.2(19)	4636.4(17)	4332.3(18)	18.2(5)
C1C	-2313(2)	3543(2)	3659(2)	20.0(6)
C2C	-3266(2)	2662(2)	3571(2)	21.2(6)
C3C	-4028(2)	2922(2)	4214(2)	21.9(6)
C4C	-3767(2)	4045(2)	4938(2)	20.5(6)
C5C	-2781(2)	4871(2)	4986(2)	17.9(5)
C6C	-1457(2)	3322(2)	2991(2)	20.1(6)
C7C	-2441(2)	6100(2)	5792(2)	19.6(6)
O1B	2117.7(18)	14957.7(17)	9670.5(18)	28.9(5)
O2B	3206.6(19)	16795.8(16)	10557.2(18)	33.5(5)
O3B	3039.9(16)	12353.2(14)	7031.0(15)	22.1(4)
O4B	4328.9(16)	12851.8(15)	6165.0(16)	21.8(4)
N1B	3537.0(19)	14550.5(18)	8401.3(18)	18.1(5)
C1B	3828(2)	15638(2)	9118(2)	18.2(5)
C2B	4792(3)	16505(2)	9201(2)	24.8(6)
C3B	5500(3)	16235(2)	8510(2)	23.9(6)
C4B	5213(2)	15118(2)	7766(2)	20.1(6)
C5B	4228(2)	14302(2)	7740(2)	17.5(5)
C6B	3042(3)	15866(2)	9851(2)	23.4(6)
C7B	3835(2)	13072(2)	6931(2)	18.8(5)
O1S	3924.8(19)	10061.3(16)	7246.3(18)	28.4(5)
C1S	4554(3)	10408(3)	8533(3)	37.1(8)

Table A7.3 Anisotropic Displacement Parameters ($Å^2 \times 10^3$). The Anisotropic displacement factor exponent takes the form: $-2\pi^2[h^2a^{*2}U_{11}+...+2hka \times b \times U_{12}]$

Atom	U_{11}	U_{22}	U_{33}	U_{23}	U_{13}	U_{12}
Na1	33.7(6)	19.0(6)	30.6(6)	3.9(5)	21.8(5)	0.0(5)
Na2	27.1(5)	19.6(6)	24.6(6)	5.2(5)	16.6(5)	1.1(4)
O1A	28.4(10)	16.4(10)	29.5(11)	3.6(9)	19.4(9)	0.4(8)
O2A	31.2(10)	25.5(11)	35.1(11)	9.8(9)	24(1)	2.7(8)
O3A	26.6(9)	17.1(10)	23.2(10)	3.4(8)	15.4(8)	1.7(8)
O4A	26.8(10)	17.1(10)	28.7(11)	3.5(9)	17.2(9)	0.3(8)
N1A	15.9(10)	18.9(12)	17.9(11)	8.3(10)	8.0(9)	4.2(9)
C1A	19.5(12)	17.3(13)	20.8(13)	8.4(11)	10.0(11)	3(1)
C2A	23.6(13)	26.1(16)	19.3(13)	8.7(12)	13.0(12)	8.1(12)
C3A	26.9(14)	19.5(14)	24.5(15)	6.7(13)	13.9(12)	5.0(11)
C4A	22.8(13)	15.7(14)	23.4(14)	5.8(12)	9.1(12)	-1.2(11)
C5A	19.0(12)	16.2(13)	21.9(13)	7.8(11)	10.5(11)	3.4(10)
C6A	20.5(13)	19.0(14)	23.0(14)	7.9(12)	10.5(12)	3.8(11)
C7A	18.8(13)	19.6(14)	21.3(14)	8.1(12)	9.9(11)	1.9(11)
O1	25.8(9)	16.4(10)	27.5(10)	7.6(8)	17.4(9)	3.3(8)
O2	23.2(9)	14.2(9)	24.1(10)	5.3(8)	13.7(8)	0.8(7)
O3	32.1(10)	14.7(10)	27.6(11)	-0.5(9)	20.7(9)	-2.2(8)
O4	23.4(9)	21.8(10)	33.7(11)	8.5(9)	20.7(9)	1.2(8)
N1	16.3(10)	19.0(12)	20.7(11)	9.4(10)	9.5(9)	2.0(9)
C1	16.5(12)	17.6(14)	20.5(13)	9.3(11)	8.5(11)	3.6(10)
C2	20.5(13)	14.2(14)	23.7(14)	4.3(12)	8.1(11)	-1.4(11)
C3	25.0(14)	22.0(15)	23.2(15)	6.6(13)	15.3(12)	4.2(11)
C4	21.0(13)	22.3(15)	20.6(14)	7.5(12)	12.5(12)	5.6(11)
C5	18.0(12)	20.3(14)	19.9(13)	7.9(12)	9.7(11)	2.3(10)
C6	15.2(12)	15.5(13)	19.6(13)	6.6(11)	7.5(11)	1.9(10)
C7	19.5(13)	22.0(15)	16.4(13)	6.4(12)	7.1(11)	3.1(11)
O1C	31.1(10)	16.9(10)	30.0(11)	6.4(9)	19.0(9)	3.1(8)
O2C	33.2(11)	21.1(11)	30.0(11)	3.5(9)	17.7(9)	3.9(9)
O3C	20.9(9)	17.2(10)	30(1)	6.8(8)	16.3(8)	1.7(7)
O4C	29.5(10)	18.7(10)	30.9(11)	4.9(9)	22.0(9)	1.8(8)
N1C	18.6(10)	17.3(12)	18.4(11)	5.5(10)	8.4(9)	3.2(9)
C1C	23.0(13)	19.7(14)	17.2(13)	8.5(12)	7.6(11)	4.2(11)
C2C	24.5(14)	12.7(14)	21.7(14)	2.7(12)	8.4(12)	1.5(11)
C3C	21.5(13)	18.7(14)	26.9(15)	10.4(12)	11.5(12)	0.3(11)
C4C	19.3(13)	23.0(15)	22.6(14)	9.4(12)	11.3(12)	5.8(11)
C5C	20.9(13)	15.1(13)	16.8(13)	6.1(11)	7.4(11)	2.5(10)
C6C	18.8(13)	21.1(15)	17.8(13)	5.7(12)	6.5(11)	2.1(11)
C7C	18.7(12)	17.1(14)	24.9(14)	7.4(12)	11.8(11)	2.1(10)
O1B	32.5(11)	25.4(12)	32.4(12)	6.4(10)	20.9(10)	2.8(9)
O2B	44.2(12)	23.8(11)	34.8(12)	0.9(10)	25.8(10)	5.0(9)
O3B	27.5(10)	14.3(9)	25.7(10)	4.7(8)	15.7(9)	-1.4(8)
O4B	23.8(9)	17.1(10)	27.5(10)	4.4(8)	17.1(8)	0.9(8)
N1B	18.7(10)	19.0(12)	16.8(11)	7(1)	7.0(9)	5.2(9)
C1B	21.5(13)	16.0(13)	20.3(13)	8.2(12)	10.3(11)	7.3(11)
C2B	26.9(14)	17.1(15)	23.2(15)	3.8(13)	7.3(12)	-0.6(12)
C3B	23.5(14)	18.7(15)	26.2(15)	6.4(13)	10.2(12)	-1.9(11)
C4B	22.6(13)	20.0(14)	21.1(14)	8.4(12)	12.7(12)	1.8(11)
C5B	21.9(13)	15.1(13)	16.1(13)	6.3(11)	8.5(11)	3(1)
C6B	27.2(14)	22.7(15)	22.5(14)	8.9(13)	12.0(12)	6.7(12)
C7B	17.0(12)	19.0(14)	21.2(13)	8.2(12)	8.7(11)	3(1)

O1S	28.8(11)	28.8(12)	31.3(12)	9.2(10)	17.4(10)	6.1(9)
C1S	32.6(18)	40(2)	31.2(18)	2.1(17)	12.9(15)	9.3(16)

Table A7.4 Bond Lengths.

Atom	Atom	Length/Å	Atom	Atom	Length/Å
Na1	Na2	3.8142(13)	O4	C7	1.228(3)
Na1	Na2[1]	3.7527(14)	N1	C1	1.334(3)
Na1	O1A	2.3860(19)	N1	C5	1.347(3)
Na1	O3A	2.5029(19)	C1	C2	1.391(3)
Na1	N1A	2.496(2)	C1	C6	1.507(3)
Na1	O1	2.3751(19)	C2	C3	1.383(3)
Na1	O3[1]	3.007(2)	C3	C4	1.386(3)
Na1	O2C[2]	2.578(2)	C4	C5	1.390(3)
Na1	O3C	2.4164(19)	C5	C7	1.508(3)
Na2	Na1[1]	3.7527(14)	O1C	C6C	1.338(3)
Na2	Na2[1]	3.7525(19)	O2C	Na1[2]	2.578(2)
Na2	O3A	2.3358(19)	O2C	C6C	1.211(3)
Na2	O1	2.5937(18)	O3C	C7C	1.275(3)
Na2	O1[1]	2.675(2)	O4C	C7C	1.251(3)
Na2	O3	2.3894(19)	N1C	C1C	1.341(3)
Na2	N1	2.451(2)	N1C	C5C	1.339(3)
Na2	O3B	2.3998(19)	C1C	C2C	1.385(3)
Na2	O1S	2.348(2)	C1C	C6C	1.498(3)
O1A	C6A	1.319(3)	C2C	C3C	1.390(3)
O2A	C6A	1.214(3)	C3C	C4C	1.385(4)
O3A	C7A	1.218(3)	C4C	C5C	1.387(3)
O4A	C7A	1.320(3)	C5C	C7C	1.513(3)
N1A	C1A	1.334(3)	O1B	C6B	1.344(3)
N1A	C5A	1.338(3)	O2B	C6B	1.210(3)
C1A	C2A	1.386(3)	O3B	C7B	1.253(3)
C1A	C6A	1.517(3)	O4B	C7B	1.274(3)
C2A	C3A	1.387(4)	N1B	C1B	1.341(3)
C3A	C4A	1.396(3)	N1B	C5B	1.340(3)
C4A	C5A	1.383(3)	C1B	C2B	1.386(3)
C5A	C7A	1.504(3)	C1B	C6B	1.496(3)
O1	Na2[1]	2.675(2)	C2B	C3B	1.388(4)
O1	C6	1.232(3)	C3B	C4B	1.383(4)
O2	C6	1.309(3)	C4B	C5B	1.390(3)
O3	Na1[1]	3.007(2)	C5B	C7B	1.508(3)
O3	C7	1.303(3)	O1S	C1S	1.415(4)

[1]-X,2-Y,1-Z; [2]-X,1-Y,1-Z

Table A7.5 Bond Angles.							
Atom	**Atom**	**Atom**	**Angle/°**	**Atom**	**Atom**	**Atom**	**Angle/°**
Na2[1]	Na1	Na2	59.45(3)	C7A	O3A	Na1	120.50(15)
O1A	Na1	Na2	160.94(6)	C7A	O3A	Na2	133.22(16)
O1A	Na1	Na2[1]	112.96(6)	C1A	N1A	Na1	121.43(16)
O1A	Na1	O3A	127.61(7)	C1A	N1A	C5A	117.7(2)
O1A	Na1	N1A	63.25(7)	C5A	N1A	Na1	120.91(15)
O1A	Na1	O3[1]	73.48(6)	N1A	C1A	C2A	123.6(2)
O1A	Na1	O2C[2]	107.81(7)	N1A	C1A	C6A	115.4(2)
O1A	Na1	O3C	75.00(7)	C2A	C1A	C6A	121.0(2)
O3A	Na1	Na2[1]	76.82(5)	C1A	C2A	C3A	118.2(2)
O3A	Na1	Na2	36.46(4)	C2A	C3A	C4A	118.9(3)
O3A	Na1	O3[1]	101.34(6)	C5A	C4A	C3A	118.3(2)
O3A	Na1	O2C[2]	98.64(6)	N1A	C5A	C4A	123.3(2)
N1A	Na1	Na2	99.93(5)	N1A	C5A	C7A	112.8(2)
N1A	Na1	Na2[1]	101.95(6)	C4A	C5A	C7A	123.8(2)
N1A	Na1	O3A	64.37(6)	O1A	C6A	C1A	110.9(2)
N1A	Na1	O3[1]	85.35(6)	O2A	C6A	O1A	126.2(2)
N1A	Na1	O2C[2]	119.91(7)	O2A	C6A	C1A	122.9(2)
O1	Na1	Na2	42.01(4)	O3A	C7A	O4A	124.2(2)
O1	Na1	Na2[1]	45.16(5)	O3A	C7A	C5A	121.3(2)
O1	Na1	O1A	146.38(8)	O4A	C7A	C5A	114.5(2)
O1	Na1	O3A	77.78(6)	Na1	O1	Na2	100.19(7)
O1	Na1	N1A	135.89(7)	Na1	O1	Na2[1]	95.82(6)
O1	Na1	O3[1]	80.51(6)	Na2	O1	Na2[1]	90.82(6)
O1	Na1	O2C[2]	86.19(6)	C6	O1	Na1	126.83(16)
O1	Na1	O3C	78.96(6)	C6	O1	Na2	116.07(14)
O3[1]	Na1	Na2	97.36(4)	C6	O1	Na2[1]	119.69(16)
O3[1]	Na1	Na2[1]	39.50(4)	Na2	O3	Na1[1]	87.33(6)
O2C[2]	Na1	Na2	88.02(5)	C7	O3	Na1[1]	106.27(14)
O2C[2]	Na1	Na2[1]	131.27(5)	C7	O3	Na2	123.12(15)
O2C[2]	Na1	O3[1]	152.98(7)	C1	N1	Na2	122.40(16)
O3C	Na1	Na2	120.11(5)	C1	N1	C5	118.1(2)
O3C	Na1	Na2[1]	88.87(5)	C5	N1	Na2	118.46(16)
O3C	Na1	O3A	156.55(7)	N1	C1	C2	123.0(2)
O3C	Na1	N1A	137.89(7)	N1	C1	C6	113.1(2)
O3C	Na1	O3[1]	77.62(6)	C2	C1	C6	123.9(2)
O3C	Na1	O2C[2]	76.81(6)	C3	C2	C1	118.6(2)
Na1[1]	Na2	Na1	120.55(3)	C2	C3	C4	119.1(2)
Na2[1]	Na2	Na1[1]	61.09(3)	C3	C4	C5	118.7(2)
Na2[1]	Na2	Na1	59.46(3)	N1	C5	C4	122.6(2)
O3A	Na2	Na1[1]	125.85(6)	N1	C5	C7	115.7(2)
O3A	Na2	Na1	39.55(5)	C4	C5	C7	121.7(2)
O3A	Na2	Na2[1]	78.57(5)	O1	C6	O2	124.2(2)
O3A	Na2	O1[1]	86.88(6)	O1	C6	C1	120.8(2)
O3A	Na2	O1	76.67(6)	O2	C6	C1	115.0(2)

O3A	Na2	O3	156.63(7)	O3	C7	C5	113.0(2)
O3A	Na2	N1	138.27(7)	O4	C7	O3	125.5(2)
O3A	Na2	O3B	80.70(6)	O4	C7	C5	121.5(2)
O3A	Na2	O1S	88.43(7)	C6C	O2C	Na1[2]	131.31(17)
O1[1]	Na2	Na1	93.06(4)	C7C	O3C	Na1	134.77(16)
O1	Na2	Na1	37.80(4)	C5C	N1C	C1C	117.3(2)
O1	Na2	Na1[1]	95.84(5)	N1C	C1C	C2C	123.8(2)
O1[1]	Na2	Na1[1]	39.02(4)	N1C	C1C	C6C	115.0(2)
O1[1]	Na2	Na2[1]	43.72(4)	C2C	C1C	C6C	121.2(2)
O1	Na2	Na2[1]	45.46(4)	C1C	C2C	C3C	118.4(2)
O1	Na2	O1[1]	89.18(6)	C4C	C3C	C2C	118.2(2)
O3	Na2	Na1[1]	53.18(5)	C3C	C4C	C5C	119.6(2)
O3	Na2	Na1	163.64(6)	N1C	C5C	C4C	122.6(2)
O3	Na2	Na2[1]	112.08(6)	N1C	C5C	C7C	116.3(2)
O3	Na2	O1[1]	87.60(6)	C4C	C5C	C7C	121.1(2)
O3	Na2	O1	125.94(7)	O1C	C6C	C1C	115.1(2)
O3	Na2	N1	65.03(7)	O2C	C6C	O1C	121.2(2)
O3	Na2	O3B	75.94(6)	O2C	C6C	C1C	123.7(2)
N1	Na2	Na1	99.10(5)	O3C	C7C	C5C	118.4(2)
N1	Na2	Na1[1]	73.47(5)	O4C	C7C	O3C	124.2(2)
N1	Na2	Na2[1]	82.89(6)	O4C	C7C	C5C	117.4(2)
N1	Na2	O1[1]	104.71(7)	C7B	O3B	Na2	134.27(17)
N1	Na2	O1	63.83(6)	C5B	N1B	C1B	117.6(2)
O3B	Na2	Na1[1]	87.95(5)	N1B	C1B	C2B	123.5(2)
O3B	Na2	Na1	120.18(5)	N1B	C1B	C6B	115.4(2)
O3B	Na2	Na2[1]	118.38(6)	C2B	C1B	C6B	121.1(2)
O3B	Na2	O1[1]	77.97(6)	C1B	C2B	C3B	118.3(3)
O3B	Na2	O1	154.51(7)	C4B	C3B	C2B	119.0(2)
O3B	Na2	N1	140.59(7)	C3B	C4B	C5B	118.8(2)
O1S	Na2	Na1	94.80(6)	N1B	C5B	C4B	122.9(2)
O1S	Na2	Na1[1]	142.72(6)	N1B	C5B	C7B	115.2(2)
O1S	Na2	Na2[1]	151.75(7)	C4B	C5B	C7B	121.9(2)
O1S	Na2	O1	107.31(7)	O1B	C6B	C1B	115.4(2)
O1S	Na2	O1[1]	161.32(8)	O2B	C6B	O1B	121.3(2)
O1S	Na2	O3	89.57(7)	O2B	C6B	C1B	123.4(2)
O1S	Na2	N1	90.75(8)	O3B	C7B	O4B	124.8(2)
O1S	Na2	O3B	83.43(7)	O3B	C7B	C5B	119.1(2)
C6A	O1A	Na1	128.85(15)	O4B	C7B	C5B	116.1(2)
Na2	O3A	Na1	103.99(7)	C1S	O1S	Na2	129.97(19)

[1]-X,2-Y,1-Z; [2]-X,1-Y,1-Z

Table A7.6 Hydrogen Bonds.						
D	**H**	**A**	**d(D-H)/Å**	**d(H-A)/Å**	**d(D-A)/Å**	**D-H-A/ °**
O1A	H1A	O4C	0.92(3)	1.61(3)	2.513(2)	165(3)
O4A	H4A	O3B	0.93(3)	1.62(3)	2.548(2)	170(3)
O2	H2	O3C	1.08(4)	1.41(4)	2.488(2)	173(4)
O3	H3	O4B	1.09(4)	1.40(4)	2.471(2)	167(3)
O1C	H1C	O2	0.89(3)	2.08(3)	2.941(3)	162(3)
O1B	H1B	O4A	0.91(4)	2.08(4)	2.934(3)	155(3)
O1S	H1S	O4[1]	0.84(3)	1.94(3)	2.776(2)	172(3)

[1]1-X,2-Y,1-Z

Table A7.7 Hydrogen Atom Coordinates (Å×10^4) and Isotropic Displacement Parameters (Å^2×10^3).				
Atom	***x***	***y***	***z***	**U(eq)**
H1A	-2410(30)	7650(30)	7330(30)	60(11)
H2A	-1990(20)	11040(20)	10250(20)	29(7)
H3A	-510(20)	12930(20)	10970(20)	25(7)
H4A	2410(30)	12550(30)	8010(30)	73(12)
H4AA	900(20)	13130(20)	10020(20)	11(6)
H2	-1020(40)	6670(40)	4900(40)	121(16)
H2B	570(20)	6060(20)	2870(20)	20(7)
H3	3700(30)	11740(30)	5340(30)	82(12)
H3B	2100(20)	6280(20)	1960(20)	15(6)
H4	3450(20)	8130(20)	2620(20)	29(7)
H1C	-800(30)	4920(30)	3440(30)	50(10)
H2C	-3310(20)	1910(20)	3090(20)	15(6)
H3C	-4710(20)	2290(20)	4150(20)	20(7)
H4C	-4260(20)	4240(20)	5340(20)	19(7)
H1B	2180(40)	14300(30)	9180(30)	87(14)
H2BA	4970(20)	17270(20)	9720(20)	18(7)
H3BA	6170(20)	16830(20)	8600(20)	13(6)
H4B	5660(20)	14910(20)	7270(20)	21(7)
H1S	4520(30)	9970(30)	6990(30)	52(11)
H1SA	3880(30)	10550(20)	8820(20)	35(8)
H1SB	5070(30)	9880(30)	8850(30)	64(11)
H1SC	5210(30)	11210(30)	8860(30)	74(12)

List of Figures

Chapter 1 Introduction

List of Tables